



University of
Nottingham

UK | CHINA | MALAYSIA

Antiferromagnetic Domain Structure in Tetragonal CuMnAs films

A picturebook of domains, domain
walls and everything in between

Sonka Reimers

Thesis submitted to the University of Nottingham
for the degree of Doctor of Philosophy

30. November 2021

*Ein Bild sagt mehr als tausend Worte.
A picture is worth more than a thousand words.*

Abstract

In antiferromagnetic (AF) materials, magnetic moments align in a regular pattern such that the moments cancel perfectly in each magnetic unit cell. Hence AF materials do not show a net magnetisation and are largely inert against magnetic fields. Thus, the hidden order of antiferromagnets has only been revealed in the last century. For spintronic applications, the use of antiferromagnets promises numerous advantages compared to conventional spintronics based primarily on ferromagnetic (FM) materials. Amongst the key materials for AF spintronics research are tetragonal, antiferromagnetic CuMnAs films, because in addition to being antiferromagnetically ordered at room-temperature, tetragonal CuMnAs is one of only two conductive AF materials, for which it has been shown that the AF order can be manipulated with electrical currents. This has raised hopes for antiferromagnetic memory devices where the AF order in CuMnAs is switched electrical between two different states.

The magnetic moments in CuMnAs films form ferromagnetic sheets (parallel alignment) which are stacked antiparallel along the crystallographic c -direction. The spin axis is confined within the ab -plane, but varies on a microscopic scale, which produces a variety of different AF domain structures. This thesis addresses the question: “what underlies the AF domain structures and how can they be manipulated efficiently? ”

Visualising antiferromagnetic domain structures remains experimentally challenging, because the domains do not show a net magnetisation. Here, it is realised by combining photoemission electron microscopy (PEEM) with x-ray magnetic linear dichroism (XMLD), which yields sensitivity to the spin axis. These measurements require x-rays with precisely tunable energy. Therefore, this work has largely been performed at a synchrotron, namely Diamond Light Source.

Here, direct imaging of the response of the AF domain structure upon the application of electrical current pulses is used to study the microscopic mechanisms of electric switching in CuMnAs films. In the films studied here, the most efficient switching was found to occur via reversible AF domain wall motion induced by electrical current pulses of alternating polarity. The measurements also reveal the limiting factors of electrical switching in CuMnAs films, namely domain pinning which limits device efficiency and domain relaxation which hinders long-term memory. This illustrates that one needs to be able to precisely tune the material properties for a specific application in order to build efficient AF spintronic devices. Hence, the factors, which govern the AF spin textures in the CuMnAs films, need to be revealed.

This is done by combining direct imaging of the AF domain structure with

complementary techniques including electrical measurements, scanning X-ray diffraction and low-energy electron microscopy and diffraction (LEEM, LEED). The measurements reveal that the AF domain patterns are highly sensitive to the crystallographic microstructure including patterned edges and crystallographic defects. In particular, crystallographic microtwin defects are found to largely define the AF domain structure in non-patterned films. The coupling between defects and AF domains can lead to magnetostructural kinetics, where defects and AF domains grow together over weeks at room temperature and over minutes at slightly elevated temperatures of 50 °C to 70 °C. In devices, patterned edges are found to influence the AF domains over tens of micrometers. Combining the knowledge about the effects of microtwin defects and patterned edges on the AF structure helps to understand the microscopic effects of electric current pulses and can form the basis for targeted AF domain engineering. Although simple functionalities can be achieved even with devices fabricated from a single magnetic film, ferromagnetic spintronic research and technology has demonstrated that device performances can be significantly improved by using multilayer structures, which allows not only to tune particular material properties, but also to exploit a full range of other effects arising at the interface. These effects depend sensitively on the interface quality and the termination of the individual layers. The surfaces of the CuMnAs films studied here are found to be rough on a microscopic scale and micrometer-sized atomically flat areas are scarce if at all present. Nonetheless, the AF domain structure is found to be imprinted on the ferromagnetic domain structure in CuMnAs/Fe bilayer structures, albeit with each AF domain corresponding to several ferromagnetic domains with mutually antiparallel orientation.

In summary, this work provides a detailed investigation of the factors which govern microscopic AF domain structures in CuMnAs films. This is directly beneficial to current and future AF spintronics research on this particular material. In addition, it shows the level of detail at which the crystallographic microstructure and its effect on the AF order need to be known in order to understand, predict and tailor the equilibrium AF domain structure and AF domain kinetics in antiferromagnetic thin films.

Acknowledgements

Who actually reads the acknowledgments? I hope at least my supervisors whom I cannot thank enough. From the University of Nottingham, there are Kevin Edmonds and Pete Wadley. Without Pete, I would not even have started my Master's project let alone continued as a PhD student. He became not only my academic supervisor, but equally one of my first point of contacts for any questions, ranging from “how do I save my blueberry plant” to how do I balance research and social life, cope with family problems and much more. I was very lucky to have two great and very different academic supervisors: Even after 5 years, Kevin is still a miracle to me. He hides a strong humour behind a calm face. No matter, how stressful a situation or how heated a discussion, once Kevin enters the room, the atmosphere is calm again and what needs to be done will be done. Also, whenever you send him a document (abstract for a conference, yearly reports or a 250 pages long draft for a thesis), he will give you feedback within less than 24 hours (bare in mind, he does not only look after PhD students, but also teaches, works as a researcher and has a family). So, according to my theory, Kev's days are longer than 24 hours.

From Diamond, there is my Diamond supervisor Sarnjeet Dhesi, who always made sure that a “students” project (=my project) has priority over other beamline activities. Without Sarnjeet's constant support, this work would not have been possible. Neither would it have been possible without Francesco Maccherozzi, who has spent days and nights with me at the beamline and we have shared the pain and fun of working at the beamline. Since I moved to Didcot, Francesco helped me a lot and became an important friend also outside Diamond.

Equally important as my supervisors, were my fellow students from room C26. Syamashree (my office-, house- and soulmate), Ollie (our in-house artist, who already won a nobel prize), Luke X. (the sensible and mature one of us) and Stu (our coder and handyman who'll fix bikes, chairs and everything else), have shared most of my PhD time with me.

I also would like to thank Richard Champion, Filip Krizek and Vit Novak, not only for providing me with (usually excellent) samples, but also for motivating me to not give up research straight away (even if you might not know, you did).

Last but not least, I'd like to thank my boyfriend Dan for his support during the time of thesis-writing: for coping with my changing moods and for making sure that I still get enough sleep and for giving up his living room to make it my thesis-writing office.

There are many other people who have made the years of my PhD so enjoyable. Unfortunately I cannot list them all.

List of Publications

Publications to which the author of this thesis contributed as a main or joint main author, which directly correspond to chapters of this thesis:

1. P. Wadley, S. Reimers, M. J. Grzybowski, C. Andrews, M. Wang, J. S. Chauhan, B. L. Gallagher, R. P. Champion, K. W. Edmonds, S. S. Dhesi, F. Maccherozzi, V. Novak, J. Wunderlich, and T. Jungwirth, “Current polarity-dependent manipulation of antiferromagnetic domains,” *Nat. Nanotechnol.*, vol. 13, no. 1, pp. 362–365, mar 2018. [Online]. Available: <https://www.nature.com/articles/s41565-018-0079-1>

cf. chapter 4

2. S. Reimers, D. Kriegner, O. Gomonay, D. Carbone, F. Krizek, V. Novak, R. P. Champion, F. Maccherozzi, A. Björling, O. J. Amin, L. X. Barton, S. F. Poole, K. A. Omari, J. Michalicka, O. Man, J. Sinova, T. Jungwirth, P. Wadley, S. S. Dhesi, and K. W. Edmonds, “Defect-driven antiferromagnetic domain walls in CuMnAs films,” *Nat. Comm.*, vol. 13, no. 724, feb 2022. [Online]. Available: <https://www.nature.com/articles/s41467-022-28311-x>

cf. chapter 5

Other publications to which the author contributed, more loosely related to this work:

- F. Krizek, S. Reimers, Z. Kaspar, A. Marmodoro, J. Michalicka, O. Man, A. Edstrom, O. J. Amin, K. W. Edmonds, R. P. Champion, F. Maccherozzi, S. S. Dnes, J. Zubac, J. Zelezny, K. Vyborny, K. Olejnik, V. Novak, J. Ruzs, J. C. Idrobo, P. Wadley, and T. Jungwirth, “Atomically sharp domain walls in an antiferromagnet,” *Science Advances*, vol. 8, issue 13, , mar 2022. [Online]. Available: <https://www.science.org/doi/10.1126/sciadv.abn3535>
- M. Wang, C. Andrews, S. Reimers, O. J. Amin, P. Wadley, R. P. Champion, S. F. Poole, J. Felton, K. W. Edmonds, B. L. Gallagher, A. W. Rushforth, O. Makarovskiy, K. Gas, M. Sawicki, D. Kriegner, J. Zubac, K. Olejnik, V. Novak, T. Jungwirth, M. Shahrokhvand, U. Zeitler, S. S.

Dhesi, and F. Maccherozzi, “Spin flop and crystalline anisotropic magnetoresistance in CuMnAs,” *Phys. Rev. B*, vol. 101, p. 094429, Mar 2020. [Online]. Available: <https://link.aps.org/doi/10.1103/PhysRevB.101.094429>

- Z. Kaspar, M. Surynek, J. Zubac, F. Krizek, V. Novak, R. P. Campion, M. S. Wörnle, P. Gambardella, X. Marti, P. Nemeč, K. W. Edmonds, S. Reimers, O. J. Amin, F. Maccherozzi, S. S. Dhesi, P. Wadley, J. Wunderlich, K. Olejnik, and T. Jungwirth, “Quenching of an antiferromagnet into high resistivity states using electrical or ultrashort optical pulses,” *Nat. Electron.*, vol. 4, p. 30, 2021.
- T. Janda, J. Godinho, T. Ostatnický, E. Pfitzner, G. Ulrich, A. Hoehl, S. Reimers, Z. Soban, T. Metzger, H. Reichlova, V. Novak, R. P. Campion, J. Heberle, P. Wadley, K. W. Edmonds, O. J. Amin, J. S. Chauhan, S. S. Dhesi, F. Maccherozzi, R. M. Otxoa, P. E. Roy, K. Olejnik, P. Nemeč, T. Jungwirth, B. Kaestner, and W. J., “Magneto-Seebeck microscopy of domain switching in collinear antiferromagnet CuMnAs,” *Phys. Rev. Mater.*, vol. 4, no. 9, p. 094413, sep 2020. [Online]. Available: <https://journals.aps.org/prmaterials/abstract/10.1103/PhysRevMaterials.4.094413>

Contents

Abstract	i
Acknowledgements	iii
List of Publications	v
1 Introduction	1
1.1 Spintronics	2
1.1.1 Antiferromagnetic spintronics	2
1.2 Basics of (antiferro-)magnetic materials	5
1.2.1 Magnetic order parameters and order-disorder transition	8
1.2.2 Magnetic interactions and energy contributions	9
1.2.3 Magnetic textures, domains and domain walls	15
1.2.4 AF dynamics	18
2 Methods and material	23
2.1 Copper manganese arsenide films	23
2.2 Material growth	27
2.3 Device fabrication	27
2.4 Synchrotron radiation	28
2.4.1 Beamline I06 at Diamond Light Source	32
2.4.2 Nanomax beamline, MAX IV	33
2.5 X-ray dichroism	35
2.5.1 X-ray (magnetic) circular dichroism	36
2.5.2 X-ray (magnetic) linear dichroism	37
2.6 Electron microscopy	41
2.6.1 LEEM	42

2.6.2	Photoemission electron microscopy (PEEM)	46
2.7	The PEEM-endstation on I06, Diamond Light Source	48
2.7.1	Operation as LEEM	53
2.7.2	Operation as PEEM	53
2.7.3	Alignment	54
2.8	X-PEEM measurement details	55
2.8.1	X-ray absorption spectroscopy	55
2.8.2	XMLD-PEEM image protocol	56
2.8.3	XLD-PEEM protocol	57
2.8.4	XMCD-PEEM protocol	58
2.8.5	Image normalisation and image processing	59
2.9	LEEM measurement details	60
2.9.1	Material and surface preparation	60
2.9.2	Experiment details	62
2.10	Electrical measurements	63
2.11	Scanning X-ray diffraction measurements	65
2.11.1	Reciprocal space maps	66
2.11.2	Microtwin mapping with scanning X-ray microscopy (SXDM)	66
2.12	Modelling AF textures in the vicinity of microtwins	69
3	Antiferromagnetic domain structure in CuMnAs thin films	74
3.1	Introduction	74
3.2	Methods	76
3.2.1	XMLD-PEEM	76
3.2.2	Interpreting XMLD-PEEM images	76
3.2.3	Defining Néel vector maps from spin axis maps	81
3.3	Results and interpretation	83
3.3.1	Uniaxial anisotropy in thin CuMnAs films	83
3.3.2	Biaxial anisotropy in 50 nm CuMnAs/GaP(001) films	85
3.3.3	Uniaxial 50 nm CuMnAs/GaP(001) films	89
3.3.4	AF domains in relaxed CuMnAs films	92

3.3.5	AF domains in $\text{CuMnAs}_{0.9}\text{Sb}_{0.1}/\text{GaAs}(001)$	95
3.4	Summary and conclusion	97
4	Electrical manipulation of antiferromagnetic domains	99
4.1	Introduction	99
4.2	Methods	101
4.3	Results and interpretation	103
4.3.1	Orthogonal switching	104
4.3.2	Polarity switching	108
4.3.3	Switching mechanism: domain wall motion	116
4.4	Additional observations	118
4.5	Summary and conclusion	122
5	Defect-driven antiferromagnetic domains in CuMnAs	126
5.1	Introduction	126
5.2	Methods	129
5.2.1	XMLD-PEEM imaging	130
5.2.2	Structural imaging using XLD-PEEM	130
5.2.3	Micromagnetic simulations	131
5.3	Results and interpretation	131
5.3.1	Imaging of defect patterns	131
5.3.2	Correlation between defect and AF domain structure	132
5.3.3	Coupling mechanism	138
5.3.4	Discussion	139
5.4	Conclusion and outlook	143
6	Edge-imposed anisotropy in CuMnAs thin film devices	145
6.1	Introduction	145
6.2	Methods	151
6.3	Results and interpretation	153
6.3.1	Patterning along the magnetic easy axes	154
6.3.2	Patterning along the magnetic hard axes	160

6.3.3	AF domains in devices with complex geometries	164
6.3.4	AF domain walls in the vicinity of edges	166
6.3.5	AF domain walls as a measure of edge-imposed anisotropy	168
6.4	Summary and conclusion	177
7	Magnetostructural kinetics in CuMnAs films	180
7.1	Introduction	180
7.2	Methods	181
7.3	Results and interpretation	184
7.3.1	Patterning-induced magnetostructural kinetics	184
7.3.2	Heating-induced magnetostructural kinetics	188
7.4	Summary and conclusion	204
8	Surface and interface effects in CuMnAs films	208
8.1	Introduction	208
8.2	Methods	210
8.2.1	X-PEEM and LEEM	211
8.3	Results	214
8.3.1	Domain imprinting in Fe–CuMnAs - bilayers	214
8.4	Conclusion and outlook	231
9	Concluding remarks	234
	Bibliography	236
	Appendices	250
A	Modelling antiferromagnetic domain walls	250
B	Device Fabrication	253
B.1	Photolithography and chemical wet etching	253
B.2	Electron beam lithography and ion beam milling	254
C	Supplementary Videos	255
D	List of Abbreviations	257

List of Tables

2.1	Beamline specification for beamline I06, DLS	33
2.2	Beamline specification of the NanoMAX beamline, MAX IV . .	35
4.1	Onset current pulse amplitudes of current-polarity dependent switching in a series of devices.	115

List of Figures

1.1	Linear chain of Fe-atoms with antiferromagnetic coupling	3
1.2	Antiferromagnetic domains in CuMnAs	4
1.3	Magnetic unit cell vs chemical unit cell in a collinear AF.	7
1.4	Spin-orbit fields in GaAs and Si	14
1.5	Torques on AF order.	20
2.1	Unit Cell of tetragonal CuMnAs and substrate registry	24
2.2	Crystallographic defects in CuMnAs films	26
2.3	Layer structure	27
2.4	From dipole radiation to synchrotron radiation	29
2.5	Schematic of a Synchrotron	32
2.6	Layout of the beamline I06, DLS	33
2.7	Layout of the NanoMAX beamline, undulator and x-ray optics	34
2.8	X-ray absorption at the Mn $L_{2,3}$ edge in tetragonal CuMnAs.	39
2.9	Angular dependence of the size of the XMLD signal in CuMnAs.	41
2.10	Schematic of a LEEM instrument	43
2.11	Omicron cartridges used on the PEEM-endstation, I06	48
2.12	PEEM endstation on beamline I06, DLS	50
2.13	Optics of the LEEM instrument on I06	51
2.14	CuMnAs surface before and after decapping	61
2.15	Measurement geometries in 8-contact devices	63
2.16	Measurement geometries in 4-contact devices	65
2.17	SXDM microtwin mapping protocol	67
2.18	Structure of microtwin defects - Schematic	70

2.19	Magnetic anisotropy energy of the matrix and inside a microtwin	72
3.1	Identifying AF domain Walls in X-PEEM images	78
3.2	Unique definition of the spin axis from the XMLD-signals measured with $\vec{E} [110]$ and $\vec{E} [010]$	80
3.3	Defining Néel vector maps from spin axis maps	82
3.4	Examples of spin axis maps which are not compatible with continuous Néel vector maps	83
3.5	AF domains in 20 nm CuMnAs/GaP(001)	85
3.6	AF domains in biaxial 50 nm CuMnAs/GaP(001)	86
3.7	AF domains in a 50 nm CuMnAs/GaP(001) in the vicinity of a MnAs inclusion	88
3.8	AF domains in a 50 nm CuMnAs/GaP(001) film with unequal domain population	90
3.9	AF domains in a 50 nm CuMnAs/GaP(001) with strong preference for one of the $\langle 110 \rangle$ domains	92
3.10	AF domains in a 50 nm CuMnAs/GaP(001) film with uniaxial anisotropy along one of the $\langle 110 \rangle$ directions.	93
3.11	AF domains in 45 nm CuMnAs/GaAs(001) films	94
3.12	AF domains in a 100 nm CuMnAs/GaP(001) film.	95
3.13	AF domains in 50 nm CuMnAs(0.9)Sb(0.1)/GaAs(001)	97
4.1	Device used in electrical measurements	102
4.2	X-PEEM device	104
4.3	XMLD-PEEM observation of orthogonal, polarity-independent switching	106
4.4	Electrical measurements of orthogonal switching along the $\{100\}$ directions.	108
4.5	Electrical measurements of orthogonal switching along the $\{110\}$ directions.	109

4.6	XMLD-PEEM Observation of polarity-dependent manipulation of AF domains.	111
4.7	Purely electrical measurements of polarity-dependent switching.	113
4.8	Current-amplitude dependence of the current-polarity dependent switching.	114
4.9	Mechanism of current-polarity dependent AF domain manipulation via domain wall motion.	117
4.10	Efficiency of orthogonal switching in the “virgin” sample.	120
4.11	Effect of a, potentially longer, 50 mA current on the AF domain structure.	121
4.12	Effect of orthogonal switching after the 50 mA current.	123
4.13	Confirmation of the sample integrity.	124
5.1	HAADF-STEM images of a microtwin	128
5.2	SXRD measurements of microtwins	133
5.3	Comparison of microtwin density and AF domain size	134
5.4	AF domain structure and direct comparison to microtwin pattern in a blanket 50 nmCuMnAs/GaP(001) film	136
5.5	Coupling Mechanism between AF domains and microtwins	138
5.6	Comparison of micromagnetic simulations and experiment	140
6.1	Origin of domains in FM single crystals	147
6.2	Lithography masks with geometric shapes	152
6.3	Effect of patterned edges along the [110] and $[\bar{1}10]$ magnetic easy axes.	156
6.4	Origin of Lens Domains	157
6.5	Patterning along the easy axis in a layer with intermediate microtwin density	159
6.6	Comparison of the AF domains and microtwin patterns in bars aligned with the magnetic hard axis	161

6.7	Patterning along the hard axis in devices with intermediate microtwin density	163
6.8	Effect of patterning along the magnetic hard axis in mostly microtwin-free devices	164
6.9	AF domain structures in a variety of shapes	166
6.10	Domain wall orientation in the vicinity of edges	167
6.11	Simulated and measured domain wall profiles	171
6.12	Protocol to measure domain wall widths	173
6.13	Dependence of the widths of 180° domain walls on the lateral position in patterned bars	174
6.14	Dependence of the widths of 90° domain walls in corners on the distance to the corner	176
7.1	Magnetostructural kinetics in CuMnAs in patterned bars	185
7.2	Progression of AF domain structures in patterned bars	186
7.3	AF domain structure in a bar oriented along the CuMnAs [100] 5 days and 3.5 months after device fabrication	187
7.4	Direct Imaging of AF dynamics in temperature cycles, Sample A cycle I	189
7.5	Formation of AF domains upon cooling through the Néel temperature, Sample A cycle I	191
7.6	AF domain changes at intermediate temperatures, when cooling, Sample A cycle I	191
7.7	Close-up of AF domain growth when cooling, Sample A cycle I .	193
7.8	Direct Imaging of AF dynamics during heating, Sample A cycle II	194
7.9	Direct Imaging of AF dynamics during cooling, Sample A, cycle II	195
7.10	Microtwin configuration at high temperatures	200
7.11	Reformation of the microtwin pattern in cooling, Sample B . . .	200
7.12	Correlation of AF domain changes and microtwin growth at intermediate temperatures, sample B	202

7.13	Direct Imaging of AF dynamics during cooling, Sample B	203
7.14	Examples of AF domain and microtwin growth at intermediate temperatures	204
8.1	Comparison of AF and FM domains in CuMnAs/Fe bilayers . .	215
8.2	Length-scale of FM domains in CuMnAs/Fe bilayers	216
8.3	Magnetic hysteresis measurements of Fe/CuMnAs bilayers . . .	217
8.4	Decay of the magnetisation of Fe/CuMnAs bilayers	218
8.5	AF and FM structure in a CuMnAs/Fe bilayer after exposure to a small magnetic field	219
8.6	LEED-IV data	224
8.7	Comparison of LEEM imaging of the surface structure and XMLD- PEEM imaging of the AF domains on an exposed CuMnAs surface	226
8.8	Potential terminations of exposed CuMnAs surfaces tested in LEED-IV fitting	227
8.9	Effect of possible, non-trivial CuMnAs step edges at the inter- faces on the Fe magnetisation in CuMnAs-Fe bilayers	232

Chapter 1

Introduction

Magnetic phenomena have fascinated humans for millennia. Written records of the attraction of iron by lodestone dating back several centuries BC can be found in texts from ancient Greece, China and ancient India, although it is assumed that these basic phenomena had already been observed prior to the written records [1, 2]. Even if the origin of the effects might have remained elusive or have been misattributed, the magnetic properties of lodestone were already used for applications, such as early compasses for navigation in ancient China [2] or “medical purposes”, the removal of arrow-heads, in ancient India [3]. All early observations and applications were based on ferromagnetic (FM) or ferrimagnetic materials, which respond strongly to applied magnetic fields. In a ferromagnet, the interaction between microscopic magnetic moments favours a parallel alignment of all moments. Therefore these materials can spontaneously order, which produces a net magnetisation and are easily magnetised by magnetic fields. Ferrimagnets can be thought of as two interlaced, antiparallel coupled ferromagnetic lattices whose magnetic moments have a different size, so that in the ordered state a non-vanishing magnetisation remains. .

1.1 Spintronics

Nowadays, the application of magnetic phenomena has become indispensable in every day life, with examples ranging from simple fridge magnets, through bicycle dynamos up to magnetic hard-disks for data storage. They consist of magnetic thin films and the magnetisation in a specific section is the physical realisation of a single bit with two logical states [4]. Magnetic hard-disks are one of the most prominent examples of a “spintronic” application. Spintronics (short for spin electronics or spin transport electronics) uses the spin moment of the electrons in addition to the electronic charge in micro- and nano-electronics [5]. The research field has been initiated by experimental discoveries of spin-dependent electron transport phenomena in the second half of the last century, including (but not limited to) giant magnetoresistance (GMR) and tunneling magnetoresistance (TMR). These phenomena have been crucial for the development of read-heads for magnetic hard-disks which are sensitive enough to allow for (market-competitively) small bit sizes.

The field of spintronics spans a variety of different research directions, reviewed for example in [6]. Considerable market share has been mainly achieved in data storage technology, using ferro- or ferrimagnetic materials with a net magnetic moment. Other fields of spintronic research are claimed to be promising for future applications, with potentially highly advantageous properties when compared to current technology. Amongst those is antiferromagnetic spintronics which is concerned with the use of antiferromagnetic (AF) materials as active components in a device.

1.1.1 Antiferromagnetic spintronics

In contrast to ferro- and ferrimagnets, antiferromagnets (AF) do not produce a net magnetisation in their ordered state: the magnetisation of the magnetic moments alternates between individual atomic sites so that their contributions cancel perfectly on non-atomic length scales [7]. Yet, their alignment is not

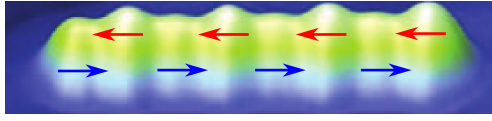


Figure 1.1: “One-dimensional” antiferromagnet. Scanning tunneling microscopy image of 8 Fe-atoms with antiferromagnetic coupling. The arrows show the spin direction. Figure from [8] reprinted from [9].

arbitrary, but characterised (in most cases) by a certain alignment axis, as shown in Fig. 1.1. Exploiting the magnetic order for spintronic devices based on antiferromagnets relies on being able to manipulate (set) and probe the AF alignment direction. This is significantly more challenging than manipulating and measuring the magnetisation direction in materials with a net magnetisation as they respond and create macroscopic magnetic fields. Thus antiferromagnets have long played only a secondary role in spintronic applications and research [8, 10].

The field was kick-started by the experimental and theoretical discovery of novel ways to manipulate AF order, *e.g.* by electric currents [11]. Since then, antiferromagnetic spintronics has quickly garnered lots of attraction, because spintronic devices based on AF materials potentially offer numerous advantages compared to their FM counterparts, highlighted in multiple review articles [8, 10, 12]. For example intrinsic AF dynamics are several orders of magnitude faster than FM dynamics; AF order is robust against external magnetic field perturbations of up to tens of teslas. The lack of stray fields prevents magnetic “cross-talk” which puts a lower limit on the distance between two independent, active FM components. The FM stray fields are also a main source for energy dissipation in FM devices and self-interaction with a field puts an upper limit on the speed at which FM domain walls can travel [13]. In summary, smaller, faster and more efficient devices, might be realised by replacing current spintronic devices with purely AF devices.

Although young, AF spintronic research already covers many different research areas, including the study of AF textures like skyrmions or vortices, materials research, and spin current generation, transmission and detection, with po-

tential applications including amongst others logic computing, neuromorphic computing, artificial intelligence and data storage. The advances made in AF spintronics are summarised in different review articles [8, 10, 12, 14–16].

Despite the early promises, novel AF spintronic devices are not on the market yet, partially because realising efficient AF spintronic devices, requires not only the discovery of novel effects (to manipulate and probe AF order) and a proof of principle, but also requires the ability to precisely tune the material properties to the application, which requires an understanding of the AF structure at the microscale. This requires detailed investigations, at the boundary between AF spintronics and materials research, which thus far, have been scarce.

In contrast, ferromagnetic spintronics can build on decades of studying ferromagnetic domains and materials research. In ferromagnets, domain formation is often governed by magnetostatic effects due to macroscopic FM magnetisation. In AFs, these are negligibly small so that the study of AF domains is also relevant for fundamental research, since the mechanisms governing domain formation in AFs are still under debate.

This thesis attempts to fill the gap by studying the antiferromagnetic (domain) structure in tetragonal CuMnAs films. Examples of AF domains in tetragonal CuMnAs are shown in Fig. 1.2. Tetragonal CuMnAs is a prime

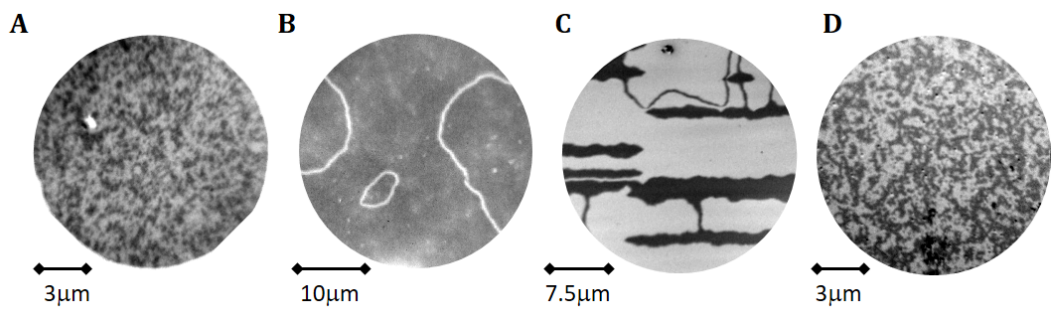


Figure 1.2: *Antiferromagnetic domains in CuMnAs imaged with X-ray photoemission electron microscopy.* Regions with horizontal magnetic axis are dark, regions with vertical magnetic are light, only the axis of the spin moments, not the direction is resolved. The individual panels show different samples. **A:** 80 nm CuMnAs/GaAs. **B:** 50 nm CuMnAs/GaP. **C:** 50 nm CuMnAs/GaP, slightly different growth conditions. **D:** 50 nm CuMnAs(0.9)Sb(0.1)/GaAs.

material candidate for future AF spintronic applications, since its AF order

can be manipulated by electrical currents as demonstrated in chapter 4. It has been primarily considered for memory and logic applications, with the “0”s and “1”s encoded as horizontal and vertical magnetic axis.

How to read this thesis The following section will give a brief introduction of the basic physics of antiferromagnets, which can be skipped by a reader with sufficient background in physics. The second chapter describes the measurement techniques in detail, which are relevant in order to reproduce the experimental results, but not necessarily required to understand the results presented in chapters 3-8. These chapters are aimed to be mostly self-contained and can be read individually. They include a brief overview of different domain morphologies in CuMnAs in chapter 3, describe the manipulation of AF domain walls in CuMnAs with electrical currents in chapter 4, elucidate the direct coupling between AF domains and crystallographic defects in chapter 5, investigate the effect of patterned edges in chapter 6, report on magnetostructural kinetics 7, and shows first measurements of surface and interface effects which might provide a tool to investigate ultrasharp AF textures in chapter 8. All chapters point at an immense importance of (crystallographic) defects for the AF properties in CuMnAs thin films, which allows for AF domain engineering (started in chapters 6, 7), unprecedented in FM materials which are often governed by magnetostatic effects, and highlight the need for combined AF spintronics and materials research.

1.2 Basics of (antiferro-)magnetic materials

The scientific background of a study of the magnetic structure in a crystalline material necessarily comprises basics of electromagnetism and solid state physics including crystallography and solid state magnetism. Introducing all of those concepts would span several long books and is not attempted here. Readers without the relevant background will find a much better intro-

duction in one of the many textbooks, for examples references [17–19]. Only some basic properties of antiferromagnetic magnetic as opposed to other types of magnetic materials are briefly described below.

Magnetic materials Magnetically ordered materials are formed of local or itinerant magnetic moments, which interact with each other. The interaction between the localised moments, “exchange interaction” or “magnetic exchange” (see below), can induce spontaneous order. The size of the magnetic moments is fixed, which gives an upper boundary on the magnetisation (per unit volume). The maximum magnetisation is achieved, when all moments are aligned parallel with each other, the “saturated state”, and correspondingly the maximum magnetisation is referred to as the saturation magnetisation M_{sat} (m_{sat} , if defined per unit volume). In magnetically ordered crystals the localised moments are associated with specific lattice positions, the “magnetic lattice”.

In ferromagnetic (FM) crystals, the periodicity of the magnetic lattice coincides with the periodicity of the crystal lattice and parallel alignment of the localised moments is favoured [19]. Ferrimagnetic and antiferromagnetic (AF) crystals consist of two or more magnetic sublattices, which align antiparallel with each other in collinear AFs or collinear ferrimagnets or at a non-zero rotation angle in noncollinear AFs and non-collinear ferrimagnets. In an antiferromagnet (AF), the localised moments of the different sublattices perfectly compensate each other in each magnetic unit cell, which can be larger than the chemical unit cell. In ferrimagnets the magnetic moments of the sublattices have different saturation magnetisation and thus, a net magnetisation remains in each magnetic unit cell [19]. A textbook example of a collinear antiferromagnetic crystal, where the magnetic unit cell is larger than the chemical unit cell is MnO, shown in Fig. 1.3. The lower symmetry of the magnetic unit cell compared to the crystalline unit cell leads to additional diffraction spots in the magnetically ordered state compared to the disordered state.

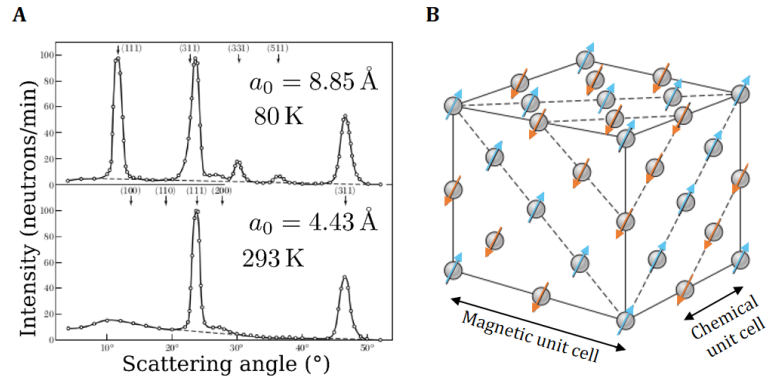


Figure 1.3: Magnetic unit cell vs chemical unit cell in a collinear AF. **A:** Neutron-diffraction scans of MnO with (top) AF magnetic order and without magnetic order (bottom) above the critical temperature, figure from [20] after C.G. Shull, W.A. Strauser and E.O. Wollan. **B:** Sketch of the MnO-lattice in the AF ordered phase. The circles show the Mn atoms, the arrows indicate the direction of the localised magnetic moments, using different colours for the two magnetic sublattice. Figure (slightly adapted) from reference [20].

Semi-classical description and Néel state The first theory that allowed for both ferromagnetic and antiferromagnetic or ferrimagnetic order was developed in the 1930s by Louis Néel [21–23]. The model introduced a coupling energy between neighbouring magnetic moments $E_c = \omega \cos(\alpha)$, where α denotes the angle between the magnetic moments and ω is a coupling constant. Néel allowed the coupling constant ω to be either negative or positive (negative in the ferromagnetic case), and concluded that, if positive, then the magnetic moments must tend to align in pairs of antiparallel orientation. This state of perfect AF order is called the Néel state. The model correctly predicts the magnetic susceptibility of AFs and also led to the discovery of another important principle: Every ferromagnetic phenomenon that is an even function of the magnetisation, should equally be present in antiferromagnets, whereas phenomena that are an odd function of the magnetisation cannot occur in collinear antiferromagnets [10]. Néel’s principle has been important in extending spin-dependent transport phenomena in FM systems to collinear AFs, but it is generally not applicable for AFs with complex geometries.

Néel state vs quantum state The classical approach, as in Néel's model, breaks down at very low temperatures. Then, only a quantum mechanical description is applicable [10]. Generally speaking, quantum mechanical descriptions predict more complex behaviour for AF systems than for FM systems. For example, the ground state of the most simple AF model system, a collinear, one-dimensional AF chain with only nearest neighbour interaction, is not the Néel state; the energy of the system can be reduced further by the onset of spin waves [10].

1.2.1 Magnetic order parameters and order-disorder transition

For non-atomic descriptions, such as a mean-field description it is convenient to introduce an order parameter which describes the magnetic order [19]. Common order parameters include the net magnetisation \vec{M} per volume or unit cell for ferromagnets and ferrimagnets and the so-called Néel vector \vec{L} defined as the difference of the sublattice magnetisations, $\vec{L} = \vec{M}_A - \vec{M}_B$. In the case of perfect parallel/antiparallel alignment, the size of the order parameter is constant and only its direction varies. In this case it can be sufficient to consider the reduced order parameter scaled to unity, *e.g.* $\vec{l} = \vec{L}/|\vec{L}|$, where $|\vec{L}| = \sqrt{\vec{L} \cdot \vec{L}}$. In many cases, the magnetic order varies spatially, which requires a local order parameter, *e.g.* the local magnetisation density $\vec{m}(x, y, z)$ or local (reduced) Néel vector $\vec{l}(x, y, z)$. This quantity is averaged over several unit cells in continuous models, such as mean-field descriptions. In thin films, often the depth-dependence is neglected, *i.e.* $\vec{l}(x, y, z) = \vec{l}(x, y)$ ($\vec{m}(x, y, z) = \vec{m}(x, y)$).

Magnetically ordered materials undergo an order-disorder transition at a critical temperature above which the magnetic order is lost, *i.e.* the order parameter vanishes [19]. It is defined by the stiffness of the exchange between the localised moments. This temperature is called the Curie temperature or Curie

point for ferro- and ferrimagnets, or the Néel temperature in the AF case.

1.2.2 Magnetic interactions and energy contributions

Any description of a system typically starts by identifying the relevant interactions and contributions to the energy of the system.

Exchange interaction and exchange energy

Exchange interaction is a quantum mechanical effect that arises from the way in which indistinguishable particles form a quantum state and cannot be derived from purely classical physics [19]. The wave function of indistinguishable particles be either symmetric (bosons) or antisymmetric (fermions) under the exchange of two particles, *i.e.* obey exchange symmetry (hence exchange interaction). Relevant for the magnetism in solids is exchange interaction between electrons. For electron, the total wave functions can be written as the product of an orbital wavefunction and a spin wave function. As electrons are fermions this implies that the orbital wave function must be symmetric and the spin wave function antisymmetric or the other way round. The energy of the system is governed by the kinetic and potential energy (electrostatic interaction between electrons and nuclei), which depend only on the orbital part of the wave function and can vary significantly between the symmetric and the antisymmetric solution. The energy difference is the “exchange energy”. If the symmetric solution of the orbital wave function has lower energy, it implies that the state of minimal energy is antisymmetric in the spin wave function (“antiferromagnetic interaction”). If the antisymmetric of the orbital wave function has lower energy, then the state with minimal energy shows “ferromagnetic interaction”. The antisymmetry requirement of the fermionic wave function implies the Pauli exclusion principle so that (magnetic) exchange interaction is often described as a result of the electrostatic interaction combined with the Pauli exclusion principle.

Often it is convenient to describe the multi-electron state as a combination of individual electron state (atomic orbitals) which overlap (direct exchange). In this case the size and sign of the exchange energy depends on the overlap of the atomic orbitals and hence on the distance of the atomic nuclei and the shape and orientation of the atomic orbitals. This implies that for localised electronic states the exchange interaction is short-range and that it is often sufficient to consider nearest-neighbour interaction. However, exchange energy can also occur between localised electronic states that do not overlap directly, but which both overlap with an atomic orbital of a non-magnetic intermediary atom. This is referred often referred to as Super-exchange and observed for example in insulators such as MnO. Here the magnetic moments are localised around the Mn atoms, but the exchange occurs via coupling to electronic states of the oxygen atoms. In metals, exchange between localised electron states (moments) can also be mediated through a coupling to the delocalised conduction electrons. This is called indirect exchange, whereas itinerant exchange in metals refers to coupling between conduction electrons. For further details of the different concepts see [24].

The exchange energy is one of the most important contributions to the total energy in magnetic materials [19, 25]. Misalignment between neighbouring moments in an atomistic picture becomes a local gradient of the magnetic order parameter in the continuum description, $\nabla\vec{l}$. The associated increase of exchange energy is modelled as $W_{\text{ex}} = A(\nabla\vec{l})^2$, where the proportionality constant A is the material-specific exchange constant, in a continuum description [25]. The associated forces with this model are short-range and isotropic. Hence, AF exchange energy is minimal if the Néel vector of a sample is constant within the sample.

For certain symmetries, the relativistic spin-orbit coupling (see below) can add an asymmetric correction to the exchange energy favouring alignment of neighbouring spins at an angle. The asymmetric exchange interaction, also known as the Dzyaloshinskii–Moriya interaction (DMI), favours a canting of

otherwise perfectly parallel or antiparallel spins. It can induce a small ferromagnetic component in antiferromagnets and can stabilise chiral magnetic structures [26–28].

Spin-Orbit Interaction

Spin-orbit-interaction (SOI) or Spin-orbit coupling (SOC) forms the basis of many spintronic applications. It is a relativistic effect that couples the spin moment with the orbital moment of an electron. At an atomic level, SOC can be explained as follows: in the rest frame of an orbiting electron, the charged nucleus becomes a moving charge and consequently produces a magnetic field depending on the orbital motion of the nucleus. This field exerts a torque on the electron's spin moment that reorients it. Similarly, reorientation of the spin moment of an electron creates a torque on the orbital moment. This coupling introduces a spin-dependent splitting of the energy states [19]. The SOI can be relevant for both localised electrons and delocalised (conducting) electrons and thus is responsible for several macroscopic phenomena, including magnetocrystalline anisotropy [8], *i.e.* preferred magnetic axes (see below), anisotropic magnetoresistance (AMR) [8] and can couple charge flow with spin flow: an electrical current thus can give rise to a non-equilibrium spin polarisation at the surface (inverse spin Hall effect) or in the bulk of the material (inverse spin galvanic Effect) and vice versa spin-currents or spin polarisations can induce electrical currents [8].

Magnetocrystalline anisotropy

In most materials, not all orientations of the Néel vector (or the magnetisation for FMs) are energetically equal and alignment of the order parameter with certain crystallographic axes, called magnetic easy axes, is energetically favoured. The opposite, energetically unfavourable directions are called magnetic hard axes. Magnetocrystalline anisotropy has only axial and not directional properties, *i.e.* two antiparallel orientations of the Néel vector are equiv-

alent [25]. The modelling of the anisotropy energy depends on the symmetry of the system. Uniaxial magnetic anisotropy energy is typically modelled as $W_{an} = K \sin^2(\theta)$, where θ is the angle between the magnetic order parameter and the magnetic easy axes and K is the anisotropy constant. Similarly $W_{an} = K \cos^2(\theta)$ is used for a single magnetic hard axis. More complex geometries require the use of several anisotropy constants K_i , $i = 1 \dots n$ along different directions and/or terms scaling with \sin^4 or higher order [25].

The physical origin of magnetocrystalline anisotropy is spin-orbit interaction.

Exchange coupling across interfaces

Exchange interaction can occur not only within one material, but also between surface spins at the interfaces in bilayer or multilayer structures. The layers can be ferromagnetic, ferrimagnetic, antiferromagnetic or any combination of the two. The interface coupling can occur when the layers are in direct contact or separated by a nonmagnetic spacing layer which acts to mediate the coupling. Several coupling mechanisms have been suggested (see for example [29–31]), but are still subject to debate. For a given system, identification of the coupling mechanism is not always possible [29, 32]. Often, an intuitive model with an interfacial energy term depending on the angle between the magnetic axes is used. If one layer is “fixed” than this coupling term can act like an additional (unidirectional) anisotropy for the other layer. For example, fixing the Néel vector orientation of an AF layer can serve to harden an FM layer and shift the hysteresis loops, which is widely exploited in the read-heads of magnetic hard-disks. For further information see [29–32].

Magnetostrictive energy

Magnetoelastic energy results from a coupling between the magnetisation and the elastic properties of the sample, called magnetostriction [25]. Typically, either a contraction or an elongation of the material along the magnetisation direction is observed. In confined systems, for example thin-films clamped to

a substrate, or at the boundary between areas with different orientations of the magnetic order, this can lead to mechanical stresses, *i.e.* increased elastic energy. Vice versa, externally applied strain (or substrate-induced strain) can induce additional uniaxial anisotropy [25].

Zeeman energy – external and current-induced field effects

The Zeeman energy is the potential energy of a magnetic moment in a magnetic field. In a magnetic material it is minimal if all localised moments are aligned with the field direction. Macroscopically, the energy scales with the net magnetisation, so that even small fields are relevant for ferro- and ferrimagnetic materials [25].

In contrast for AF systems, the Zeeman energy competes with the AF exchange energy, favouring antiparallel alignment [23]. The latter is typically much larger for common magnetic field sizes [10]. If the spin axis is perpendicular to the field direction, Zeeman energy can be gained by a canting of the sublattices in the field direction which induces a small net magnetisation. This can induce a spin-flop transition, in which the spin axis rotates perpendicular to the field at a critical field magnitude [23].

Fields from spin-polarised currents Magnetic fields can be applied externally, but effective magnetic fields can also arise from a non-equilibrium spin polarisation of the carrier electrons, *e.g.* by injecting a spin-polarised current. The effective fields exert torques, so-called spin-transfer-torques (STT) on the localised moments [12].

Spin-orbit fields Additionally, in materials with broken inversion symmetry, a non-polarised electrical current can gain a non-equilibrium spin-polarisation due to spin-orbit coupling (see above). If misaligned with the local magnetic moments, the localised moments experience a torque (spin orbit torque, SOT) [10]. The spin-polarisation of the electric current can be modelled as a current-

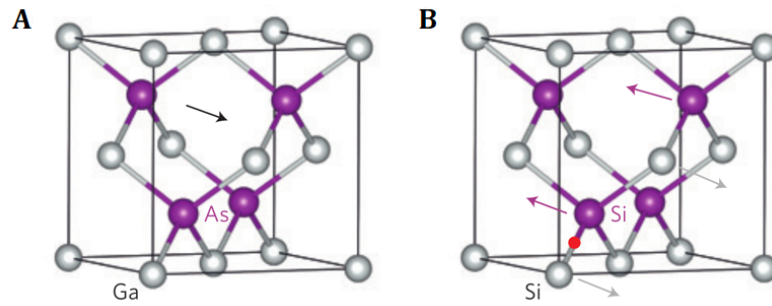


Figure 1.4: Spin orbit fields in GaAs and Si. **A:** Inversion asymmetric unit cell of GaAs. A current gives rise to a net effective field (black arrow). **B:** Unit cell of silicon, which is inversion symmetric, but composed of two interlaced inversion asymmetric sublattices shown in grey and violet. The sublattices are space-inversion partners; the centre of inversion is given by the yellow circle. As such, current-induced fields (small arrows) arise locally on each sublattice. These are equal in size and alternate in sign, so that there is no net magnetisation [36]. Figures taken from [8].

induced effective field that depends on the local position in the crystal. In inversion symmetric systems, the first moment of the polarisation vanishes if averaged over the entire unit cell. Consequently, ISGE has mainly been studied in inversion asymmetric systems. It was discovered experimentally in GaAs [33–35]. Although most obvious in globally inversion asymmetric systems, the SOC-induced spin polarisation originates fundamentally from atomic site inversion asymmetry. This results, as noted by Liu et al in 2014 [36], in a “hidden spin polarisation” in centrosymmetric systems with inversion asymmetric sublattices and that form space inversion partners, like for example in (non-magnetic) silicon. This is depicted in Fig. 1.4.

If in an AF material, the alternating current-induced fields match the alternating AF spin axis, then the torques exerted on each sublattice are equal in size, but opposite in sign. This torque, also called the Néel spin orbit torque, will tend to rotate the Néel vector whilst keeping the perfect antiparallel alignment of the sublattices. This observation has led to the theoretical prediction of current-induced spin-orbit torques in the AF material Mn_2Au [37]. The existence of NSOT puts strict restrictions on the symmetry of the material, namely that the material is a collinear AF, composed of two magnetic sub-

lattices which are themselves inversion asymmetric, but form space inversion partners.

Magnetostatic energy

The magnetic moments of finite samples can create magnetic stray fields (demagnetising field) around the samples. The magnetostatic energy, which is the energy associated with the self-interaction of the sample with the demagnetising field, depends on the local magnetic structure and scales with the magnetic moment of the sample. It can be large for ferro- and ferrimagnetic materials and here often dominates the behaviour in macroscopic finite size samples. It can lead to the formation of magnetic domains, areas of different magnetisation, in finite samples (referred to as “shape anisotropy”, see also 6.1), affects the microscopic structure of ferromagnetic domain walls (see [25]) and leads to the famous “Walker-breakdown”, which limits the speed at which FM domain walls can propagate [13]. For spintronics applications often efforts are made to suppress the demagnetising field effects, by constructing “synthetic antiferromagnets”, ferromagnetic multilayer structures with antiparallel coupling between adjacent layers [6]. In fully compensated AFs however, magnetic stray fields are almost vanishingly small and hence, this energy term can usually be neglected [10, 19].

1.2.3 Magnetic textures, domains and domain walls

Most samples often do not show uniform magnetic order across the entire specimen, but the magnetic order parameter varies locally. In the simplest case, the crystalline specimen is composed of regions, “magnetic domains”, of different magnetic orientation, but homogeneous magnetic order within each domain. For the entire section below compare [25].

The concept of domains for ferromagnets was developed by Weiss in 1907 to explain the experimentally measured magnetisation curves, even before it was

possible to directly image the local magnetic structure. Domain formation has been confirmed in numerous experiments. As discussed in an early review [38], the formation of domains can be seen as a natural consequence of competing energy terms, namely the magnetostatic energy which, in finite macroscopic samples, is large for a single-domain state and can be reduced by the formation of a multi-domain state. As noted already in the early (theoretical and experimental) investigations, a large variety of different domain structures and morphologies, depending on the magnetocrystalline anisotropy of the material, the shape of the sample, due to the dependence of the magnetostatic energy on the sample in FMs, the presence of external strains or fields and the (magnetic) history of the sample can be observed.

The boundaries between different domains are called “domain walls” (DWs). They are classified according to the total rotation across the wall, for example 90° domain walls (DWs) separate areas with orthogonal magnetic order parameter and 180° domain walls separate regions with antiparallel alignment. 90° DWs are observed in systems with two orthogonal easy axes (biaxial anisotropy). 180° are intrinsic to systems with uniaxial anisotropy, but can also be observed in FM systems with biaxial anisotropy. In the absence of uniaxial anisotropy, these would be unstable towards splitting into two 90° domain walls, but it has been shown that small magnetostriction is sufficient to stabilise the walls: two domains with antiparallel magnetic order are elastically identical, hence their strains are compatible, whereas the strains in two domains with orthogonal spin axis are incompatible with each other so that the energy of a 180° is slightly reduced compared to the case of two 90° domain walls.

Unless magnetic exchange is broken (e.g. by a grain boundary), sharp domain walls result in a large exchange energy. Consequently the rotation of the magnetic order parameter occurs over an extended region, the domain wall width, which also defines the typical lengthscale of the domain structure. Other, well defined, spin-textures which have recently attracted lots of attention both ex-

perimentally and theoretically, are vortices and skyrmions. A skyrmion can be envisioned as a “localized, particle-like excitation in which the magnetization (in a FM) or the staggered magnetization (in a collinear AF) is whirling and twisting in all directions” [39], embedded into a uniform background. See [40] for a precise (mathematical) definition and description of skyrmions.

Although mostly studied in FM structures, the concepts of domains can equally be applied to antiferromagnets. However, in AFs, domain formation cannot be attributed to minimisation of magnetostatic energy and the underlying mechanisms are still poorly understood [41, 42].

The domain structure in AF thin films is often attributed to poor crystalline quality, *i.e.* grain boundaries, whereas domain formation in single-crystalline AF specimens (bulk samples or epitaxially grown single crystalline thin films) [43], however, has been related to inhomogeneous nucleation during the initial domain formation or to magnetoelastic effects [41, 42].

Intuitively, it can be seen that the domain wall width results from the competition between the magnetocrystalline anisotropy (favouring a very narrow wall) and magnetic exchange (favouring very broad wall). In a stationary configuration, the two must balance each other, which can be used to derive the shape and widths of a domain wall. The mathematical description for two examples, a 180° and a 90° domain wall, in a thin-film (quasi 2-d) antiferromagnetic material, where the Néel vector is restricted within the film plane can be found in section A in the appendix. The domain wall widths sets the characteristic length-scale of the domain structure.

We note that AF domain walls are considerably easier to model than FM domain walls, since the magnetic stray field effects can be neglected. A discussion of FM domain walls is found in reference [25].

However, not all spin-textures can be described within the concept of domains and excitations such as vortices, skyrmions and domain walls. In contrast, as the example in Fig. 1.2A shows, there are AF domain morphologies in CuMnAs thin films which show smooth, continuous spin variation everywhere.

These are better described as a “spin-soup” or “rolling hills and dales” rather than “extended plateaus, valleys and ridges”. Defining domains and domain walls in similar textures, where the Néel vector varies everywhere over similar lengthscales, would be arbitrary and predict domains and domain walls of the same size. Hence the concept cannot be applied here.

1.2.4 AF dynamics

Thus far, primarily stationary configurations, defined by energy minimisation, have been considered and also the experimental work in this thesis exclusively measures stationary or quasi-stationary AF configurations¹. Measurements of the intrinsic AF dynamics are not attempted here. However, manipulating domain and domain wall configurations, is the basis for AF spintronic applications and is investigated in Chapter 4.

Below, some key points of AF dynamics are summarised. The entire section is based on [10, 39], which contains detailed theoretical discussions of AF dynamics.

Equation of motion and torques If the magnetic energy W of an AF system is known, than the AF dynamics can be modelled with a phenomenological Landau-Lifshitz-Gilbert (LLG)-equation. This is similar to the one used for FM dynamics, but the AF LLG-equation consists of two **coupled** equations of motion, one for each sublattice magnetisation \vec{m}^i , $i \in \{A, B\}$. Each equation contains two terms, a precessional (field-like) term and a damping like-term. The energy of the system is translated into an effective field on each sublattice, given by the (vector) derivative of the magnetic energy of the system with respect to the sublattice magnetisation:

$$H_{\text{eff}}^i = \left(\vec{e}_x \frac{\partial}{\partial \vec{m}_x^i} + \vec{e}_y \frac{\partial}{\partial \vec{m}_y^i} + \vec{e}_z \frac{\partial}{\partial \vec{m}_z^i} \right) W(m_A, m_B),$$

¹The dynamics of the magnetostructural changes are governed by the crystallographic changes, which can be seen as stationary for the magnetic system.

where \vec{e}_j are the unit vectors of the (Cartesian) coordinate system. This exerts a torque on each sublattice:

$$\tau_{\text{field}} = -\gamma \vec{m}^i \times H_{\text{eff}}^i,$$

where γ is just a constant, similar to the gyromagnetic ratio. This torque, the precessional term of the LLG equation, acts perpendicular to the magnetisation and the field and results in a precessional motion of the magnetisation vector around the effective field.

The second term of the LLG equation, the damping term, depends on the time-derivative of the sublattice magnetisation

$$\tau_{\text{damp}} = \alpha \vec{m}^i \cdot \partial_t \vec{m}^i,$$

where α is a (phenomenological) damping constant. The torque acts perpendicular to the sublattice magnetisation and its time-derivative and rotates the spin axis towards the effective fields.

In total the AF LLG equation reads

$$\partial_t \vec{m}^A = -\gamma \vec{m}^A \times \vec{H}^A + \alpha \vec{m}^A \times \partial_t \vec{m}^A \quad (1.1)$$

$$\partial_t \vec{m}^B = -\gamma \vec{m}^B \times \vec{H}^B + \alpha \vec{m}^B \times \partial_t \vec{m}^B. \quad (1.2)$$

The magnetic energy must contain the magnetic exchange:

$$W_E = H_E M_s \vec{m}^A \cdot \vec{m}^B, \quad \text{where } H_E = J_{\text{AF}} S^2 / \mu_B. \quad (1.3)$$

Here, J_{AF} is the (system specific) antiferromagnetic exchange constant and M_s the saturation magnetisation. The magnetic exchange couples the equations for the two sublattices.

The most general ansatz allows to include all other contributions to the energy of the system, too, as long as their vector derivative with respect to the

sublattice magnetisation is known.

Often considered, due to their relevance for (spintronic) applications, are the effects of external fields, non-equilibrium spin polarisations, achieved via the injection of spin-polarised currents or as current-induced spin-orbit fields (see above), including Néel order spin orbit fields. The resulting torques including the effect of magnetic exchange (exchange torques), on the AF order is schematically depicted in Fig. 1.5.

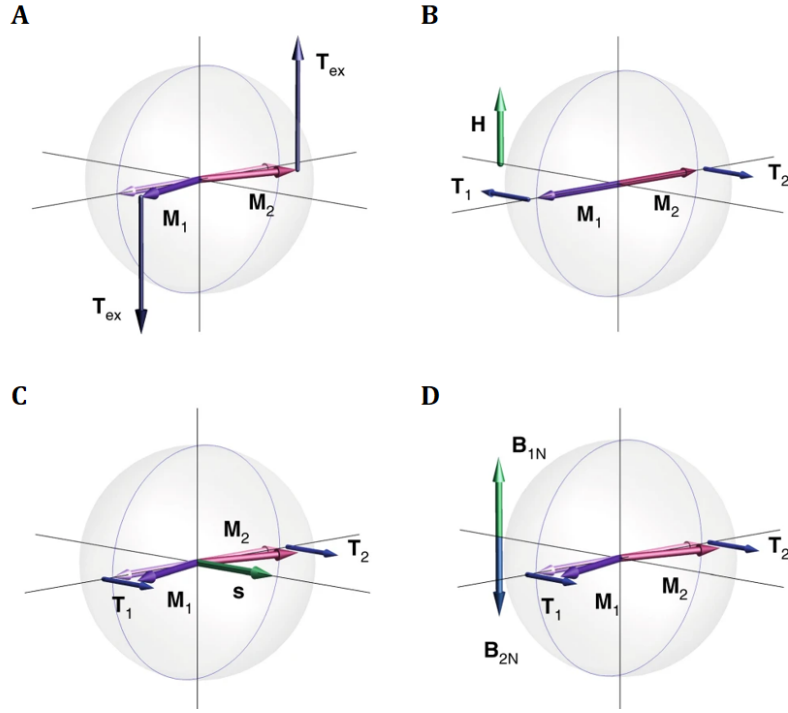


Figure 1.5: Torques on AF order. Figure from reference , $\mathbf{M}_{1,2}$ correspond to the sublattice magnetisations ($m_{A,B}$ in the text), and \mathbf{L} is the Néel vector. **A:** \mathbf{M}_1 and \mathbf{M}_2 are antiparallel in equilibrium. A small tilt of \mathbf{M}_1 and \mathbf{M}_2 triggers oppositely directed large exchange torques $\tau_{\text{ex}} \sim H_{\text{ex}}$, which induce a fast rotation of the magnetic moments. Oppositely, due to the tilting, any rotation of \mathbf{M}_1 and \mathbf{M}_2 is associated with a non-zero dynamic magnetization. **B:** A magnetic field \mathbf{H} generates antiparallel torques $\tau_{1,2}$, which compensate each other and, thus, hamper magnetisation dynamics. **C,D.** A current with spin polarisation s (**C**) and staggered Néel spin orbit fields $\mathbf{B}_{1,2}$, matching the staggered magnetisation (**D**) generate parallel torques $\tau_{1,2}$. These cant the sublattice magnetisations, which creates internal exchange torques τ_{ex} , which cause a rotation of magnetic sublattices.

Characteristics of AF dynamics It can be illustrative to transform the two LLG equations of the sublattice magnetisations into coupled equations for the AF order parameter $\vec{l} = \vec{m}^A - \vec{m}^B$ and the magnetic spin density

$$\vec{m} = \vec{m}^A + \vec{m}^B.$$

In the limit of large magnetic exchange (often applicable), the magnetic spin density becomes a slave variable of the Néel vector and one can derive an for the Néel vector only; the so-called sigma model. The sigma model for the Néel vector is a single equation which is second order in time derivative like Newton's equation of motion, whereas the FM LLG equation is first order. The second order arises from the combination of two coupled first order equations. As a consequence, the dynamics of the AF order parameter are similar to the inertial dynamics in classical dynamics. The kinetic term $\partial_t^2 \text{vecl} \times \vec{l}$ acts like an acceleration, which has important consequences for the dynamics of AF textures. Amongst others, an (infinitely) short lasting driving force, such as the time-dependent magnetic field of a short optical light pulse can trigger Néel vector dynamics and the Néel vector keeps evolving even after the driving force is switched off. Additionally, in the equations for the Néel vector, the damping and anisotropy terms are both multiplied (enhanced) by the AF exchange field, which leads to extremely fast, though short-lived precessional dynamics. Typical AF resonant frequencies lie in the range of hundreds of GHz to THz [10]. In contrast, in FMs the effective field driving the precessional dynamics contains only externally applied fields and magnetocrystalline anisotropy, and hence are typically orders of magnitude smaller and lead to GHz frequencies [10]. The enhanced anisotropy also "stiffens" AF domain walls and allows AF domain walls to propagate at speeds which are limited by the magnon velocity only. Thus AF domain walls can propagate at speeds, two orders of magnitude faster than FM domain walls, which suffer from "Walker breakdown" at critical driving fields. The mathematical description and derivation can be found in reference [44].

The magnetic spin density m , is (by definition) perpendicular to \vec{l} scales inversely proportional to the exchange field and consists of two additive terms; one scaling $\sim \partial_i \vec{l}$ and one scaling $\sim H_{\text{eff}} \cdot \vec{l}$. The second term "hides" the spatial derivative of the Néel vector $\partial_i \vec{l}$, as the exchange energy, and hence

one contribution to H_{eff} scales with the spatial variation of the Néel vector. Hence, both Néel vector dynamics ($\partial_t \vec{l} \neq 0$) and non-uniform AF spin textures ($\partial_i \vec{l} \neq 0$) have a small net magnetisation. However, this is reduced by $1/H_{\text{ex}}$, so typically very small.

Chapter 2

Methods and material

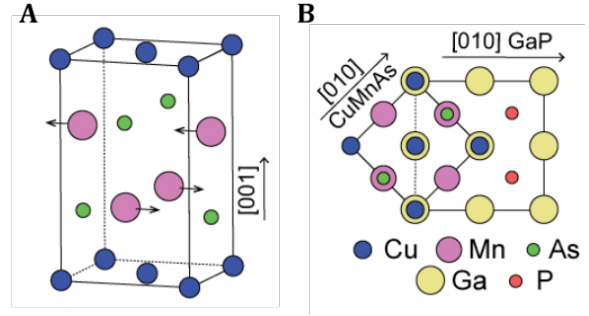
2.1 Copper manganese arsenide films

Copper manganese arsenide (CuMnAs) films have become a popular material for research in antiferromagnetic spintronics and a promising candidate for spintronic applications, because it is antiferromagnetically ordered at room temperature, can be grown with high quality and its symmetry allows for electrical manipulation of the AF structure via Néel spin orbit torque [45, 46]. CuMnAs exists in two different crystalline configurations; an orthorhombic ($a \neq b \neq c$) and a tetragonal ($a = b \neq c$) lattice structure. In the bulk, CuMnAs crystallises in the orthorhombic structure [47], whereas it assumes the tetragonal structure when prepared as a film [48, 49].

Most interesting for AF spintronics are thin films of CuMnAs. CuMnAs films can either be sputtered [50] or grown via molecular-beam epitaxy (MBE) on suitable substrates, including (001)-oriented GaP, GaAs and Si [46, 49, 51]. The unit cell is shown in Fig. 2.1. The antiferromagnetic ordering of tetragonal CuMnAs films at room temperature has been shown in exchange-bias [52], neutron diffraction and XMLD measurements [49, 51]. The source of magnetic moments are the Mn atoms due to their half-filled 3d subshells. At room temperature, studies of thick films of tetragonal CuMnAs have measured the local moments to $3.6 \mu_B$ per Mn atom by density functional theory fitting of

neutron diffraction peaks [49].

Figure 2.1: *Unit Cell of tetragonal CuMnAs and substrate registry.* Reprint from [46]. **A:** Unit cell of tetragonal CuMnAs. The arrows indicate the spin arrangement of the Mn-atoms. **B:** Registry with a GaP-substrate.



The work described in this thesis is done exclusively on MBE-grown films grown on GaP and GaAs. On these substrates it grows with an in-plane rotation of 45° , as illustrated in Fig. 2.1. The a and b axes are within the film plane, the c -axis is parallel to the surface normal. The unit cell consists of two formula units (6 atoms). The Cu atoms lie in the basal plane of the tetragonal unit cell. The Mn atoms and the As atoms each form two layers parallel to the ab plane.

Below the Néel temperature, the magnetic moments of tetragonal CuMnAs in a layer parallel to the ab plane align ferromagnetically, whereas they align antiferromagnetically along the $[001]$ direction, illustrated in figure 2.1. Hence, CuMnAs is a collinear, fully compensated AF with vanishing net magnetisation. Ab-initio studies reveal a large anisotropy energy barrier between in-plane and perpendicular-to-plane directions which restricts the Néel vector within the ab -plane of the film [53]. Consistently, experimental studies have not reported an out-of plane component of the Néel vector. In contrast, no significant in-plane variation of the magnetic anisotropy was found theoretically and experimentally conflicting observations were made between different layers [53]. Chapter 3 reports on further investigations of the in-plane anisotropy and the resulting AF domain structure in CuMnAs films.

The non-magnetic unit cell is centrosymmetric with the Mn-sites forming space inversion partners. Each sublattice considered alone, however, is inversion asymmetric. This allows for Néel spin orbit torque.

Ab initio-studies suggest for optimal lattice parameter (minimal energy) $a =$

$b = 3.69 \text{ \AA}$ and $c = 6.4 \text{ \AA}$ [48]. Therefore, the in-plane lattice parameter is well lattice-matched to the half-diagonal of GaP substrates. The lattice-mismatch is similar for Si substrate, but the mismatch is considerably higher for GaAs substrate. The highest crystalline quality is achieved in the films grown on GaP[46, 51]. The experimental lattice parameters and crystalline quality depends on the substrate choice. With optimal growth conditions for 50 nm films, out-of-plane lattice parameter of $a = 6.278(1) \text{ \AA}$ on GaP, $a = 6.299(3) \text{ \AA}$ on GaAs and $a = 6.300(11) \text{ \AA}$ on Si were reported [46]. For the in-plane lattice parameter of $a = 3.853 \text{ \AA}$ on GaP, $a = 3.822 \text{ \AA}$ on GaAs and $a = 3.830 \text{ \AA}$ on Si were found [46]. For films on GaAs and Si, significant mosaic tilt (order of 0.5° to 1°) was reported. For details see [46].

Films can only be grown fully strained up to a thickness of approximately 50 nm on GaP. In thicker films and in the films on GaAs and Si-substrate the films relax [46, 51].

Crystallographic defects Experimentally, two main types of crystallographic defects have been identified in CuMnAs layers on GaP(001)[46], referred to as “microtwins” and “antiphase boundaries” (APBs) respectively. High-angle annular dark-field (HAADF) scanning transmission electron microscopy (STEM) images of the defects are shown in Fig. 2.2. The microtwins, Fig. 2.2 **A**, are thin slabs with the CuMnAs crystal lattice rotated by 81.9° , which corresponds to the angle between (111) and $(\bar{1}\bar{1}1)$ planes. The lattice on either side of the microtwin is considerably distorted. On the surface the microtwins project as lines aligned with the CuMnAs $\langle 110 \rangle$ directions, where they form a measurable step.

The APBs, Fig. 2.2 **B**, originate from the two different ways the CuMnAs lattice can start growing at the substrate. The lattices on either side of the defect are shifted along the c -direction with respect to each other, but otherwise crystallographically identical. The size of the shift corresponds to the distance between two adjacent As-layers, as can be seen from Fig. 2.2 **B**. In contrast to

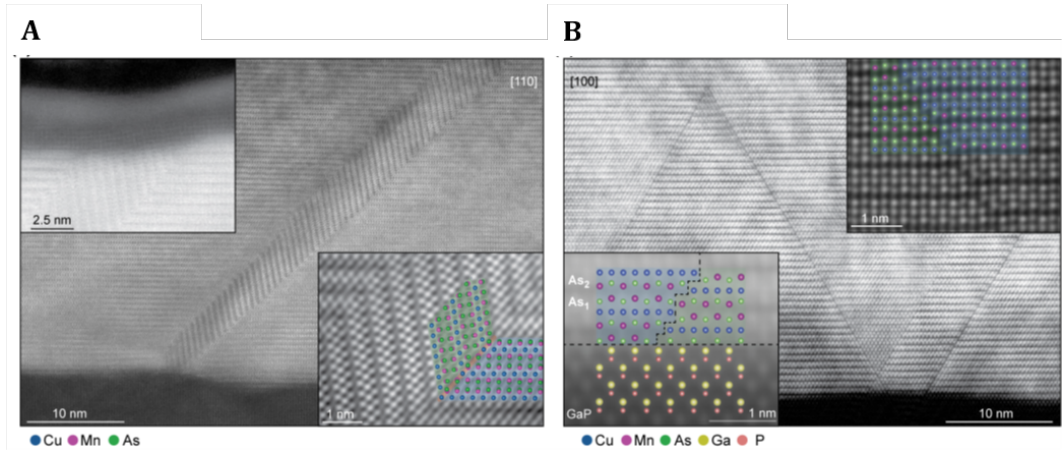


Figure 2.2: Crystallographic defects in CuMnAs films. Reprint from [46]. Shown are HAADF-STEM micrographs from a 50 nm film grown on GaP. **A:** Microtwin defect viewed from the CuMnAs [110] direction. Lower inset: zoom in on the atomic structure of the defect, overlaid with expected positions of Cu (blue), Mn (purple) and As (green). Upper inset: Detail of the top interface with the Al cap. The twin produces a “step” at the surface. **B:** Slip dislocations viewed from the CuMnAs [100] direction. Lower inset: atomic model overlay at the interface with the substrate (Ga (yellow), P (orange)), where the first layer from the GaP substrate starts with either As layer. Upper inset: zoom in on the atomic structure of one of the defects, with the atomic model overlay representing the expected structure. See [46].

the microtwins, no lattice distortion or strain is associated with an APB. The APBs are the most abundant crystallographic defect and occur considerably more frequently than the microtwin defects. For the entire section see [46] for more information.

Electrical properties Tetragonal CuMnAs films are semi-metals. The longitudinal resistivity of tetragonal CuMnAs increases with temperature, with an inflection point at T_N [51]. For low temperatures, transport studies of thick films of CuMnAs have found a residual resistivity of around $90 \mu\Omega \text{ cm}$ at 5 K [45]. The resistivity can be influenced by the growth conditions, the capping layer and the thickness of the films. The conductivity is highest in the films with highest crystalline quality [46]. The samples grown in Nottingham usually show a resistivity around $160 \mu\Omega \text{ cm}$ at 300 K that rises approximately linearly for not too high temperatures [51].

2.2 Material growth

The CuMnAs films used in this work have been grown on GaP(001) and GaAs(001) substrates using molecular beam epitaxy (MBE), see [54, 55].

Unless stated otherwise, all layers investigated have the layer structure shown in Fig. 2.3. Industrial, polished GaP or GaAs (001)-oriented 2 inch wafers serve as substrates. To improve the surface quality of the substrates, a 10 nm to 100 nm thick buffer layer, of the same material as the substrate, is grown in MBE before growing the CuMnAs film. The thickness of the CuMnAs layers investigated in this work varies within the range 20 nm to 200 nm. The CuMnAs layers are grown at approximately 200 °C. The surfaces of the CuMnAs films are protected with an additional 2.5 nm Al layer or with a 30 nm As layer to prevent oxidation. The As caps can be removed by heating for measurements on exposed CuMnAs surfaces.

The growth work has been done by Richard Campion, Victoria Hills and Luke Barton at the University of Nottingham and by Filip Krizek and Vit Novak at the Institute of Physics, Prague. The MBE-growth is described in detail in [46, 51].

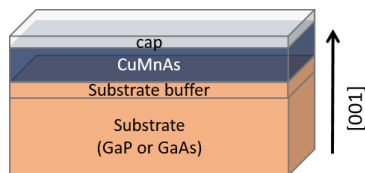


Figure 2.3: Layer Structure. Schematic of the layer structure. The arrow indicates the $[001]$ stacking direction. The layer thicknesses are not to scale.

2.3 Device fabrication

The measurements are either performed on non-patterned, rectangular chips, scribed from the 2-inch wafers along the cleave edges of the substrate, or on patterned devices fabricated from those chips. It is assumed that the cleaving does not affect the properties of the film, hence the non-patterned chips are identified with the blanket or as-grown film. To fit the PEEM-sample holder and the electrical sample holder, the lateral widths of the chips must be in

the range 5 mm to 10 mm. The wafers break preferentially along the $\langle 110 \rangle$ directions of the substrate, *i.e.* along the CuMnAs $\langle 100 \rangle$ directions. Hence the edges of the samples are aligned with the CuMnAs $\langle 100 \rangle$ directions.

Device fabrication removes the capping layer, CuMnAs layers, and usually the top part of the substrate in selected regions. This is done using either photolithography and chemical wet etching or electron beam lithography and Ar⁺ ion beam milling. All effects studied here are assumed to be independent of the fabrication process used.

In both procedures the samples have to be heated. Care is taken that the sample temperature does not exceed 80 °C to 90 °C, since temperatures above ~ 100 °C induce a reaction at the CuMnAs/Al interface, thus hampering surface-sensitive XMLD-PEEM measurements of the samples. The maximum temperature during fabrication is well below the Néel temperature of the samples. All devices were fabricated using the cleanroom facilities at the University of Nottingham.

Only some of the devices, fabricated by photolithography and chemical wet etching, have been fabricated by the author with the help of Mu Wang and Carl Andrews. The majority of the device fabricated with this technique have been fabricated by Jas Chauhan and Oliver Amin. Device fabrication by e-beam lithography has been done by Khalid Omari and Andrew Rushforth. A detailed description of the fabrication processes can be found in the appendix B.

2.4 Synchrotron radiation

Synchrotron radiation, also known as magnetobremstrahlung, is electromagnetic radiation emitted due to radial acceleration of a charged particle in a magnetic field travelling with speeds close to the relativistic limit. It follows directly from classical electrodynamics [56] and has been already discussed in 1912 in a book by Schott [57]. The mechanism is similar to dipole radiation.

The power of the emitted light in the forward direction scales proportional to the square of the centripetal acceleration and to the fourth power of the particles' kinetic energy, which leads to highly collimated, highly intense radiation when the particle travels at relativistic speeds. The angular power distribution as a variation with the particle speed is depicted in Fig. 2.4.

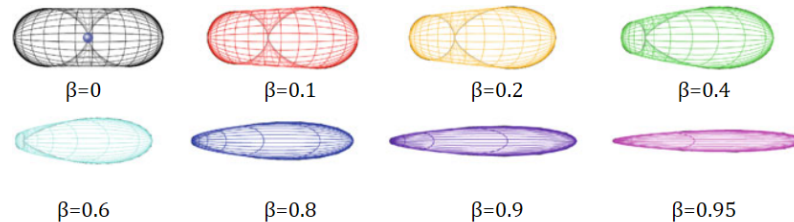


Figure 2.4: From dipole radiation to synchrotron radiation. Reprint from [58]. Sketched is the angular power distribution of radiation emitted by an electron travelling (horizontally) at a fraction of the speed of light $\beta = v/c$ and experiencing a centripetal acceleration \vec{a} perpendicular to the motion (vertically). $\beta = 0$ corresponds to dipole radiation.

The name synchrotron radiation stems from the first observation [59] in a 70 MeV synchrotron ([60]). A synchrotron is a cyclic particle accelerator, in which the accelerating (charged) particle beam travels around a fixed closed-loop path using magnetic fields, synchronised to the increasing kinetic energy, to bend the particle beam into the closed path.

Nowadays there are several large scale facilities operating on synchrotron principles, amongst them particle accelerators designated to achieve maximal particle speeds, such as the large-hadron collider (LHC) as well as electron synchrotrons dedicated exclusively for the production of synchrotron radiation for research.

Synchrotron lightsources

Synchrotron lightsources can provide highly collimated, coherent x-ray beams six to twelve orders of magnitude more intense than laboratory sources [58] with tunable polarisation and energy and high spectral brilliance. This allows higher angular resolution for diffraction, higher energy resolution for spectroscopy (or magnetic dichroism measurements, as in this work) and higher

spatial resolution for imaging, depending on how the electron path is modulated. In addition, common synchrotron lightsources have an intrinsic time structure, which can be exploited in time-resolved measurements. Most synchrotrons are “User-facilities”: the operation of the synchrotron machine, carried out by (permanent) members of staff, provides (external) “users” with x-ray beams to carry out their experiment in dedicated beamtime slots. The bridge between the machine and the users are beamline-staff, who support the user experiments and can sometimes also do their own research using the x-rays.

For a more detailed description of synchrotron light sources and other large-scale x-ray sources, such as x-ray free-electron lasers (XFELs), see references [58, chapter 1] and [61].

The performance of a synchrotron lightsource is typically quantified using spectral flux, brilliance and emittance. The spectral flux is the number of photons per second per unit bandwidth (BW). The brilliance is defined as

$$\text{Brilliance} = \frac{\text{photons/seconds}}{(\text{mrad})^2(\text{mm}^2 \text{ source area}(0.1 \text{ BW}))}, \quad (2.1)$$

and is inversely proportional to the source size and beam divergence. Hence it can be seen as a measure of how tightly the spectral flux is collimated and how small the source is. The product of the linear source size and the beam divergence in the same plane is called the emittance of the beam, which has contributions from the electron and photon beams. The photon emittance is fundamentally limited by Heisenberg’s uncertainty principle. The electron contribution depends primarily on the electron optics. In third generation synchrotrons, the emittance is dominated by the electron contributions. In fourth generation synchrotrons, this contribution is suppressed by sophisticated electron optics such that the photon contribution dominates and the corresponding sources are referred to as a “diffraction-limited” lightsource.

A schematic of a third-generation synchrotron, showing the basic components,

can be found in Fig. 2.5.

Electrons from an electron source (*e.g.* a heating filament in an electron gun), are accelerated with a linear accelerator (LINAC) and injected into a booster ring. The booster ring further accelerates the electrons which are then fed into the storage ring. The electrons in the storage ring travel on a closed loop with velocities close to the relativistic limit. In each loop, the electron beam loses energy, which must be compensated for. This is achieved with radio frequency (RF) cavities installed in at least one place of the ring. The RF cavities boost the energy of electrons. The amount of energy that an electron receives depends on which point of the RF cycle the electron enters the cavity, which forces the electrons into narrow “bunches” and thus sets the intrinsic time structure of the synchrotron. The entire electron path must be enclosed in an evacuated vessel to prevent the absorption of the electron beam by gas molecules.

Although called a ring, the storage ring is formed of straight sections joined by curved sections. The curved sections are bend achromats consisting of one bending magnetic (BM), two BMs (double-bend achromat) or more BMs (multi-bend achromat). The bend achromats are necessary to keep the electrons on the closed loop. In the straight sections additionally insertion devices (IDs) are placed. The IDs are periodic magnetic arrays (usually permanent magnets) with alternating polarity. The magnetic field perturbs the electron path and the electrons execute a slalom motion around the central axis. The IDs serve to produce x-ray beams with specific properties, tunable by the ID settings. The x-ray beams produced at bending magnets and IDs are harvested with beamlines installed on the axes of emission. Experiments with the x-ray beam are carried out on endstations attached to the beamline.

Bending magnets produce incoherent x-ray beams with a broad energy spectrum and wide opening angle, *i.e.* low brilliance. In IDs, x-rays are emitted at each bend of the electron slalom motion. If the electron paths deviate strongly from the central axis, then the x-rays produced at different bends add inco-

herently. The spectrum resembles the one produced by bending magnets, but the flux scales proportional to $2M$, where M is the number of magnets in the array. These IDs are called wigglers.

If the deviation of the electron path from the straight trajectory is small, then the x-rays produced at different bends of the slalom motion add coherently and the x-rays interfere with each other. This leads to intensity peaks at specific x-ray energies defined by constructive interference. Hence the spectral flux is concentrated in evenly separated, narrow bands of radiation, defined by the spacing, strength and periodicity of the magnet arrays. These IDs are called undulators. The work in this thesis is done exclusively at undulator beamlines, namely beamline I06 at Diamond Light Source and the Nanomax beamline at MAX IV.

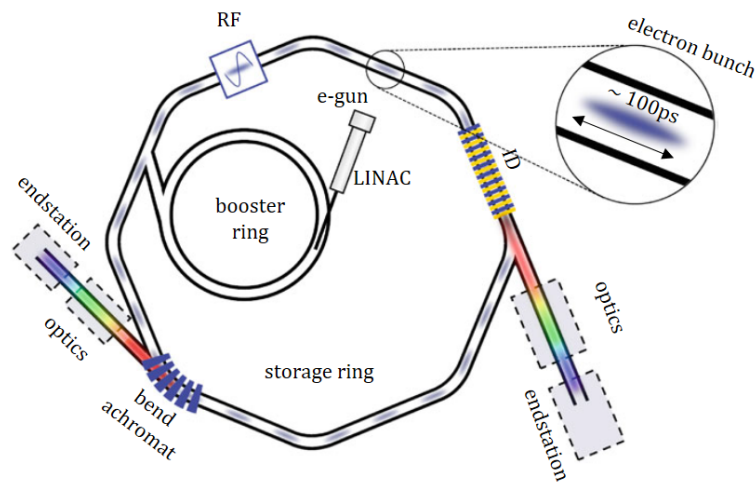


Figure 2.5: Schematic of a Synchrotron. Reprint (slightly adapted) from [61]. For simplicity, only one example of an insertion device (ID) beamline, bending magnet beamline and a radio frequency (RF) cavity is shown.

2.4.1 Beamline I06 at Diamond Light Source

The majority of the work is done on beamline I06 at Diamond Light Source (DLS). The Diamond Light Source is classed as a third-generation synchrotron featuring a LINAC, booster and storage ring. The storage ring operates at an energy of 3 GeV and has a circumference of 561.571 m. The maximum electron

beam current is 300 mA. For further details see [62].

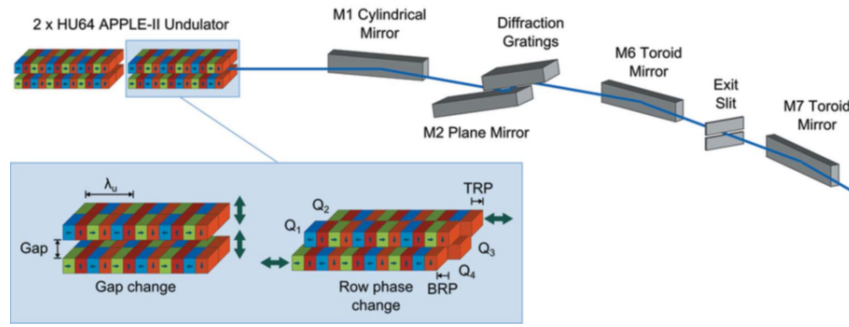


Figure 2.6: Layout of beamline I06, DLS Reprint (slightly adapted) from [63]. The x-ray beam is produced in the undulator. The mirrors serve to focus and direct the beam. The diffraction grating improves the energy resolution. The exit slit limits the beam size.

I06 is an undulator beamline designed for magnetic materials research in the soft-X-ray regime with tunable x-ray polarisation. This is achieved with an APPLE (Advanced Planar Polarized Light Emitter) II undulator, consisting of 4 arrays of four magnet arrays with magnet periodicity λ_u . By shifting the magnet arrays relative to each other almost every polarisation state can be achieved across the majority of the energy range. See for example reference [61] for the mechanism. A schematic of the beamline undulator and the x-ray optics is shown in Fig. 2.6. The details relevant for experimentalists (Users) on the I06 beamline are given in table 2.1.

$h\nu$ energy range	circular	106 eV to 1300 eV
	linear vertical	80 eV to 2100 eV
	linear horizontal	130 eV to 1500 eV
Resolving power $\Delta h\nu/h\nu$	measured at 400 eV	10 000
Temperature range	150 K to 1800 K	

Table 2.1: **Beamline specification for beamline I06, DLS.** The temperature range refers to the X-PEEM endstation.

2.4.2 Nanomax beamline, MAX IV

The Nanomax beamline at MAXIV has been used in this work for scanning X-ray diffraction measurements. It is a hard X-ray beamline at the MAX IV.

MAX IV is a fourth-generation synchrotron which instead of a booster ring has two storage rings, one operating at 1.5 GeV with circumference of 96 m and one operating at 3 GeV with a circumference of 528 m. The 3 GeV ring is a diffraction-limited storage ring. See [64] for further information.

The Nanomax beamline is attached to the 3 GeV ring. A schematic of the Nanomax beamline is shown in Fig. 2.7.

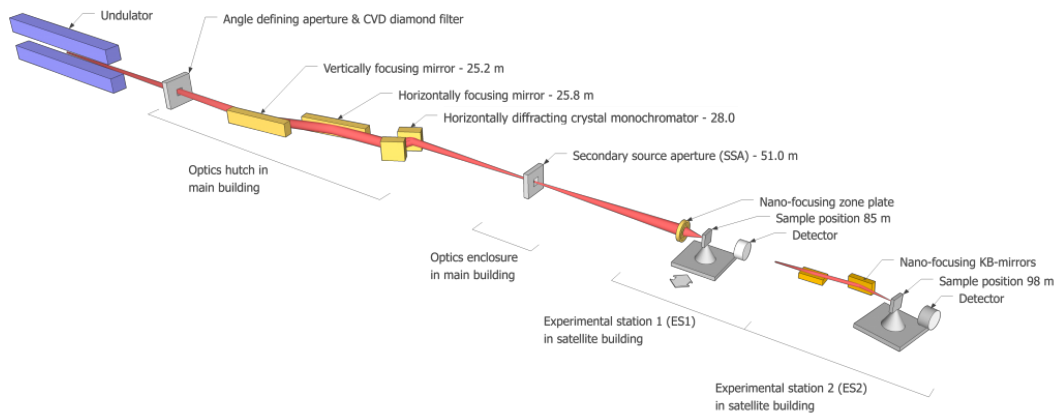


Figure 2.7: *Layout of the NanoMAX beamline.* Reprint from [65]. The undulator is installed inside the electron vacuum vessel. Some of the optics and the experimental stations are in satellite buildings, due to the length of the beamline, extending over nearly 100 m.

The undulator is a 2 m long in-vacuum undulator (*i.e.* installed inside the electron vacuum vessel which allows a smaller gap between the undulator arrays) with a periodicity of 18 mm. The experimental stations are nearly 100 m away from the primary source. The very long optics set-up, with a secondary source aperture over 50 m away from the primary source, allows to achieve a fully coherent x-ray beam at the experimental stations. For details see [66, 67].

The x-ray energies are in the hard x-ray regime and are not easily absorbed in air so that the experiments can be performed in ambient pressure, *i.e.* in air. For details see Table 2.2. The nanofocus and brilliance of the beam has been used in this work, but coherence has not been exploited here.

$h\nu$ energy range	5 keV to 28 keV	Routine operation 5 keV to 28 keV
Focal spot	50 nm to 200 nm	Diffraction limited spot (energy dependent, see [66])
Focused beam divergence	~ 1.2 mrad	energy independent
Coherent Flux in (photons/s)	6×10^{10} @ 8 keV 3×10^{10} @ 10 keV 8×10^9 @ 14 keV	Flux at sample position depends on energy, see [66] fully coherent beam

Table 2.2: **Beamline specification of the NanoMAX beamline, MAX IV.** Information from [68].

2.5 X-ray dichroism

X-ray dichroism is defined as the difference of the x-ray absorption cross section of a material measured for two orthogonal polarisation states of the incident x-ray beam [58, chap. 4].

Different types of x-ray dichroism are distinguished based on the type of polarisation used, referred to as **linear dichroism**, for linear x-ray polarisation and as **circular dichroism**, if circularly polarised light (comparing positive circular and negative circular polarisation) is used [58, chap. 4].

The dichroism spectra are either defined as the asymmetry of the absorption spectra for the two polarisation A_1, A_2 :

$$XD_{\text{asym}} = \frac{A_1 - A_2}{A_1 + A_2} \quad (2.2)$$

or as difference spectra

$$XD_{\text{diff}} = A_1 - A_2. \quad (2.3)$$

Dichroism can occur if (and only if) the symmetry of the interaction of the x-ray beam with the material is broken accordingly. The symmetry can be broken by the crystallographic structure or by magnetic order. The corresponding dichroism effects are referred to as natural or structural dichroism and magnetic dichroism respectively [58, chap. 4].

X-ray magnetic dichroism, which results from the effect of the modification of the electronic structure of a material in the presence of magnetic order on its interaction with x-ray photons, is a resonant effect that occurs almost exclusively in the near edge X-ray absorption fine structure of the magnetic atoms. Due to the strong spin-orbit interaction at the 2p core levels and the strong exchange splitting of the 3d valence levels [69], the $L_{2,3}$ absorption edges have been primarily used in experimental and theoretical studies. Combined with spatial resolution, such as in X-PEEM (see below) or by scanning a (nano-)focused beam across the sample, it becomes *i.e.* x-ray magnetic dichroism spectro-microscopy. This allows element-specific imaging of local magnetic (domain) structures [58, chap. 4]. A correct, theoretical description is highly non-trivial and relies on the electronic structure of the absorber, which can be treated within band-structure theory [70], or with density-functional theory (DFT) or ligand-field multiplet (LFM) theory [58, chap. 4]. Hand-wavy explanations, such as the “x-ray polarisation acts like a search-light for the direction of maximum charge, which depends on the magnetisation direction” (in the case of linear polarisation) are given, but these are often wrong and give a false picture of simplicity.

A few general and CuMnAs-specific principles, relevant for this work are outlined below.

2.5.1 X-ray (magnetic) circular dichroism

Circular dichroism arises if the two directions parallel and antiparallel to the incident x-ray beam, *i.e.* parallel/antiparallel to the x-ray momentum, are non-equivalent. This is the case in non-centrosymmetric crystals, x-ray natural circular dichroism, or by the presence of a net magnetic moment $\langle M_{\parallel} \rangle$ along the beam direction, x-ray magnetic circular dichroism (XMCD).

The XMLD effect scales linearly with the average magnetic moment along the beam direction $\langle M_{\parallel} \rangle = \langle M \rangle \cos(\theta)$, where θ is the angle between the incoming

x-ray beam and the magnetisation direction. Hence, it occurs in ferro- and ferrimagnetic materials, but vanishes in fully compensated AF systems. Being a first order effect, XMCD signals can be large, reaching for example up to 50% in transition metals [69].

Tetragonal CuMnAs films Tetragonal CuMnAs is inversion-symmetric and hence exhibits no natural circular dichroism. Several circular dichroism measurements in magnetic fields up to 6 T, show no measurable XMCD signal either, which have confirmed that tetragonal CuMnAs is a fully compensated antiferromagnet.

2.5.2 X-ray (magnetic) linear dichroism

X-ray linear dichroism effects arise in materials with two non-equivalent orthogonal axes, parallel and perpendicular to the x-ray polarisation. Structural linear dichroism therefore occurs in most in non-cubic crystals, as well as non-crystalline materials like bio-macromolecules (e.g DNA) and polymers. Pronounced polarisation dependence of the x-ray absorption can also arise from rough surfaces. In this case one can try to normalise the signal to account for the topographic effects, but a correct interpretation can be highly complicated¹.

Linear polarisation has only axial and no directional properties. Hence linear dichroism induced by magnetic order should be equally present in antiferromagnetic systems as well as in ferro- and ferrimagnets. It is a second order effect scaling with $\langle M_{\parallel}^2 \rangle$ and hence often considerably smaller than XMCD in ferromagnetic systems. Yet, x-ray magnetic linear dichroism (XMLD) has been established as a probe to study antiferromagnetic as well as ferro- and ferrimagnetic materials, largely resulting from pioneering experimental and theoretical work by van der Laan and (many) coworkers during the last few decades and the effects summarised in the introduction to reference [71].

¹It is much better to have a flat sample.

Several theoretical calculations and experiments have shown that the XMLD effect shows pronounced anisotropy depending on the angle between the polarisation and the crystallographic directions. In particular, an opposite sign of the XMLD signal for two different high-symmetry axes (e.g. $\langle 100 \rangle$ compared to $\langle 110 \rangle$ in cubic or tetragonal systems) has been predicted theoretically and confirmed experimentally for several systems. As such, the XMLD effect depends not only on the angle between the polarisation and the magnetisation direction, but also on the angle of the polarisation with respect to the crystallographic directions, often referred to as “angular-dependent XMLD”. In cubic symmetry the angular-dependent XMLD can be described by a linear combination of two independent spectra along two non-equivalent high-symmetry axes, called fundamental spectra. A detailed discussion of the model restricted to the (001) plane in the cubic lattice symmetry is given in reference [71].

XMLD in tetragonal CuMnAs films

Experimental absorption and dichroism spectra measured at the Mn $L_{2,3}$ edge are shown in Fig. 2.8. The data are taken from reference [49].

Restricted to the (001)-plane, *i.e.* within the film plane, tetragonal CuMnAs has four-fold symmetry. Hence for two in-plane perpendicular x-ray polarisations no structural dichroism is expected and has not been reported. Yet, structural dichroism can arise with respect to the c -axis, which is out-of-plane. The structural dichroism spectrum, measured as the difference of the absorption of x-rays with out-of-plane and in-plane polarisation, is shown in Fig. 2.8 C. At the $L_{2,3}$ edge the spectrum shows a maximum and two pronounced minima located 0.5 eV below and 1 eV above.

For magnetic linear dichroism in CuMnAs only in-plane effects have been studied both theoretically and experimentally, since the strong magnetocrystalline anisotropy restricts the Néel vector within the film plane.

Figure 2.8 B shows two experimental XMLD spectra, measured as the differ-

ence of the absorption for Néel vector parallel and perpendicular to a fixed x-ray polarisation direction aligned with the CuMnAs [110] and [010] directions. Due to the crystallographic symmetry this is exactly equivalent to comparing the parallel and perpendicular polarisation for a fixed Néel vector direction along the same $[xy0]$ direction.

The spectra show similar shape, but opposite sign for the two high-symmetry axes, which has been confirmed by theoretical calculations [53] and recent LFM calculations performed by Hebatella Elnaggar (unpublished). Near the $L_{2,3}$ edge, the spectra show two extrema, minimum and maximum, located with x-ray energies $h\nu$ at the peak of the XA spectrum (E_1) and 0.9 eV below (E_2). We define the size of the signal as $I = XA(E_1) - XA(E_2)$, which yields a negative value for the [110] crystallographic direction and a positive value for polarisation along the [010] direction and a relative size of of $I_{[110]} : I_{[010]} \approx 1 : 0.6$

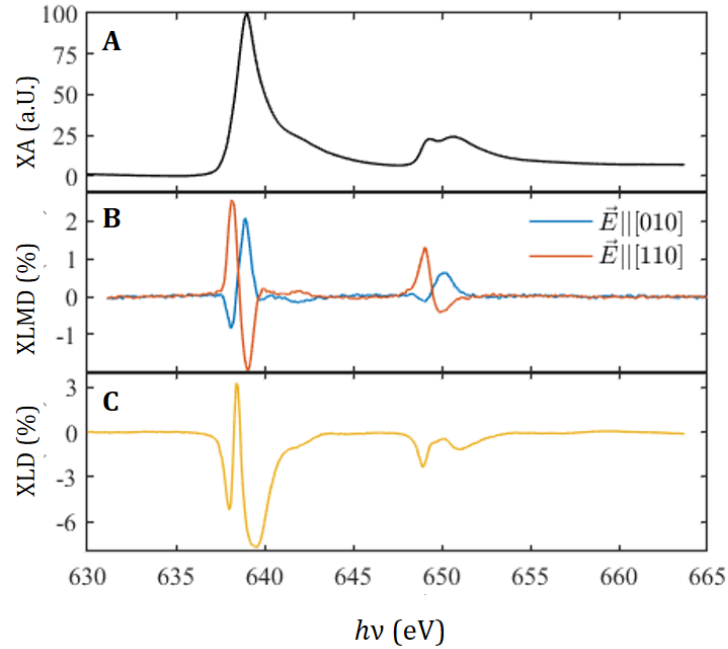


Figure 2.8: X-ray absorption at the Mn $L_{2,3}$ edge in tetragonal CuMnAs. **A:** X-ray absorption (XA) spectrum. **B:** X-ray magnetic linear dichroism (XMLD) - asymmetry of absorption spectra for magnetisation parallel and perpendicular to the respective x-ray polarisation \vec{E} . **C:** Non-magnetic x-ray linear dichroism (XLD)-asymmetry of absorption spectra with x-ray polarisation parallel and perpendicular to the c -axis.

The cubic symmetry of the (001)-plane allows to adapt the phenomenological model discussed in reference [71]. Hence, the angular-dependent XMLD in CuMnAs can be described as a linear combination of the two fundamental spectra $XMLD_{[110]}$ and $XMLD_{[010]}$. Defining ε and μ as the angles of the x-ray polarisation and the magnetic axis with respect to the CuMnAs [110], it is found that

$$XMLD(\varepsilon, \mu) = I_{[110]} \cos(2\mu) \cos(2\varepsilon) + I_{[010]} \sin(2\varepsilon) \sin(2\mu) \quad (2.4)$$

For a fixed polarisation direction, this can be rewritten as

$$XMLD(\mu) = I_\varepsilon \cos(2(\mu - \mu_{max})), \quad (2.5)$$

where I_ε and $\mu_{max} \in [0, \pi)$ are constants depending on the polarisation directions. Only for x-ray polarisation aligned with one of the high symmetry axes, $\mu_{max} = \varepsilon$ or $\mu_{max} = \varepsilon \pm \pi/2$. Hence maximum XMLD contrast is observed parallel and perpendicular to the polarisation only if the polarisation is along a high-symmetry axis.

This is illustrated in Fig. 2.9 **A**. The variation as a function of the spin angle is what generates the the contrast in XMLD-PEEM images. The case of fixed magnetic axis and varying x-ray polarisation is similar - due to the symmetry of equation (2.4) under the exchange of ε and μ .

A further complication when interpreting XMLD-based image data arises from the non-linearity of the XMLD signal, as Fig. 2.9 **B** comparing a linear colour map to a colour map based on the $XMLD_{[110]}$ and $XMLD_{[010]}$ signals. Both maps give the false impression of extended dark and white areas.

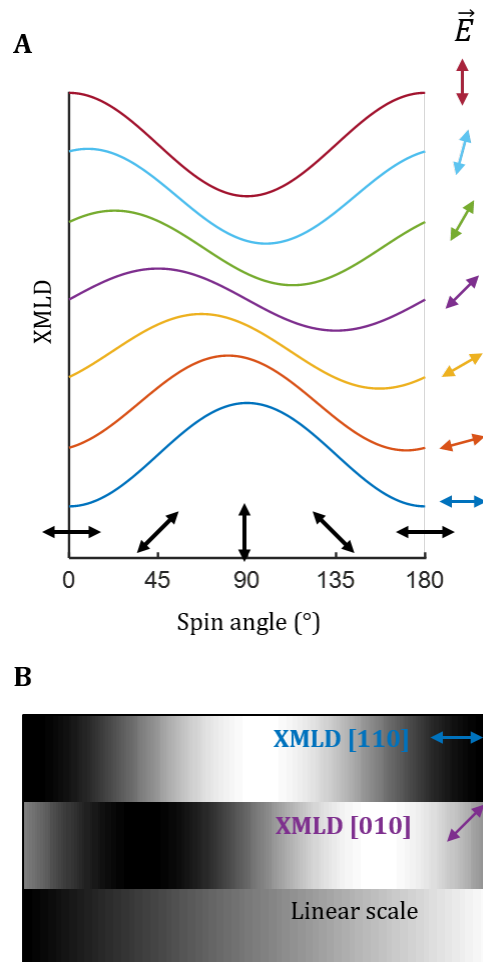


Figure 2.9: Angular dependence of the size of the XMLD signal in CuMnAs. **A:** Size of the XMLD signal $XMLD(E_1) - XMLD(E_2)$ as a function of the spin angle (contrast in XMLD-PEEM images) for different x-ray polarisation directions, indicated by the coloured arrows on the right. The black arrows represent the spin axes. The angle is measured with respect to the CuMnAs [110]. The curves are shifted relative to each other in the vertical direction, for visibility. **B:** Linear rotation of the spin axis by 180° shown in a linear scale (bottom), and using the colour map defined by the XMLD signal for x-ray polarisation along the CuMnAs [010] (middle) and [110] (top) crystallographic axes, i.e. showing the contrast in XMLD-PEEM images.

2.6 Electron microscopy

Electron microscopy works on similar principles as optical microscopes, but uses electrons rather than light as illumination and electrostatic instead of glass lenses, which allows much higher spatial resolution. The concepts of imaging and diffraction plane, the role of the objective lens and apertures are equally applicable. The performance of the electron optics depends on the kinetic energy of the electrons. Optimal resolution imaging can only be achieved

with a monochromatic beam with high kinetic energy. Thus, high-resolution electron microscopes typically use a high voltage (typically 10 kv to 20 kv) to accelerate the beam into the microscope lenses. For a detailed introduction and a description of the various techniques see reference [72].

In this work, two types of electron microscopy, photoemission electron microscopy (PEEM) and low-energy electron microscopy (LEEM) are used, which can be combined in one instrument.

2.6.1 LEEM

Low-energy electron microscopy generates an image from an elastically scattered electron beam. For a crystalline specimen, the backscattered electrons are focused in discrete diffracted beams with emission angles satisfying the Bragg conditions for constructive interference. Amorphous surface create diffuse scattering, with low intensity in every direction and hence cannot be imaged in LEEM. The probing depths of the technique is limited to the top 10 Å, due to the limited mean free paths of low-energy electrons. Below, we give a brief overview on LEEM as far as it is concerned to the work here. The section is largely based on reference [73] and reference [74], an introductory paper to LEEM written by Ernst Bauer who invented LEEM in 1962. A schematic of a typical LEEM instrument is shown in Fig. 2.10.

An electron gun is used to generate a beam of electrons. The electrons are accelerated to high-kinetic energies by a high-accelerating voltage 10 kV to 20 kV into the first set of optics, (illumination lenses), which focus the high-energy beam and direct it into a beam-separator. The beam-separator, consisting of several magnetic field sectors, redirects the beam to the objective lens placed just in front of the sample. Between the objective lens and the sample the electrons are retarded, since the sample is kept at a small potential (the start voltage) close to ground. Hence, the electrons reach and interact with the sample with a low kinetic energy. The backscattered electrons travel through the

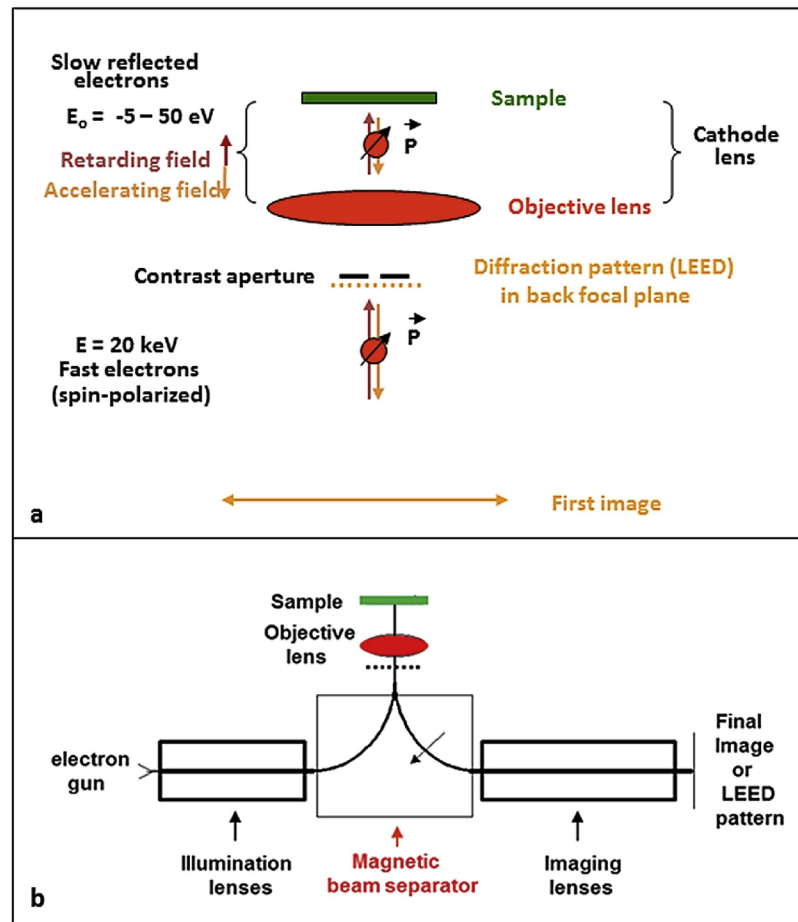


Figure 2.10: *Main components of a basic LEEM instrument* Reprint from reference [74]. **a:** *Close-up of the objective lens and sample, here for a system with the contrast aperture in the first diffraction plane.* **b:** *Overview of the whole instrument. The dotted lines indicate diffraction planes, the arrows an image plane.*

same objective lens. The retarding voltage now acts as accelerating voltage, as illustrated in Fig. 2.10.

The electron beam, now at high-kinetic energy, is sent through the beam separator into another set of electron optics (imaging lenses), which focuses the electron beam onto the detector. The detector is placed in an image plane for LEEM imaging, and in a diffraction plane for low-energy electron diffraction (reciprocal space imaging).

Additionally, one or more apertures can be placed into the beam paths. These include the illumination aperture, which restricts the illuminated area on the sample, and the contrast aperture, which restricts the emission angle of the backscattered electrons and is placed in a diffraction plane. If the contrast aperture is positioned in the first diffraction plane between the objective lens

and the beam separator, then the same aperture acts simultaneously as illumination and contrast aperture. In more complex setups, the contrast aperture and illumination aperture are placed on either side of the beam separator.

The quality of LEEM measurements typically increases with decreasing sample temperatures, since thermal motion increases the amount of diffuse scattering and broadens the diffracted beams, *i.e.* the emitted electrons have a larger range of kinetic energies and emission angles. LEEM allows for several specialised imaging modes, some of them discussed below, see references [73] and [74] for more details.

Low-energy electron diffraction LEEM instruments can also be used for low-energy electron diffraction (LEED) measurements, by placing the detector in the diffraction plane and not in the image plane. This is realised not by moving the detector physically, but by adjusting the electron lens setting accordingly [73]. LEED is measured with positive start voltages and without contrast aperture. Qualitatively, a LEED pattern gives information on the symmetry of the surface. Quantitative information can be retrieved by measuring the intensity of the diffraction spots depending on the start-voltage (LEED-IV) and comparing to theoretical models, see [75].

Usually LEED is a spatially averaged technique. LEED inside a LEEM additionally allows to obtain LEED from selected areas only, by restricting the illuminated area with the illumination aperture. However, a non-centered position of the illumination aperture leads to a distortion of the LEED pattern and hence experimentally cleaner data are obtained by moving the sample and keeping the position of the aperture fixed.

Bright field microscopy Bright field microscopy (BF-LEEM), uses the specular (0,0)-diffraction beam for imaging, *i.e.* electrons with normal emission. Electrons leaving the sample with a different emission angle are removed by the contrast aperture. In this imaging mode, performed with positive start-

voltages, contrast arises from different crystalline structures, different number of heteroepitaxial layers or different surface composition, also referred to as “reflectivity contrast”. Depth-sensitivity is increased with increasing start-voltage, yet this results in a loss of intensity and is restricted to $\approx 10 \text{ \AA}$.

Dark field microscopy In dark field microscopy (DF-LEEM) the image is generated from a higher order, non-specular diffraction beam. Electrons contributing to the specular (0,0)-diffraction beam and the other diffraction beams are removed by the contrast aperture. This can be realised either by moving the contrast aperture off-centre or by using the optics to deflect the electron beam such that the selected reflection passes through the contrast aperture. If possible, the latter is preferred since non-centred position of the contrast aperture distorts the image.

DF-LEEM is highly sensitive to the crystallinity of the sample. Any non-crystalline areas or areas which have a different lattice parameter, orientation or symmetry do not give intensity, *i.e.* appear black on the image. Therefore, in polycrystalline samples, individual crystallites can be imaged separately by using the corresponding reflection. In this thesis, dark-field imaging was used to separate areas with different surface reconstructions.

Dark-field microscopy is performed with positive start voltage. Due to the reduced intensity of the higher-order reflection spots, DF-LEEM has lower intensity than corresponding BF-LEEM images. For optimal intensity, the start-voltage has to be close to a maximum of the corresponding LEED-IV curve.

In dark field imaging, all electrons contributing to the image have the same kinetic energy and emission angle which allows for very high spatial resolution.

Mirror electron microscopy In mirror electron microscopy (MEM) the start-voltage is close to zero or has a small negative value. Hence the incident electrons are reflected before reaching the sample surface and only interact

with the near-surface region and not the sample itself. Contrast arises from the variation of the retarding potential due to work function differences, which can be very complicated. Assuming overall atomically flat surfaces, a main contribution to the contrast results from height differences, e.g. atomic step edges. No scattering events occur and no LEED pattern is formed. Therefore MEM has a high intensity and can also be performed on non-crystalline sample surfaces.

2.6.2 Photoemission electron microscopy (PEEM)

In photoemission electron microscopy (PEEM in physics, PEM in biology), the electrons used to generate an image are emitted from the sample itself (hence emission microscopy). This is achieved by illuminating the sample with UV-light (UV-PEEM) or x-rays (X-PEEM), which interacts with the sample via the photoelectric effect. The emitted electrons are mostly not the electrons excited directly by the photon beam, but secondary electrons and Auger electrons which can undergo several inelastic electron scattering processes before some of them escape into vacuum. As such a wide spectrum of electrons is emitted with energies between the energy of the illumination and the work function of the sample and a range of emission angles. The wide electron distribution is the principal source of image aberration in the microscope. The imaging optics are similar to a LEEM instrument, and the same in a combined LEEM/PEEM instrument, differing only in the illumination. PEEM operates with the sample close to ground, with a small negative bias which helps to prevent the build-up of large charges near the surface and stops the emitted electrons from being redirected into the sample.

Contrast arises from local variation of the emission of the sample, which, in many cases, scales with the photon absorption coefficient within good approximation.

The probing depth is typically ~ 5 nm mostly limited by the mean free paths

of the electrons, whereas the penetration depth of the photons is usually much larger, though dependent on the incident photon energy.

Drawbacks of LEEM and PEEM instruments

Emission electron microscopy is usually limited to conductive specimen, connected to ground, since the (removal) of electrons would otherwise result in a built-up of a positive charge on the sample, which shifts the work-function making it successively harder for emitted electrons to reach the detector.

For CuMnAs grown on insulating substrates, this means that the sample needs to be connected to ground via the surface (e.g. by wire-bonding or by a conductive cap) and that the sample design must not feature isolated CuMnAs “islands” since these can neither be imaged.

Parasitic charging effects can also arise in conducting, well-grounded samples if locally high densities of photoelectrons occur (“space charge”). The electrons in free space interact (repel) each other, limiting the performance of the electrostatic lenses, and can induce mirror charges, which further affects the electron paths. This shifts the electron energy distribution and deteriorates the spatial resolution. It is reduced by reducing the flux, *i.e.* illuminating with less intensity.

LEEM and PEEM measurements with high resolution require fast electrons, hence a large potential between the sample and the objective lens which creates a large electric field. This can result in rapid electric discharge (“sparks”) between the sample and the optic system. The high voltage drops, no electrons reach the detector and locally a large current flows through the sample which can severely damage the sample. The risk of electric discharge can be minimised by improving the vacuum and ensuring a flat sample surface. Isolated conductive islands and dirt on the surface act like lightning conductors and can trigger the discharge.

The ultra-high vacuum conditions (below 1×10^{-8} mbar) imply that the sample holders and the material must be UHV stable.

As in all electron microscopy techniques additional (not part of the lens system of the microscope) magnetic and electric fields perturb the electron paths. Therefore, the system must be well shielded and imaging with in-situ electric and magnetic fields is difficult and limited to very small fields only.

2.7 The PEEM-endstation on I06, Diamond Light Source

The data presented in this work are obtained on the PEEM-endstation on beamline I06 at Diamond Light Source. The endstation is a commercial electron microscope (manufacturer: Elmitec, model: SPELEEM) but is also equipped with a UV-lamp and connected to the beamline. Hence it can be used for X-PEEM, UV-PEEM and LEEM.

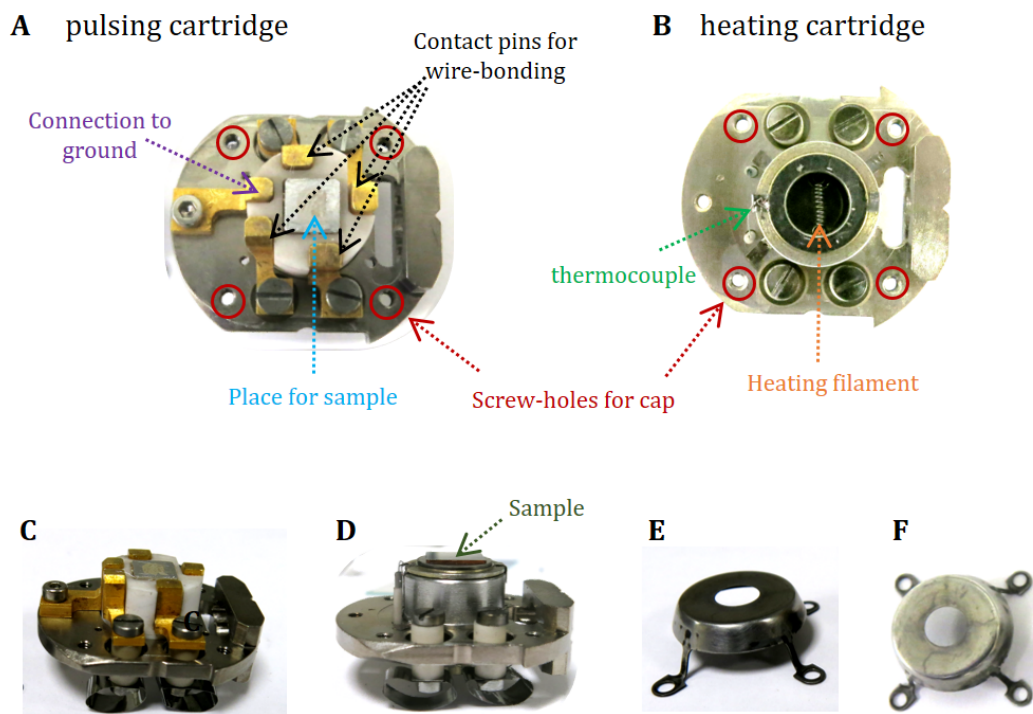


Figure 2.11: *Photographs of the omicron cartridges used on the PEEM-endstation, I06. A: Top-view of a pulsing cartridge (without sample and cap). B: Top-view of a heating cartridge (without sample and cap). The hole over the filament is covered with a circular Ta-plate on which the sample is placed. C: Side-view of a pulsing cartridge. D: Side-view of a heating cartridge, with Ta-plate and sample. E: Side-view of a cap. F: Top-view of the cap. The cap is screwed onto the cartridges through the holes of the feet into the holes indicated in panels A and B.*

The instrument is operated routinely at ambient temperatures. The sample environment can be cooled to ≈ 150 K by cooling the manipulator with liquid nitrogen. The manipulator and sample stage contract when reducing the temperature, so that sufficient time needs to be given for the system to stabilise and the systems needs realigning before measuring. Vibrations arising from the nitrogen flow can be a significant source of noise. The samples are mounted on customized Omicron cartridges, shown in Fig. 2.11. Two types of cartridges are commonly used “pulsing cartridges” (Fig. 2.11 **A**) and “heating cartridges” (Fig. 2.11 **B**). The heating cartridges are equipped with a electron bombardment heater, including a heating filament, located behind the sample stage. Using the filament current of the heater only, the cartridge temperature can be raised by a few 100 K, controlled by the filament current. Up to 1800 K can be achieved by electron bombardment heating. The temperature of the sample cartridge can be measured with a W/Re thermocouple spot-welded onto a Ta plate which is in thermal contact with the back of the sample. This gives an estimate of the sample temperature. Thermocouple and filament are connected to the feet of the cartridge. Direct measurement of the sample temperature is not possible. The samples are positioned on a Ta plate and kept in place with a Mo cap, which also connects the sample surface to ground. For in-situ electrical manipulation pulsing cartridges are used. Here, the samples are glued with silver paint onto the sample mount. Electrical contact is established by wire-bonding from the sample surface to the four contacts pads connected with the feet of the sample.

Attached to the electron microscope is a UHV-preparation chamber, with a low-resolution LEED. The preparation chamber is connected to a STM system, as well as the load lock. A photo of the set-up is shown in Fig. 2.12 **A**. The STM chamber is hidden behind the preparation chamber and cannot be seen. In addition, a UHV-chamber, referred to as the decap chamber, dedicated to the removal of As cap can be attached to the preparation chamber. A photo of the chamber is shown in Fig. 2.12 **B**. The sample-cartridges can be transferred

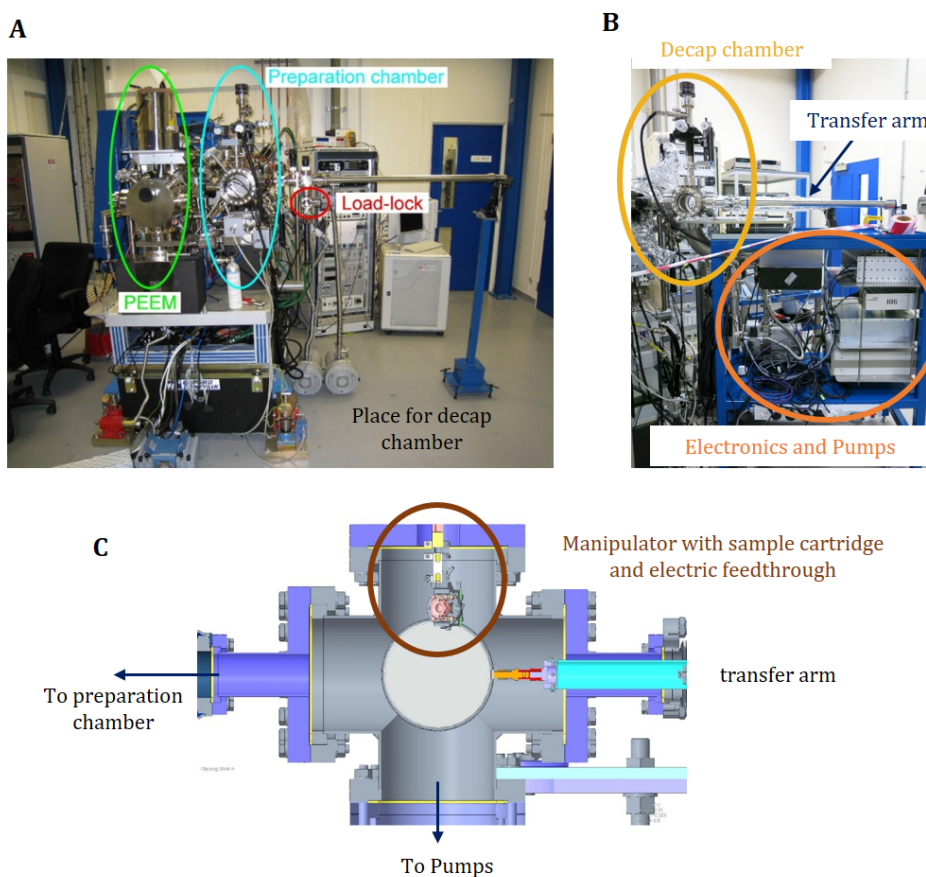


Figure 2.12: *PEEM endstation on beamline I06, DLS.* **A:** Photo of the PEEM endstation, without the decap chamber, showing the PEEM chamber, the preparation chamber and the load lock, photo from reference [76]. The STM chamber is hidden behind the preparation chamber. **B:** Photo of the mobile decap chamber, attached to the preparation chamber. **C:** Schematic of the main part of the decap chamber showing the manipulator with an omicron cartridge, and the tip of the transfer arm. The arrows indicate where it is connected to the pumping system and the preparation chamber. The height, rotation and horizontal position of the manipulator and the angle of the transfer arm can be adjusted.

in UHV between the chambers, by using transfer arms. For measurements and storage, the cartridges are placed on manipulators in the chambers, marked for the decap chamber in the schematic in Fig. 2.12 C. The manipulators in the PEEM, preparation and decap chamber are compatible with the same Omicron cartridges.

All manipulators have at least four electrical feedthroughs, which are used for the thermocouple and filament on heating cartridges and for the four contact pads on pulsing cartridges.

Microscope A schematic of the electron microscope optics, showing the electron paths for (a) LEEM/PEEM imaging and (b) imaging of the focal plane (diffraction, LEED) are shown in Fig. 2.13. In addition to the basic illumination and imaging optics, the instrument has an energy analyser which allows to select electrons with a specific energy for imaging and for imaging of the dispersive plane (not relevant in this work). For details, of how the different imaging modes are achieved, see reference [77].

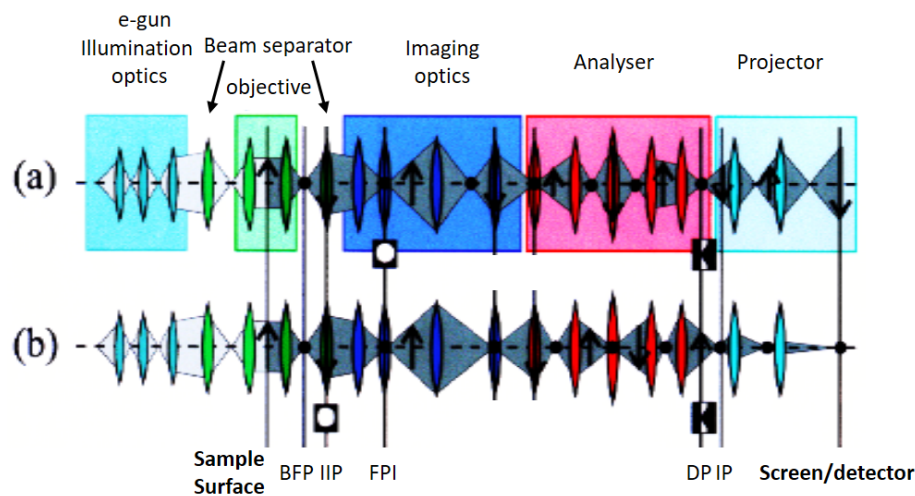


Figure 2.13: *Optics of the LEEM instrument on I06 Reprint (slightly adapted) from ref. [77]. (a) imaging mode used for LEEM, PEEM. (b) imaging of the focal plane (diffraction plane) used for LEED. Shown are the reflected/emitted electron beam starting at the surface in dark gray and the illuminating electron beam in light gray. The arrows represent the images of the sample surface and dots the images of the back focal plane (diffraction plane). The white circles indicate inserted apertures in the intermediate image plane (IIP) and in the focal plane image (FPI). The slit in the dispersive plane (DP) is also shown. See [77].*

The imaging optics and the path of the electron beam between the sample and the detector/screen are the same for all illumination techniques. Therefore, also the same area is imaged when switching between UV-PEEM, X-PEEM and LEEM imaging as long as the measurements use the same imaging lens settings.

In this work, the instrument was operated with 12 keV acceleration voltage. For this configuration imaging with field-of views covering $\approx 2.5 \mu\text{m}$ to $80 \mu\text{m}$ is possible.

Image acquisition Images have been acquired with a CCD camera (PCO-2000, see [78]) until December 2018 and since January 2019 with a medipix2-electron detector (see [79]).

The CCD-camera setup consists a microchannel plate (MCP), a phosphorus screen and the CCD camera. The MCP act as an (adjustable) electron multiplier, the phosphorus screen transforms the electron beam into light, which can be detected by the CCD camera. The camera has 1024×1024 pixels for imaging, but the imaged area is restricted to the central circle with diameter of 1024 pixels. Overexposure can damage the camera, hence the intensity on the camera needs to be monitored and adjusted with the MCP settings. The sensitivity (gain) of the pixels varies slightly, which can be accounted for with a flat-field normalisation image.

The Medipix2-detector is a direct electron-detector, which can be operated as a noise-less detector [80]. Advantages of medipix-detectors compared to MCP/phosphorus screen/CCD camera setups for LEEM and PEEM imaging are described in reference [80]. The detector has 512×512 pixels and the entire area is imaged. The pixels in the central two columns and rows sum the intensity of the two pixels, so that the measured intensity is doubled and quadrupled in the 4 central pixel. Hence the value of the central rows and columns need to be scaled by 0.5 in the raw images during processing. Additionally, the detector has dead pixels, which do not work. The number of dead pixels increases with lifetime of the camera. For later measurements dead-pixel images are available which can be used to identify relevant pixels. As in the PCO-camera, there is a pixel-to-pixel variation of the sensitivity which requires flat-field correction.

Flat-field images F are obtained by imaging a feature-less area with uniform illumination and defocussed objective-lens. The images can be normalised by pixel-wise division of the raw image; $I_{\text{corr}} = I_{\text{raw}}/F$. The same flat field images can be used for LEEM and PEEM imaging, since it accounts for properties of the detectors only.

Software control The microscope is controlled using the LEEM2000 software [81], provided by the manufacturer. Data acquisition, including Camera control, and control of the polarisation and energy of the x-ray beam is performed via the “General Data Acquisition” (GDA) client, a jython based software tool developed and provided by the DLS IT department. The beam focus on the sample, the sample position and rotation is furthermore adjusted in a separate graphical interface, developed at DLS. The sample tilt and the position of the contrast aperture and illumination aperture is adjusted manually (turning screws).

2.7.1 Operation as LEEM

The instrument is equipped with an electron gun which illuminates the sample with constant, tuneable flux and energy, defined by the start voltage. The illuminated area is approximately $\sim 80 \mu\text{m} \times 80 \mu\text{m}$ large and can be restricted by a circular apertures with various diameters, the smallest being 400 nm. Polarisation control of the electron beam is not possible.

Upon request, the beamline staff can add pre-settings for dark-field imaging. However, since they depend on the position of the diffraction spots, they need to be redefined for different samples. With the medipix-detector, LEED-IV curves with the same imaging settings can be measured over a large range of start-voltages between 15 V to 250 V.

2.7.2 Operation as PEEM

On I06, the x-ray beam is at grazing incidence, forming an angle of 74° to the surface normal. The polarisation can be set to negative circular (nc), positive circular (pc) or linear, with linear horizontal (lh) polarisation corresponding to a polarisation vector \vec{E} aligned within the sample, and linear vertical (lv) polarisation being almost out of plane. The x-ray energy and polarisation can be tuned within the soft x-ray regime. The details are given in table

2.1. The beam size and focus is controlled by the optics, in particular the exit slit (see section 2.4.1). Defocusing the beam beyond a 10 μm spotsize results in significant energy dispersion across the beam profile. Monochromatic illumination of larger areas requires rastering the beam across the surface.

To achieve various orientation of the polarisation vector with respect to the in-plane crystallographic axes, the sample needs to be rotated, since the direction of the x-ray beam is fixed.

Large area maps

The large area maps are a stitch of 30 μm XMLD-PEEM asymmetry images with sample positions over an xy -mesh with a stepsize of 15 μm , ensuring considerable overlay between the images. The sample position was rastered automatically and the beam-position was not adjusted in-between which can lead to a slight drift of the illuminated area. In order to illuminate the 30 μm field-of view, the 10 μm beam-spot on the sample surface was rastered in x and y across the sample using the KB-mirrors, since static defocussing beyond 10 μm introduces energy dispersion across the sample of more than 0.5 eV. This amount of energy dispersion can cancel or revert the magnetic contrast in different areas of one image.

The beam-rastering can introduce stripe-like artefacts in the recorded images.

2.7.3 Alignment

Alignment of the entire instrument is a highly non-trivial problem. Users on I06 rely on beamline staff to align the majority of the instrument. Most of the lens settings do not need to be adjusted regularly.

However, some features are highly sensitive to the orientation and distance of the sample surface. Therefore they need to be adjusted frequently, whenever swapping sample, rotating the sample or moving the sample over several micrometers. Namely:

- Sample tilt: the surface normal needs to be aligned with the optic axis (normal emission).
- Contrast aperture: needs to be centred.
- Objective lens: defines the depth-focus and can vary for LEEM images with different start-voltages.

2.8 X-PEEM measurement details

In this work, all X-PEEM measurements are carried out on the PEEM endstation on beamline I06. The instrument is operated with accelerating voltages of 12 kV. The samples are mounted either on heating cartridges or on pulsing cartridges, with the CuMnAs $\langle 100 \rangle$ directions, which correspond to the cleaving edges of the sample aligned with the sample holder. We arbitrarily define the direction along which the x-ray beam impinges on the default orientation of the manipulator as the CuMnAs [100].

Unless stated otherwise, the measurements are performed at ambient temperature. This work includes microscopic x-ray absorption spectroscopy (XAS) and microscopy x-ray dichroism measurements on CuMnAs thin films and thin film devices, using the experimental protocols below.

2.8.1 X-ray absorption spectroscopy

X-ray absorption (XA) spectra of characteristic absorption edges are obtained with a beam spotsize of 10 μm to ensure monochromatic illumination. An XA scan consists of a series of X-PEEM images taken with x-ray energies scanned stepwise across the the absorption edge with a stepsize of 0.1 eV. The x-ray polarisation is kept fixed. For each energy an image is acquired with typical exposure times of 1 s. XA spectra for a selected area are retrieved from the dependence of the intensity integrated over the area on the x-ray energy, shown as a graph or in a table.

In this work, XAS measurements across the Mn $L_{2,3}$ edge are used to ensure sample integrity. Samples or areas which show significant sign of oxidation, recognisable as a second shoulder of the peak, are not measured further. Additionally, the peak of the Mn $L_{2,3}$ edge, measured over a large area, is used to calibrate the energy of the beamline at the beginning of an experiment.

2.8.2 XMLD-PEEM image protocol

In this work, most x-ray magnetic linear dichroism measurements are taken with the x-ray beam impinging either along the CuMnAs [100] or along the CuMnAs $[1\bar{1}0]$ direction, corresponding to 0° and 45° rotations of the manipulator.

As discussed in section 2.5.2, the CuMnAs XMLD spectrum at the $MnL_{2,3}$ edge has two extrema, minimum and maximum, at x-ray energies $h\nu$ located at the peak ($h\nu = E_1$) and 0.9 eV below, $E_2 = E_1 - 0.9$ eV. Therefore, if the x-ray energy is tuned to either of those values, then variation of the angle between the magnetic axis and the x-ray polarisation generates local contrast in X-PEEM images.

To enhance the signal to noise ratio a dichroic image is calculated from a scan measured as follows.

- define x-ray polarisation (lh or lv)
- set energy to E_1
- take N (usually $N = 20$) images I_1
- set energy to E_2
- take N images I_2

The exposure time for each image is 1 s and, unless stated otherwise, $N = 20$. The XMLD-image is then defined as the asymmetry of the mean of the images

for each energy:

$$XMLD = \frac{\langle I_1 \rangle - \langle I_2 \rangle}{\langle I_1 \rangle + \langle I_2 \rangle} \quad (2.6)$$

where $\langle * \rangle$ is the pixel-wise arithmetic mean over all images with the same configurations. Hence one XMLD-PEEM image is obtained from $2N$ ($= 40$ typically) individual images.

To further increase the signal to noise ratio typically several of such XMLD-PEEM images are acquired and normalised.

For the tetragonal CuMnAs films studied here, the spin axis is restricted within the film plane. Hence magnetic contrast is achieved with linear horizontal polarisation. For linear vertical (lv) polarisation, the magnetic axis is almost orthogonal to the x-ray polarisation everywhere, hence little to no magnetic contrast arises. A small signal, reduced by a factor of $\sin 16^\circ$, results from the in-plane projection of the lv-polarisation vector of the measurement geometry. Instead of changing the energy and keeping the polarisation fixed, the asymmetry of images with lh and lv polarisation for fixed energy could be considered. Yet, changing the polarisation between the two orthogonal directions requires large changes of the undulator and can take a few minutes, whereas changing the energy by 0.9 eV requires only a small change of the undulators, hence is much faster.

2.8.3 XLD-PEEM protocol

Structural XLD-PEEM imaging uses the same experimental protocol as XMLD-PEEM, but with photon energies at a minimum and a maximum of the non-magnetic linear dichroism XLD-spectrum, with sensitivity to the orientation of the local c -axis. XLD imaging in this work uses linear vertical polarisation. Hence areas where the c -axis is locally rotated away from the surface normal can yield contrast and sensitivity to magnetic order is reduced.

Here XLD-PEEM imaging is used to image the microtwin-pattern in a sample. The identification is largely based on the similarity of the imaged pattern with

other, direct measurements of the twin structure (see reference [46] and chapter 5.3.1). The microtwins are only a few nm wide, *i.e.* below the instrument resolution, and form an angle with the sample surface. Hence the XLD contrast is averaged over regions containing the twin and the surrounding matrix. As a consequence, the twins appear with faint contrast and significantly broadened on the X-PEEM images.

2.8.4 XMCD-PEEM protocol

Using circular polarisation, sensitivity to ferromagnetic order can arise from x-ray magnetic circular dichroism effect at a specific absorption edge.

Similar to XMLD-PEEM and XLD-PEEM images, an XMCD-PEEM image, for a particular absorption edge with energy E_{max} is calculated from a scan of images taken with the following protocol:

- set the polarisation to positive circular (pc)
- set the energy to E_{max}
- take N images I_{on}^+
- set the energy off-edge, here $E_{max} - 4\text{ eV}$
- take N images I_{off}^+
- set the polarisation to negative circular (nc)
- set the energy to E_{max}
- take N images I_{on}^-
- set the energy off-edge, here $E_{max} - 4\text{ eV}$
- take N images I_{off}^-

Hence, a scan consists of 4 sets of N images taken with x-ray energies on and off edge and pc and nc polarisation respectively.

The XMCD image is then defined (pixelwise) as:

$$XMCD = \frac{\langle I_{\text{on}}^+ \rangle + \langle I_{\text{off}}^+ \rangle - \langle I_{\text{on}}^- \rangle - \langle I_{\text{off}}^- \rangle}{\langle I_{\text{on}}^+ \rangle + \langle I_{\text{off}}^+ \rangle + \langle I_{\text{on}}^- \rangle + \langle I_{\text{off}}^- \rangle + \text{thresh}} \quad (2.7)$$

“thresh” is a binary image, vanishing almost everywhere and with a large value where the X-PEEM images have low intensity.

These XMCD-PEEM images reveal the component of the magnetisation vector along the beam with minimum/maximum for parallel/antiparallel alignment. Thus two measurements with orthogonal x-ray direction (*i.e.* sample orientation) give access to both in-plane components of the magnetisation.

2.8.5 Image normalisation and image processing

Before calculating the dichroic images, according to equations eqs. (2.6) and (2.7), first camera artefacts need to be removed (image normalisation) and the corrected individual images need to be aligned (drift correction). Normalisation of the raw images includes flat-field correction for both cameras and appropriate scaling of the intensity of the central columns/rows and dead pixel removal for the medipix-detector only. The dead pixels are removed by replacing the value with the average value of the nearest neighbours. This part has not been done on all images.

The image normalisation, drift correction, dichroism calculations and further processing (e.g. drift correction and averaging of several XMLD-PEEM images) is performed in Igor, using routines “PIMMs” written by Francesco Maccherozzi based on ideas from Andrea Locatelli, or python procedures written by Stuart F. Poole ([82]). The python procedures are based on the Igor routines and on the image processing tools available from reference [83] and discussed in reference [84].

The Igor routines and the python procedures have implemented the same image normalisation and dichroism calculations, but differ in the implementation of the drift correction. The Igor routines use a selected area, the python

procedures uses an edge-detection filtered version of the entire image. In both procedures, the images are aligned with respect to the first image of the stack. The Igor routines keep the original image size, and crop the other images to the area of the first image so that data can be lost. The python procedure embeds the images in a larger image. This results in dark borders, but no data is lost.

2.9 LEEM measurement details

The LEEM measurements and combined LEEM/PEEM measurements are performed on the PEEM endstation on I06 at Diamond Light Source, described above.

2.9.1 Material and surface preparation

LEEM measurements require exposed, ideally atomically clean surfaces, hence the CuMnAs films with 2.5 nm Al cap cannot be imaged. Instead 50 nm CuMnAs/GaP(001) epilayers, grown with similar conditions by Richard Campion or Filip Krizek, but capped with 30 nm As were used. The As caps were removed prior to the measurements as described below by heating the samples to the evaporation temperature of AsO_x . The removal of the As cap was found to be recognisable as a change of the sample surface from black and shiny to blue-grey and speckled. This is shown in Fig. 2.14. It does not always occur uniformly across the sample, *i.e.* some areas can decap earlier than others. This can be attributed to inhomogeneous heating and variations of the cap thickness and oxidation.

The samples are mounted on the standard Omicron cartridges and transferred into the dedicated decap chamber. The samples are left overnight at temperatures below 100 °C, to ensure that the vacuum is below 3×10^{-9} mbar before starting the decapping procedure. During the decap, the pressure of the chamber, the sample temperature and the sample surface are monitored constantly.

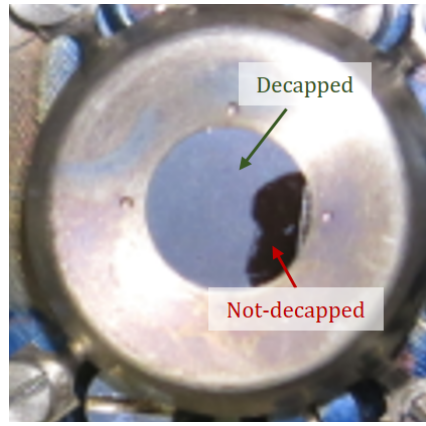


Figure 2.14: *CuMnAs surface change during decapping.* Photo of a partially decapped sample. The dark shiny area on the right is not decapped, the speckled area with blue/grey colour is decapped.

The temperature of the sample is estimated with the thermocouple and a low-temperature pyrometer, using an emissivity value of $\epsilon = 0.1$. The pyrometer only works for temperatures above 200 °C and does not give a reading for lower temperatures.

The samples are heated slowly, starting with a filament current of 0.5 A. The pressure in the chamber is left to settle below 3.5×10^{-9} mbar before the filament current is increased in steps of 0.2 A. Once the thermocouple gives a reading, the stepsize is decreased to 0.1 A. This usually occurs around 1.1 A. The temperature measurement of the pyrometer has been found to differ by approximately 50 °C in this temperature range and by over 100 °C close to the decap point. Decapping typically occurred at temperatures around 360 °C, measured by the pyrometer, 200 °C to 250 °C on the thermocouple, recognisable as a significant pressure rise, a drop of the thermocouple reading by 1 °C to 6 °C and a change of the sample surface. The sample is left at this temperature until the pressure has dropped to the base pressure of 3×10^{-9} mbar.

After decapping, the samples are transferred in UHV through the preparation chamber into the PEEM chamber. Before transfer, the samples need to be left to cool down for approximately 30 min, because thermal expansion of the cartridge and manipulator makes the cartridge too large to be removed from the manipulator at higher temperatures.

The surfaces are found to last over up to 24 hours in good vacuum (below 1×10^{-9} mbar), but degrade under the x-ray and electron beam and at higher

pressures, mainly due to carbon deposition and oxidisation.

2.9.2 Experiment details

Most LEEM measurements are bright-field measurements, using the specular (0,0)-diffraction beam and positive start-voltages of either 35 eV, the first maximum of the LEED-IV curve or 13 eV. The higher start voltage yields better bulk resolution and reduced sensitivity to surface edges. The lower start voltage yields higher intensity and has been found to be possible on slightly degraded surfaces. Mirror electron microscopy of surface steps has been done with a negative start voltage of 0.5 eV. Dark-field imaging and LEED-IV measurements have also been done, but are relevant only for the last section, reporting on unfinished work and hence will be described there.

The LEEM measurements comprise room-temperature measurements and measurements during temperature cycles between room-temperature and the decap point. The sample temperature is increased using the same filament as during the decap. Since the filament heater is mounted on the cartridge, it is expected that the same temperature is reached when heating with the same current amplitude while decapping and in the LEEM/PEEM chamber.

2.10 Electrical measurements

In-house electrical measurements

In-house electrical measurements are typically performed on star-shaped devices with eight contact channels aligned with the CuMnAs crystallographic directions. Current-spreading in these devices has been studied previously, and is described in [85]. Figure 2.15 depicts how the different writing geome-

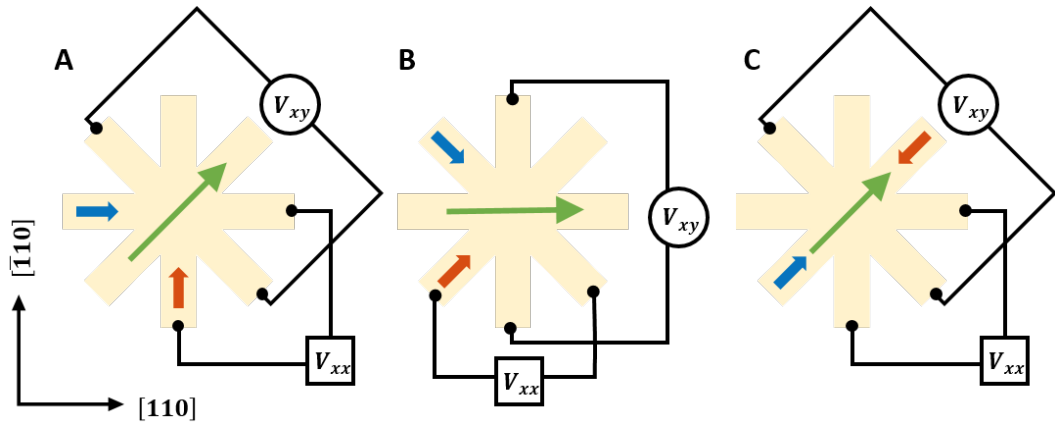


Figure 2.15: Measurement geometries in 8-contact devices used in purely electrical measurements. The bold blue and red arrows show the directions of the writing current pulses. V_{xx} and V_{xy} are the voltages measured during the application of the continuous probing current along the green arrow to probe the longitudinal resistance and transverse resistance (planar Hall). Panel **A** and **B** correspond to orthogonal switching with current pulsing along the CuMnAs $[110]$ and $[\bar{1}10]$ (**A**) and with current pulsing along the $[100]$ and $[010]$ (**B**) directions. Panel **C** shows the geometry used in polarity-switching.

tries and electrical probing geometries are realised in the 8-contact devices used in the purely electrical measurements. In these devices, the writing current pulses were set between two electrical contacts only and the voltage of each current pulse recorded. The direction of the current pulse is indicated by the blue and red bold arrows. The thin green arrows indicate the direction of the probing current used to measure the (change) of the longitudinal and transverse resistance, via the longitudinal and transverse voltage drops, V_{xx} and V_{xy} , as indicated. In this probing geometry, an uneven population of domains aligned parallel and perpendicular to the writing current pulses and the current-induced effective fields results in a planar Hall voltage due to the

AMR. Hence a change of the relative domain population results in a change of V_{xy} . For details see [85]. Panel **A** and **B** refer to orthogonal pulsing, with the writing current pulses along the CuMnAs [110] and $[\bar{1}10]$ directions (panel **A**) and along the CuMnAs [100] and [010] directions (panel **B**).

Panel **C** shows the geometries used for polarity switching. Here, both the writing and the probing currents are always along one of the CuMnAs principal axes, ($\{010\}$), and the transverse AMR is sensitive to changes of the AF spin axis between the CuMnAs [110] and $[\bar{1}10]$ directions.

Experimental set-up Electrical measurements were performed with Keithley 2400 source meters and Keithley 2000 meters. The Keithley 2000 is used only in the purely electrical measurements to measure the longitudinal voltage during the read-out. The meters are connected to the sample holder via an in-house built, multichannel switch-box which uses relays to open and close selected channels thus allowing to switch the contacts connected to the input and output of the (source) meter. Unused contacts of the device are always set to open circuit.

XMLD-PEEM measurements with in-situ electrical manipulation

Electrical measurements in-situ in the X-PEEM chamber are limited to four electrical feedthroughs, that can be connected to the device, which puts significant restrictions on the device geometry. Nonetheless, all electrical pulsing geometries can be realised in the centre of a simple cross-device with 4 electrical contacts, but electrical probing is limited to measurements of the transverse resistance along the directions of the cross, as illustrated in Fig. 2.16. Here, we use a device with the cross structure aligned with the CuMnAs [100] and [010].

In this device geometry, orthogonal switching along the CuMnAs [110] and $[\bar{1}10]$, combined with electrical read-out via transverse AMR can be realised as depicted in Fig. 2.16 **A**. Orthogonal current pulse directions in the centre

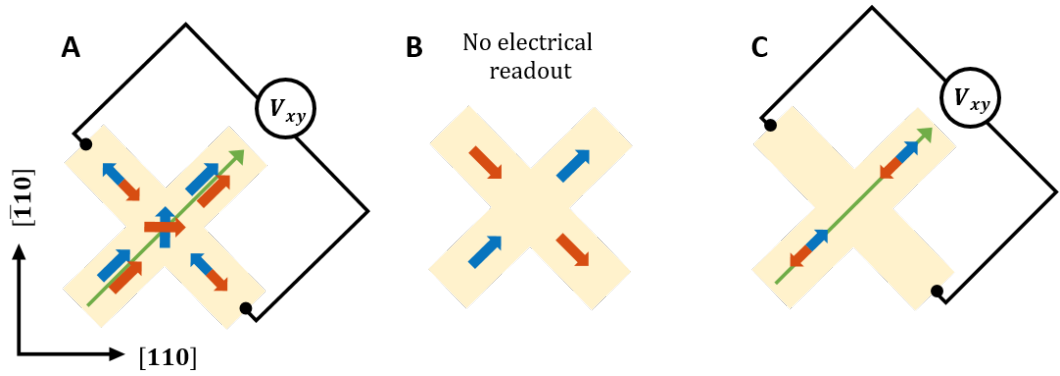


Figure 2.16: *Measurement geometries in 4-contact devices used for in-situ electrical manipulation in the X-PEEM chamber. The writing current pulses are applied in the directions of either the blue or red bold arrows. The green arrow shows the direction of the probing current, for which the transverse resistance in the device centre can be measured as indicated. A and B correspond to orthogonal switching with current pulsing along the CuMnAs [110] and $[\bar{1}10]$ (A) and with current pulsing along the [100] and [010] (B) directions. C shows the geometry used in polarity-switching.*

of the device are achieved by sending the writing current pulses through all four channels, which add vectorally in the centre. The direction of the probing current and the transverse resistance matches the alignment of the cross.

Orthogonal writing current pulses along the CuMnAs [100] and [010] directions can also be achieved in the device centre, as illustrated in Fig. 2.16 B. However, measurements of the transverse resistance with a probing current at 45° to the current pulses is not possible.

For polarity switching, this device geometry is ideally suited for writing current pulses along the CuMnAs [100] or [010]. The writing requires only two of the electrical contacts. Current-induced changes of the antiferromagnetic domain between $\pm 45^\circ$ could in principle be measured via transverse AMR, as long as the changes occur in the centre of the device.

2.11 Scanning X-ray diffraction measurements

The X-ray diffraction measurements were performed at the hard X-ray nanoprobe beamline at Max IV, NanoMAX (see section 2.4.2 and [67]). The beam was focused to a lateral diameter of 100 nm and the x-ray energy tuned to 10 keV.

The measurement geometry is determined by three angles, the detector angle δ , measured from the direction of the incident beam in the vertical plane, and determining the position of the Bragg vector, and two angles which describe the rotation of the sample with respect to the beam, ϕ and Θ , with Θ defining the incidence angle with respect to the sample surface in the vertical diffraction plane and ϕ being the sample azimuth. In a scan, the sample is scanned laterally in a 2d-mesh (*xy*-mesh scan) through the x-ray beam with fixed sample orientation and a detector image of the diffracted intensity is recorded at each position. The diffracted intensity is measured with a Merlin Si Quad area detector with 512×512 pixels sized $55 \times 55 \mu\text{m}^2$ placed at a distance of 0.650 m from the sample.

2.11.1 Reciprocal space maps

Several measurements with various sample rotations Θ give access to 3 dimensions in reciprocal space, as described in reference [86].

Three-dimensional reciprocal space maps are obtained from several *xy*-mesh scans with various sample rotations around a chosen Bragg reflection, here for the CuMnAs 003 reflection. The measurements are spatially averaged (real-space) over selected areas of the sample. The analysis was performed using the `xrayutilities` toolbox described in reference [86] under the guidance of Dominik Kriegner.

2.11.2 Microtwin mapping with scanning X-ray microscopy (SXDM)

The nanofocus of the beam allows to garner information from specific positions on the sample, *i.e.* for real space scanning x-ray diffraction microscopy (SXDM), here of the microtwin configuration in a sample as described below. SXDM imaging of the microtwin configuration utilised the CuMnAs 003 peak with the x-ray beam impinging along the CuMnAs [100] direction at $\Theta = 0$.

The presence of microtwins has previously been related to wing-like broadening along 4 crystallographic directions of the diffraction spot [46]. The relationship is confirmed by the measurements presented in section 5.3.1. The wings can clearly be identified in RSMs (see Fig. 2.17 D and section 5.3.1). RSMs require many scans with various sample rotations around the Bragg angle Θ_{Bragg} . However, if the x-ray beam impinges along the CuMnAs [110], then additional intensity in the wings can also be inferred from measurements with only two orientations, $\Theta = \Theta_{\text{Bragg}} + 0.4^\circ$ and $\Theta = \Theta_{\text{Bragg}} - 0.4^\circ$. This is illustrated in Fig. 2.17 and allows efficient SXDM imaging of the microtwin configuration.

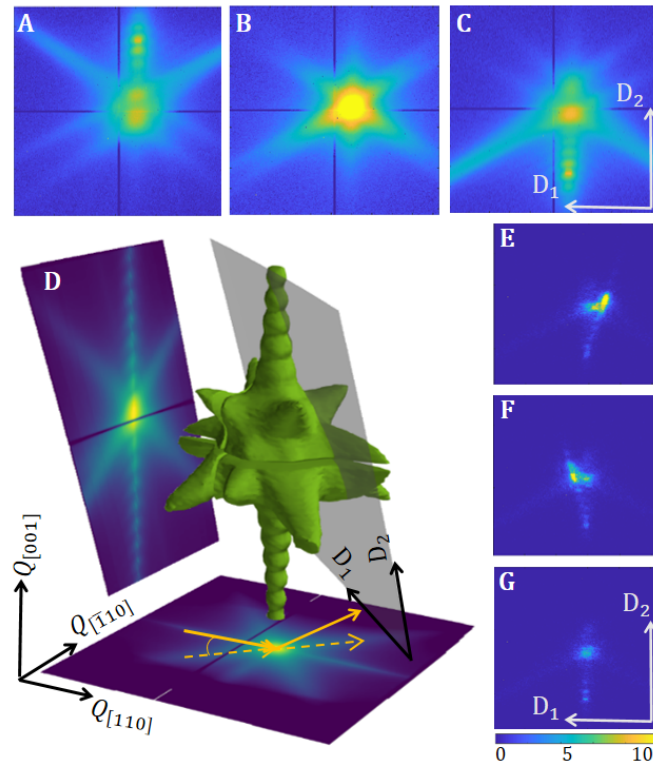


Figure 2.17: Principle of SXDM microtwin mapping. A-C, Summed detector images of scans with the three different geometries used for microtwin mapping (log-scale): sample rotation of $\Theta = \Theta_{\text{Bragg}} - \Delta\Theta$ (A), $\Theta = \Theta_{\text{Bragg}}$ (B) and $\Theta = \Theta_{\text{Bragg}} + \Delta\Theta$ (C). D, RSM of the 003 reflection of an area with microtwin defects. The grey plane illustrates the detector plane in defect mapping for the condition $\Theta = \Theta_{\text{Bragg}} + \Delta\Theta$. The solid yellow arrows show the incident and diffracted x-ray beam during defect mapping, the dashed yellow arrows their projection onto the $Q_{[110]}/Q_{[1\bar{1}0]}$ plane. E-F, Detector images (linear scale) with $\Theta = \Theta_{\text{Bragg}} + \Delta\Theta$ summed over 5 sample positions on one microtwin (E), on a microtwin with different orientation (F) and from a microtwin-free area (G).

Panel A, B and C show detector images summed over an entire xy -mesh scan

with $\Theta = \Theta_{\text{Bragg}} - 0.4^\circ$ (**A**), $\Theta = \Theta_{\text{Bragg}}$ (**B**) and $\Theta = \Theta_{\text{Bragg}} + 0.4^\circ$ (**C**).

The geometry for the configuration $\Theta = \Theta_{\text{Bragg}} + \Delta\Theta$ is illustrated in Fig. 2.17 **D** featuring the isosurface of the CuMnAs 003 RSM sliced by a grey plane which corresponds to the detector plane. The direction of the incoming and diffracted x-ray beams during mapping is indicated by the yellow arrows. Note that the sample was rotated in plane by 45° during the microtwin mapping with respect to the measurements of the RSM. This schematic shows that in this geometry ($\Theta = \Theta_{\text{Bragg}} + \Delta\Theta$) the detector plane does not cut the central spot, but slices one set of the thickness fringes, three of the streaks as well as two of the microtwin-related wings. The configuration ($\Theta = \Theta_{\text{Bragg}} - \Delta\Theta$) can be obtained via symmetry and slices the remaining two microtwin wings. During an xy mesh-scan with $\Theta = \Theta_{\text{Bragg}} + \Delta\Theta$ we thus observe increased intensity on one or the other half of the detector when a microtwin is within the illuminated area and lower intensity in a microtwin-free area, as shown in panels **E-G**. The images show the sum of five detector images measured on one microtwin (**E**), on a microtwin with perpendicular orientation on the sample surface (**F**) and measured on a microtwin-free area (**G**). The colour scale is the same for all three images. Compared to the detector image from a microtwin-free spot, the detector images obtained on microtwins show significantly higher intensity in the regions marked by the red ovals on one or the other half of the detector, depending on the microtwin orientation. Mapping the intensity of each detector half over an xy mesh-scan with $\Theta = \Theta_{\text{Bragg}} + \Delta\Theta$ thus allows to map the spatial pattern of the microtwins with corresponding orientation.

Since the configuration $\Theta = \Theta_{\text{Bragg}} - \Delta\Theta$ similarly gives access to the two remaining wings, the sum of the real space intensity maps with $\Theta = \Theta_{\text{Bragg}} + \Delta\Theta$ and $\Theta = \Theta_{\text{Bragg}} - \Delta\Theta$ produces a map of all microtwins.

The real-space intensity maps are produced using the **Nanomax-ScanViewer**.

2.12 Modelling AF textures in the vicinity of microtwins

The magnetic energy density of an antiferromagnetic layer with microtwin defects consists of three contributions: the magnetic anisotropy energy of the matrix (= the “non-disturbed”, surrounding film), w_{matr} , the magnetic anisotropy energy of the microtwins, w_{twin} , and magnetoelastic energy, $w_{\text{m-e}}$. The magnetoelastic energy can contain a contribution of defect-induced strain.

Based on the tetragonal symmetry of CuMnAs the magnetic anisotropy of the matrix is modelled as

$$w_{\text{matr}} = \frac{1}{2}M_s H_{\text{oop}} n_z^2 - \frac{1}{4}M_s H_{\text{ip}} (n_x^4 + n_y^4), \quad (2.8)$$

where $\vec{n} = (n_x, n_y, n_z)$ is the reduced Néel vector ($|\vec{n}| = 1$), whose direction coincides with the direction of the spin axes, $M_s/2$ is the sublattice magnetisation, and the positive constants H_{oop} and H_{ip} correspond to the out-of-plane and in-plane magnetic anisotropy fields with the axes x and y parallel to the magnetic easy axes within the film plane, here the CuMnAs $[110]$ and $[\bar{1}\bar{1}0]$.

To define the other contributions, w_{twin} and $w_{\text{m-e}}$, the microtwin defects need to be understood in detail. The lattice of the twins is coherent with the lattice of the matrix and can be mapped onto the matrix lattice by a reflection in a $\{101\}$ mirror plane, which is called the twinning plane. The twinning plane makes an angle of $\psi = \arctan(c/\tilde{a})$ with the (001) plane, where \tilde{a} and c are the lattice parameters of the tetragonal unit cell (see Fig. 2.18 A). The in-plane lattice parameter \tilde{a} is defined perpendicular to the twin, *i.e.* along the CuMnAs $\{110\}$, so that it corresponds to the diagonal of the ab -plane of the conventional unit cell of CuMnAs used in previous publications [45, 46, 48, 49]. Substituting $\tilde{a} = a_{[110]} = 5.449 \text{ \AA}$ and $c = 6.278 \text{ \AA}$ yields $\psi = 49^\circ$. From the tetragonal symmetry of the material, it follows that there are two possible twin pairs corresponding to the (101) and (011) mirror planes. In each case the

mirror (twin) plane can make an angle of ψ or $\pi - \psi$ with the film plane, thus giving four possible types of the microtwin orientations. The lattice vectors within the microtwin region are rotated with respect to the matrix lattice through the angle $\pi - 2\psi \approx 82^\circ$ (see Fig. 2.18).

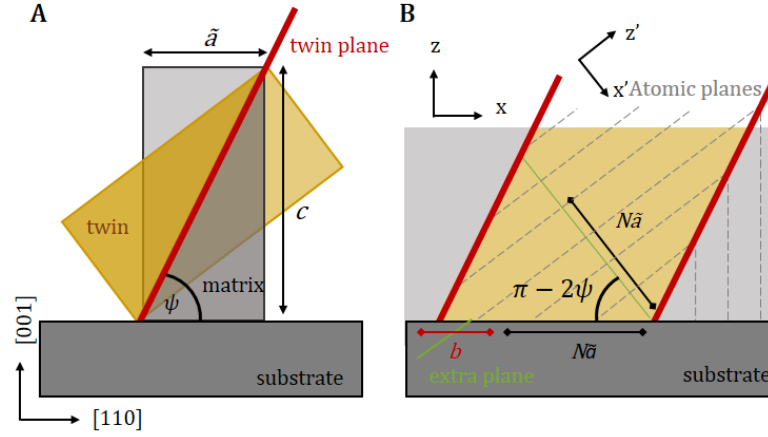


Figure 2.18: **A**, **B** Schematics explaining the Orientation of the microtwin defects and the corresponding reference frames (not to scale). Yellow corresponds to the microtwin, light grey represents the surrounding matrix and dark grey to the substrate. **A** Schematic explaining the orientation of the microtwin plane. Shown is the unit cell of the matrix, with in-plane lattice parameter \tilde{a} (here measured along the $[110]$) and out-of plane lattice constant c and the rotated unit cell of the microtwin defect. The twinning plane is the $\{101\}$ mirror plane between the lattice of the matrix and the lattice inside the twin, forming an angle of ψ with the substrate interface. **B**, Microtwin-induced incompatibility at the film-substrate interface. Primed and non-primed reference frames refer to the microtwin area and to the matrix respectively. Inside the microtwin region N atomic planes have a width of $N\tilde{a}$ which is smaller than the projection of the microtwin on the film plane, which leads to incompatibility at the substrate interface.

The magnetic anisotropy energy inside a microtwin can be calculated from equation (2.8) with account of lattice rotation through the angle 2ψ :

$$\tilde{x} = x \cos(\pi - 2\psi) + z \sin(\pi - 2\psi),$$

$$\tilde{z} = -x \sin(\pi - 2\psi) + z \cos(\pi - 2\psi)$$

$$\tilde{y} = y.$$

Taking into account that $H_{\text{oop}} \gg H_{\text{ip}}$, it follows that

$$w_{\text{twin}} = \frac{1}{2}M_s H_{\text{oop}} \cos^2(2\psi)n_z^2 + \frac{1}{2}M_s H_{\text{oop}} \sin^2(2\psi)n_x^2 - \frac{1}{4}M_s H_{\text{ip}}n_y^4 + \dots \quad (2.9)$$

The cross-terms (order of $n_x^l n_z^{4-l}$) are irrelevant for the analysis, because $H_{\text{oop}} \gg H_{\text{ip}}$, and have therefore been omitted.

The second term in equation (2.9) removes the degeneracy between the x and y axes (parallel and perpendicular to the twin) and makes the orientation of the Néel vector perpendicular to the twin unfavourable. Since \vec{n} is normalised, the full dependence of the anisotropy energy w_{an} , can be expressed in terms of the angle θ between the Néel vector and the sample surface normal, and the ϕ measured in-plane with respect to the microtwin line on the surface. The anisotropy energy surfaces as a function of θ and ϕ are plotted in Fig. 2.19 for a ratio of $H_{\text{oop}} : H_{\text{ip}} = 10 : 1$, which enhances the in-plane anisotropy. A ratio of $H_{\text{oop}} : H_{\text{ip}} = 100 : 1$ would be a more realistic value, but the in-plane variation would be impossible to observe in the plots. The top surface shows the anisotropy energy inside a microtwin along the CuMnAs [110] directions (including the higher-order crossterms) and the bottom surface corresponds to the surrounding matrix. The two energy surfaces have been shifted by a constant offset with respect to each other.

The anisotropy energy of the surrounding lattice has four equivalent minima, along the CuMnAs [110], $[\bar{1}10]$, $[\bar{1}\bar{1}0]$ and $[1\bar{1}0]$ directions arising from the tetragonal symmetry of the film. Two of those minima have a large anisotropy energy inside the twin, whereas the other two coincide with minima of the anisotropy inside the microtwin, and thus are the preferred orientations for the entire area, here along the CuMnAs $[\bar{1}10]$ and $[1\bar{1}0]$ directions, corresponding to the two possible signs of a Néel vector parallel to the microtwin line on the surface.

The strains induced by the microtwins and the corresponding contribution to the magnetoelastic energy can be calculated by considering the incompatibil-

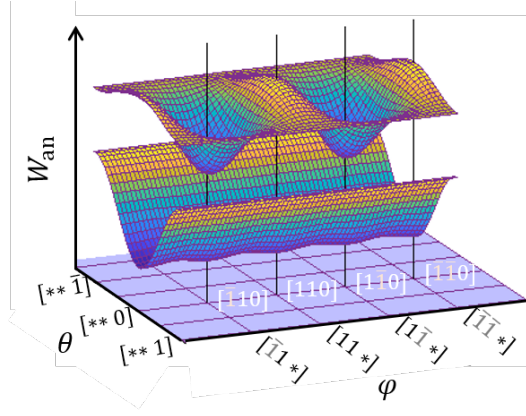


Figure 2.19: Normalised magnetic anisotropy energy W_{An} as a function of the in-plane angle ϕ and the out-of plane angle θ of the Néel vector. Top and bottom correspond to W_{An} inside a microtwin along the $[110]$ (top) and in the surrounding lattice (bottom).

ity at the interface between CuMnAs film and the substrate that is induced by the lattice rotation inside the twin, as depicted in Fig. 2.18 B. The projection on the substrate interface w_{interf} of N microtwin lattice planes (widths $w_{\text{twin}} = N\tilde{a}$ inside the twin), is larger than the widths inside the microtwin $w_{\text{interf}} = w_{\text{twin}} / \cos(\pi - 2\psi) > w_{\text{twin}}$. The corresponding structural defect can be interpreted as an edge dislocation localised at the interface between the microtwin boundaries (parallel to y axis), with the Burger's vectors b parallel to the x axis. We model this defect with a dislocation density which has a constant distribution of

$$\alpha_{xy}(x, y) = \tilde{a} \left(\frac{1}{\cos(\pi - 2\psi)} - 1 \right) = \tilde{a} \frac{c^2 - \tilde{a}^2}{c^2 + \tilde{a}^2} \quad (2.10)$$

inside the microtwin area, and which is zero outside. Equation 2.10 is invariant upon the transformation $\psi \rightarrow (\pi - \psi)$, *i.e.* two defects with the same surface terminations and opposite tilt are modelled with the same dislocation density. According to elasticity theory [87] an edge dislocation creates an in-plane strain field $u_{xx}^{\text{twin}}(x, z) \propto b/\rho$ that slowly decays with the distance ρ from the defect. To simplify the model, here the weak space dependence of u_{xx}^{twin} for a singular defect is neglected and the strain field is modelled with a constant function $u_{xx}^{\text{twin}} = u_0$ for the microtwins aligned along the y axis and $u_{yy}^{\text{twin}} = u_0$ for the

microtwins aligned along the x axis. The strain field of two parallel y -oriented defects is doubled, $u_{xx}^{\text{twin}} = 2u_0$, between the defects and $u_{xx}^{\text{twin}} = u_0$ outside (see Fig. 2.18 C). The strain field of T-junctions is represented as a superposition of the strain fields produced by the microtwins, as shown in Fig. 2.18 D.

The magnetoelastic energy due to the strain field $u_{jk}^{\text{nanodef}}(x, y)$ of the microtwins is modeled as

$$w_{\text{m-e}} = M_s H_{\text{me}} (u_{xx}^{\text{nanodef}} - u_{yy}^{\text{nanodef}}) (n_x^2 - n_y^2), \quad (2.11)$$

where the constant H_{me} characterizes the strength of the magnetoelastic coupling (expressed in the unit of the magnetic field). Here, we omitted the terms with the shear strain u_{xy} as irrelevant for the present model.

The distribution of the Néel vector $\mathbf{n}(x, y)$ in the presence of different microtwin configurations is simulated using `Matlab PDE Tools` to solve the two-dimensional equation

$$\mathbf{n} \times [A \nabla^2 \mathbf{n} + \mathbf{H}_{\mathbf{n}}] = 0 \quad (2.12)$$

with von Neumann boundary conditions. Here A is the magnetic stiffness, ∇^2 is the Laplace operator, and in simulations which consider the effect of strain

$$\mathbf{H}_{\mathbf{n}} = -\frac{\partial}{\partial \mathbf{n}} (w_{\text{matr}} + w_{\text{twin}} + w_{\text{m-e}}). \quad (2.13)$$

For simulations, that disregard the effect of strain, instead of equation (2.13), the expression of the energy is reduced to

$$\mathbf{H}_{\mathbf{n}} = -\frac{\partial}{\partial \mathbf{n}} (w_{\text{matr}} + w_{\text{twin}}). \quad (2.14)$$

The micromagnetic simulations are done by Helen Gomonay. The lengthscale in the simulations was set by the domain wall widths (d_{DW}) which are in turn defined by the ratio of magnetocrystalline anisotropy and exchange.

Chapter 3

Antiferromagnetic domain structure in CuMnAs thin films

3.1 Introduction

At the heart of each (AF) spintronic device is the antiferromagnetic material. The functionality of the device is closely tied to the material properties, including its structural, electronic and magnetic properties. Thin film devices require materials which grow on suitable substrates with sufficient crystalline quality; electrical measurements also require conductive specimens and the operation temperature of the device must be compatible with the Néel temperature of the material. Additionally, the magnetic anisotropy needs to be considered. If for example, (stable) switching between domains with two mutually orthogonal orientations of the Néel vector is attempted, then these orientations must coincide with a magnetic easy axis, separated by an energy (anisotropy) barrier which is sufficiently large to stop relaxation, but not too large to make switching impossible. If, in contrast movement of 180° domain walls (DWs) is attempted, then the material must show 180° domain walls.

Finding or realising suitable materials is often difficult.

In particular electrical manipulation via Néel spin orbit torque puts strict requirements on the crystallographic symmetry, electric as well as magnetic

properties of the material, largely met by tetragonal CuMnAs thin films (see section 2.1). Yet, the magnetic anisotropy of tetragonal CuMnAs is still only partially understood. Ab initio calculations, [49], have predicted a large magnetocrystalline anisotropy, which makes the c -axis energetically unfavourable (hard axis) and restricts the Néel vector in the ab -plane of the sample. Within the ab -plane only a small anisotropy, approximately 100 times smaller than the out-of plane anisotropy, close to the precision of the calculations, was reported. Disentangling the “intrinsic material properties” from substrate, growth and defect induced effects in AF thin films is challenging. Typically (001) oriented CuMnAs films are investigated. In these films the CuMnAs c -axis [001] is out-of plane and the ab -plane is the film plane. Consistent with the theoretical predictions, to date all experimental studies, as well as this work, have found Néel vector orientations within the film-plane only.

From early reports of experimental evidence of biaxial anisotropy in thicker CuMnAs films and a uniaxial anisotropy in thin (5 nm) thin films, the existence of 180° domain walls and 90° domain walls has been inferred [44], and ultra-fast domain wall propagation speeds under the application of electrical current pulses have been predicted [44]. Additionally, electrical measurements are often interpreted using a “ 90° domains picture” or “ 180° domains picture”, even if it has not been possible to image the microscopic domain structure of the particular sample, since this typically requires access to a synchrotron.

In addition to microscopic spin textures which can be described with a continuous vector field, sufficiently smooth to be described by the micromagnetic equations, evidence of atomically sharp 180° domain boundaries in tetragonal CuMnAs films has been reported in reference [88]. Although the XMLD-PEEM imaging technique is fundamentally insensitive to these sharp domain boundaries, the existence of AF domain boundaries below the spatial resolution of the X-PEEM can also be inferred from XMLD-PEEM measurements.

This chapter will give an overview on the different domain structures observed in different layers, showing a huge range of different morphologies. Evidence

of sharp domain boundaries, below the X-PEEM spatial resolution, will also be presented.

3.2 Methods

Material Most data presented here are obtained on (001) oriented CuMnAs films with varying thickness MBE-grown either on GaAs(001) or GaP(001). Most of the films are capped with 2.5 nm Al to prevent oxidation. Only one film was initially capped with 30 nm As which was removed before the measurement leaving an exposed CuMnAs surface. Additionally, measurements on an antimony-doped 50 nm layer CuMnAs_{0.9}Sb_{0.1}/GaAs(001), capped with 2.5 nm Al are shown.

3.2.1 XMLD-PEEM

The AF domain structure is imaged using X-PEEM on beamline I06 at Diamond Light Source, with sensitivity to the spin axis due to x-ray linear dichroism. For details see sections 2.5.2 and 2.7. For CuMnAs spin axis dependence of the XMLD signal has been established experimentally (see section 2.5.2). For CuMnAs_{0.9}Sb_{0.1}, the XMLD signal is expected to be similar due to the similar atomic structure and composition.

Some of the images show maps of large areas. These combine images with large field of view during which the beam was rastered across the imaged area, which can lead to stripe-like artefacts on the images.

The orientation of the coordinate system is arbitrary with respect to in-plane rotations of 90°, *i.e.* arbitrary under redefinition $[100] \rightarrow [010]$.

3.2.2 Interpreting XMLD-PEEM images

The XMLD-signal scales non-linearly with the angle of the AF axis. Hence, interpreting XMLD-PEEM images can be complicated. In principle, the AF

spin axis can be uniquely defined from just two images with different x-ray polarisation angle, if the angular dependence of the XMLD is known, but this requires high-quality images and pixel-to-pixel correspondence between the two images.

Qualitative interpretation

The following section briefly describes how to interpret XMLD-PEEM images of tetragonal CuMnAs films qualitatively, if the x-ray polarisation vector \vec{E} is aligned with a high-symmetry axis, in this case any of the $\langle 100 \rangle$ or $\langle 110 \rangle$ directions. Interpretation of images with x-ray polarisation along a different axis is more complicated. For images acquired with x-ray polarisation along a $\langle 100 \rangle$ direction, maximum signal (light) is measured on areas aligned parallel to the polarisation vector and minimum signal (dark) on areas with perpendicular orientation. Hence, if there are regions which show significant contrast, then they can most likely be identified with spin axes parallel and perpendicular to the x-ray polarisation. This can be confirmed, if the two areas show no contrast (grey) in images with x-ray polarisation along a $\langle 110 \rangle$ direction.

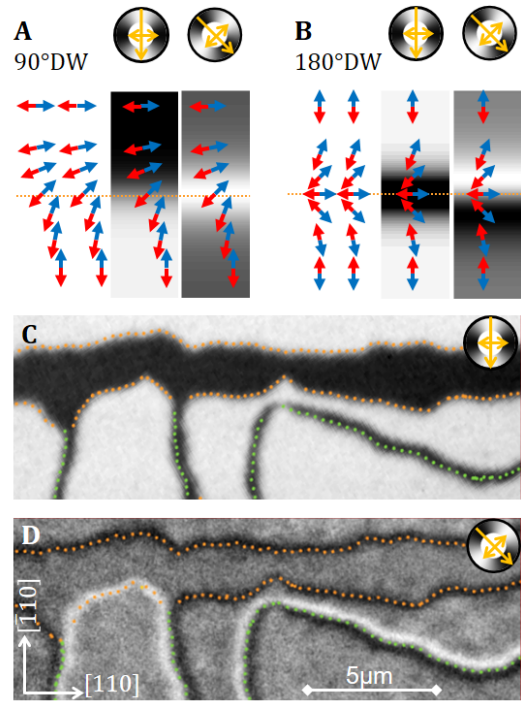
Similarly, regions with large contrast in images with $\vec{E} || \langle 110 \rangle$ are indicative of spin axes parallel and perpendicular to the polarisation, which can be confirmed if the areas show little contrast in images with x-ray polarisation along a $\langle 100 \rangle$ direction. Due to the angular dependence of the XMLD, in images with $\vec{E} || \langle 110 \rangle$ maximum signal (light) corresponds to spin axis perpendicular to the polarisation and minimum signal (dark) to spin axis parallel to the polarisation.

Since the XMLD-signal varies non-linear with the angle at least images with polarisations along a $\langle 100 \rangle$ and a $\langle 110 \rangle$ direction should be considered. Extended light or dark areas can only be identified with domains along the corresponding high-symmetry axes, if they are clearly separated and contrast on the domain boundary is achieved when rotating the x-ray polarisation by 45° . Then, the area can be described in terms of domains and domain walls. Here,

we consider two types of domain walls between domains aligned with a high-symmetry axes: 90° domain walls, separating two areas with orthogonal Néel vector orientation and 180° domain walls separating two areas with antiparallel orientation. If the Néel vector rotates continuously within the sample plane across the wall, then they have a unique signal in the XMLD PEEM images, as illustrated in Fig. 3.1 for domains aligned with the $\langle 110 \rangle$ crystallographic directions. In particular, 90° domain walls, between $\langle 110 \rangle$ domains, appear as single-colour light or dark lines in images with $\vec{E} \parallel \langle 100 \rangle$ and 180° domain walls between $\langle 110 \rangle$ domains show up as two-colour lines with minimum and maximum contrast in images with $\vec{E} \parallel \langle 100 \rangle$ and as narrow single-colour lines in the images with $\vec{E} \parallel \langle 110 \rangle$. The case of domains aligned with the $\langle 100 \rangle$ high symmetry axes is analogous.

Figure 3.1: Identifying AF Domain Walls in X-PEEM images.

A: Schematic of a 90° domain wall (DW) between two orthogonal $\langle 110 \rangle$ directions and corresponding, calculated XMLD-signal for x-ray polarisations along a $\langle 110 \rangle$ and a $\langle 100 \rangle$ direction, indicated by the yellow arrows, yielding sensitivity of the XMLD signal to the spin axis as shown the greyscale wheel. The red and blue arrows indicate the two sublattice magnetisations. The orange line marks the centre of the DW. **B:** Same as **A**, but for a 180° DW. **C:** XMLD-PEEM image of a sample with $\vec{E} \parallel \langle 110 \rangle$. 90° DWs and 180° DWs are marked with orange and green dotted lines. **D:** Same as **C**, but for $\vec{E} \parallel \langle 100 \rangle$.



The concept of domain and domain walls cannot be used to describe domain structures, if images with $\vec{E} \parallel \langle 110 \rangle$ and images with $\vec{E} \parallel \langle 100 \rangle$ look qualitatively similar and no clear domain boundaries can be observed, since smooth AF vector fields without regions of uniform Néel vector orientations can create the false impression of domains aligned parallel/perpendicular to the spin axis due to the non-linearity of the XMLD-signal (see section 2.5.2).

Calculation of spin axis maps

The calculation of spin axis maps (vector maps) from two XMLD-PEEM images with $\vec{E}||\langle 100 \rangle$ and with $\vec{E}||\langle 100 \rangle$ is based on “inverting” the two fundamental XMLD spectra, which describe the angular dependence of the XMLD signal (see section 2.5.2). Neglecting the sign of the Néel vector, to which the XMLD signal is fundamentally insensitive to, the fundamental spectra can be mathematically treated as surjective maps

$$XMLD_{[110]} : \quad (3.1)$$

$$[0, \pi) \rightarrow [I_{[110]}, -I_{[110]}]$$

$$\theta \mapsto I_{[110]} \cos(2\theta)$$

$$\text{and } XMLD_{[010]} : \quad (3.2)$$

$$[0, \pi) \rightarrow [-I_{[010]}, I_{[010]}]$$

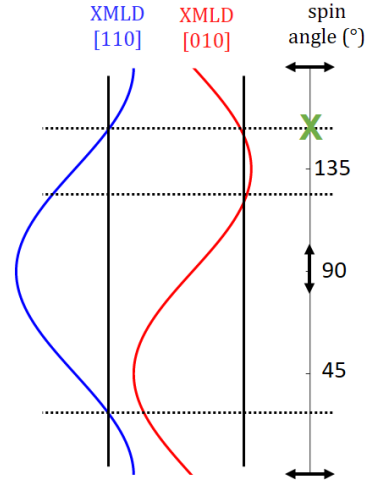
$$\theta \mapsto I_{[010]} \sin(2\theta).$$

Here θ is the angle of the spin axis measured counterclockwise with respect to the CuMnAs [110] direction, $XMLD_{[110]}$ ($XMLD_{[010]}$), is the XMLD signal measured with x-ray polarisation along the [110]([010]) and $I_{[110]}$ and $I_{[010]}$ describe the size and of the signal for each polarisation direction, with $I_{[110]}$ negative and $I_{[010]}$ positive.

Considered separately, equations eq. (3.1) and eq. (3.2) are not bijective, but have two solutions in the range $[0, \pi)$. However, there is only one unique solution in $[0, \pi)$ which simultaneously satisfies the conditions $XMLD_{[110]}(\theta) = I_1$ and $XMLD_{[010]}(\theta) = I_2$. This is illustrated in Fig. 3.2 and defines a spin axis map for given XMLD intensities maps.

In practice, several issues arise: The size of $I_{[110]}$ and $I_{[010]}$ are often not the same as the measured intensity range due to image processing and non-perfect energy calibration and misalignment with the crystallographic axes.

Figure 3.2: *Illustration of the (non-)ambiguity of the spin axis defined from the XMLD-signals measured with $\vec{E}||[110]$ and $\vec{E}||[010]$. Considered separately, the XMLD spectra are not injective, but the same intensity is observed for two angles. However, considered together, there is only one unique solution (green x) in the interval $[0, 180^\circ)$.*



The following procedure was found to work for images, $Im_{[110]}$ and $Im_{[010]}$, taken with $\vec{E}||[110]$ and $\vec{E}||[010]$ respectively, mostly uniform illumination and the same field-of-view from an area which shows maximum and minimum XMLD signal for both polarisations.

1. align the images and correct distortion such that there is a one-one-correspondance between the pixel of the images
2. crop to an area, where the images overlap
3. scale both images to the range $[-1, 1]$
4. for each pixel, with values $im^{[110]}$ in $Im^{[110]}$ and $im^{[010]}$ in $Im^{[010]}$:
 - (a) find the two solutions $\theta_{1,2}^{[110]} \in [0, \pi)$ which satisfy $im^{[110]} = -\cos(2\theta_{1,2})$
 - (b) find the two solutions $\theta_{1,2}^{[010]} \in [0, \pi)$ which satisfy $im^{[010]} = \sin(2\theta_{1,2})$
 - (c) find the best pair $\{\theta_i^{[110]}, \theta_j^{[010]}\}$
 - (d) average $\theta_i^{[110]}$ and $\theta_j^{[010]}$ (mean)
5. construct the spin axis map
6. inspect the result, if necessary, improve the image distortion correction or scaling and repeat

Step 1. , is done with the image distortion correction function in the Igor PIMMs procedures developed by F. Macchorozzi. One image is used as a ref-

erence, the other is rotated, shifted and skewed until good overlap is achieved. The correction must not rely on magnetic features, but on topographic features.¹ Steps 2.-5. are realised as matrix operations in MATLAB. Step 3.(c) and 3.(d) must consider the π -periodicity, *i.e.* the distance between 0 and $\pi - \epsilon$, $\epsilon < \pi/2$ is ϵ and the mean is $\pi - 0.5\epsilon$.

3.2.3 Defining Néel vector maps from spin axis maps

Continuity assumption Micromagnetic theory is based on the assumption that the magnetic order parameter (Néel vector \vec{l} for AFs) can be described as a smooth vector field almost everywhere $\vec{l}(x, y, z, t)$, here $\vec{l}(x, y)$ neglecting the depth dependence and time-dependence of the vector field. This requires that the sign of the Néel vector, once defined (arbitrarily) depending on the labelling of the magnetic sub lattice, is kept consistent over a continuous region.

Mathematically, if a vector map $\vec{A}(x, y)$, can be mapped onto a which continuous, differentiable Néel vector map $\vec{l}_a(x, y)$, with $\vec{l}_a(x, y) = \pm \vec{A}(x, y)$, then there is one and only one other continuous, differentiable vector map $\vec{l}_b(x, y)$, which satisfies the above condition and $\vec{l}_b(x, y) = -\vec{l}_a(x, y)$.

Vice versa, this allows for a spin axis map, to “track” the sign of the corresponding Néel vector map once this is arbitrarily defined in one point.

This can be used to retrieve a Néel vector map from a spin axis map calculated from XMLD-PEEM images, if the Néel vector varies on lengthscales larger than the pixel-size. The procedure used here is illustrated in Fig. 3.3: The sign is arbitrarily chosen on the top left corner. Then, iteratively, the sign of the next neighbour in the row is defined such that the angle between the vectors is minimal, continuing with the second up to the last row of the image, where the sign of the first pixel is defined from the pixel above. If the continuity assumption is fulfilled, then the resulting vector map should not show any sharp boundaries (close to 180° reversals between neighbouring pixels). Furthermore, the same result should be obtained, if the Néel vector is traced with a similar

¹It can be tedious.

routine along a different path. If this is not the case, then either the continuity assumption breaks down or that the rotation occurs below the resolution of the image.

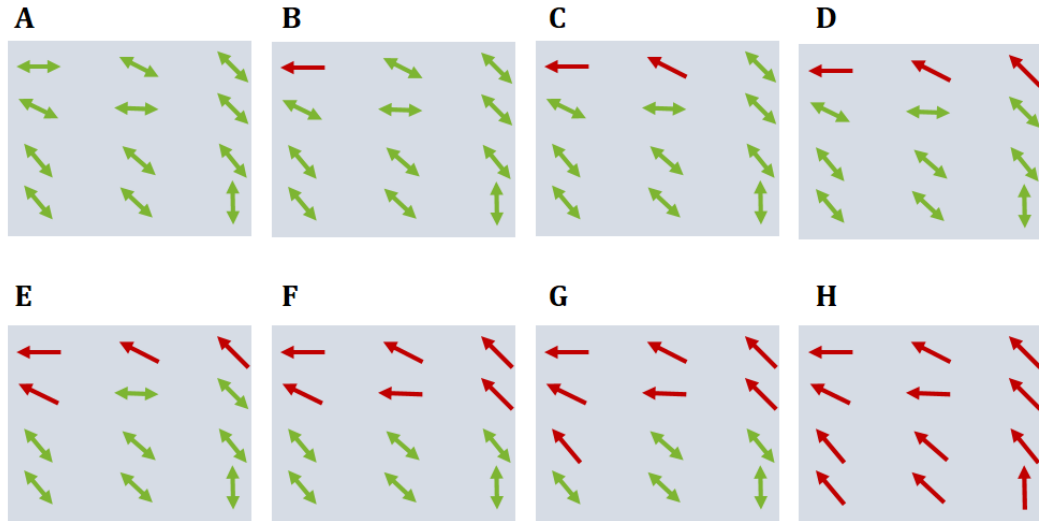


Figure 3.3: *Defining Néel vector maps from spin axis maps.* Illustration of the procedure. The sign is arbitrarily defined in one corner and then “traced” across the area.

Observing Inconsistencies

For a domain structure which can be described in terms of domains and domain walls, a similar tracing of the sign of the Néel vector can be done, without a full vector map, as long as the spin axis in the domains and in the domain walls is known.

This is illustrated in Fig. 3.4 for two examples, where tracing the Néel vector across two different paths yields inconsistencies. Figure 3.4 **A** shows two domains (top and bottom) with horizontal (dark) and vertical (light) spin axis. They are separated by a 90° domain wall with the central spins along one diagonal on the left hand side and along the other diagonal on the right hand side. In the middle the domain wall becomes narrow and reverses orientation (somehow, not resolved). Figure 3.4 **B** shows an attempt to define a Néel vector map for this configuration. The sign is arbitrarily set in the top domain. This defines the sign in the domain wall. Yet, crossing the domain wall on the

left hand (yellow path) and crossing the domain wall on the right hand side (purple path) yield opposite signs for the domain at the bottom. Hence this configuration is incompatible with the continuity assumption.

Similar inconsistency is found for the second example, depicted in Figs. 3.4 C, D, which consists of a 180° domain wall which ends within the area (“dangling end”).

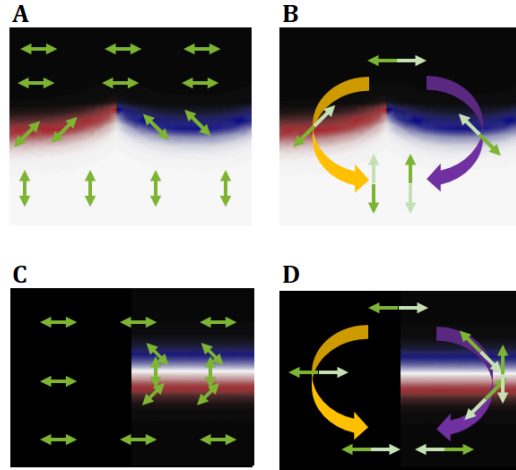


Figure 3.4: *Examples of spin axis maps which are not compatible with continuous Néel vector maps. A:* Illustrative spin axis map (double-headed green arrows) with a 90° domain with two different orientations. The colour of the map decodes the spin axis and is analogous to an overlay of XMLD contrast with horizontal and diagonal x-ray polarisation. *B:* Tracing the sign of the Néel vector (fixed in the top domain) along two different paths (yellow and purple arrows) yields opposite results. *C,D:* Same as A and B but for a 180° domain wall which ends abruptly.

3.3 Results and interpretation

3.3.1 Uniaxial anisotropy in thin CuMnAs films

The island growth of CuMnAs puts a lower limit to the layer thickness for continuous films. Very thin layers with thicknesses of a few nanometers, are typically perforated [51]. Here, only films with thicknesses > 20 nm are investigated. Typical XMLD-PEEM images of AF domain structures in a 20 nm CuMnAs/GaP(001) film are shown in Fig. 3.5. Panels A and B show the same area imaged with $\vec{E}||\langle 110 \rangle$ and $\vec{E}||\langle 100 \rangle$, yielding sensitivity of the XMLD-

signal to the spin axis as indicated by the greyscale wheels. Figure 3.5 **B**, with sensitivity to spin axis along the $\langle 100 \rangle$ reveals that the spin axis in the majority of the area is aligned perpendicular to the x-ray polarisation, *i.e.* along one of the CuMnAs $\langle 100 \rangle$. Additionally, the whole image shows pronounced variation of the signal on the scale of less than 100 nm is observed. Additionally, it can be seen that the top and bottom area of the sample are separated by a narrow line with maximum XMLD-signal which crosses almost the entire width of the imaged area. This white line is interpreted as a 180° domain wall separating two domains with antiparallel Néel vector, whereas the “granularity” is interpreted as a local variation within the large domains. Consistent with this interpretation, the XMLD-PEEM image measured with $\vec{E} \parallel \langle 110 \rangle$, Fig. 3.5 **A** shows little XMLD-contrast in the majority of the area and both maximum and minimum contrast on the domain wall. This confirms the interpretation as a 180° domain wall between two domains aligned parallel and antiparallel to the CuMnAs $[100]$. Measurements with out-of-plane x-ray polarisation show no signal which confirms that the contrast is magnetic and not topographic. Strikingly, the domain wall “ends” at the left hand side of the area, since the Néel vector needs to rotate by 180° between the area above and below the domain wall. A similar observation on a different film is discussed in detail in reference [88], where it has been associated to the presence of atomically sharp 180° domain boundaries, which do not give contrast in X-PEEM images. However, the granularity within the two domains, might also hide a continuous rotation occurring below the spatial resolution of the instrument.

The area shown in Fig. 3.5 is representative for the sample. Domains aligned primarily with the CuMnAs $[100]$, with sizes up to $100 \mu\text{m}^2$, have been observed on all investigated areas of the sample, with similar granularity within the domains. Narrow, 180° domain walls though scarce, were found to be the only other characteristic feature in the X-PEEM images, indicating (in-plane) a uniaxial anisotropy with magnetic easy axis along (one of the) CuMnAs $[010]$. Uniaxial anisotropy along one of the CuMnAs $\langle 100 \rangle$ directions in this layer has

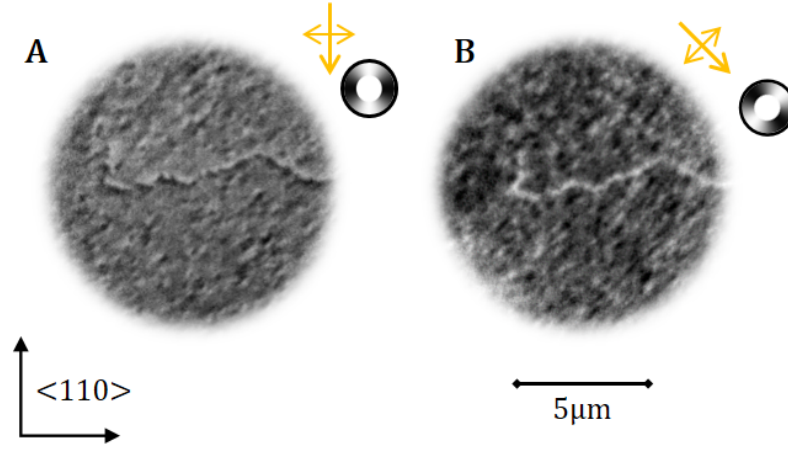


Figure 3.5: *AF domains in a typical 20 nm CuMnAs/GaP(001) film. XMLD-PEEM images of an area of the film with a 180° domain wall (DW). A: measured with $\vec{E} \parallel \langle 110 \rangle$ and B: measured with $\vec{E} \parallel \langle 100 \rangle$, perpendicular to the hard easy axis of the film. Similar granular AF domains aligned with primary spin axis along one of the $\langle 100 \rangle$ directions, were observed across all areas of the film. 180° DWs of similar width and morphology as the one imaged here, are the only other characteristic feature observed.*

also been inferred from spatially averaged X-ray magnetic linear dichroism and magnetoresistance measurements in in-plane magnetic fields [89], and reported in previous studies for a 10 nm CuMnAs/GaP film [53]. In analogy to uniaxial anisotropy observed in ferromagnetic thin films grown on III-V semiconductor substrates [90, 91], the uniaxial anisotropy in the thin CuMnAs films has been attributed to an interfacial effect resulting from a reduced symmetry of the bonding at the interface [53].

3.3.2 Biaxial anisotropy in 50 nm CuMnAs/GaP(001) films

With increasing thickness of the CuMnAs layer, interfacial effects should become less relevant compared to intrinsic anisotropy of tetragonal CuMnAs. On GaP(001) substrates, CuMnAs films can be grown fully strained up to a thickness of ~ 50 nm. Figure 3.6 shows XMLD-PEEM images of characteristic domain structures, measured in three different, fully strained 50 nm CuMnAs films, grown on high-quality GaP(001) substrates. The sample shown in panel A, was capped with 30 nm As and de-capped in ultra-high vacuum just before the measurements, the samples shown in panels B and C are capped

with 2.5 nm Al. The AF domain structures in the three films largely resemble each other and are characterised by two types of domains with mutually orthogonal spin axes along the CuMnAs $[110]$ and $[\bar{1}10]$ and approximately equal domain population indicating a biaxial anisotropy with two mutually orthogonal, equivalent magnetic easy axes.

The three samples show very similar domain morphology, but the average domain sizes varies significantly from a few μm^2 (**A**) to over tens of μm^2 (**C**). This domain morphology has been found to be characteristic for fully strained 50 nm CuMnAs/GaP(001) and similar domain morphology, with individually varying typical lengthscales has been observed in more than 5 other films.

Although the 50 nm CuMnAs/GaP(001) samples are the CuMnAs films with the highest crystalline quality, the measurements presented in chapter 5 will reveal that the AF domain structures are dominated by certain structural defects, “microtwins” (see section 2.1) which terminate at the surface as characteristic lines along the CuMnAs $\langle 110 \rangle$ directions. The rectangular defect pattern governs the domain morphology and the defect density dictates the average domain size.

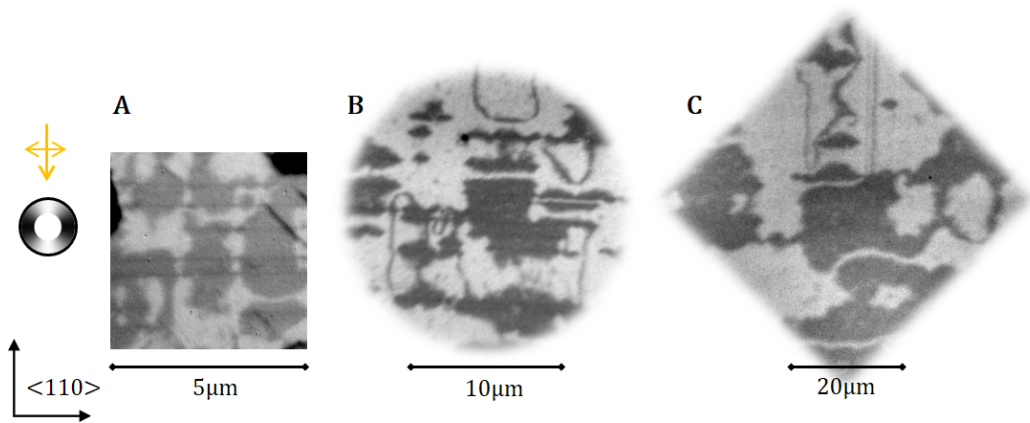


Figure 3.6: *AF domains in biaxial 50 nm CuMnAs/GaP(001) layers.* XMLD-PEEM images with $\vec{E} \parallel \langle 110 \rangle$ of three different 50 nm CuMnAs/GaP(001) layer with characteristic “biaxial domain structure” consisting of two types of domains aligned with mutually orthogonal spin axis along the $[110]$ and $[\bar{1}10]$. Panels **A**, **B** and **C** have a different scale bar to match the different domain sizes of the layers.

Local deviation from the biaxial structure The degree of variation (granularity) of the contrast within the big domains of the biaxial 50 nm CuMnAs/GaP(001) films was found to vary between different growths, presumably depending on the crystalline quality, *i.e.* the presence of other defects. The image shown in Fig. 3.6 C shows a film which was grown slightly manganese-rich which results in MnAs inclusions. XMLD-PEEM images of AF domain structures in the vicinity of MnAs inclusions can show a more gradual contrast variation. High-resolution XMLD-PEEM images of one same area next to a MnAs inclusion, obtained with 5 different x-ray polarisation directions indicated by the yellow arrows, are shown in Fig. 3.7 A. The two images in the top row are obtained with $\vec{E}||[110]$ and $\vec{E}||[\bar{1}10]$, yielding opposite contrast, with maximum sensitivity to the spin axes aligned with the two magnetic easy axes. The images below are measured with x-ray polarisation closely aligned with the CuMnAs [010] direction (middle), and polarisation rotated by -15° (left) and 5° (right) away from the CuMnAs [010] direction. In addition to magnetic contrast, very thin horizontal lines can be seen in the bottom half of the images, which are indicative of microtwin defects.

The images have been drift and distortion corrected such that there is a pixel-to-pixel correspondence between the images. A “movie” of the data, which also contains six additional images with further polarisation angles covering almost the full 180° can be found in the supplementary video S1 here shorturl.at/awAU9. In the movie, it looks as if there is a wave-like motion, but this is an optical illusion resulting from the dependence of the XMLD-contrast on the polarisation angle. The AF domain structure is stable. A vector map, retrieved from the distortion-corrected dataset is shown in Fig. 3.7 B. The area is cropped slightly to not include the MnAs inclusion and ensure overlay of all XMLD-PEEM images. Although the XMLD signal has a periodicity of π , *i.e.* insensitive to the sign of the Néel vector, the data in vector map in Fig. 3.7 B are uniquely defined for a $[0, 2\pi)$. This has been done by calculating a spin axis map first and then finding a Néel vector map following the procedure in

section 3.2.3.

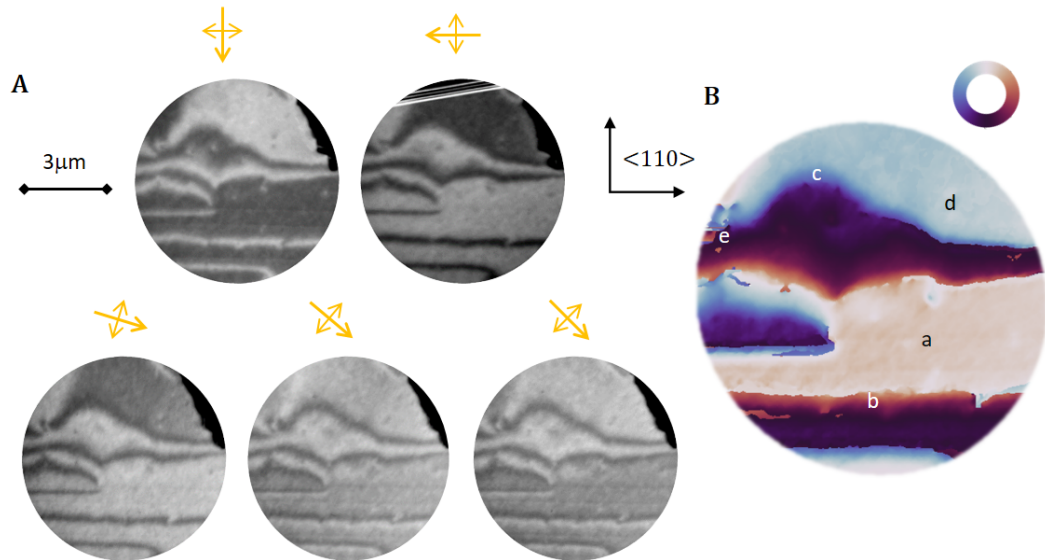


Figure 3.7: *AF structure in a biaxial 50 nm CuMnAs/GaP(001) film in the vicinity of a MnAs inclusion* **A:** High-resolution XMLD-PEEM images of one area with varying x-ray polarisations, as indicated by the yellow arrows. The MnAs inclusion is the black region at the top-right and served to align the images. The black/white lines on the top left of the image at the top right, is where the area of interested has drifted out of the imaged range. The full dataset, with 6 more polarisation angles, is available in the supplementary video S1 here shorturl.at/awAU9. **B:** Vectormap of the region, cropped slightly to exclude the MnAs inclusion and ensure overlap of all images, calculated from the images shown in **A**.

The small letters indicate one example of the following characteristic features: (a) Domains mostly aligned with the two magnetic easy axes; (b) well-defined 180° domain walls; (c) broader 90° domain walls; (d) almost continuous, gradual spin axis rotation, here from the easy axis towards the edge normal of the edge of the MnAs inclusion; (e) complex, frustrated vortex-like structures. The area shows no sharp $\sim 180^\circ$ boundaries between neighbouring pixels, hence is consistent with the continuity assumption.

Evidence of sharp domain boundaries has neither been found in any other of the biaxial 50 nm CuMnAs/GaP(001) films, although these have been intensively and extensively studied in this work (see chapters 4, 5, 6 and 7).

3.3.3 Uniaxial 50 nm CuMnAs/GaP(001) films

In some 50 nm CuMnAs/GaP(001) films the two $\langle 110 \rangle$ domains are not equally populated, but one (or the other) of the $\langle 110 \rangle$ domain types dominates, as shown in Fig. 3.8. The XMLD-PEEM images are obtained from the 50 nm CuMnAs/GaP(001) film with the highest crystalline quality and lowest microtwin density. Figure 3.8 **A** shows a large area map measured with $\vec{E} \parallel \langle 110 \rangle$, which shows extended domains aligned with the CuMnAs $[110]$ and $[\bar{1}10]$, but a clear preference for domain aligned perpendicular to the x-ray polarisation is observed. Figure 3.8 **B** shows approximately the same area, but imaged with $\vec{E} \parallel \langle 100 \rangle$ which yields contrast on the domain walls. Both 180° DWs and 90° DWs are clearly visible. The insets shows high-resolution images of selected areas. The XMLD-PEEM image with $\vec{E} \parallel \langle 100 \rangle$, shows two places, where a 90° domain wall abruptly reverses its spin axis orientation. In contrast to the measurements on the biaxial sample shown above, it is not possible to find a continuous solution for the Néel vector including its sign for a region which contains these points. Tracing the Néel vector on a closed loop around the points results in inconsistencies, indicative of AF domain boundaries below the resolution of the XMLD-PEEM imaging technique, discussed (for this particular example) in reference [88].

Some films have even shown stronger preference for one of the $\langle 110 \rangle$ domains, shown for one example in Fig. 3.9. In this sample extended minority domains, with spin axis along the orthogonal $\langle 110 \rangle$ direction, are restricted to $\sim 0.5 \mu\text{m}$ wide stripe-like domains, oriented parallel to the ($\langle 110 \rangle$) spin axis of the stripe-domain.

Narrower 180° domain walls, without clear alignment to the crystallographic axes, and local spin texture variation within the big domains (“white blobs”) are also observed. The 180° domain walls are often found to connect stripe domains (marked by the blue circle), but in some cases also to have “dangling ends” (marked by the purple circle). XMLD-PEEM images with $\vec{E} \parallel \langle 100 \rangle$ of

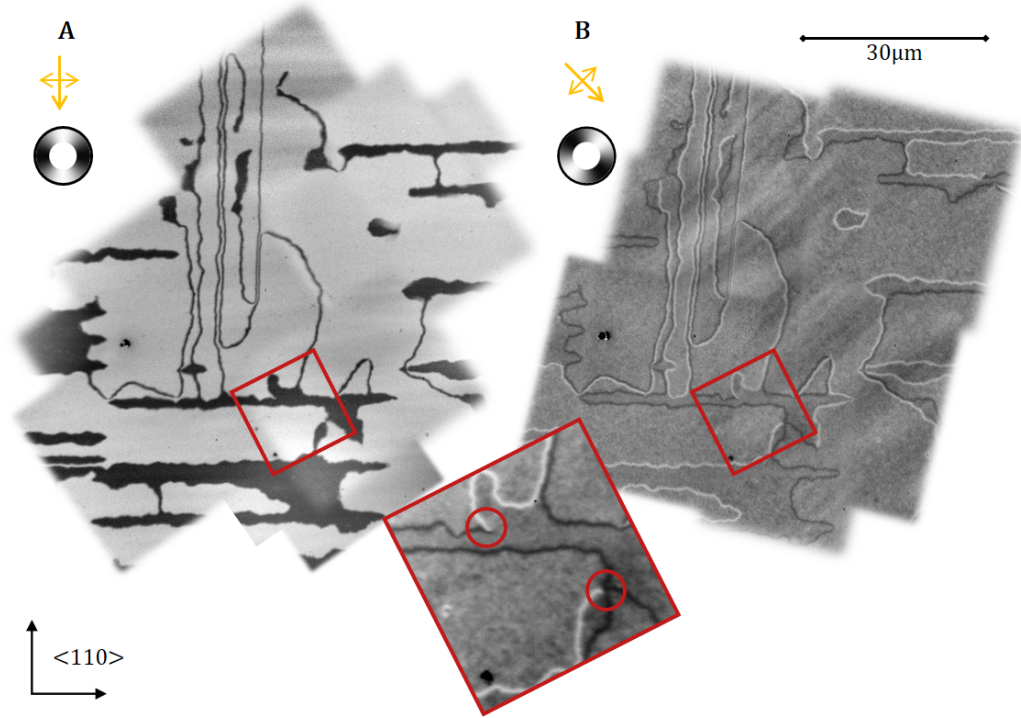


Figure 3.8: *AF domains in a 50 nm $\text{CuMnAs}/\text{GaP}(001)$ film with unequal domain population.* Large area maps of the XMLD-PEEM images in a 50 nm $\text{CuMnAs}/\text{GaP}(001)$ film showing large, extended AF domains aligned with all $\langle 110 \rangle$ direction, but uniaxial preference for one of the CuMnAs $\langle 110 \rangle$ directions. **A:** Stitch of XMLD-PEEM images measured with $\vec{E} \parallel \langle 110 \rangle$. **B:** Stitch of XMLD-PEEM images measured with $\vec{E} \parallel \langle 100 \rangle$ yielding contrast on the domain walls. **A** and **B** show approximately, but not exactly the same area. The inset (below) is a high-resolution XMLD-PEEM images with $\vec{E} \parallel \langle 100 \rangle$ of the area marked by the red square. It shows two cases, for which no continuous solution of the Néel vector can be found, indicated by the red circles.

the two areas are shown in Fig. 3.9 **B**. Close to dangling ends, the domain wall broadens slightly. The exact termination cannot be resolved from the available data. They could be seen as evidence for atomically sharp domain boundaries, but the data quality is not sufficient to rule out a continuous rotation. When terminating at a stripe domain, the 180° domain wall splits into two 90° domain walls which clearly separate the stripe domain from the surrounding majority domain. The area in the blue circle also shows a point, where the domain wall reverses chirality, *i.e.* dark/light becomes light/dark. This point coincides with a sharp angle of the domain wall path, which is attributed to local defect pinning. Such kinks are discussed in reference [92]. The stripe domains can be attributed to the local coupling to microtwin de-

fects, as will be evident from the measurements shown in chapters 5 and 6. A high-resolution image of a 180° domain wall without obvious pinning measured with $\vec{E}||\langle 110 \rangle$ is shown in Fig. 3.9 C. Measurements with $\vec{E}||\langle 100 \rangle$ of the same area are shown in panel D. During the scan of 20 XMLD-PEEM images, the domain wall was found to spontaneously move: In the first 15 images of the sequence the domain wall bends downwards (left panel). In the last 4 images, the domain wall bends upwards (middle panel), and the XMLD-PEEM image measured in between (right) shows an overlay of the two positions the domain, *i.e.* the domain wall moved during the scan. The observation of spontaneous domain wall movement during imaging has been not uncommon, but always been restricted to 180° domain walls without clear alignment with the crystallographic directions, indicating that these are considerably less strongly pinned than 90° domain walls or 180° domain walls aligned with the crystallographic axes.

Clear preference for domains aligned with one of the CuMnAs $\langle 110 \rangle$ have also been observed in another 50 nm CuMnAs/GaP(001). The large area maps of XMLD-PEEM images shown in Fig. 3.10 show AF domains with sizes exceeding several tens of μm^2 , local spin texture (white blobs) within the large domains and 180° DWs without obvious alignment to the crystallographic directions. In contrast to the previous samples, no stripe domains are observed which suggests that no microtwin defects are present in the sample (or at least within the imaged area). The data shown here were recorded more than 5 years after the sample was grown and show 180° domain walls with “dangling” ends, which could be seen as an indication of non-X-PEEM resolvable AF domain boundaries. These have not been observed in measurements on this sample, performed prior to this work within one year of the sample growths. Here, the domain walls had been found to either form closed loops or terminate at patterned edges.

As for the sample studied above, the domain walls widen at the dangling ends. Resolving the precise spin texture is not possible from the available dataset and

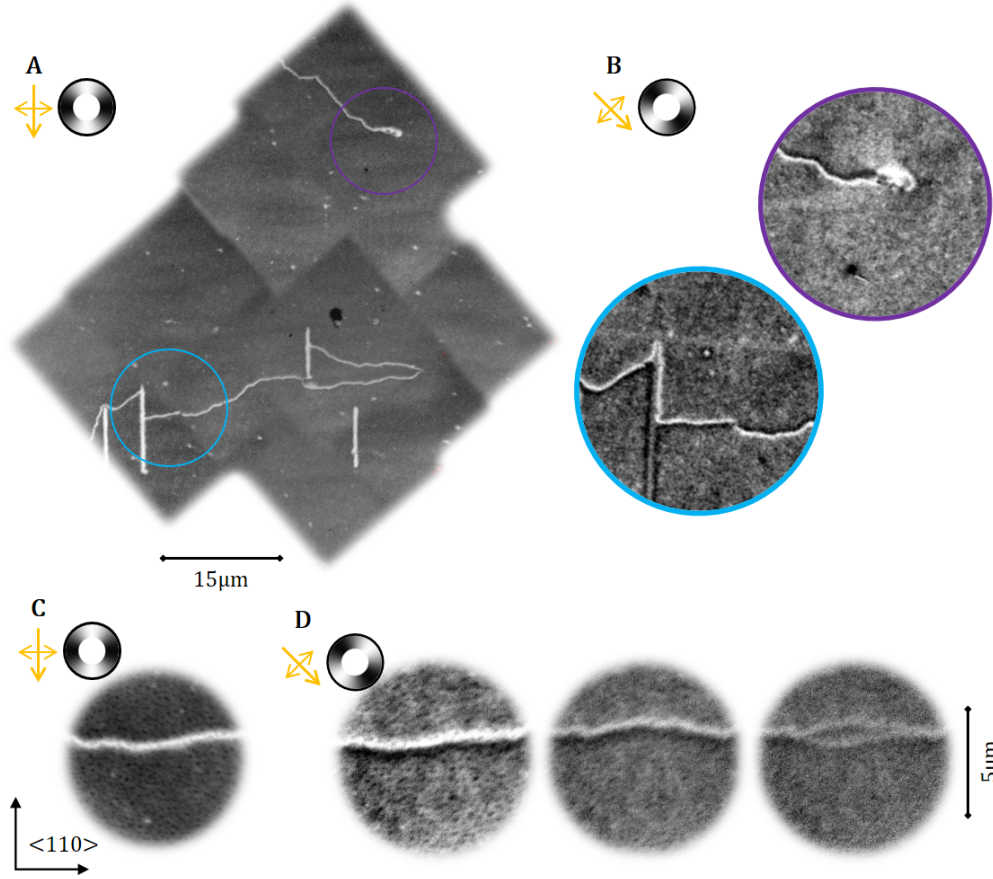


Figure 3.9: *AF domains in a 50 nm CuMnAs/GaP(001) with strong preference for one of the $\langle 110 \rangle$ domains.* **A:** Large area map stitched together from (low-resolution) XMLD-PEEM images with $\vec{E} \parallel \langle 110 \rangle$. **B:** XMLD-PEEM images (low-resolution) with $\vec{E} \parallel \langle 100 \rangle$ of the two areas marked with the coloured circles in panel **A**, showing a “dangling” end of a 180° domain wall (upper panel) and a 180° domain wall terminating at a stripe domain, with a point where the chirality reverses (lower panel). **C:** High-resolution XMLD-PEEM image of a 180° domain wall $\vec{E} \parallel \langle 110 \rangle$ (average of 15 images). **D:** XMLD-PEEM images of the same area measured with $\vec{E} \parallel \langle 100 \rangle$. Left: average of the first 15 images of a scan, the domain wall is bent downwards. Middle: average of the last 4 images of the scan, the domain wall is bent upwards. Right: Image measured in-between, showing an overlay of the two domain wall position.

would require measurements with higher spatial resolution and preferentially several x-ray polarisation angles.

3.3.4 AF domains in relaxed CuMnAs films

The previous discussion was limited to CuMnAs samples grown fully strained on GaP(001). If grown thicker or on less well lattice-matched substrates, like GaAs, the CuMnAs films relax (see [46]) the strain across the depth of the

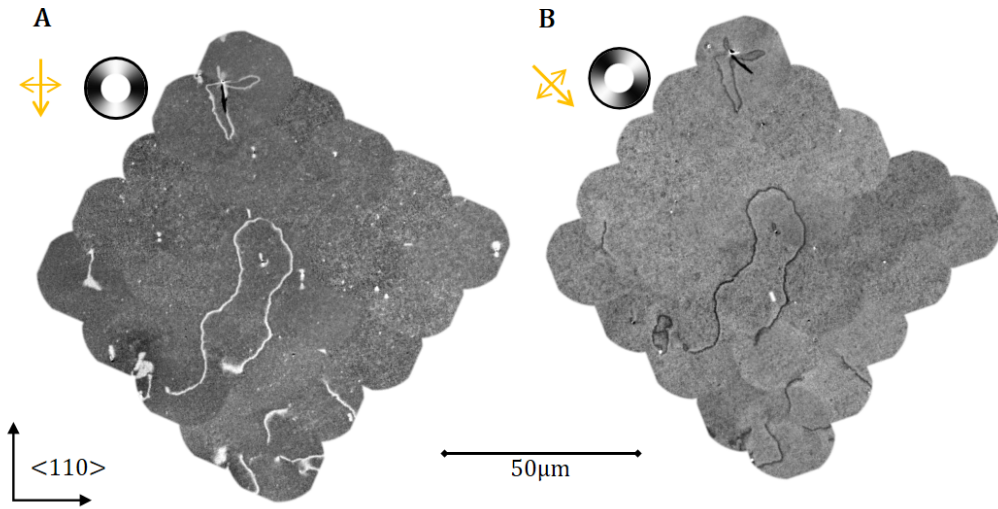


Figure 3.10: *AF domains in a 50 nm CuMnAs/GaP(001) film with uniaxial anisotropy along one of the $\langle 110 \rangle$ directions. A: Large area map of the sample stitched together of XMLD-PEEM images with x-ray polarisation along a $\langle 110 \rangle$ direction. B: Same as A, but with x-ray polarisation along a $\langle 100 \rangle$ direction.*

film.

Figure 3.11 shows XMLD-PEEM images of AF domain structures observed in two typical 45 nm CuMnAs films grown on GaAs(001). The areas are representative for each film. One of the films, shown at the bottom panels is grown on an additional 1 nm seeding layer. The typical lengthscale of the AF domain structure is on the sub-micron scale. For both polarisation directions, $\vec{E}||\langle 110 \rangle$ and $\vec{E}||\langle 100 \rangle$, the XMLD-PEEM images create the impression of two types of domains, parallel and perpendicular to the polarisation vector, but this is an “optical illusion” resulting from the nonlinear, $\cos(2\theta)$ dependence of the XMLD signal. The spin textures cannot be classified into domains and domain walls. The data suggest that the AF anisotropy is mostly easy-plane in both samples.

For the sample without the seeding layer, the XMLD-PEEM image with $\vec{E}||\langle 110 \rangle$ shows an imbalance between dark and light areas, whereas the image with $\vec{E}||\langle 100 \rangle$ shows no imbalance and larger “grey” areas without XMLD contrast. This indicates of a small uniaxial anisotropy component along one of the CuMnAs $\langle 110 \rangle$ directions. No such preference is observed in the XMLD-

PEEM images of the sample grown with a seeding layer. The larger contrast in the X-PEEM image with $\vec{E}||\langle 110 \rangle$ compared to the image with $\vec{E}||\langle 100 \rangle$ can be attributed to the relative size of the XMLD-signals ($|I_{[100]}/I_{[110]}| = 0.6$) only.

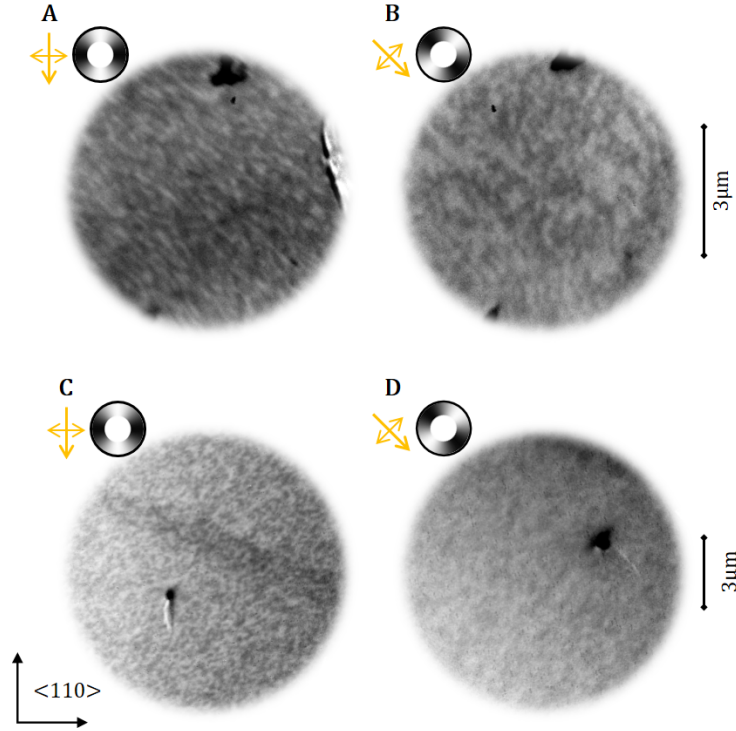


Figure 3.11: *AF domains in two 45 nm $\text{CuMnAs}/\text{GaAs}(001)$ films grown with and without CuMn seeding layer. **A:** XMLD-PEEM image with $\vec{E}||\langle 110 \rangle$ of a typical area of the film grown without a seeding layer, showing a slight preference for one of the $\langle 110 \rangle$ domains. The feature at the right hand side is the shadow of a defect. **B:** Same area as **A**, measured with x-ray polarisation along a $\langle 100 \rangle$ direction. **C:** XMLD-PEEM image with $\vec{E}||\langle 110 \rangle$ of a typical area of a 45 nm $\text{CuMnAs}/\text{GaAs}(001)$ film grown with an addition 1 nm CuMn seeding layer. The dark “stripe” is not magnetic contrast, but an area with reduced intensity, independent of the x-ray polarisation. **D:** XMLD-PEEM image with $\vec{E}||\langle 100 \rangle$ of the same film. The imaged area is shifted slightly with respect to panel **C**. The black spots in the two images are (shadows of) the same topographical defect (hills), which appears different due to the different orientation of the incoming x-ray beam.*

AF domains observed in a 100 nm $\text{CuMnAs}/\text{GaP}(001)$ film with strain relaxation are shown in Fig. 3.12. Most notably, the XMLD-PEEM image with $\vec{E}||\langle 110 \rangle$ shows a pattern of light and dark lines aligned with the CuMnAs $\langle 110 \rangle$ and spin axis parallel to the lines. As for the stripe domains in the sample shown in Fig. 3.9, it will be evident from the discussion in chapter 5, that the light and dark lines result from the local coupling of the AF spin axis to

a microtwin defect. In this sample, the XMLD-PEEM images with $\vec{E}||\langle 100 \rangle$ show no clear boundary of defect-coupled AF domains, but faint lines in the centre, considerably thinner than the AF domains in the image $\vec{E}||\langle 110 \rangle$ which are attributed to structural contrast arising on the defect.

The areas between the line-pattern show a granular, continuous contrast variation on a sub-micron scale in the XMLD-PEEM images with both polarisations. Thus, the microtwin-free areas of the relaxed film on GaP show a spin texture reminiscent of the spin textures observed in the samples grown on GaAs(001) suggesting easy-plane anisotropy.

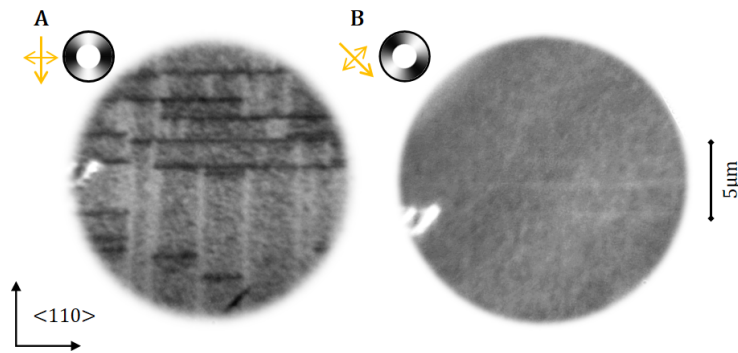


Figure 3.12: *AF domains in a 100 nm $\text{CuMnAs}/\text{GaP}(001)$ film. **A:** XMLD-PEEM image of a typical area imaged with $\vec{E}||\langle 110 \rangle$. The light and dark lines are magnetic contrast. **B:** Approximately the same area imaged with $\vec{E}||\langle 100 \rangle$. The bright area at the left is a defect, present in both images, can be used for reference. The faint, thin lines are structural contrast on microtwin defects.*

Testing, if the observed spin textures can be described by a continuous vector field, or if there is evidence of sharp, discontinuous domain boundaries, has not been attempted, since the (complex) spin variation occurs on a length-scale close to the spatial resolution of the images.

3.3.5 AF domains in $\text{CuMnAs}_{0.9}\text{Sb}_{0.1}/\text{GaAs}(001)$

Complex spin textures, with slightly larger typical lengthscale, are observed in XMLD-PEEM measurements of a 45 nm $\text{CuMnAs}_{0.9}\text{Sb}_{0.1}/\text{GaAs}(001)$, illustrated in Fig. 3.13. The substitutional incorporation of antimony is expected to yield better lattice-match with the GaAs(001) substrate, and is discussed in detail in reference [93]. Although in principle the size of the XMLD signal

could be different for this sample compared to the CuMnAs samples, maximum contrast can be expected between spin axis parallel and perpendicular to the x-ray polarisation if the polarisation vector is aligned with a high symmetry-axis ($\langle 110 \rangle$ and $\langle 100 \rangle$, $[001]$). XMLD-PEEM images with out-of plane x-ray polarisation have shown no contrast indicating that, as in the non-doped CuMnAs samples the spin align within the film plane. Figure 3.13 **A** and **B** show 10.5 μm field-of-view images of a representative area of the sample imaged with $\vec{E} \parallel \langle 110 \rangle$ and $\vec{E} \parallel \langle 100 \rangle$ respectively. The image $\vec{E} \parallel \langle 100 \rangle$ shows a maze-like pattern with primarily two contrast levels and a slight imbalance between light and dark areas. Interestingly, the contrast appears larger for this imaging configuration than for $\vec{E} \parallel \langle 110 \rangle$ which has larger contrast in pure CuMnAs samples. The image with $\vec{E} \parallel \langle 100 \rangle$, Fig. 3.13 **A**, area shows a higher number of contrast levels and suggests the domain pattern appears smaller than in Fig. 3.13 **B**, although almost the same area is shown.

For further insight into the complex structure, high resolution images of (a different) representative area with various x-ray polarisation angles have been taken. The measurements are illustrated in Fig. 3.13 **B**. The images have been drift and distortion corrected to yield a one-to-one pixel correspondence. The full dataset, 11 angles, can be seen in the supplementary video S2 here shorturl.at/awAU9. As expected, the contrast between X-PEEM images with orthogonal x-ray polarisation reverses, yet the correlation between images with non-normal angles between x-ray polarisation is difficult to see, highlighting how the XMLD-effect can trick the eye. All XMLD-PEEM images show a maze-like pattern with varying number of contrast levels, being largest for x-ray polarisation along the $\langle 100 \rangle$ and smallest for $\vec{E} \parallel \langle 110 \rangle$.

The data suggest that retrieving a vector map might reveal interesting AF spin textures. Yet, the more detailed analysis was postponed until the sign and size of the XMLD effect in this material is established either experimentally or by theoretical calculations.

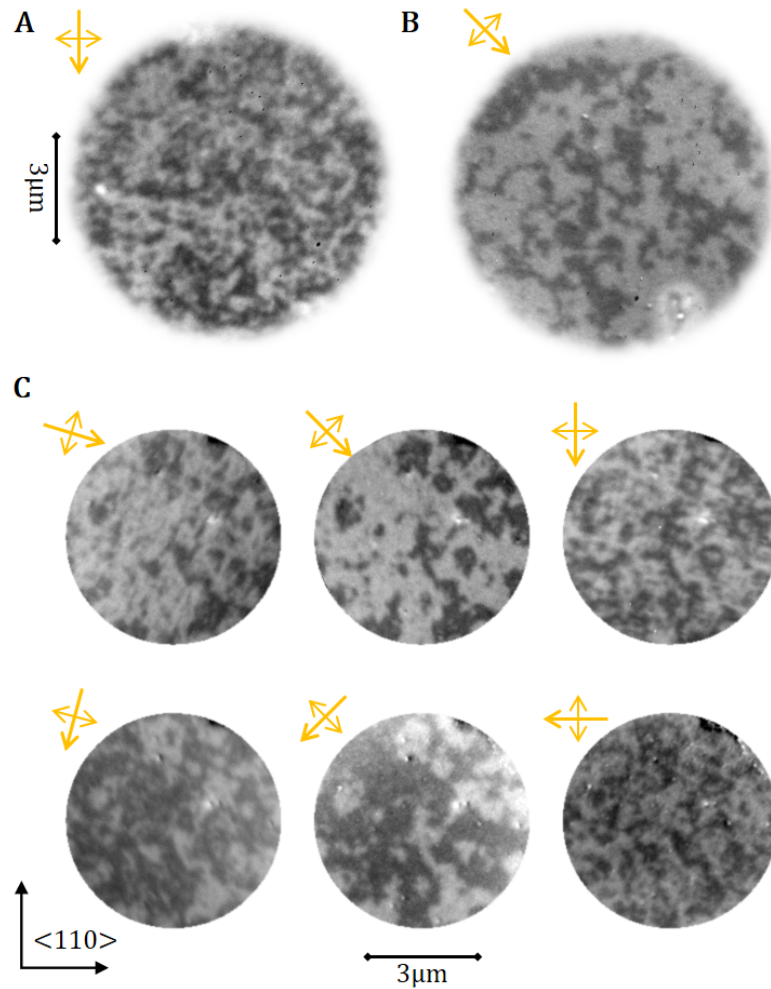


Figure 3.13: *AF domains in 50 nm $\text{CuMn}(0.9)\text{Sb}(0.1)/\text{GaAs}$. **A:** Medium resolution XMLD-PEEM image of a typical area imaged with x-ray polarisation along a $\langle 110 \rangle$ directions. **B:** Same as **A**, but imaged with $\vec{E} \parallel \langle 100 \rangle$. The areas do not overlap perfectly. **C:** High-resolution XMLD-PEEM images of one area imaged with various x-ray polarisation angles as indicated by the yellow arrows. The images are drift and distortion corrected to show (almost) exactly the same area.*

3.4 Summary and conclusion

In summary, the above examples show that a wide range of different AF domain textures are realised in different samples, depending on substrate choice and layer thickness. Even in samples with nominally similar growth conditions qualitatively different domain patterns can be observed.

Fully strained thin films, below 20 nm, typically show a uniaxial anisotropy with the easy axes along one of the $\langle 100 \rangle$ directions which has been attributed to an interface effect. Thicker, fully strained films were found to be either biaxial, with the magnetic easy axes aligned with the CuMnAs $\langle 110 \rangle$ or show

a uniaxial preference for one of the $\langle 110 \rangle$ directions. It will be shown that these domain structures are dominated by a characteristic microtwin defects (see chapter 5).

In thicker samples, with pronounced strain relaxation, the domain structures indicate an easy-plane anisotropy and continuously varying spin textures on a sub-micron scale are found, in samples grown on GaP coinciding with domains related to microtwin defects. Even in the uniaxial or biaxial samples, inhomogeneous spin texture within the large domains can often be observed, presumably due to sensitivity of the AF spin axis to (other) local defects.

Hints for atomically sharp domain boundaries, reported in reference [88], have been found in samples with a uniaxial magnetic anisotropy component. No such evidence was found in biaxial samples or samples with easy-plane anisotropy, though these cannot be excluded. This indicates that the additional uniaxial anisotropy component may be necessary to stabilise these features.

The strong layer-to-layer, and sometimes sample-to-sample, variation suggests that the intrinsic in-plane anisotropy is small compared to the effect of growth, substrate and crystallographic defects. Hence, the magnetic properties of the sample are defined by the sample's crystallographic (defect) structure. This makes it difficult to predict the domain morphology and anisotropy for a new growth, but this allows to choose a specific sample for a particular measurement or application and offers huge potential for domain engineering if the coupling to the crystallographic properties was understood.

Chapter 4

Electrical manipulation of antiferromagnetic domains

4.1 Introduction

The demonstration of electrical manipulation of the AF domain configuration in CuMnAs has been one of the key experimental achievements that triggered the surge of interest in AF materials and the huge increase of AF spintronic research in the last decade.

In the original experiments, two orthogonal writing current pulses were used to cause a shift of the average domain population, measurable as a change of the transverse resistance due to the AMR effect. Due to spin-orbit coupling, combined with the specific symmetry properties of CuMnAs, the electrical currents induce effective magnetic fields perpendicular to the current pulse with alternating sign on the two magnetic sublattices. As such, domains with spin axis perpendicular to the current and the individual sublattice magnetisations parallel to the respective effective fields are energetically favoured. The switching was interpreted as AF domain reorientation perpendicular to the current pulse, matching the symmetry of the measured resistance changes in detailed electrical studies [85]. The interpretation was confirmed with direct imaging of the electrical switching using XMLD-PEEM [94].

In these early studies, the electrical measurements and the XMLD-PEEM images were performed on devices fabricated from a CuMnAs layer epitaxially grown on GaAs. The AF domain structure of this layer shows a non-uniformity of the spin axis on a sub- μm scale and weak in-plane anisotropy (see the previous chapter 3). Electrical measurements with varying pulse amplitude and number of current pulses indicated multi-domain switching, with successively more areas switching with increasing writing current amplitudes or number of pulses per direction. The direct imaging confirmed the multi-domain character of the switching and showed that the switching is generally highly inhomogeneous. Many areas remain unchanged and in some regions even a reorientation parallel to the writing current was observed.

Efforts have been made to achieve larger signals and switching area by tailoring the growth parameter towards larger domains and reducing the size of the device [95]. Here, we investigate switching in CuMnAs films with AF domain structures with larger domains with spin alignment along two orthogonal axes, thus matching the symmetry of the switching experiment. The measurements are performed on devices fabricated from approximately 50 nm thick layers grown fully strained on GaP(001)-substrates, in which micron-sized domains, with spin axes along the CuMnAs [110] and $[\bar{1}10]$ have been realised.

In contrast to the expectation, it is found using X-PEEM imaging and purely electrical measurements that electrical manipulation of the “large” AF domains with orthogonal writing current pulses is less efficient, *i.e.* shows an even smaller switching signal and faster decay than reported previously for layers with more gradual spin variation over sub-micron scales. The findings, though counterintuitive, are consistent with what has been found in purely electrical measurements that compared the characteristics of electrical switching in different layers [96].

In the main part of this chapter, it is shown that the large AF domain structure of the 50 nm CuMnAs/GaP films can be manipulated efficiently, when electrical current pulses are directed along the magnetic hard axes and used to trig-

ger domain wall motion from one pinning point to another. Reversible domain and domain wall reconfigurations between two stable positions are observed upon reversing the polarity of the current pulses only. XMLD-PEEM images of the current-induced domain and domain wall reconfigurations suggest that the switching occurs via domain wall motion. Electrical measurements performed in a series of devices fabricated from the same wafer show that the effect can lead to a measurable change of the transverse resistance. This type of electrical switching does not only allow for a more simple device geometry, but also shows increased stability and can occur at considerably lower current pulse amplitudes. In the following, the two types of switching are referred to as “orthogonal-switching” and “polarity-switching” respectively.

The last part of the section shows further X-PEEM measurements which illustrate that the reversible current-induced changes with orthogonal switching are restricted to a small area only. The observations are compared to a much more dramatic, but irreversible change of AF domain structure induced by a longer duration current pulse. It is found that in the majority of the device, the large domain structure is fragmented into domains of sub-micron scale. Domain coarsening dynamics are found to occur on the time scale of hours.

4.2 Methods

Material All data presented here are obtained from one 50 nm CuMnAs layer grown on GaP(001) and capped with 2.5 nm Al to prevent oxidation. As-grown, the non-patterned film shows a typical biaxial AF domain pattern with intermediate domain sizes (see Fig. 3.6 in chapter 3).

Device fabrication The devices were fabricated by photolithography and chemical wet etching (see section 2.3). Additionally gold-contact pads were evaporated onto the sample. The samples were contacted electrically by wire-bonding from the gold-contact pads to sample holder.

In-house electrical measurements The measurements are performed on three identical replicates of the star-shaped device shown in Figure 4.1. In the optical micrographs, the CuMnAs film appears light-brown; dark-brown areas are where the CuMnAs layer has been etched away and the GaP substrate is exposed. The bright yellow patches are the gold-contact pads. The overview

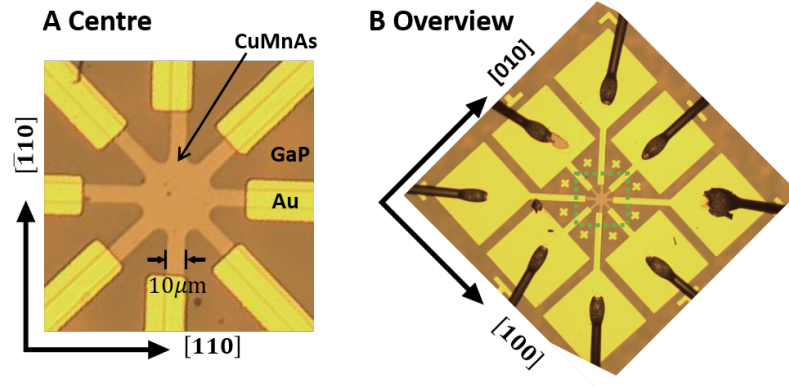


Figure 4.1: Optical micrograph of the device used in electrical measurements. **A** Close-up of the centre of the device. Light-brown areas are the CuMnAs film. Regions, where the film has been etched away and the GaP substrate is exposed appear dark brown. Bright yellow areas are the gold contact pads. **B** Overview image showing the bonding wires and the alignment of the chip edges with the CuMnAs crystalline axes and the reference frame used in this thesis. The green rectangle marks the region shown in **A**.

image, panel **B**, shows the whole device. The dark-lines are the bonding wires. The chip edges, aligned with the CuMnAs [100] and [010], are at 45° to the reference frame used throughout this thesis. Figure 4.1 **A** shows a close-up of the central, active area of the device. All channels are nominally 10 μm wide. The resistivity of the devices was around $2 \times 10^{-4} \Omega\text{cm}$ at room temperature. Electrical writing is done with 50 ms long current pulses. The current pulses are alternating between two orthogonal directions during orthogonal-switching experiments. In polarity-switching experiments the current pulses have alternating polarity with fixed direction. Probing uses continuous probing currents with fixed direction and amplitudes, 0.25 mA (0.025 MA /cm²) in orthogonal switching experiments and 0.5 mA (0.05 MA /cm²) in polarity-switching experiments. In orthogonal-switching experiments, the probing current is directed at 45° to the writing currents, in polarity-switching it is parallel to the

writing current. The longitudinal and transverse resistances are measured. The minimum time between the current pulse and the measurement is 2 s. For details see section 2.10.

All measurements are performed at ambient temperature without temperature control. The orthogonal switching experiments have been conducted in air. Some of the polarity switching experiments are conducted in low vacuum of $\approx 1 \times 10^{-5}$ mbar.

X-PEEM imaging with in-situ electrical manipulation AF domain imaging is achieved using XMLD-PEEM on beamline I06 at Diamond Light Source, using the protocol described in section 2.8.2. For further information see also sections 2.5.2 and 2.7. The X-PEEM measurements are performed on a cross-shaped device with the $10 \mu\text{m}$ wide channels aligned with the CuMnAs [100]/[010] directions. For in-situ electrical manipulation, the sample is mounted on a PEEM-pulsing cartridge and electrically connected by wire-bonding to the four electrical feedthroughs. In-situ electrical manipulation uses 2.5 ms current pulses. For further information see section 2.10. All measurements are done at ambient temperature.

4.3 Results and interpretation

Figure 4.2 **A** shows an optical micrograph of the device used in the X-PEEM measurements. The dark grey areas are, where the CuMnAs has been etched away and the GaP substrate is exposed. Due to overetching, the channel widths are around $8 \mu\text{m}$ wide, slightly narrower than in the optical mask used for device fabrication.

Figure 4.2 **B, C** are XMLD-PEEM images of the antiferromagnetic domain structure obtained from the centre of the “virgin device”, *i.e.* before the application of electrical currents. The yellow arrow indicates the direction and polarisation of the x-ray beam. The spin axis dependence of the XMLD

contrast is indicated by the colour wheels. Panel **B**, x-ray polarisation along the CuMnAs $[110]$ shows that the sample is largely composed of two types of domain populations with respective AF spin axis along the CuMnAs $[\bar{1}10]$ (light) and $[110]$ (dark). In the XMLD-PEEM image with x-ray polarisation along the CuMnAs $[100]$, panel **C**, contrast arises mainly on the domain walls. Single-colour white lines are 90° domain walls with the spins in the centre of the wall aligned with the CuMnAs $[010]$, dark lines are 90° domain walls with the spins in the centre of the wall aligned with the CuMnAs $[100]$. Double-colour lines correspond to 180° domain walls (see also section 3.2.2).

Although the majority of the AF domain structure can be interpreted in terms of domains and domain walls, there are areas where the XMLD-PEEM images show a more gradual contrast variation, for example close to the patterned edge at the top of the images, as well as additional spin texture within the big domains.

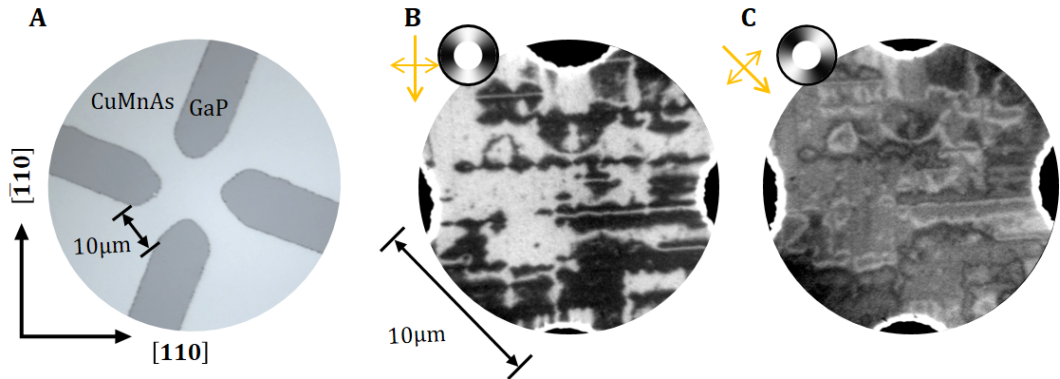


Figure 4.2: X-PEEM device. *A* Optical micrograph. *B* and *C* XMLD-PEEM images of the centre of the device with x-ray polarisation \vec{E} along the $[110]$ (**B**) and $[010]$ (**C**) crystalline directions, both showing a $20\ \mu\text{m}$ field of view. Yellow arrows indicate the direction of the incident x-ray beam and polarisation. The colour wheels show the spin axis dependence of the XMLD-contrast for each imaging configuration.

4.3.1 Orthogonal switching

Observation in XMLD-PEEM 2.5 ms long current pulses are applied along different directions with varying polarities and the AF domain structure is imaged with XMLD-PEEM after each pulse. For current pulses up to

48 mA aligned with the CuMnAs [110] and $[\bar{1}10]$, no significant effect on the virgin AF domain structure is observed. However, changes of the virgin AF domain structure could be observed for writing current directions along the CuMnAs [100] and [010] in localised regions of the device. The sample shows reversible, direction-dependent and polarity-independent AF domain reconfigurations (orthogonal switching), as well as reversible, polarity-dependent changes with fixed current direction (polarity switching).

The green rectangle in the XMLD-PEEM image in Fig. 4.3 **A** marks a $2\ \mu\text{m} \times 2\ \mu\text{m}$ region that shows orthogonal switching for current pulse amplitudes of or larger than 35 mA. The light brown arrows indicate the current pulse direction. The observed changes in the region during a sequence with 35 mA current pulses and a 90° rotation of the current direction between the pulses are shown in Fig. 4.3 **B**. The top row shows a sequence of close-ups of the XMLD-PEEM images measured initially and after each pulse of the sequence. The bottom row shows the difference images between two subsequent images shown directly above. The contrast inversion between sequential difference images highlights the reversibility of the observed changes and comparison of the first two with the second two difference images confirms that the switching occurred indeed independent of the polarity of the current pulse.

The effect of the switching area on the resistance of the sample is minute and well below the noise level of the electrical measurement system in the X-PEEM chamber, so that the observed changes could not be correlated with an electrical signal.

The observed response of the AF structure to orthogonal current pulses are considerably smaller than what has been observed previously in similar devices by Grzybowski et. al. [94, 95] for similar current densities using the same experimental set-up for electrical manipulation and AF domain imaging, but consistent with the findings of purely electrical measurements on a series of devices fabricated from the same wafer, described below.

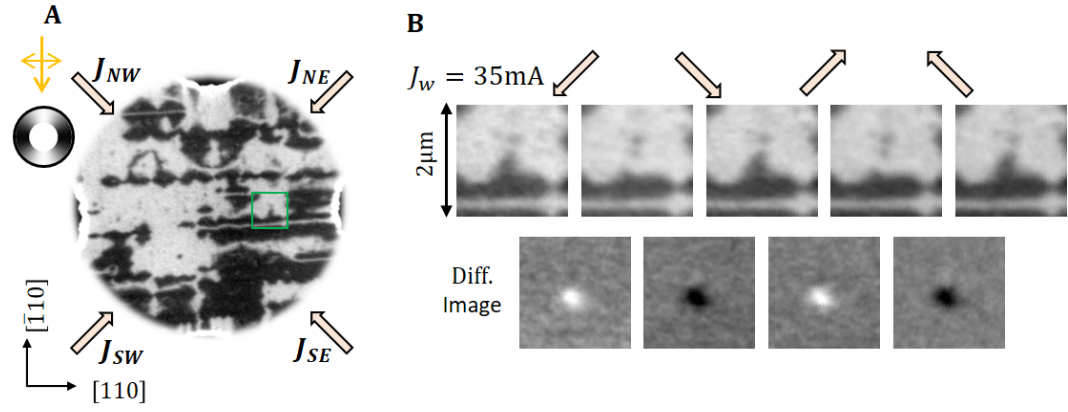


Figure 4.3: *XMLD-PEEM observation of orthogonal, polarity-independent manipulation of AF domains.* **A** Overview of the device centre and directions of the writing current pulses (bold, light brown arrows). **B** Close-ups of the area marked with the green square in **A** during a pulsing sequence. Top: XMLD-PEEM images. Between consecutive images, 2.5 ms long current pulses with amplitude 35 mA were sent along the directions indicated by the light brown arrows. Bottom row: Difference image of consecutive images shown directly above revealing reversible switching of a domain in the centre of the image.

Purely electrical measurements Electrical measurements of orthogonal switching with writing currents along the CuMnAs [100] and [010] are shown in Fig. 4.4. The measurement geometry is depicted in panel Fig. 4.4 **B**. The longitudinal resistance of the sample at room temperature was found to be $\approx 12 \Omega$. The top panel, Fig. 4.4 shows a typical time-sequence of resistance measurements above the switching threshold, here for a writing current amplitude of 42 mA. Top (circles) and bottom (squares) correspond to the transverse and longitudinal resistance respectively, defined according to the geometry depicted in panel **B**. Shown is the deviation from the mean value $\Delta R_{ii} = R_{ii}/\text{mean}(R_{ii})$. Each datapoint is the average of 6 consecutive measurements. No further data manipulation was performed. The colour of the symbols indicates the direction of the previous writing current pulse, as defined in panel **B**. The vertical, dashed lines indicate the time of the orthogonal writing current pulses. Following each current pulse, we observe an initial deviation of the measured resistance from its mean value which decays to a steady-state value which is independent of the current pulse direction. In the case of the longitudinal resistance, the resistance measured closer to a pulse is, for both current pulse

directions, larger than the steady state value. Thus it can be explained as the temperature-related induced resistance change due to Joule-heating during the pulse and following heat dissipation. For the transverse resistance, the deviation alternates in sign, depending on the current pulse direction. For further comparison, the data are shifted in time relative to the time of the previous current pulse. Figure 4.4 C shows the average over all datasets with the same pulse direction. The averages show that the transverse and longitudinal resistance decay over different timescales, with the decay of the transverse resistance being slower. The initial deviation, measured within 10 s after each pulse, is in the order of $200 \text{ m}\Omega \leq 2\% R_{xx}$. Any remanent signal, after approximately 120 s, is below the noise level. The observed change in the longitudinal resistance is larger for pulses along the CuMnAs [100] than for pulses along the CuMnAs [010], which we attribute to imperfections in the sample fabrication and thus slightly different (contact) resistances which lead to different amounts of Joule-heating.

Figure 4.5 shows the same as Fig. 4.4, but for current pulses along the CuMnAs [110] and $[\bar{1}10]$ directions. We observe similar characteristics of the longitudinal and transverse resistance as for the previous measurement geometry. The averaged data, Fig. 4.5, show a slightly smaller initial signal in the transverse resistance, than for current pulses along the magnetic hard axes. The decay of the signal occurs over similar timescales. For both pulsing configurations, the changes observed in the longitudinal resistance have a similar size as the changes in the transverse resistance, the decay of the longitudinal and transverse resistances occur over different time-scales which suggests a magnetic origin of the signal measured in the transverse resistance.

The fact that no significant signal can be measured after 2 min following the current pulse is fully consistent with the minuteness or lack of changes observed in X-PEEM, as it takes approximately 5 min between the pulse and the first acquired X-PEEM image so that the X-PEEM measurements are mainly sensitive to remanent effects.

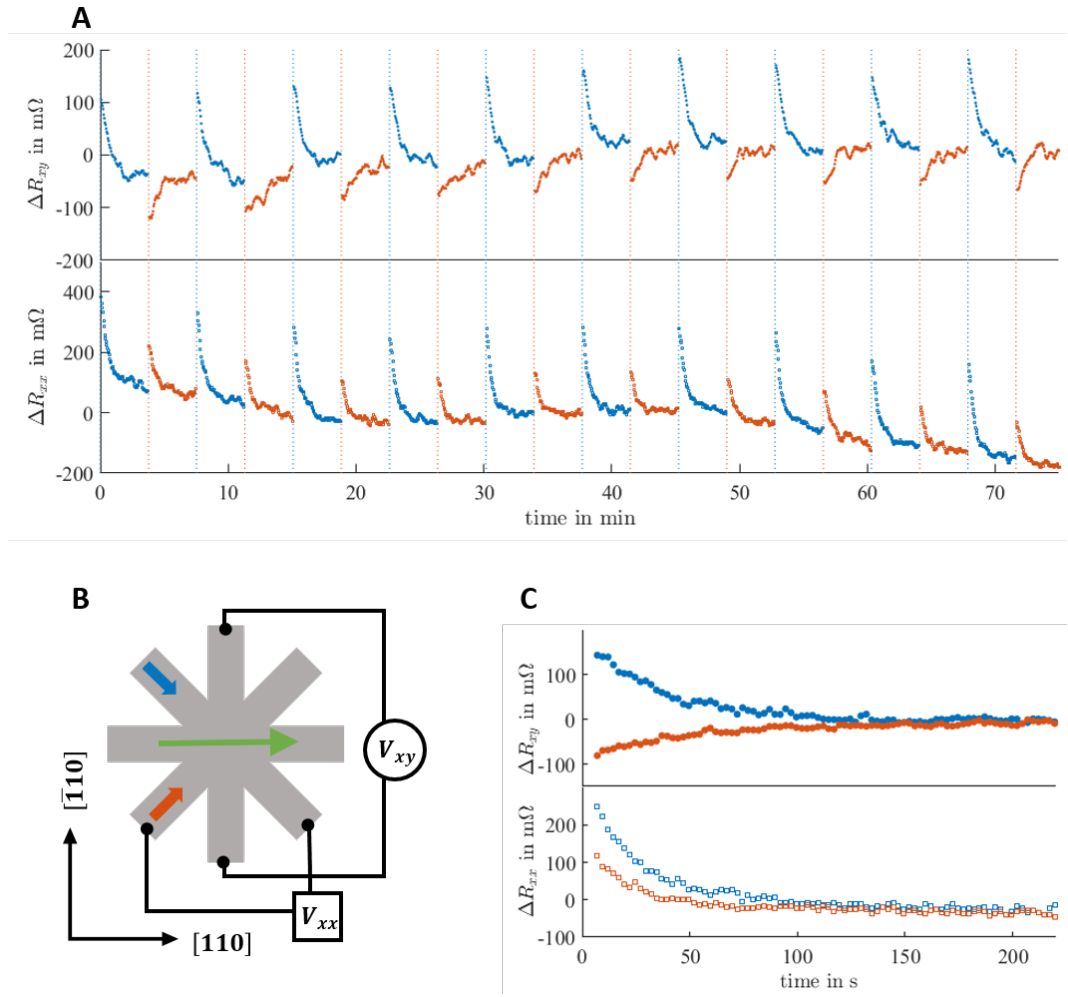


Figure 4.4: Electrical measurements of orthogonal switching along the $[100]$ and $[010]$ directions. **A** Time-sequence of transverse (top) and longitudinal (bottom) resistance changes following 42 mA current pulses J_w with alternating direction, along the CuMnAs $[100]$ (blue) and $[010]$ (red). The dashed lines mark the time of the writing current current pulses. Each datapoint is the average of 6 consecutive measurements. A constant offset, the average of the entire measurement sequence, has been subtracted from both datasets. **B** Schematic of the measurement geometry. The bold red and blue arrows show the direction of the writing current pulses, the thin green arrow represents the reading current. **C** Average over of the data for all pulses in one direction after shifting them in time relative to the time of the previous writing current pulse.

4.3.2 Polarity switching

In the following part, it is shown that the large AF domains in this layer can be manipulated more efficiently by changing the polarity of the current pulses only.

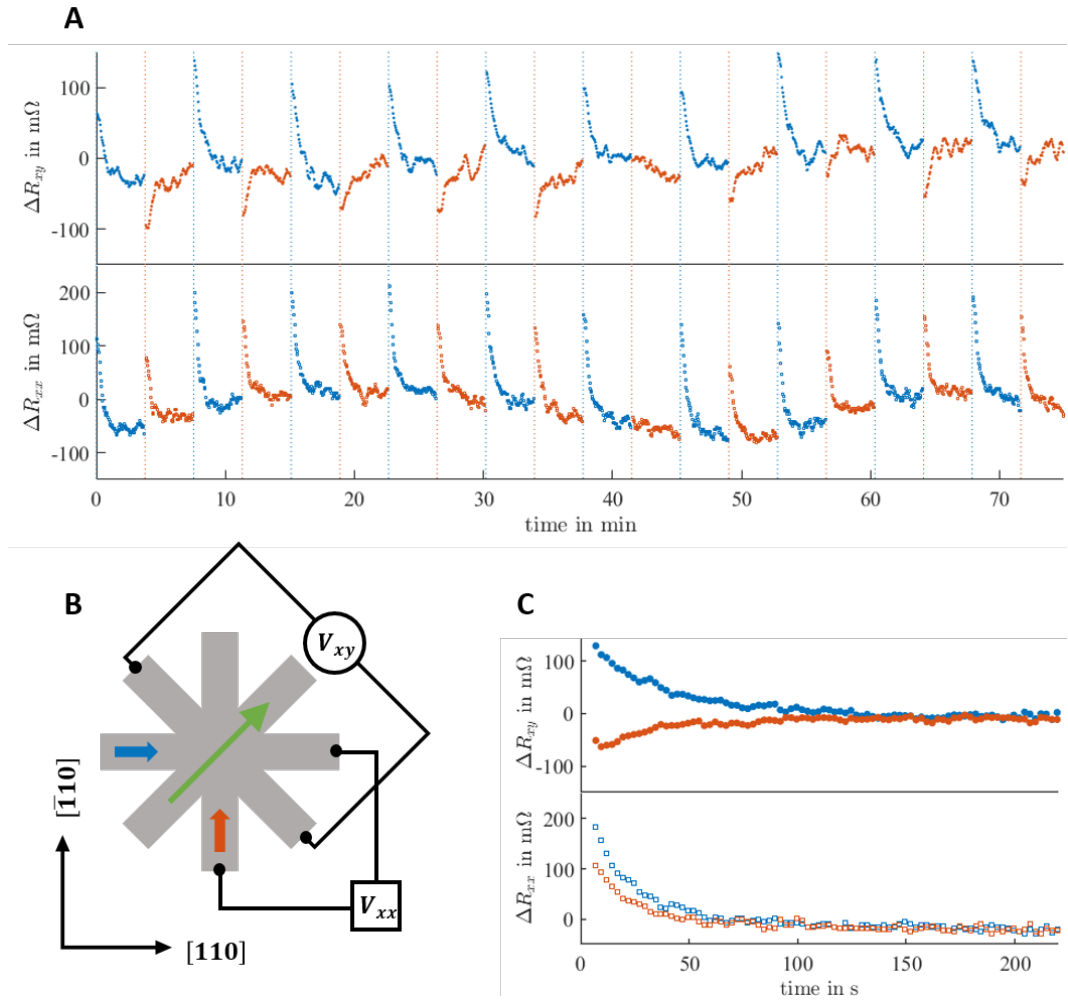


Figure 4.5: Electrical measurements of orthogonal switching along the $[110]$ and $[\bar{1}\bar{1}0]$ directions. **A** Time-sequence of transverse (top) and longitudinal (bottom) resistance changes following 42 mA current pulses J_w with alternating direction. Each datapoint is the average of 6 consecutive measurements. A constant offset, the average of the entire measurement sequence, has been subtracted from both datasets. **B** Schematic of the measurement geometry. The bold red and blue arrows show the direction of the writing current pulses, the thin green arrow represents the reading current. **C** Average over of the data for all pulses in one direction after shifting them in time relative to the time of the previous writing current pulse.

Observation in XMLD-PEEM Figure 4.6 shows XMLD-PEEM measurements of current-induced AF domain reconfigurations in a contact channel of the device, *i.e.* in an area of the device where the direction of the current is fixed parallel to the edge, and only the polarity and amplitude can be varied. In the following, the current polarity is referred to as *positive* for current along $[010]$ (bottom left to top right of figure) and as *negative* for current along $[0\bar{1}0]$, labelled J_+ and J_- in Fig. 4.6.

Panel 4.6 **B** shows close-ups around the switching area, corresponding to the green square in panel **A**. The top row compares XMLD-PEEM images measured with $\vec{E}||[110]$, *i.e.* contrast primarily on the domains following current pulses with different polarities, as indicated by the bold arrow above. Following current pulses with positive polarity (left), the central part of the region shows a “light” domain with (mainly) vertical spin axis, bound above and below by “dark” domains with (mainly) horizontal spin axes. After a current pulse with negative polarity (right), the spin axis in the centre of the area has switched from vertical to horizontal. The dark domain at the top of the image extends over the middle and nearly touches the dark domain underneath. In this imaging configuration, it is difficult to determine if the two dark domains remain separated or merge. The images underneath show the two states imaged with $\vec{E}||[010]$, which yields primarily contrast on the domain walls and confirm that the two dark domains remain separated. The images with $\vec{E}||[010]$ show that the two different states correspond to two different positions of a domain wall, marked by a red dashed line, *i.e.* the switching can be seen as a domain wall movement from one pinning point to another. The positive XMLD contrast of the domain wall indicates that the spins in the centre of the wall and the direction of the electrical current are aligned parallel.

The stability, reversibility and current-amplitude dependence of the domain and domain wall reconfigurations was investigated using a sequence of current pulses with varying current amplitudes. The current polarity was swapped after pulses that induced switching. The measurements are illustrated in Fig. 4.6 **C**. The top row of images shows XMLD-PEEM measurements with $\vec{E}||[110]$ of the switching area. The sequence of current pulses between the images is depicted above. The bottom row are difference images of the two XMLD-PEEM images shown directly above. We have observed no decay of the two states over the entire measurement time between two pulses, varying from 10 min to over 30 min. Over a period of over 8 hrs (overnight) only a minor change occurred.

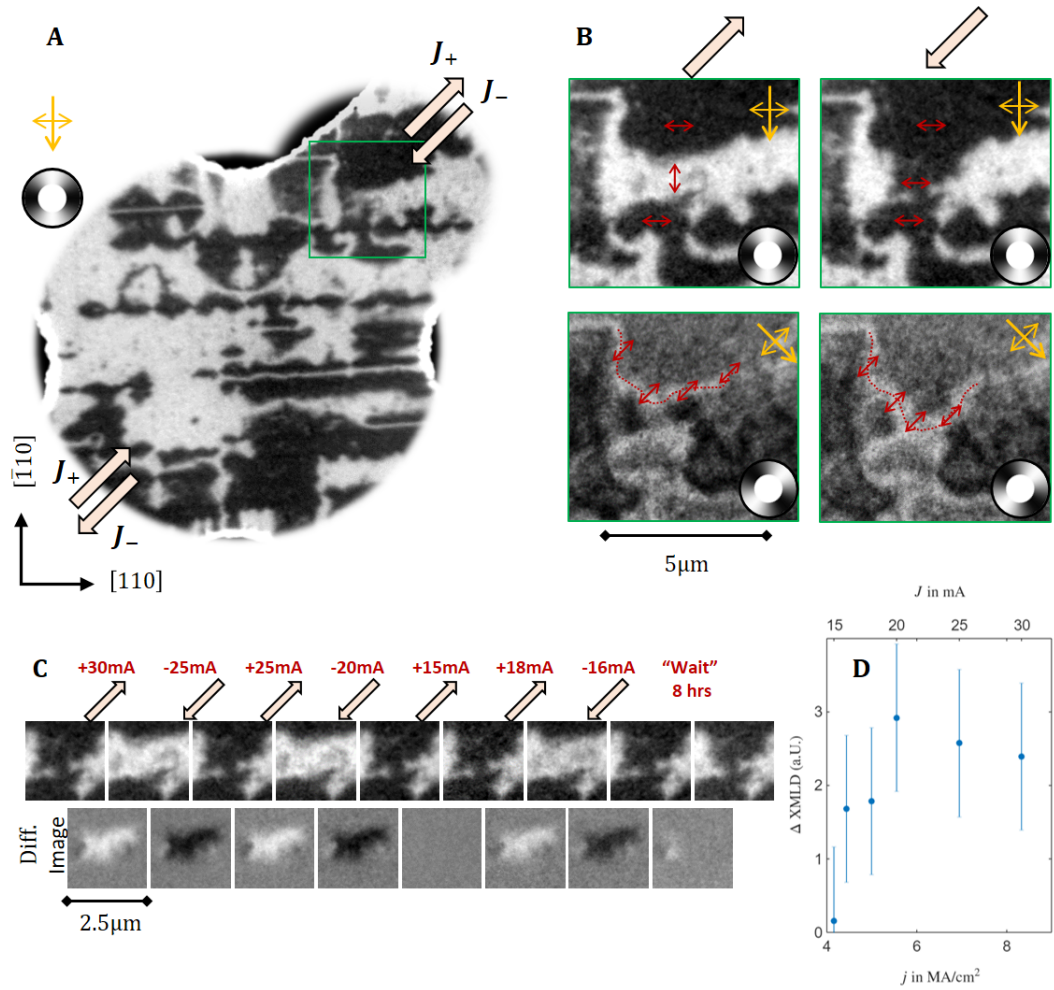


Figure 4.6: XMLD-PEEM Observation of polarity-dependent manipulation of AF domains. *A* Experiment geometry and overview of the AF domain structure in the centre of the device and the contact channel in which switching was observed. The bold light brown arrows show the direction of writing current pulses. *B* Close-Up of the switching area, marked with the green square in *A*, measured after current pulses with positive polarity (left) and negative polarity (right). Top and bottom correspond to XMLD-PEEM images with $\vec{E} \parallel [110]$ and $\vec{E} \parallel [010]$ as indicated by the yellow arrows, yielding sensitivity to the spin axis as shown in the colour wheels. The double-headed red arrows indicate the spin axis in the domains and in the moving domain wall respectively. The dotted red line serves as a guide to the eye and highlights the domain wall position in the two configurations. *C* XMLD-PEEM images (top) and difference images (bottom) during a pulsing sequence with 2.5ms long pulses. The amplitudes and directions of the pulses are indicated directly above. Between the last two images, the sample was left unperturbed for $\approx 8\text{hrs}$. *D* Dependence of the XMLD-signal on the current pulse amplitude. ΔXMLD is defined as the absolute value of the integrated intensity of the difference images in *C*. The error is estimated from the variation of the XMLD-PEEM image intensity in an area of similar size that did not switch.

The time sequence shows that the switching was not only highly stable, but also reversible, highly reproducible and largely independent of the current pulse amplitude: The difference images show contrast on (within the resolution) the

same region for all current pulses with $|J| \geq 16$ mA and inverted contrast for the opposite pulse polarities. The change-amplitude dependence is summarised in Fig. 4.6 **D**. The plot shows the dependence of the current-induced change (ordinate), quantified as the absolute value of the integrated intensity of the difference images in 4.6 **C**, on the current pulse amplitude (abscissa). The graph shows a sharp onset, but the variation with currents larger than the critical onset current is within the noise of the measurement technique. The onset current of 16 mA corresponds to a local current density of approximately 4.5 MA /cm^2 in the channel.

In this example, the switching area was located in one of the contact channels, so that it is not possible to correlate the antiferromagnetic changes with an electrical signal in the transverse resistance of the device.

Electrical measurements

In the following, it is shown in purely electrical measurements of devices fabricated from the same wafer that switching of the AF domain configuration based on changing the polarity of the writing current only, can indeed lead to a measurable electrical signal and confirm that the switching is present in more than one sample.

The measurements are performed on 8-contact devices so that both the longitudinal and transverse resistances can be measured. Figure 4.7 **A** shows a typical time-series of measurements with alternating writing current pulse polarity using the measurement geometry shown in panel **B**. The writing current sequence, consisting of 31 mA current pulses with alternating polarity, is shown in the top row of Fig. 4.7. The width of the bars does not represent the pulse length of 50 ms.

The changes of the transverse and longitudinal resistance measured during the sequence with a 0.5 mA probing current are shown directly underneath in the middle (ΔR_{xy}) and bottom (ΔR_{xx}) row. Here, each datapoint is the average of 6 consecutive measurements. The transverse resistance R_{xy} shows two current-

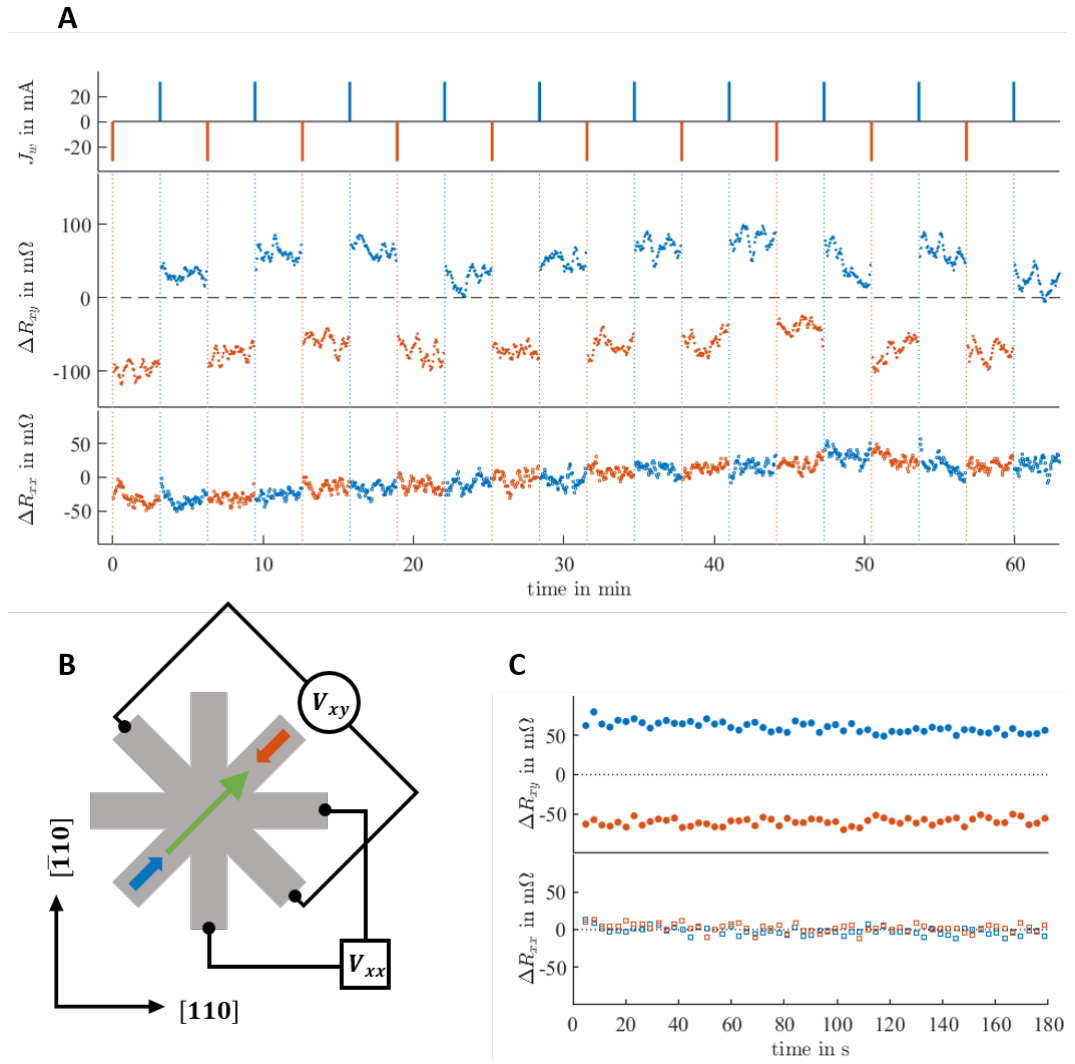


Figure 4.7: Purely electrical measurements of polarity-dependent switching. **A** Time-sequence of transverse and longitudinal resistance following 31.5 mA current pulses J_w along the CuMnAs $[100]$ with alternating polarity. Top: Writing pulse sequence. Middle: Transverse resistance (filled circle). Bottom: Longitudinal resistance (open squares). Each datapoint is the average of 6 consecutive measurements. A constant offset, the average value of the entire datasets, has been subtracted from the longitudinal and transverse resistance measurements. **B** Schematic of measurement geometry. Bold red and blue arrows show the direction of the writing current pulses, defining the colour code used in the figure. The green arrow is the reading current. **C** Average of all datasets for a given current pulse polarity, shifted in time relative to the writing current pulse.

polarity dependent states that, despite the considerable noise level, remain clearly separated throughout the entire measurement sequence and show no obvious decay. The longitudinal resistance shows a small, slow drift and higher frequency noise.

The time-shifted, averaged data, shown in Fig. 4.7 C, confirm that the current-

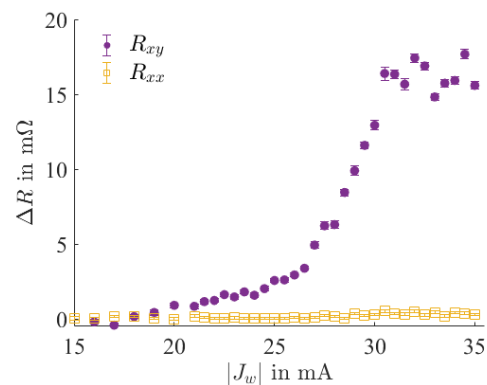
polarity dependent switching signal in the transverse resistance ΔR_{xy} is constant throughout the entire time measured after each pulse.

The time-averaged data of the longitudinal resistance (bottom of Fig. 4.7 C), show that current-induced heating and heat dissipation is negligible, in contrast to the orthogonal switching experiments. The difference can be attributed to the lower electrical current used.

The dataset shown is representative for all performed electrical measurement sequences of polarity-dependent switching above the onset current of the switching. The lack of decay of the transverse resistance signal has been found to be a main characteristic and is consistent with the stability of the switching observed in XMLD-PEEM. Furthermore, the stability of the signal allows to quantify the size of the switching signal simply as the difference of the writing current polarity-dependent averages of resistances.

The dependence of the size of the switching signal on the writing current amplitude for this sample is plotted in Fig. 4.8. Purple circles correspond to the transverse resistance changes and yellow squares show the same for the longitudinal resistance which gives an estimate the noise of the measurement. The transverse resistance shows a gradual increase up to between 20 mA and 27 mA, then a sharper increase and saturation around 30 mA.

Figure 4.8: *Current-amplitude dependence of the current-polarity dependent resistance changes measured in one CuMnAs device. Purple filled circles correspond to the transverse resistance, the electrical read-out signal, orange squares to the longitudinal resistance. The data are obtained on the same device as the data shown in Fig. 4.7.*



Similar behaviour, characterised by a lack of decay of the signal and the step-wise current-amplitude dependence of the switching signal, has been observed in the series of devices. However, the size of the signal as well as the critical onset current was found to be highly sample-dependent. The range of onset cur-

rents of polarity-dependent switching in the devices studied is listed in Tab.4.1. All critical onset currents are lower than typical current densities at which orthogonal switching occurs. The lowest value observed, 4 mA corresponding to a current density of $\approx 0.4 \text{ MA/cm}^2$, is one order of magnitude smaller than typical current densities used in orthogonal switching experiments.

Device #	J_{\min} in mA	j_{\min} in MA/cm ²
1	25(3)	2.5(3)
2	15(3)	1.5(3)
3	4(2)	0.4(2)
4	5(2)	0.5(2)
5	20(3)	2(3)
6	30(3)	3(3)
7	5(3)	0.5(3)

Table 4.1: Onset current pulse amplitudes J_{\min} and current densities in the centre of the device j_{\min} for current-polarity dependent in a series of CuMnAs devices patterned from the same wafer.

Comparison of orthogonal and polarity-dependent switching The observed current-polarity dependent domain manipulation differs not only in the experimental geometry from orthogonal switching, but also exhibits several other different characteristics. First, in orthogonal switching, the current pulse shifts the domain populations such that more domains are aligned perpendicular to the current, *i.e.* parallel to the current-induced effective fields. In polarity-dependent domain manipulation, the switching occurs between domains aligned at 45° to the current and the effective fields. Second, orthogonal switching in this material shows significant decay at room temperature (see the detailed study in [97]). In contrast, the observed polarity-dependent domain manipulation show no or only minute decay and the states are largely stable. Third, typical onset current densities of orthogonal switching are in the order of several MA/cm², and although the critical current densities have been found to vary between different layers, they are largely sample-independent, *i.e.* approximately the same for different samples fabricated from the same wafer. In contrast, the onset of polarity-dependent switching shows strong

sample-dependence and we observe a large range of critical current densities in devices fabricated from the same wafer. The onset current densities can be considerably lower than for orthogonal switching. Fourth, the orthogonal switching signal grows continuously as a function of pulse amplitude, length and number of consecutive pulses in the same direction, as discussed in detail in [85], whereas the switching signal in polarity-dependent domain manipulation shows a more step-wise dependence on the current pulse amplitude.

4.3.3 Switching mechanism: domain wall motion

The differences suggest that the switching occurs via a different mechanism.

Interpretation as domain wall motion In the following, it is shown that the switching can be explained as domain wall motion driven by Néel spin orbit torques. The experimental setting, switching between domains with mutually orthogonal spin axes, aligned at 45° to the writing current pulses, allows for two different scenarios: The rotation of the spin axis can be via a parallel (**A**) or perpendicular (**B**) alignment of the current and the spin axis in the centre of the domain wall. This is schematically depicted in Fig. 4.9, showing the spins in the two domains (yellow and blue arrows), the domain wall (green arrows), the electrical writing currents (light brown) and the current-induced fields H_{eff} (black). Solid and dashed arrows refer to the two magnetic sublattices respectively. The top part, considers the configuration with parallel alignment of the spin axes in the wall and the bottom the case of perpendicular alignment. All other geometries are related by symmetry.

In scenario **A**, parallel alignment of the spin axis in domain wall and the current, the angles between the current-induced fields and the spins (θ) on either side of the wall are 135° and 45° . Hence, one domain is energetically favoured due to Zeeman energy. The torque on the spins is largest in the domain wall. Here, it acts such that the spins are rotated in the spin axis direction in the energetically favoured domain. Hence, the domain wall moves

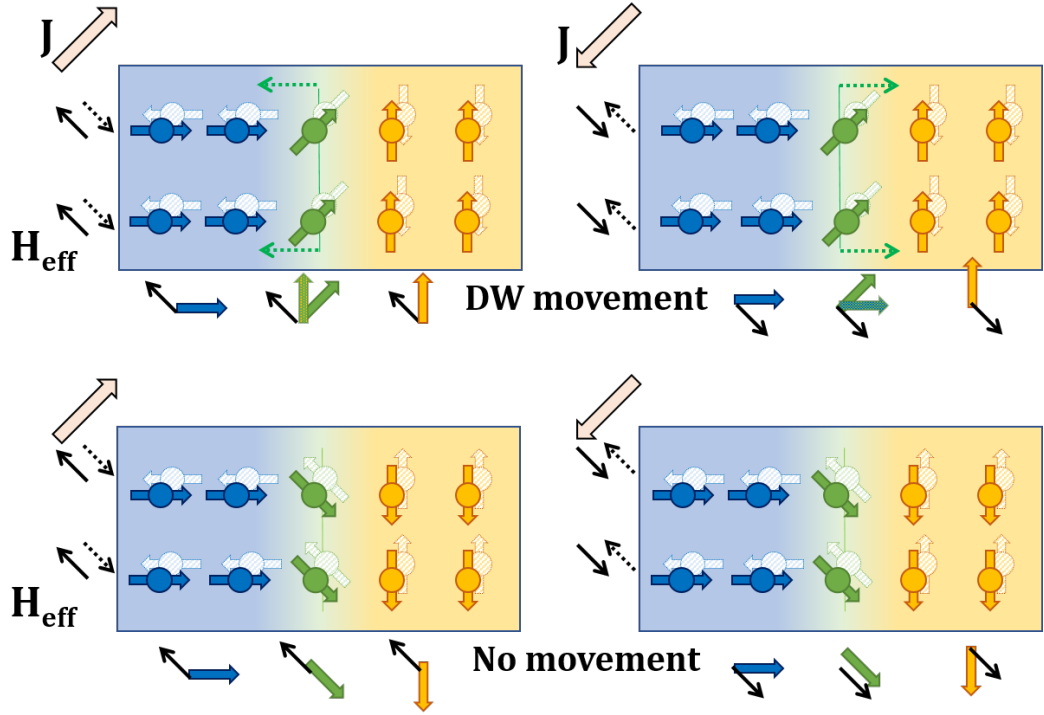


Figure 4.9: *Proposed mechanism of current-polarity dependent AF domain manipulation via domain wall motion.* Schematic representations of possible spin and current configurations. Blue, yellow and green arrow represent the spins in the domains (blue, and yellow) and in the domain wall (green). Solid and dashed lines correspond to the two magnetic sublattices. The thin black arrows are the directions of the effective fields on the two sublattices, induced by the current pulses (light brown arrows). For clarity, the effective field and the spins in the top sublattice are shown separately underneath each panel. In scenario **A** (top), the fields induce a rotation of the spins as shown, which leads to reversible, current-polarity dependent DW movement in the direction indicated by the thin, green dotted arrows. In scenario **B** (bottom), the torque on spins in the domain wall vanishes and no motion occurs.

such that the energetically favoured domain grows. Reverse of the current-polarity, reverses the current-induced fields and the direction of the domain wall motion.

If the spins in the centre of the domain wall are rotated perpendicular to the current (scenario **B**), then the Zeeman energy of the domains on either side has the same value and the torque on the domain wall vanishes. Hence, no domain wall motion occurs.

The XMLD-PEEM data had revealed parallel alignment of the electrical current pulses and spin axis in the centre of the domain wall, scenario **A**, which confirms that our observation is consistent with this interpretation.

Furthermore, the concept of switching via domain wall propagation from one pinning site to another also explains the characteristics of the switching measured in XMLD-PEEM, namely, **(a)** the observed range of onset current densities, **(b)** the current-amplitude dependence and **(c)** the lack of decay.

(a) The current only needs an energy large enough to overcome the pinning energy of the domain wall. This energy can be considerably lower than the energy required for coherent domain rotation. Thus, the threshold current of the switching is dictated by the pinning energy to move the domain wall which can vary strongly between different devices or between different areas on the same device.

(b) The size of the switching signal depends on the size of the switched area. This is dictated by the distance between the two pinning sites. As such, above a further increase of the current density above the onset current does not necessarily move the domain wall further and the switching signal remains constant. A larger switching signal is only achieved if current can depin more domain walls or overcome the pinning energy of both states.

c The stability of the signal can be attributed to the fact that the domain wall exhibits pinning at both positions so that both states are (meta-)stable.

4.4 Additional observations

The data considered so far are limited to a subset of observations during the X-PEEM experiment, both of the electrical pulsing sequence and of the area of the device. The last part of this chapter will show the previous findings in the context of the observations on the entire device and the rest of the pulsing sequence, including more striking observations, which will lead on to the next chapters.

Figure 4.10 shows the XMLD-PEEM images and difference images between consecutive images of the entire centre of the device during the sequence of orthogonal pulses along the CuMnAs [100] and [010], discussed in section 4.3.1.

The images in Fig. 4.3 **B** are subsets of the images shown in Fig. 4.10 **A**. The images show the size of the switching area in relation to the area of the device, highlighting the minuteness of the change. Due to the position of the region on the device, the local current direction will deviate from the CuMnAs [100] and [010] axes. The image sequence also demonstrates that remnant AF domain manipulation with orthogonal current pulses up to this amplitude are limited to the switching of this one small region, in particular when considering that current pulsing using all 4 contacts has led to no measurable changes for currents of up to 48 mA.

Higher current pulses along the [100] and [010] have triggered additional small changes, highlighted in the coloured boxes, but the changes remain minute and can only be seen in the difference image and in the close-ups shown in Fig. 4.10 **B**. Most of them are small expansions of areas where the spin axis is not exactly aligned with the [110] and $[\bar{1}10]$, *i.e.* where it deviates from the spin axis in the main domains. As such, the changes are difficult to interpret and, additionally, they did not necessarily occur reversibly. On the whole, the initial pulsing sequence mainly demonstrates that a large part of the AF domain structure of this layer is strongly pinned. The contact-channel in which current-polarity dependent switching via domain wall motion occurred, was not in the field-of view during the image sequence.

Up to this point, the pulse length of the current pulses was kept at 2.5 ms. A 100 ms long current pulse of 50 mA sent along the NW direction - led to a considerably more dramatic remnant change of the AF domain structure, shown in Fig. 4.11. The direction of the current can be clearly seen from the changes in the structure. In the centre of the device and in the contact channels used for the pulse, the AF domain structure has changed completely. The large domains with spin axes along the CuMnAs [110] and $[\bar{1}10]$ have been erased and replaced by a more granular texture with more gradual spin variation. Areas with (approximately) uniform spin axis in the affected part of the device are located only in the vicinity of the rounded corners, where

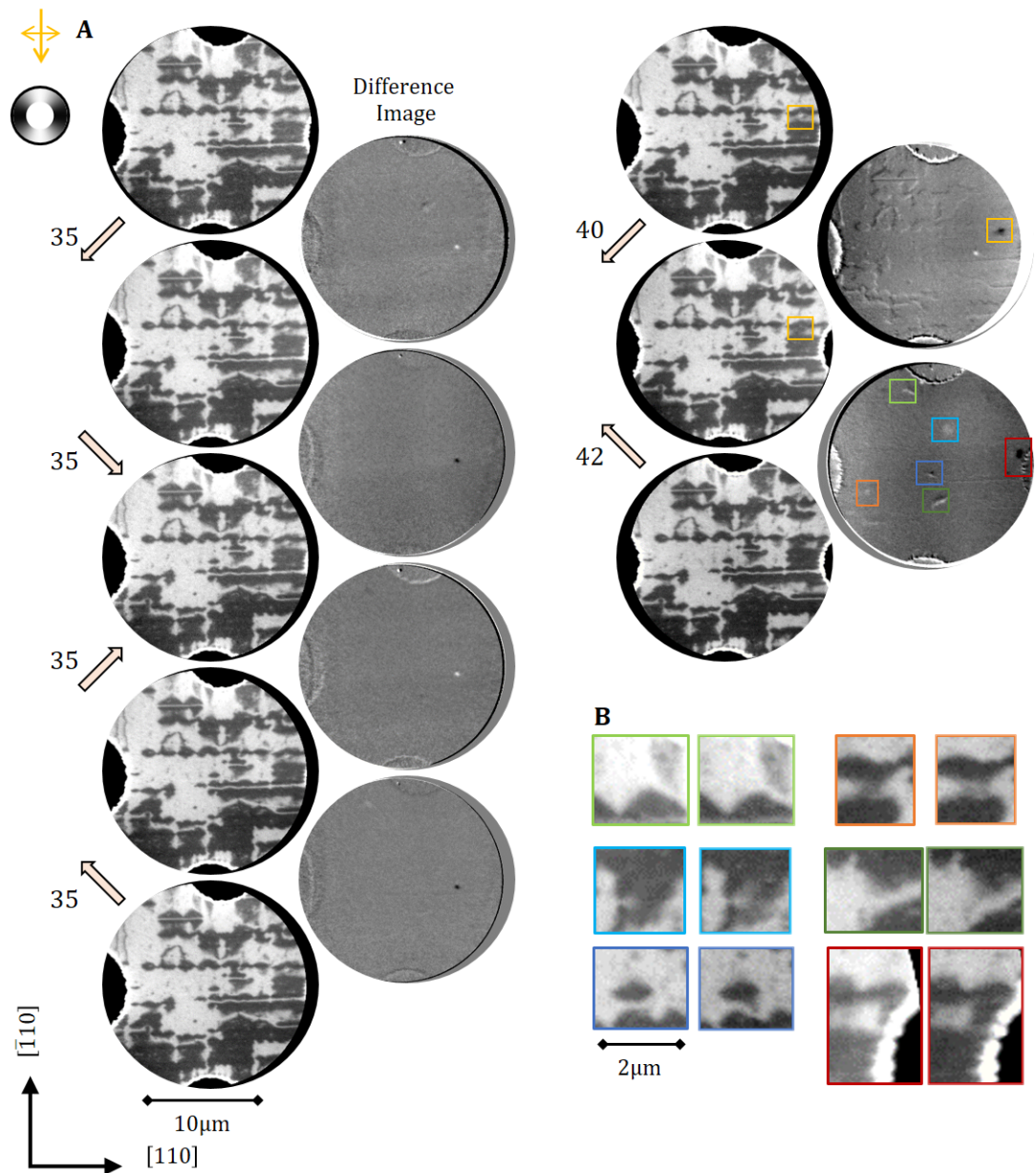


Figure 4.10: Effect of orthogonal switching (Overview). *A.* Time series of XMLD-PEEM images and difference images during a pulsing sequence with 2.5 ms long pulses along the CuMnAs [100] and [010] crystalline directions. The amplitude (in mA) and directions of the current pulses between consecutive X-PEEM measurements is indicated by the light brown arrows at the left. *B* Close-up of the last two X-PEEM images of the areas marked in the last difference image to highlight the changes.

the device edge is approximately aligned with the CuMnAs [110] and $[\bar{1}10]$ directions, with “light” domains at the left and right and “dark” domains at the top and bottom, *i.e.* the spin axis is locally aligned parallel to the edge. The relevant areas are marked with coloured boxes.

This state was largely stable over the timescale of minutes. Although the

lengthscale of this domain pattern is considerably smaller than prior to the current pulse, “granular” domains of a similar length-scale are commonly observed in other CuMnAs layers, *e.g.* the ones grown on GaAs. Changes to this structure, observed approximately 2 hours later (Fig. 4.11), occurred primarily in the vicinity of the rounded corner edges marked by the coloured boxes, where lens-shaped domains aligned perpendicular to the edge have appeared. Domain coarsening seems to be stronger in areas with larger domain sizes. The area with the smallest domains and highest granularity (“south-east”) on the contrary, is largely unchanged.

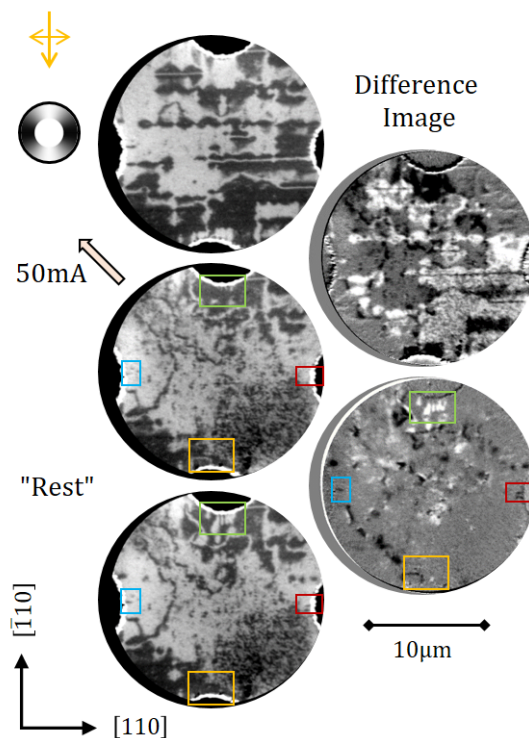


Figure 4.11: *Effect of a, potentially longer, 50 mA current on the AF domain structure. Left: XMLD-PEEM images of the domain structure. Right: Difference image of consecutive XMLD-PEEM images. The coloured boxes mark areas with characteristic changes explained in the main text.*

Figure 4.12 shows that the new AF domain state is susceptible to current-pulses, even in the geometry of “orthogonal” switching. The figure shows XMLD PEEM measurements during a pulsing sequence with electrical current pulses with current directions along the CuMnAs $[110]$ and $[\bar{1}10]$. In the “virgin” state, prior to the 50 mA current, the same electrical pulsing sequence had not induced measurable changes in the centre of the device. The difference images reveal changes which occur reversibly, current-direction dependent and current-polarity independent, as well as irreversible current-induced changes

and spontaneous reconfigurations happening between two consecutive pulses. The circle (“north-east”) is the feature in the contact channel that changes with the polarity of the current. This area, in which polarity-dependent switching was studied (section 4.3.2), was not affected by the current pulse and the data shown in section 4.3.2 and Fig. 4.6 were measured, prior to the 50 mA current. The reversible changes, marked by the orange, yellow and purple boxes, can be interpreted as “standard” orthogonal switching, thus AF domain manipulation via Néel spin-orbit torques.

This is not the case for the irreversible changes, but most likely part of the coarsening dynamics occurring current-assisted or thermally assisted, for the spontaneous change.

The dramatic effect of the long 50 mA current pulse on the AF domains resulting in a qualitatively different domain morphology with seemingly different (lower) anisotropy, raises the question, if the induced change was purely magnetic. If so, then the coarsening dynamics may be expected to occur on much faster timescales than observed. Dynamics on the time-scales of hours are more commonly seen for structural dynamics. However, XMLD-PEEM images with out-of plane X-ray polarisation, XAS measurements and XMCD images (see Fig. 4.13) confirm the integrity of the sample surface, its magnetic ordering and the crystal structure. As the measurements in chapter 7 show, the timescale of the observed domain dynamics is dictated by structural changes (defect growth) in the sample.

4.5 Summary and conclusion

The results shown in this chapter reveal a novel means of electrical manipulation of AF domains in CuMnAs samples with large domains which depends on the polarity of the current only. The current-polarity dependent AF domain manipulation shows several characteristics which render it particularly favourable for applications. Firstly the simpler writing geometry allows to re-

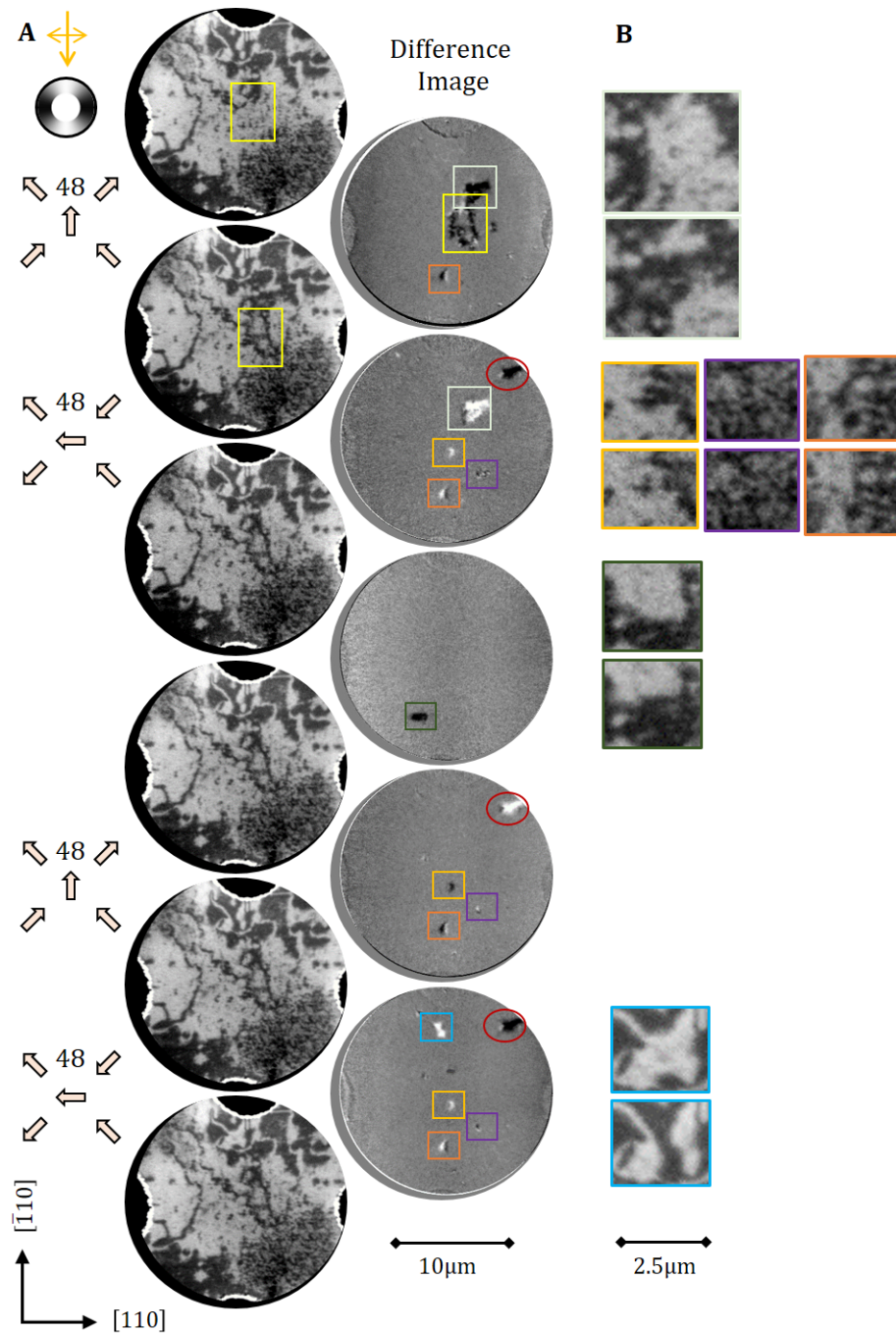
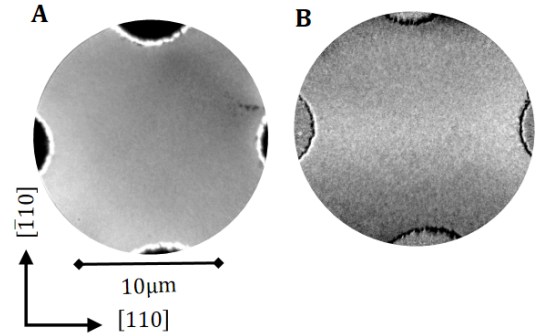


Figure 4.12: *Effect of orthogonal switching after the 50 mA current.* **A** XMLD-PEEM images (left) and difference images (right) during a pulsing sequence with 2.5 ms long current pulses along the CuMnAs [100] and [010] crystalline directions. The geometries and amplitude (in mA) of the current pulses is shown by the light brown arrows. Relevant changes are highlighted by the coloured rectangles. The red oval shows the area with current-polarity dependent switching. **B** Close-ups of the areas marked by the coloured rectangles from the corresponding X-PEEM images.

duce device complexity and size. Second, the stability of the signal is a prerequisite to long-term memory. Third, orthogonal switching has been interpreted as a thermally activated process (see [98]) relying on significant heat generation

Figure 4.13: *Measurements to confirm sample integrity. A* XMLD-PEEM image of the centre of the device, taken with out-of plane x-ray polarisation. *B* XMCD-PEEM image of the centre of the device. The contrast variation is more than an order of magnitude smaller than for the XMLD-PEEM images and presumably due to local work function differences or topographic effects. This confirms **A** that the AF spin axis varies purely in-plane and **B** that there is no measurable ferromagnetic signal.



during the pulse. In contrast, polarity-dependent switching shows negligible heat generation during the pulsing. Heat generation leads to device degradation and is a major source of energy dissipation, thus polarity-dependent switching offers both longer device lifetime and reduced energy consumption. The switching is likely to occur via domain wall propagation from one pinning point to another. As such, these findings also give a tool to study domain wall pinning effects and domain wall propagation in this material. A detailed understanding of these effects will become crucial for the realisation of efficient devices for application.

The dramatic current-induced change showing “domain fragmentation” cannot be explained without a better understanding of the parameters that govern the anisotropy and the AF domain pattern in CuMnAs.

A large part of this thesis is devoted to revealing those factors. The following chapters will show that the observations are a consequence of the strong sensitivity of the antiferromagnetism to the (local) crystallographic micro- and nanostructure. In particular, measurements of the nanoscale defect structure will reveal that the AF domain structure in this sample is directly coupled to characteristic elongated defects, “microtwins”, which locally pin the AF spin axis and stabilise the domain pattern. The findings will allow to correlate the observed current-induced dramatic change of the domain pattern and the following coarsening dynamics to thermal annealing and subsequent reformation

of the microtwin pattern.

Chapter 5

Defect-driven antiferromagnetic domains in CuMnAs

5.1 Introduction

The previous chapter described electrical manipulation of antiferromagnetic domains in CuMnAs films. The system studied is one example among several AF systems in which electrical switching has been realised. The resulting current-induced domain modifications have been attributed to spin-orbit torques or thermo-magnetoelastic effects [11, 99–101]. The aggregate of the experimental achievements of electrical manipulation of AF order has triggered a surge of interest in AF materials for spintronic applications, as the intrinsic properties of AF materials would - in principle - allow to exceed current FM technology both in device efficiency and speed.

Yet device efficiency and specific functionality often rely sensitively on the domain structure. For example, domain pinning can limit device performance whilst creep affects long-term memory stability. Direct imaging of electrical switching has revealed pronounced non-uniformities and pinning effects during domain switching, see for example [94, 99, 102–104] and Chapter 4. The findings highlight the need for a detailed understanding of the factors that govern the AF domain structure and AF domain formation.

In ferro- and ferrimagnets, domain formation has been extensively studied for decades and is well-known to be largely governed by the minimisation of the demagnetising field energy [25, 105]. On the other hand, domain formation in fully compensated antiferromagnets remains largely unexplored. With magnetic stray fields being negligibly small, here other effects will become important. Domain morphologies in AF thin films vary considerably with thickness and nanostructure shape which has been ascribed to strain effects, but the studies neither show experimental evidence for a direct relationship nor a precise theoretical model reproducing the observed effects in numerical simulations [106–110].

This chapter reports on the investigation of the antiferromagnetic domain structure in unpatterned 45 nm to 50 nm CuMnAs films epitaxially grown fully strained on GaP substrates, similar to the one used in chapter 4. Films of this thickness and growth conditions are amongst the CuMnAs films with the highest crystalline quality and are fairly frequently used for high-resistive electrical switching experiments [111]. The data presented in this chapter reveal that the AF domain structure in this material is highly sensitive to the crystallographic microstructure, including nanoscale defects.

Previous high-angle annular dark field scanning transmission electron microscopy (HAADF-STEM) measurements have identified elongated microtwins and atomically sharp anti-phase boundaries [46] as the most prominent defects in this type of epitaxially grown CuMnAs/GaP(001) layer, see section 2.1. The microtwins, which are at the focus of this chapter, are shown to have a dramatic influence on the AF domain structure in the CuMnAs films.

Microtwinning in metals is known to strongly affect the mechanical properties of a material and the plastic deformations of a solid under stress. Although known since almost a century, microtwinning in solids continues to be a subject of ongoing research due to its relevance for developing and improving novel materials like twinning-induced plasticity (TWIP) steels for light-weight applications primarily for the automotive, shipbuilding, and oil and gas industries

[112].

HAADF-STEM images of a microtwin are shown in Fig. 5.1. The microtwins are crystalline slabs of a microtwinned phase in which the unit cell is rotated by $\approx 82^\circ$ in the vertical direction. The slab extends nearly over the whole thickness of the CuMnAs film, and gradually grows thicker towards the sample surface on which they produce a characteristic rectangular pattern along the $[110]$ and $[\bar{1}\bar{1}0]$ axes.

Figure 5.1 **B** shows a close-up on the microtwin defect where the atomic columns are marked. The twin and surrounding lattice form a coherent boundary, with the slabs aligned along one of the $\langle 111 \rangle$ planes. Consequently, for each defect line direction on the surface there are two possible defect orientations with opposite tilts (see Ref. [46]).

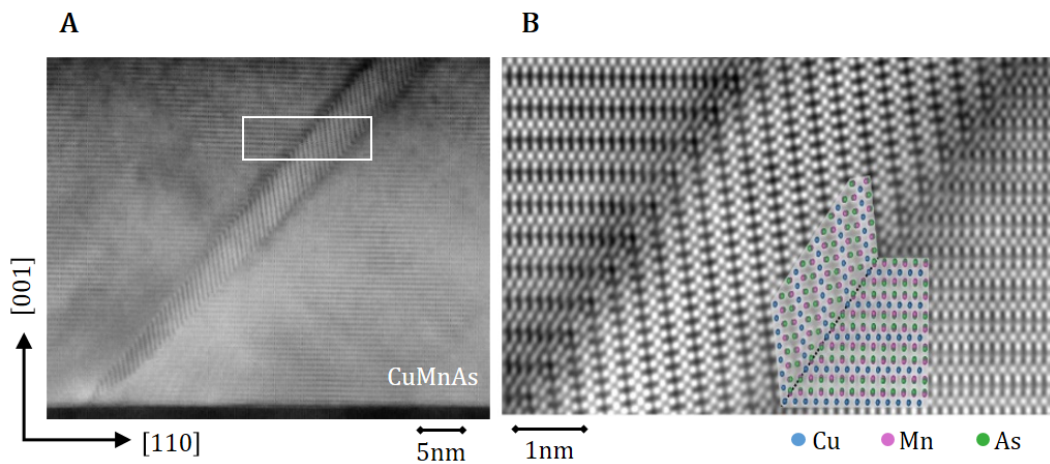


Figure 5.1: HAADF-STEM images of a microtwin **A**, Overview image, **B**, Close-Up of the region in the white square and atomic overlay. Image Courtesy of F. Krizek.

In this chapter, it will be shown by combining AF domain imaging with structural imaging that the microtwins largely control the domain structure, leading to confined 180° domain walls and pinning points for 90° domain walls.

5.2 Methods

Material This chapter is based on observations on different 50 nm CuMnAs/GaP(001) films with varying crystalline quality. Four of the films are capped with 2.5 nm Al, the remaining three were capped with 30 nm As, which was removed thermally before the measurements.

The measurements presented in detail in section 5.3.1 and section 5.3.2 are performed on two different 50 nm CuMnAs/GaP(001) films capped with 2.5 nm Al. The sample studied in section 5.3.1 has the highest crystalline quality of the 7 CuMnAs films. The sample studied in section 5.3.2 shows several other defects, including MnAs inclusions, not observed in the previous sample.

Scanning X-ray diffraction (SXRD) measurements The scanning x-ray diffraction measurements utilise a 10 keV x-ray beam focused to a lateral diameter of 100 nm. In a scan, the sample is scanned laterally in a 2d-mesh (xy -mesh) through the x-ray beam with fixed sample orientation. An image of the diffracted intensity is recorded at each position, with an area detector placed at a distance of 0.650 m from the sample. For a detailed description see section 2.11.

Reciprocal space maps Reciprocal space maps of the CuMnAs 003 reflection are obtained from xy -mesh scans with a stepsize of 200 nm in real space at different angles Θ around the Bragg reflection, with an incremental variation of the sample rotation of $\Delta\Theta = 0.02^\circ$. During these measurements the x-ray beam was impinging along the CuMnAs [110] direction. For details see section 2.11.1.

SXDM mapping of microtwins SXDM imaging of the microtwin configuration utilised the CuMnAs 003 peak with the x-ray beam impinging along the CuMnAs [100] direction at $\Theta = 0$. The microtwin configuration is mapped with the sample at an angle $\Delta\Theta = \pm 0.4^\circ$ tilted away from the Bragg angle, *i.e.*

$\Theta = \Theta_{\text{Bragg}} \pm \Delta\Theta$. For each one of these selected angles, the detector plane slices through two of the microtwin-related wings in reciprocal space. Consequently, if a microtwin is in the illuminated area, significantly higher intensity is recorded on one or the other side of the detector is recorded, depending on the microtwin orientation. Mapping the intensity of one side of the detector against sample position thus reveals the spatial pattern formed of microtwins with a fixed orientation, for details see section 2.11.2.

5.2.1 XMLD-PEEM imaging

AF domain imaging was performed using XMLD-PEEM, as described in section 2.7, with sensitivity to the magnetic axis due to the x-ray magnetic linear dichroism (XMLD) effect, see section 2.5.2. Large area maps of the sample were obtained by rastering a 10 μm wide x-ray beam across the 32.2 μm field-of-view. The beam rastering can lead to stripe-like artefacts in the XMLD-PEEM images. High-resolution images of the AF domains are measured without beam rastering.

5.2.2 Structural imaging using XLD-PEEM

X-ray linear dichroism PEEM images of the microtwin configuration were obtained from the asymmetry between images recorded using photon energies corresponding to the peak and the minimum of the Mn $L_{2,3}$ non-magnetic x-ray linear dichroism (XLD) spectrum, with \vec{E} almost out-of-plane.

However, contrast can arise from any local changes in the charge anisotropy along the beam polarisation. The identification of the observed features in the XLD-PEEM images with the microtwin defects is primarily based on the similarity of the pattern with the one measured in SXDM.

5.2.3 Micromagnetic simulations

The simulations were done by Helen Gomonay. The distribution of the Néel vector $\vec{l}(x; y)$ in the presence of different microtwin configurations is simulated using the Matlab PDE Toolbox to solve the micromagnetic equation

$$\mathbf{n} \times [A\nabla^2\mathbf{n} + \mathbf{H}_\mathbf{n}] = 0 \quad (5.1)$$

with von Neumann boundary conditions. Here A is the magnetic stiffness, ∇^2 is the Laplace operator, and

$$\mathbf{H}_\mathbf{n} = -\frac{\partial}{\partial \mathbf{n}} (w_{\text{matr}} + w_{\text{twin}} + w_{\text{m-e}}), \quad (5.2)$$

where w_{matr} , w_{twin} and $w_{\text{m-e}}$ are the magnetic anisotropy energy density of the matrix, the magnetic anisotropy energy density of the microtwin, and the magnetoelastic energy density, respectively. For details see section 2.12.

5.3 Results and interpretation

5.3.1 Imaging of defect patterns

Figure 5.2 shows scanning x-ray diffraction measurements using the CuMnAs 003 Bragg peak. Panels **A** and **B** are reciprocal space maps (RSM) of the CuMnAs 003 reflection obtained from a microtwin-free area (**A**) and from an area with microtwins (**B**). The full angular dependence of the three-dimensional RSMs can be found in the video in the appended information. Both RSMs present a structured, modulated intensity along $Q_{[001]}$, recognisable as film thickness fringes [113] as well as strong diffuse scattering along the $Q_{\langle 101 \rangle}$ -type directions. The diffuse scattering has been attributed to $c/2$ -slip dislocations resulting in anti-phase boundaries along the $\{011\}$ planes [46]. Additionally, sharper intensity streaks (hereafter referred to as “wings”) along the $Q_{\langle 110 \rangle}$ -type directions are present in the RSM averaged over the entire

region, Fig. 5.2 **B**, only.

Real-space maps of the sample can be produced from separated elements of the RSMs, to isolate specific structural features of the sample. Examples of these maps are shown in Fig. 5.2 **D-I**. The regions of reciprocal space used to produce the maps are marked in Fig. 5.2 **B** and **C**. Maps produced using the intensity of only one of the wings, as the ones in Fig. 5.2 **D**, show a set of defect lines, all perpendicular to the direction of the selected wing. Real space maps produced from the intensity of all wings, Fig. 5.2 **H** reveal a rectangular defect pattern along the CuMnAs $[110]$ and $[\bar{1}\bar{1}0]$ as bright lines with high contrast. Thus, the SXRD measurements confirm the identification of the wings with the microtwin defects discovered and characterised previously in HAADF-STEM measurements [46] (cf. Fig. 5.1).

For a single defect, x-ray diffracted intensity is measured in only one wing of the diffraction peak, which suggests that there is a one-to-one correspondence between the direction of the wing in reciprocal space and the orientation of the microtwin slab.

Maps from the diffuse scattering along the $Q_{\langle 101 \rangle}$ directions, Fig. 5.2 **I**, show uniform sample structure, proving that the slip dislocations they originate from are present everywhere in the sample.

5.3.2 Correlation between defect and AF domain structure

Figure 5.3 compares the microtwin density to the average AF domain size of four 50 nm CuMnAs/GaP films with similar growth conditions. The average AF domain size is measured as the average distance between AF domain walls from XMLD-PEEM images, and the microtwin density is characterised by the average distance between neighbouring defects, in both cases measured parallel to the CuMnAs $[110]$ and $[\bar{1}\bar{1}0]$ directions, away from patterned edges. The microtwin densities have been measured using LEEM or SXDM, *i.e.* tech-

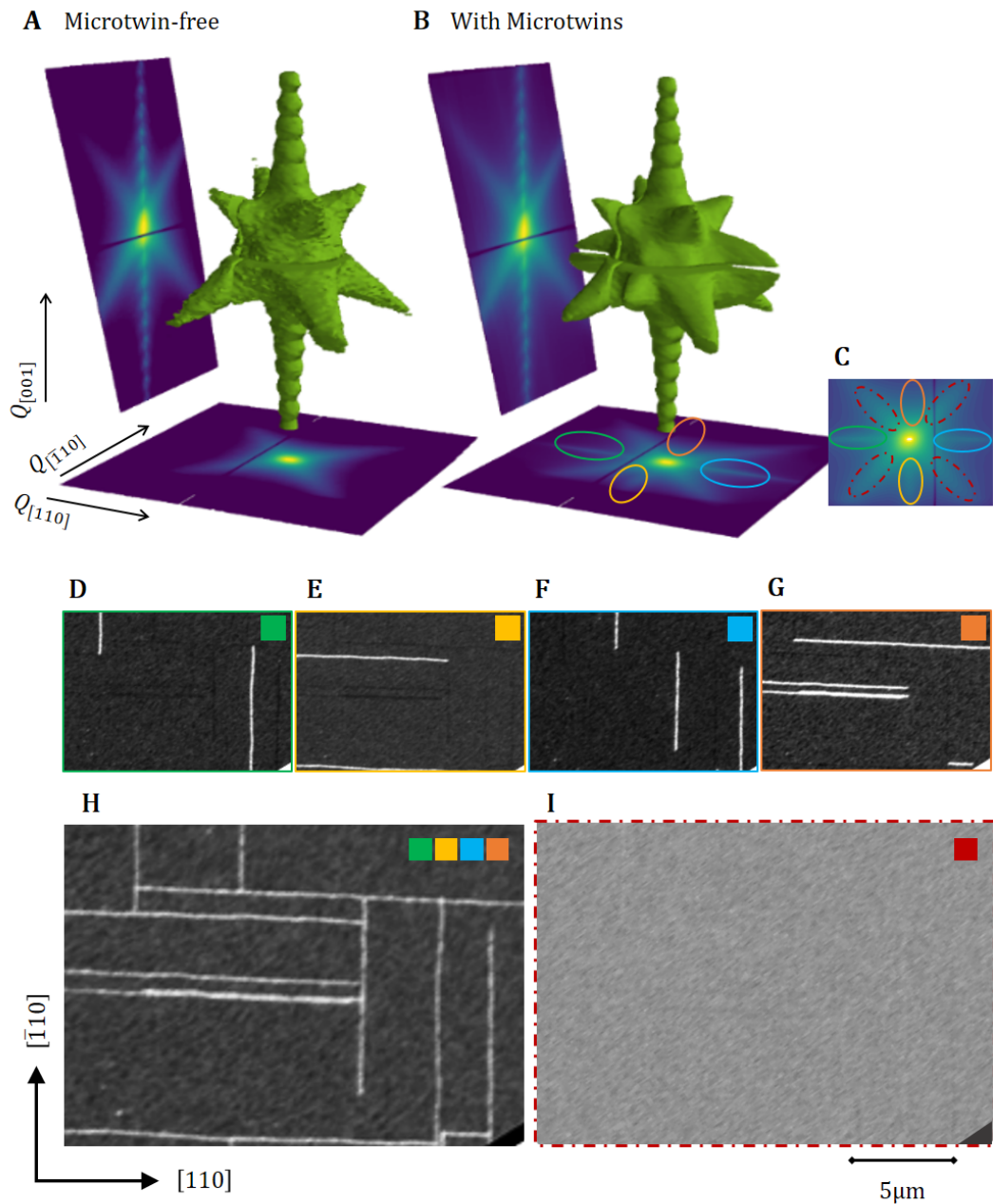


Figure 5.2: **A**, *CuMnAs* 003 RSM isosurface (green solid) along with projections onto the $Q_{[110]}$ (left panel) and the $Q_{[001]}$ (bottom panel) planes from a microtwin-free area. **b**, Same as **A**, but from an area with microtwins. **C**, Projection of the RSM in **B** onto the $Q_{[110]}/Q_{[110]}$ plane. The solid ovals mark the “wings”, which are not present in the RSM from a microtwin-free area. The dashed ovals mark “streaks” which are present in **A** and **B**. **D-G**, Real space SXDM intensity maps from the wings, the colour code indicates the area of reciprocal space used in panel (**B**) which is marked with the corresponding coloured ovals (solid). **H**, Composite image of all the line defects shown in panel **D-G**. **I**, Real space SXDM intensity map of the same area produced from the streaks. The scale bar refers to panels **H**, **I**, Panels **D-G** show the same area.

niques which are unambiguously sensitive to structural features only. The areas investigated all cover at least 3 distinct areas with a minimum of 10

microtwins in each. The errorbars are calculated from the variation of the average distances obtained for the individual areas and the two directions and give an upper limit. The areas used for the measurements of the microtwin density and the average domain size do not necessarily overlap. Despite the considerable errorbars, the graph shows an approximately linear dependence, indicating a strong correlation between AF domains and microtwin defects in CuMnAs films, which we will investigate in the following.

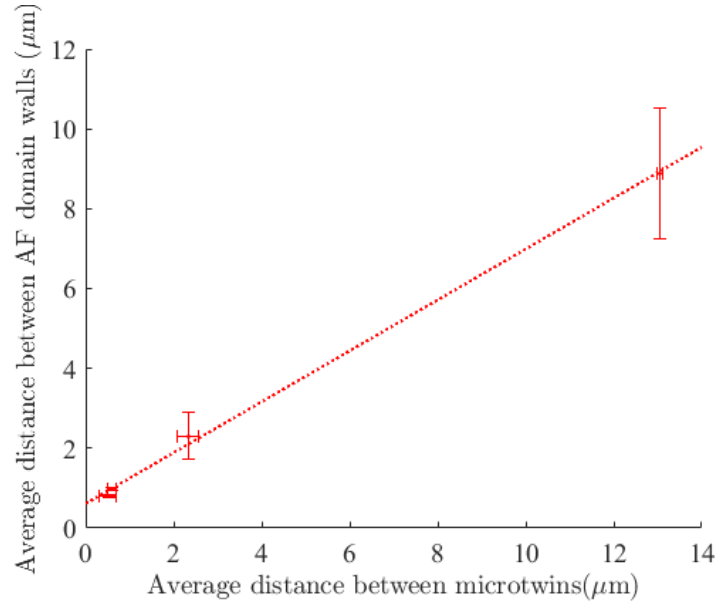


Figure 5.3: Comparison of microtwin density and AF domain sizes Plot of the average distance between AF domain walls, versus the average distance between microtwin defects for four different 50 nm thick CuMnAs/GaP(001) samples. The distance between AF domain walls is measured along the CuMnAs {110} from XMLD-PEEM images. The distance between microtwins is measured in the same directions from SXDM maps or bright-field LEEM images. Structural and magnetic data are not obtained from the same area of the layer. The errorbars correspond to the statistical error. The dotted line is a fit to the data.

Direct comparison of defect and AF domain pattern

Structural defects locally change the electronic charge anisotropy and can thus yield contrast in x-ray linear dichroism PEEM measurements. This allows to image the AF domain structure and the microtwin pattern of an area with the same microscope and the same microscope settings, *i.e.* the same optical distortions and aberrations. As such combined XLD/XMLD-PEEM imaging provides a unique tool to directly investigate the correlation between microtwins

and AF domains.

Figure 5.4 **A** and **B** show large area maps of the AF domain structure imaged with the x-ray polarisation vector (\vec{E}) along the CuMnAs [110] and [010], respectively. The maps are composite images of 30 μm field-of view images obtained with beam rastering (see section 2.7.2). As introduced in chapter 3, films of this thickness typically form AF domains with spin axes along the [110] and $[\bar{1}10]$ crystalline axes. Figure 5.4 **A** is obtained with $\vec{E}||[110]$ which yields maximum XMLD-contrast between those two domain types.

The large area map in figure 5.4 **A** shows an approximately even population of light and dark areas corresponding to the domains with local spin axis parallel to [110] or $[\bar{1}10]$. The typical domain size exceeds several μm^2 and the AF domains generally have serrated edges.

In Fig. 5.4 **B** with $\vec{E}||[010]$ the two domains give the same XMLD-contrast and maximum contrast is obtained on the domain boundaries. 90° domain walls appear as well separated black or white lines, depending on the average direction of the spin across the domain wall. Adjacent black and white lines in 5.4 **B** correspond to 180° domain walls (see section 3.2.2). The map shows a continuous distribution of 180° domain wall widths, ranging from over 750 nm to the resolution limit of ≤ 100 nm of the large area maps. The narrow 180° domain walls are found to run along straight lines, closely aligned with the crystallographic axes and perpendicular to the spin axis in the centre of the wall, appearing as light lines in the horizontal direction and dark lines in the vertical direction in Fig. 5.4 **A**.

Figures 5.4 **C** and **D** show high-resolution XMLD-PEEM images of the area marked with the red square in Fig. 5.4 **A** and **B** with contrast on the domains (**A**) and on the domain walls (**B**) respectively. Figure 5.4 **E** shows the microtwin configuration in that area measured with XLD-PEEM (see section 5.2.2). For direct comparison, Fig. 5.4 **F** shows the AF domain structure superimposed with the domain wall contrast (blue and red lines) along with the structural microtwin pattern (broken yellow lines). Similar overlay images of

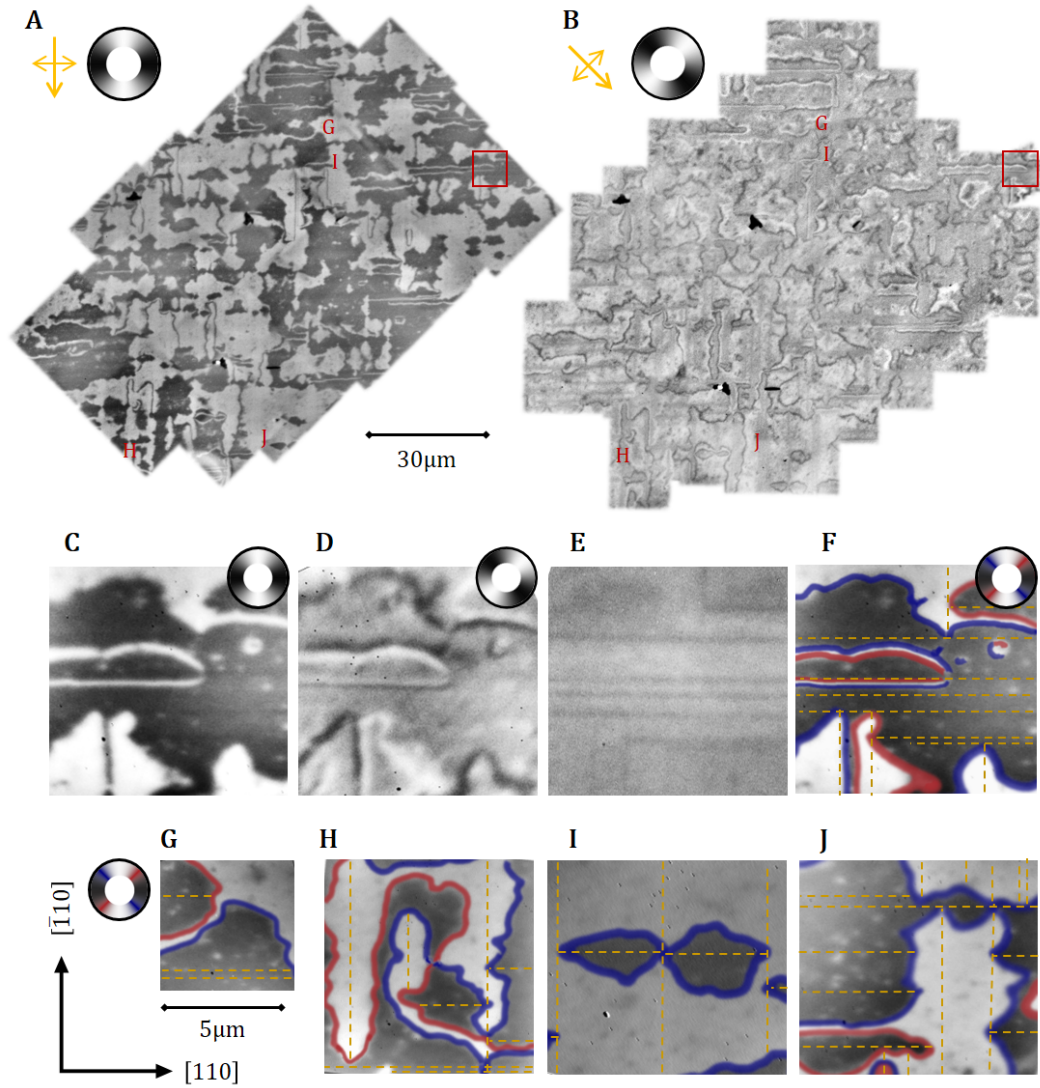


Figure 5.4: Direct Comparison of the AF domain structure and the microtwin pattern in a blanket film. **A** Large area map of the AF domain structure composed of XMLD-PEEM images with $\vec{E} \parallel [110]$ yielding sensitivity to AF domains with spin axes parallel to $[110]$ (dark areas) or $[\bar{1}10]$ (light areas). **B** Similar composite XMLD-PEEM image recorded over the same area as (A), but with $\vec{E} \parallel [010]$ showing AF domain walls with spin axes parallel to $[100]$ (dark) or $[010]$ (light). The colour wheels indicate the local spin axis in each image. **C** High-resolution XMLD-PEEM image of the domains from the area in marked with the red rectangle (A). **D** High-resolution XMLD-PEEM image of the domain walls from the circled area in (B). **E** High-resolution XLD-PEEM image of the same area as in (C) and (D) revealing the microtwin pattern. **F** Composite image showing the relationship between the XMLD-PEEM and XLD-PEEM images, based on the contrast of XMLD-PEEM images with $\vec{E} \parallel [110]$ giving contrast on the AF domains overlaid with solid red and blue lines indicating the domain wall orientation (red for spin axis parallel to $[010]$ and blue for spin axis parallel to $[100]$), the local spin axis for the colour code is depicted by the green arrow in the coloured squares next to (G). The red broken lines indicate the microtwin pattern observed in XLD-PEEM. **G-J** Similar overlay images as (F) of different areas. The red letters in (A) and (B) serve to locate the corresponding area in the large area maps.

other areas are shown in Fig. 5.4 **E-H**. The corresponding positions in the large area maps are indicated by the red letters in Fig. 5.4 **A** and **B**. The positions are chosen to contain examples of all characteristic features of the AF domain pattern.

All overlay images show strong, direct correlation of AF domains, domain walls and microtwins. In particular, the AF spin axis locally always aligns parallel to the microtwin-line on the surface. Areas with two orthogonal microtwins show 90° domain walls which align at roughly 45° with the microtwins and which form the serrated edges in Fig. 5.4 **A**. This can best be seen in Fig. 5.4 **H** and in the bottom half of Fig. 5.4 **F**. The 90° domain wall is pinned at the crossing (“T-junction”) of the microtwins.

The area between two parallel microtwins either shows homogeneous spin orientation or feature a 180° domain wall, confined between the two neighbouring microtwins. In some cases these domain walls become highly constricted between two neighbouring microtwins as seen in the middle of Fig. 5.4 **F**. In this case, the spin rotation occurs over a very narrow region and the domain wall is closely aligned with the crystalline directions. These form the characteristic, straight and narrow 180° domain walls observed in the large area maps.

When the microtwins are further apart from each other, the domain walls are wider, the alignment with the crystalline directions is lost and the domain wall path becomes more undulating. One example of such a wide, undulating domain wall can be seen in Fig. 5.4 **G**.

In short, the data show a strong, direct correlation between microtwins and AF domains, such that the AF order parameter always aligns parallel to the microtwin-line on the surface which explains the correlation between the AF domain size and the microtwin density and leads to pinning of 90° domain walls and confined 180° domain walls.

5.3.3 Coupling mechanism

The atomic structure of the microtwins yields an intuitive explanation of the observed coupling between microtwin defects and domains. Twin and the surrounding lattice form a coherent boundary (see also Fig. 5.1 B) with shared Mn-atoms. This suggests that AF exchange is neither reversed nor broken, though potentially reduced across the boundary. As such, magnetocrystalline anisotropy energy and exchange energy can only be simultaneously minimised, if the Néel vector is aligned with an easy axis of both the microtwin and the surrounding lattice.

Tetragonal CuMnAs has a large out-of plane anisotropy where the magnetic easy plane is perpendicular to the c axis [53]. In a microtwin, the unit cell, and consequently the magnetic easy plane, is rotated by $\sim 82^\circ$ with respect to the matrix. Consequently, the microtwin region and matrix have exactly one common axis, the intersection of the easy planes, which is indicated by the yellow line in Fig. 5.5. Thus, this is the magnetic easy axis for the area with the microtwin. For both possible microtwin tilts, the intersection line is parallel to the microtwin line on the surface.

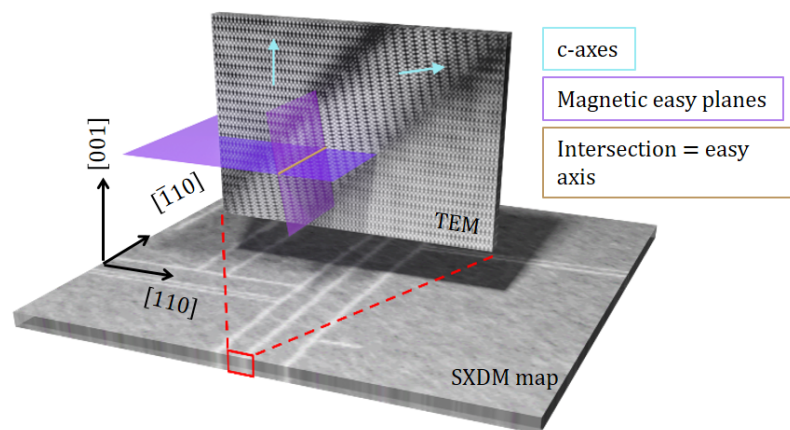


Figure 5.5: SXDM map of defect lines on the CuMnAs(001) surface (horizontal panel) and HAADF-STEM image (vertical plane) of a microtwin defect. Teal arrows give the local orientation of the c -axis. Purple rectangles indicate the magnetic easy planes in the microtwin and the surrounding film. The yellow line shows the intersection of the magnetic easy planes which determines the magnetic easy axis for the entire region.

5.3.4 Discussion

The results unambiguously show a strong coupling between microtwins and antiferromagnetic domains and the argument presented in the previous section (see Fig. 5.5) gives an intuitive explanation of a preferred spin axis orientation parallel to the microtwin line.

However, it is not evident that a local change of the magnetocrystalline anisotropy in the vicinity of a microtwin is sufficient to explain the observed domain characteristics. For example crystallographic defects can alter not only the magnetocrystalline anisotropy, but also affect the magnetic exchange and magnetoelastic energy via defect-induced strain. Decoupling the different effects is experimentally impossible, but can be done in (atomistic) simulations or by (numerically) solving analytical model, in the following where the antiferromagnetic texture is modeled as a continuous two-dimensional vector field in terms of the reduced Néel vector.

The theoretical model considers a two-dimensional antiferromagnetic film with biaxial in-plane anisotropy in a non-perturbed part of the film. A two-dimensional continuum model cannot include an atomistic description of a microtwin, but, as described in section 2.12, the illustrative argument presented above (Sec. 5.3.3) can be mathematically translated into a local change of the magnetic anisotropy around a microtwin region. Additionally, the model can incorporate magnetoelastic energy which can contain a contribution of microtwin-induced strain. For details see section 2.12. The simulations are done by Helen Gomonay.

A change of the AF exchange is not considered, since twin and matrix form a coherent boundary with shared Mn-atoms and without sublattice swap which strongly suggests that exchange is maintained across the boundary.

To investigate if the intuitive argument of a local anisotropy change is sufficient to describe the observed phenomena, the results of two sets of simulations for selected microtwin configurations are compared. The first set of

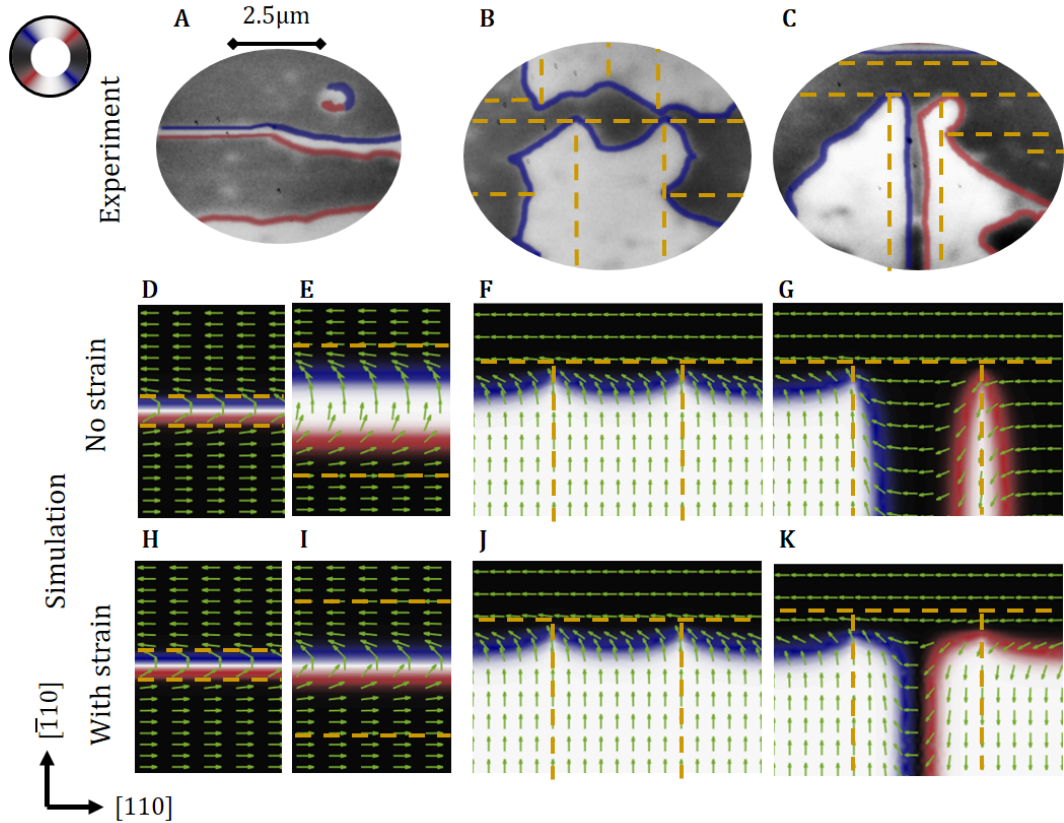


Figure 5.6: *Comparison of micromagnetic simulations and experiment* **A-C** XMLD-PEEM images of AF domains overlaid with the microtwin pattern measured in XLD-PEEM (yellow broken lines), similar to Fig. 5.4 **F**. **D-G** Micromagnetic simulation disregarding magnetoelastic energy of AF domain structures in areas with different microtwin configuration (indicated by the broken yellow lines): **D** parallel microtwins $2 d_{\text{DW}}$ apart, **E** parallel microtwins $8 d_{\text{DW}}$ apart, **F** two parallel microtwins and one perpendicular microtwin forming 2 T -junctions $8 d_{\text{DW}}$ apart. **G** same microtwin configuration as **F** but with different initial conditions. **H-K**, same as **D-G** but including the magnetoelastic energy term and microtwin-induced strain. The green arrows show the local orientation of the Néel vector. The color map is based on the contrast which would be measured in XMLD-PEEM.

simulations considers only a microtwin-induced local change of the magnetocrystalline anisotropy, *i.e.* magnetoelasticity is “switched off”. The second set of simulations “switches on” magnetoelasticity and incorporates defect-induced strain in a small, additional magnetoelastic term. The magnetoelastic energy term is locally approximately two orders of magnitude smaller than the anisotropy change.

The micromagnetic simulations (see section 2.12) are performed for the following microtwin scenarios: Parallel microtwins at various distances D away from each other and microtwin patterns with two microtwin T-junctions formed by two parallel twins and one twin with perpendicular orientation. The results are compared to experimental data in Fig. 5.6.

Figure 5.6**A-C** show typical experimental measurements with similar microtwin configurations, featuring 180° domain walls confined between two defects (**A**), pinning of 90° domain walls in microtwin T-junctions which forms the serrated edges of the domains (**B**) and “opening” of a 180° domain wall, confined between two microtwins, into two 90° domain walls (**C**) at the end of the twins. The images show the XMLD-PEEM contrast measured with $\vec{E} \parallel [110]$ overlaid with the contrast on the domain walls (red/blue), similar to the colour code used in Fig. 5.4**F-J**. The broken yellow lines indicate the microtwin pattern measured in XLD-PEEM.

The panels in the middle row, **D-G** show vector maps of the AF domain pattern obtained from micromagnetic simulations with the simplest model which considers only local change of the anisotropy energy. The green arrows show the Néel vector orientation, *i.e.* the direction of the magnetisation of one sublattice. The colour map of the vector maps and the visualisation of the microtwin pattern matches the colour code used for the experimental data.

Figure 5.6**D** considers two microtwins close together, at a distance of $D = 2$ domain wall widths (d_{DW}) from each other. Here the model without strain correctly reproduces the formation of a 180° domain wall confined between the two defects. Including defect induced strain, shown directly below in panel **H**,

does not lead to an notable change.

In contrast, for two microtwins further away from each other at $D = 8 d_{\text{DW}}$, panels **E** and Fig. 5.6**I**, only the simulations which include strain reproduce the formation of a 180° domain wall between the defects (panel **I**). In contrast, in simulations without strain result in two 90° domain wall separated by an extended domain (Panel **E**), showing that 180° domain walls are unstable in the model which only considers the local anisotropy change.

Panels **F**, **G** and **J**, **K** show simulation results for different initial conditions, but for the same microtwin configuration, formed of two parallel vertical microtwins ($D = 8 d_{\text{DW}}$) which terminate at a horizontal microtwin, forming two T-junctions. In panel **F** the simulation converges to state with only one 90° domain wall. The 90° domain walls separate a domain with Néel vector aligned with the horizontal microtwins and a domain with Néel vector alignment parallel to the two vertical domains, the Néel vectors in the vicinity of either horizontal twin are parallel and the area between the two parallel microtwins is largely homogeneous. The results are not changed notably by including strain in the model (see panel **J**).

For different initial conditions in the simulations without strain (panel **G**), two 90° domain walls separate both the horizontal and vertical microtwins. Similar to panels **E** and **I**, it is found that including strain leads to a 180° between the parallel defects instead which opens into two 90° domain walls at the T-junctions, in agreement with the experimental data.

All panels **F-G**, **J-K** show pinning of the 90° domain walls at the microtwin T-junctions and the 90° domain walls locally align at an angle of 45° with the microtwins, similar to the experimental observations at microtwin T-junctions. In simulations, the alignment of the 90° domain walls is lost after approximately one domain wall width away from the T-junction and the domain wall straightens parallel to the boundaries of the simulated area. Whether the domain wall aligns with the vertical or the horizontal edge away from the T-junctions depends sensitively on the initial conditions, as seen in panel **G**.

Consequently, the behaviour of 90° domain walls away from microtwins, as well as the difference of panels **G** and **K** in the bottom right corner, must be considered as an artefact of the simulations. The domain wall alignment parallel to the boundaries of the simulated area can be explained as corresponding to a state with minimal domain wall lengths, *i.e.* the minimisation of exchange energy in the absence of other contributing factors.

Experiments never consist of isolated, non-disturbed areas, but parts of larger domain and microtwin pattern and other inhomogeneities. Here, we observe a large variety of domain wall alignments away from the junctions, which is likely to be governed by the surrounding microtwin pattern and other local crystallographic inhomogeneities.

5.4 Conclusion and outlook

The previous section shows that the large-scale AF domain structure in unpatterned CuMnAs films is largely determined by microtwin defects within the film. The preferred spin axis is shown to be parallel to a defect line which leads to either large AF domains or characteristic 180° domain walls aligned parallel to the crystallographic directions. A perpendicular orientation of two defect lines leads to 90° domain walls that form characteristic serrated edges locally pinned at microtwin T-junctions. From micromagnetic simulations, it is found that the 90° domain wall pinning and the formation of characteristic 180° domain walls between two parallel microtwins close to each other can be explained from the change of the magnetocrystalline anisotropy in the defect region alone. In contrast, the simulations also show that 180° domain walls between microtwins further apart from each are unstable towards splitting into two 90° in the absence of an additional stabilising term. It is found that incorporating a small, magnetoelastic term with a contribution of microtwin-induced strain, about two orders of magnitude smaller than the local anisotropy change, is sufficient to stabilise the 180° domain walls between two

parallel defects at larger distances. This term does not lead to notable changes in the close vicinity of the microtwins, *i.e.* here the behaviour is governed by the local anisotropy change.

Chapter 6

Edge-imposed anisotropy in CuMnAs thin film devices

6.1 Introduction

Chapter 5 demonstrated how the equilibrium AF domain structure in 45 nm CuMnAs/GaP(001) films is dominated by the underlying structural microtwin-defect pattern. The observations emphasize the sensitivity of the AF domain pattern to the crystallographic structure which might become a tool for AF domain engineering for specific spintronic applications.

However, most applications require patterned devices fabricated from thin films. Patterned devices inevitably incorporate another defect type: the patterned edges. The effect of patterned edges on the domain structure has long been investigated and with the increasing availability of imaging techniques for AF order it has also been investigated for selected AF systems, as discussed in the following.

Shape anisotropy in FM systems

Domain formation in ferromagnets and their sensitivity to the shape and size of a sample has been studied since the early 1900s, first predicted theoretically, before imaging techniques of FM domains were widely available [38, 114, 115].

The early theory, summarised well in reference [38], predicts the existence, shape and size of domains based on minimisation of the internal energy of a FM system, with the main contribution of exchange, anisotropy, magnetostrictive and magnetostatic energy in the demagnetising field outside the FM sample. In a single crystal, exchange, anisotropy and magnetostrictive energy can be simultaneously minimised with a single-domain configuration. However, in a finite sample, a single domain state has magnetic “poles” at the surface (edge), associated with high magnetostatic energy. The magnetostatic energy can be reduced considerably by the formation of a domain structure with diminishing magnetic stray fields. For specific domain configurations, the magnetic stray field vanishes. They are characterised by domains near the surface, which close the flux circuit within the sample and are hence referred to as “closure domains” [38]. This is illustrated in Fig. 6.1, which shows how the subdivision into magnetic domains reduces the extent of the demagnetising field and hence the magnetostatic energy. The optimal domain configuration is a balance of the gain in magnetostatic energy compared to the cost in exchange, magnetocrystalline anisotropy and magnetoelastic energy required to form the particular state. Hence, it depends both on the material and on the sample size and shape.

From the argument above it is evident that, although exchange, anisotropy and magnetostrictive energy are also relevant, the domain structure in a single crystal is highly sensitive to the geometric shape and size of the sample.

In contrast, the exchange, anisotropy and magnetostrictive energy are important at the boundary between domains, the domain walls, and determine their widths and crystallographic orientation. [38]

The first clear experimental evidence for the model was found in “microphotographs of domain boundaries obtained by the technique of magnetic powder patterns” [38], in the late 1940s [116–118]. Since then, the domain theory has been validated in numerous direct imaging experiments of FM domains and has formed the basis of the understanding of FM domain formation

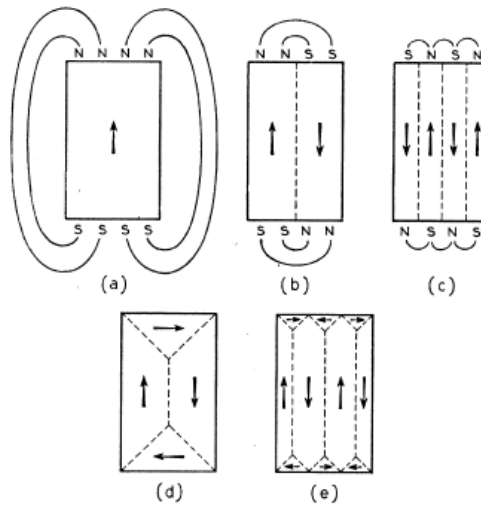


Figure 6.1: Origin of domains in FM single crystals. Reprint of Fig. 9 from reference [38]. Shown are schematic domain configuration in a FM single crystal and corresponding demagnetising field. The domain division from panels (a) to (c) reduces the demagnetising field and hence lowers the magnetic energy of the sample. Panels (d) and (e) show two configurations with typical closure domains which act to close the flux circuit within the sample, hence the magnetostatic energy of the domain configurations vanishes. All domain configurations (c)-(e) are realised in materials, depending on the magnetocrystalline anisotropy, magnetoelastic and exchange energy of the configuration.

in solids over the past century [25].

The magnetostatic energy, which leads to the strong sensitivity of FM domains to the shape and size of the sample in (larger samples single crystal), becomes less relevant with decreasing sample sizes approaching the nanoscale and can be suppressed in synthetic antiferromagnets, (complex) coupled multilayers with alternating magnetisation. This allows other effects to become relevant. Thin films epitaxially grown on a nonmagnetic substrate (discussed in the following) and exchange-coupled multilayers (not discussed here) in particular, have become increasingly relevant for applications, but are also more complex than the single crystals considered so far. In particular the different surfaces of a device, consisting of the interface with the substrate, the free surface (potentially protected by a capping layer) and the lithographically fabricated lateral edges, are not equivalent. For example, for (Ga,Mn)As-nanostructures, lithographically patterned from an epitaxially grown (Ga,Mn)As/GaAs thin film, the shape of the device shape was found to also influence the magnetic

domain structure via lithography-induced strain relaxation which alters the magnetic anisotropy of the sample [119]. The low moment of the diluted magnetic semiconductor (Ga,Mn)As reduces the relevance of the magnetostatic energy and the observed domain patterns were interpreted in a single domain model. Although induced by the patterned edges, the strain may be relaxed across the entire device. In contrast, in micron-sized bars fabricated from magnetostrictive $\text{Fe}_{81}\text{Ga}_{19}$ films with high magnetic moments, lithographically induced strain relaxation has been found to stabilise flux closure magnetic domain patterns, which are distorted compared to the pattern observed in wider bars, where the effects of the lattice relaxation are less significant [120]. Here, strain relaxation was limited to $\lesssim 150$ nm from the edge.

Additionally, there are phenomena which occur only locally at or a few atomic layers below a surface (or interface). These are studied in the field of surface magnetism. A detailed discussion can be found in reference [121]. These phenomena include largely system-independent effects, *e.g.* that a surface has reduced dimensionality compared to the bulk which leads to a change in the ordering temperature such that magnetic ordering occurs first at the surface, and a multitude of highly system-dependent effects. Examples are a local shift of the electronic states at the surface, intra-atomic s-d charge transfer, change in the s-d hybridization the band-narrowing due to the reduction of the coordination number of the surface atoms. These effects are relevant when studying interface effects, when considering (very) thin films consisting of a few monolayers or for their relevance in the initial domain formation when cooling across the ordering temperature. Additionally, they can influence the boundary conditions on the domain structure of a (bulk) sample, but do not affect magnetic properties, such as anisotropy, over long-distances. Thus, they will be referred to as “surface effects” in contrast to the “shape-imposed” phenomena discussed before.

Shape anisotropy in AF systems

In fully compensated AFs, magnetic stray fields are negligibly small. Hence, the sensitivity of AF domain structure to the shape and size of a device cannot arise from the minimisation of magnetostatic energy, as dominant in many FM systems. In contrast, surface effects (including surface magnetic anisotropy as discussed at the end of the previous section), and sensitivity of the magnetic anisotropy in thin film devices to patterning induced strain-relaxation due to magnetostrictive effects, can be expected to be equally present in AF systems, and moreover to become even more relevant in the absence of demagnetising field effects. Thus, AFs are an ideal testbed system to study these effects which are often suppressed in FMs. However, both the theoretical treatment and experimental investigation of AF domain structures in general, and in finite samples in particular, has only recently been given attention.

The theoretical study of AF domain formation in AF thin films and finite size-samples has largely been led by work from Gomonay et al., who have developed a theoretical model for AF domain structure in thin films and finite sample, which incorporates surface magnetic anisotropy and long-range magnetoelastic forces [42, 122]. Experimental evidence for the model is still scarce and mainly limited to studies of AF domains in epitaxial LaFeO₃ (LFO) thin film devices and LSMO/LSFO bilayers and superlattices. For these systems, however, Folven et al., have carried out multiple detailed studies on the effect of patterning, substrate and film thickness on the AF [43, 108, 110, 123, 124]. For LFO thin films, different studies report either spin alignment within the film plane or an out-of-plane canting of the spin axis by 20° to 45° [107, 108, 123, 125, 126]. The work by Folven and coworkers is focused on the in-plane projection of the spin angle. The non-patterned films were found to consist of sub-micron AF domains aligned along specific intrinsic magnetic easy axes, aligned with the $\langle 100 \rangle$ crystallographic directions only or with the $\langle 100 \rangle$ and $\langle 110 \rangle$ crystallographic directions depending on the substrate choice and film thickness [43]. Patterned

edges aligned with any of the magnetic easy axes were found to stabilise AF domains in nanofabricated devices leading to larger domains or single domain states in devices with widths below 200 nm to 500 nm in LFO thin films [123] and up to 1 μm to 2 μm in (antiferromagnetic) LFO/(ferromagnetic) LSMO superlattices, above the ordering temperature of the FM which is below the Néel temperature of LFO. If parallel or perpendicular alignment with the patterned edges occurs was found to depend on the following: film thickness, the crystallographic orientation of the edge, if the patterned edge is embedded (created by Ar^+ ion implantation in the surrounding lattice) or free-standing (achieved by ion-beam milling) [123]. Effects of edges not aligned with an intrinsic magnetic axis were either not observed or only in a narrow region localised in the direct vicinity of the edges [108, 124]. It was also shown for exchange-coupled (antiferromagnetic) LFO/(ferromagnetic) LSMO bilayers that the shape-induced anisotropy change of the AF layer can be used to control the switching field of the FM layer [110].

The observations were considered to be compatible with the theoretical model proposed by Gomonay et al., although a precise theoretical description of the system has not been given. The work on LFO thin films and LFO/LSFO bilayers and superlattices was focused on the effect of patterned edges on the domains and magnetic anisotropy in thin film devices fabricated from thin films with several easy axes and domains of sub-micron size in blanket films.

A more subtle effect of surfaces on the alignment of antiferromagnetic domain walls was reported for Cr_2O_3 single crystals [127]. Due to strong uniaxial magnetocrystalline anisotropy, Cr_2O_3 single crystals show only domains with spin axis parallel to the easy axes. The domain sizes can exceed several tens of μm^2 . Two domains with antiparallel alignment of the Néel vector separated by well-defined 180° domain walls are observed. The 180° domain walls were found to form straight lines without obvious alignment to the crystallographic directions, but along a path which minimises the domain wall length on the

surfaces. This results in a deviation of the domain wall path at topographical features (patterned mesas) and domain wall pinning effects. The study also reported a local deviation of the domain wall orientation towards the surface normal. The effect was found to be limited to the direct vicinity of the topographical edges (surfaces) and has been attributed to minimisation of exchange interaction by normal incidence at surfaces. For this material, no long-range effects of the surfaces on the AF properties were reported.

Chapter overview This chapter reports on the effect of patterning on the AF domain structure and domain walls in 45 nm CuMnAs/GaP(001) films. XMLD-PEEM imaging of AF domains in devices with a variety of geometrical shapes reveal that patterned edges strongly affect the AF domain morphology and population. It is shown how the AF domain structure in patterned devices can be understood as a result of the competition the effect of microtwins and an additional, edge-imposed anisotropy term. The edge-imposed anisotropy leads to a measurable change of the width of AF domain walls and can dominate the AF domain pattern over distances exceeding several micrometers, up to over 20 μm in devices fabricated from layers with the highest crystalline quality. No evidence for a dependence on the sample surface, which was kept with 2.5 nm Al was observed.

6.2 Methods

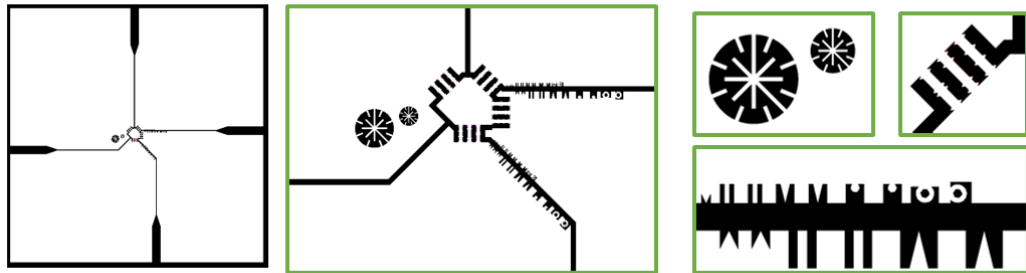
Material The measurements in this chapter are performed on six 50 nm CuMnAs/GaP(001) films, capped with 2.5 nm Al to prevent oxidation. The films show intermediate or low microtwin density, but the findings were also confirmed on films with high microtwin density.

Device fabrication Devices were fabricated either by photolithography and chemical wet etching, or electron beam lithography and Ar^+ ion milling. Since the data show no dependence on the fabrication technique, it is not explicitly

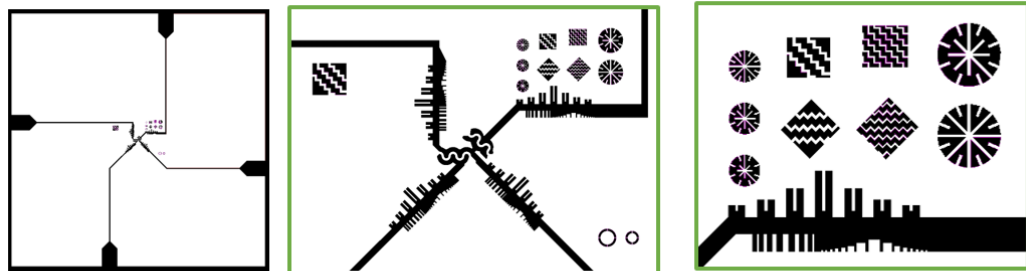
indicated for each measurement. See section 2.3 for devices fabrication.

Device geometries Images of the most often used lithographic masks used for patterning can be found in Fig. 6.2. On each chip there are a series of devices with various different geometric shapes. Specific simple geometries, bars with different sizes and orientations are present on all masks. More complex geometries, like rings, wheels, “snakes” are on selected masks only.

“Anticroc”



“Snakes”



“Wheatstone”

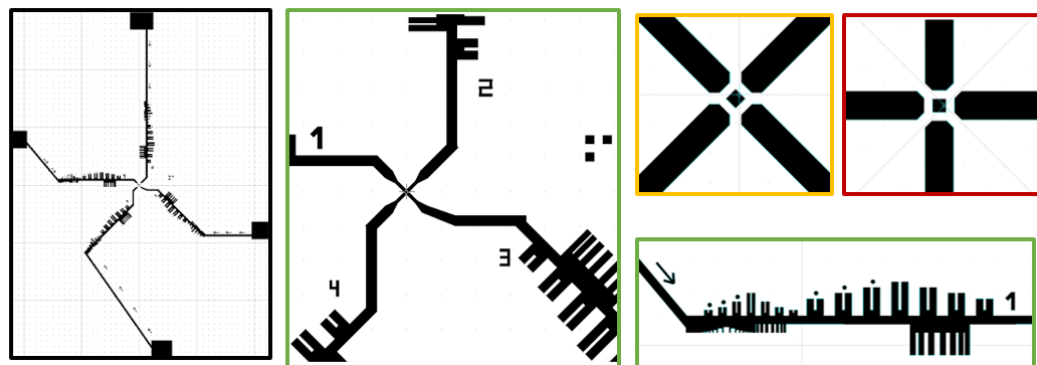


Figure 6.2: *Lithography masks with geometric shapes.* Overview images (left) and close ups on selected areas (green border). Black areas correspond to etching areas, white areas to the non-perturbed CuMnAs layer. The “Anticroc” and “Snakes” masks are 10 mm × 10 mm squares. The “Wheatstone” mask is rectangular. The thin grey lines (dots) indicate a 100 μm 10 μm square pattern as a guide, but are not part of the mask design. The “Wheatstone” mask has been realised with two different centres, shown in the red and yellow boxes. The edges of all mask are aligned with the CuMnAs $\langle 100 \rangle$ directions in sample fabrication.

Electrically isolated CuMnAs islands cannot be imaged in XMLD-PEEM, due to charging. Therefore all devices are connected to the rest of the CuMnAs film (have an “open side”).

For each lithographic mask, at least one replica on different CuMnAs films was fabricated.

X-PEEM imaging The AF domain structure was imaged using XMLD-PEEM on beamline I06 at Diamond Light Source as described in section 2.8. Most measurements were performed at room-temperature. For some measurements the samples were cooled to approximately 200 K, which enhances the XMLD signal. The AF domain structure is not affected by the cooling within the measurement uncertainty, as confirmed by direct comparison of measurements on selected areas.

Imaging of the microtwin configuration For selected samples the microtwin configuration was imaged using scanning x-ray diffraction microscopy (SXDM) on the NanoMAX beamline at MAX IV, similar to the measurements shown in the previous chapter (see section 2.11.2 for experiment details). The measurements utilise the CuMnAs 003 reflection. A real space map of the microtwin intensity is obtained from the sum of intensity maps for two sample rotations, at $\pm 0.4^\circ$ away from the Bragg angle. In these maps, the microtwins show up as bright lines. As microtwins form a small step on the surface, microtwins with surface termination perpendicular to the x-ray polarisation can also lead to small, additional contrast, recognisable as thin, faint dark lines, in the XMLD-PEEM image.

6.3 Results and interpretation

The results presented in the following can only be understood if the coupling of the AF domains to microtwin defects, inherent to these films, is taken into account. In this context, it is sufficient to consider the microtwins as line-

defects along the CuMnAs [110] and $[\bar{1}10]$ directions which pin the AF spin axis parallel to the defect. A detailed discussion of the crystallographic nature of the defects and the coupling to the AF domains can be found in the previous chapter 5.

In blanket films, *i.e.* before device fabrication in the absence of patterned edges, the films show two types of domains with mutually orthogonal spin axes aligned with the CuMnAs [110] or $[\bar{1}10]$, parallel to the microtwin defects. The domain population is approximately equal. The size of the domains varies from under $1\ \mu\text{m}^2$ to over $10\ \mu\text{m}^2$ and is governed by the microtwin density of the particular layer (see section 5.3.2).

Amongst the simplest device geometries are bars with the edges aligned along the crystallographic directions. The domain morphologies observed in these devices will be discussed in the following first for bars aligned with the magnetic easy axes and second for magnetic hard axis.

6.3.1 Patterning along the magnetic easy axes

Figure 6.3 shows XMLD-PEEM images of AF domains in a series of $80\ \mu\text{m}$ long bars with different widths. Each bar has three patterned edges with one of the short sides connected to the rest of the AF film. The devices are fabricated from the CuMnAs film with the lowest microtwin density. In a blanket film the layer has an average distance of over $10\ \mu\text{m}$ between neighbouring defects and correspondingly large AF domains (see Fig. 3.8) As in the blanket film, two clearly distinct types of domains with spin axes along the CuMnAs [110] (“dark”) and $[\bar{1}10]$ (“light”) can be observed. However, compared to the non-patterned case the domain population is shifted. In each bar the spin axis mostly aligned parallel to the long edges (majority domains), whereas areas with spin axis parallel to the short edge (minority domains) are sparse. This suggests that the patterned edges change the anisotropy of the system such that spin axis alignment parallel to the edge is energetically favoured. This

will be referred to as edge-imposed anisotropy in the following.

The bars in panels **A-C** of Fig. 6.3, oriented along the CuMnAs $[\bar{1}10]$, appear mainly light in the XMLD-PEEM images. Dark minority domains are localised at the closed short edges or form characteristic lens-shaped domains oriented perpendicular to the long edge. These features are referred to as “end domains” and “lens domains” in the following. Thinner, 180° domain walls (dark) are also observed. In the bars with orthogonal orientation, panels **D-G**, the XMLD-contrast is reversed and the bars appear largely dark with light 180° domain walls, lens domains and end-domains. In panels **D-G** additional, very faint contrast arises within the majority domains showing on lines parallel to the long edge. The very faint “darker lines on dark background” are indicative of microtwins.

The end domains have a roughly triangular shape. In some cases, the end domains are intersected by a lens domain located at the short edge (*e.g.* Fig. 6.3 **D**) or by the majority domain over a width similar to the lens domains.

The lens domains are approximately $0.5\ \mu\text{m}$ wide at the centre, independent of the widths of the bar. The lens domains often cross the entire widths of the bar, but shorter lens domains, with one endpoint located at a boundary and the other located somewhere in the centre of a bar, are also observed. At device edges the lens domains show sharp endpoints, whereas endpoints away from edges are rounded. The number of lens domains is generally larger in thinner bars.

Further information on the lens domains can be obtained from XMLD-PEEM images with $\vec{E}||[010]$, like the one of a section of the $5\ \mu\text{m}$ wide stripe shown in Fig. 6.3 **H**. The corresponding area in panel **G** is marked by the orange square. The area features five lens domains, all of them are clearly separated from the surrounding majority domain by 90° domain walls, which show up as either dark or light lines in this imaging configuration. The two neighbouring lens domains with matching domain walls have merged to form a single domain. Here, all lens domain have the same orientation of the domain wall

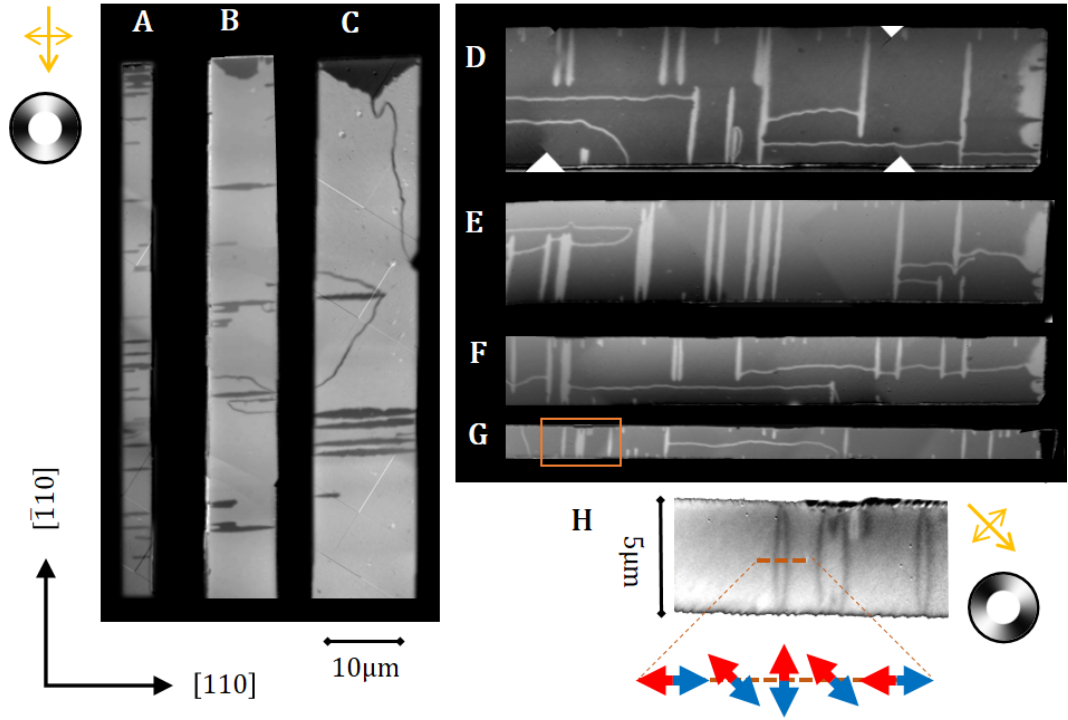


Figure 6.3: *Effect of patterned edges along the magnetic easy axis XMLD-PEEM images of AF domain structures in 80 μm long bars fabricated from a 45 nm CuMnAs/GaP layer with low microtwin density. A-C: 5 μm , 10 μm and 15 μm wide bars aligned with the CuMnAs $[\bar{1}10]$ direction. The top short edge is closed, the bottom side is connected with the rest of the CuMnAs film (open edge). D -G: 20 μm , 15 μm , 10 μm and 5 μm wide bars with orthogonal orientation. Here the open edge is at the left. H XMLD-PEEM image of the area marked with the orange rectangle in panel G, but with x-ray polarisation along the CuMnAs $[010]$ yielding contrast on the AF domain walls as indicated by the greyscale wheel. The red and blue arrows underneath depict the orientation of the Néel vector across a lens domain.*

on either side. This has been found to be typical for lens domains and allows to clearly distinguish lens domains from 180° domain walls. Although in the image shown here four of the five lens domains have “dark” boundaries, no significant imbalance between the two orientations could be observed across larger datasets.

By comparing images with $\vec{E}||[010]$ and $\vec{E}||[110]$, the rotation of the Néel vector across a lens domain can be determined, as depicted in the subset in Fig. 6.3. From the fact that the spin axis orientation in the centre of the domain wall of the lens domain is constant, it follows that the Néel vector rotates back to its initial orientation when crossing a lens domain, *i.e.* the sign of the Néel vector in the surrounding majority domain is the same on

either side of the domain. This implies that, in contrast to 180° domain walls, the lens domains are topologically trivial and in principle could annihilate and disappear. If only antiferromagnetic exchange, magnetocrystalline anisotropy and edge-imposed anisotropy is considered, then the uniform state should be energetically favoured over the state with lens domains. Hence, an additional energy term is required to stabilise the lens domains.

In the following, it is shown that the lens domains result from underlying microtwin defects which locally alter the AF anisotropy as demonstrated in chapter 5.

Figure 6.4 **A - D** compares XMLD-PEEM images of the AF domains to the microtwin configuration measured using SXDM (see section 2.11.2) in two bars (shown also in panels **B** and **C** in Fig. 6.3). The SXDM intensity maps and the XMLD-PEEM images show a strikingly strong correlation, revealing a one-to-one correspondence between the microtwins and the lens domains. The central axis of each lens domain coincides with a microtwin oriented perpendicular to the edge and vice versa, each microtwin oriented perpendicular to the edge is surrounded by a lens domain. As such, the lens domains can be seen as a direct result of the microtwin defects which locally change the AF anisotropy and pin the AF spin axis parallel to the defect (see chapter 5).

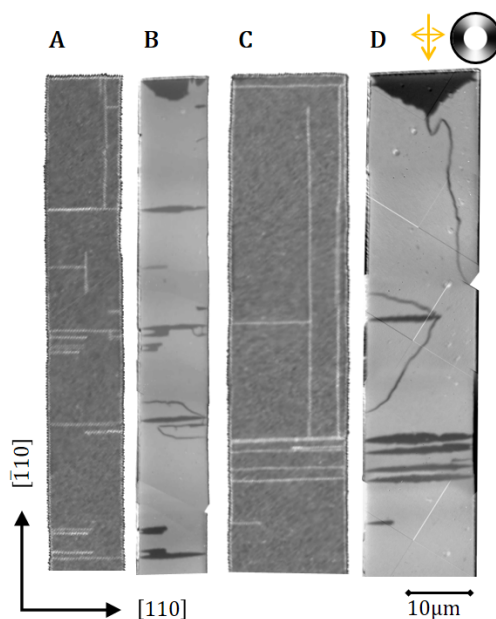


Figure 6.4: *Formation of lens domains in bars aligned with the magnetic easy axes. A, C: SXDM maps of the $10\ \mu\text{m}$ wide and $15\ \mu\text{m}$ wide bars from Fig. 6.3 **B** and **C**. The microtwins appear as light lines. B, D, AF domain structure of the same bars for direct comparison, imaged with x-ray polarisation along the CuMnAs $[110]$ yielding contrast on the magnetic easy axes, as indicated by the greyscale wheel.*

Microtwins oriented perpendicular to the bar seemingly have a less pronounced influence on the AF domain structure. Here, the spin axis pinning on the microtwin matches the edge-imposed anisotropy of the long bar. However, the “intersections” of the end domains correlate with microtwins oriented parallel to the long-edges. In places where these microtwins “meet” a lens-domain, the lens domain boundary has a “dip”. This can be seen for example in the lens-domains which cross the entire widths of the bar shown in Fig. 6.4 **D** or in the lens domains close to the right end in the bars shown in Fig. 6.3 **D** and **F**. For these images, the existence of microtwins can be inferred from the faint dark lines in the background.

The devices considered so far have been fabricated from the CuMnAs film with the lowest microtwin density. The bars have large areas which are microtwin-free and are found to be single domain or feature only 180° domain walls.

A qualitatively similar picture arises in bars fabricated from the layer with intermediate microtwin density with average distance between two neighbouring microtwins of just over 2 μm and similar lateral AF domain sizes (see Fig. 3.6 **B**) in the blanket film. Representative examples of AF domain patterns observed in bars aligned with the magnetic easy axis fabricated from this layer are shown in Fig. 6.5. The 30 μm long bars have a similar geometry, with one open and three closed edges, but are smaller to match better with the AF domain size of the layer. Panels **A-D** and panels **E-H** show two sets of bars with widths varying between 2.5 μm and 10 μm aligned with the CuMnAs [110] and $[\bar{1}10]$ directions.

The bars show the same characteristic features as the ones fabricated from the layer with low microtwin density: A shift of the average domain population such that the majority is aligned parallel to the long edge, lens domains and 180° domain walls. The end-domains are less pronounced and the number of lens-domains is considerably higher than in the previous examples. Both can be attributed to the higher number of microtwins. Many of the lens-domains have merged forming one larger domain. We also note, that here some lens domains

are attached to a patterned edge, but have both endpoints in the middle of the bar. We interpret these as lens domains forming around microtwins which are oriented perpendicular to the long edge and located between two microtwins which run parallel to the long edge. The fact that lens domains in the middle of the bar in panels **E-H** terminate at faint dark, horizontal lines on top of the dark background (indicative of horizontal microtwins) can be seen as direct evidence of this interpretation.

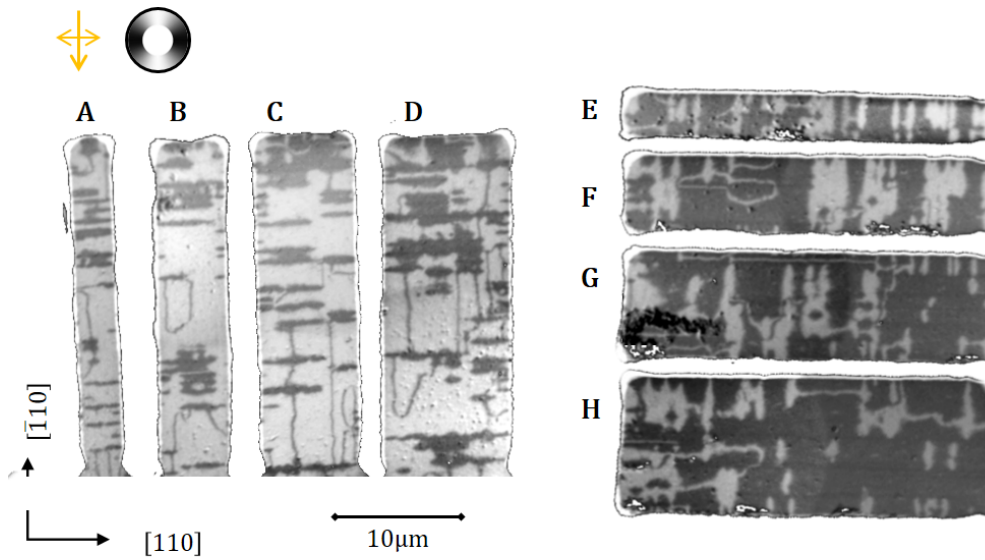


Figure 6.5: *Effect of patterned edges along the magnetic easy axis on a layer with intermediate microtwin density.* XMLD-PEEM images of AF domain structures in $30\ \mu\text{m}$ long bars fabricated from a $45\ \text{nm}$ CuMnAs/GaP layer with intermediate microtwin density. **A-D:** $2.5\ \mu\text{m}$, $5\ \mu\text{m}$, $7.5\ \mu\text{m}$ and $10\ \mu\text{m}$ wide bars aligned with the CuMnAs $[\bar{1}10]$ direction. The top short edge is closed, the bottom side is open. **E-H:** Same as **A-D**, but for bars with orthogonal orientation. Here the closed edge is at the left.

In summary, in bar devices aligned with the magnetic easy axes the majority of the domains align parallel to the edge. Extended domains with spin axis perpendicular to the long edge are only found in the vicinity of the short edge or in the vicinity of microtwins. Away from the short edge and in microtwin-free areas, the alignment of the spin axis parallel to the edge is kept across the entire width of the bar, even in the widest bars studied.

6.3.2 Patterning along the magnetic hard axes

In the bar devices discussed in the previous section, the directions of the patterned edges match with the microtwin directions and the (intrinsic) magnetic easy axes. This is not the case if the bar is aligned along the CuMnAs [100] or [010] directions, another important device geometry for electrical measurements which will be discussed in the following.

Figure 6.6 shows the AF domain structure alongside the microtwin configuration of a 10 μm wide bar and a 5 μm wide bar aligned with the CuMnAs [100] directions. The devices are fabricated from the layer with the lowest microtwin density. The XMLD-PEEM images of the bars (panels **B**, **D**) are obtained with x-ray polarisation along the CuMnAs [110] which yields maximum contrast between domains oriented at 45° and 135° to the bar, whereas domains with spin axis parallel and perpendicular to the bar cannot be distinguished.

As before, the data show clear correlation between microtwins and AF domain structure, such that locally the spin axis aligns parallel to the defect. However, the AF domain structure shows a completely different morphology than in the bars aligned with the magnetic easy axis. In contrast to non-patterned areas and in devices with patterned edges along the magnetic easy axis, minimum and maximum XMLD contrast is only observed in the vicinity of a microtwin or in domain wall like features. Around the microtwin defects, the contrast in the XMLD-PEEM images decays more gradually than for lens domains in the easy axis bars which have a clear domain boundary. The more gradual contrast variation is most easily seen in the wider, 10 μm wide bar.

Most of the domain walls show both minimum and maximum XMLD-contrast across the wall, indicative of a 180° domain wall with a Néel vector at 45° to the x-ray polarisation. One example of such a 180° domain wall is marked with the red dashed oval in Fig. 6.6 **D**. The area on either side of the wall shows the same XMLD contrast for this imaging configuration which indicates that indeed the spin axis rotates by 180° , and the spin axis in the surrounding

areas on either side are aligned either both with the CuMnAs [100] (parallel to the bar) or both with the CuMnAs [010] (perpendicular to the bar) axes, *i.e.* away from microtwins the edge-imposed anisotropy fully overcomes the intrinsic anisotropy of the layer. In the vicinity of microtwins, due to the edge imposed anisotropy a more gradual variation of the spin axis is observed which can be interpreted as frustration arising from the incompatibility of the edge-imposed anisotropy with the effect of microtwins.

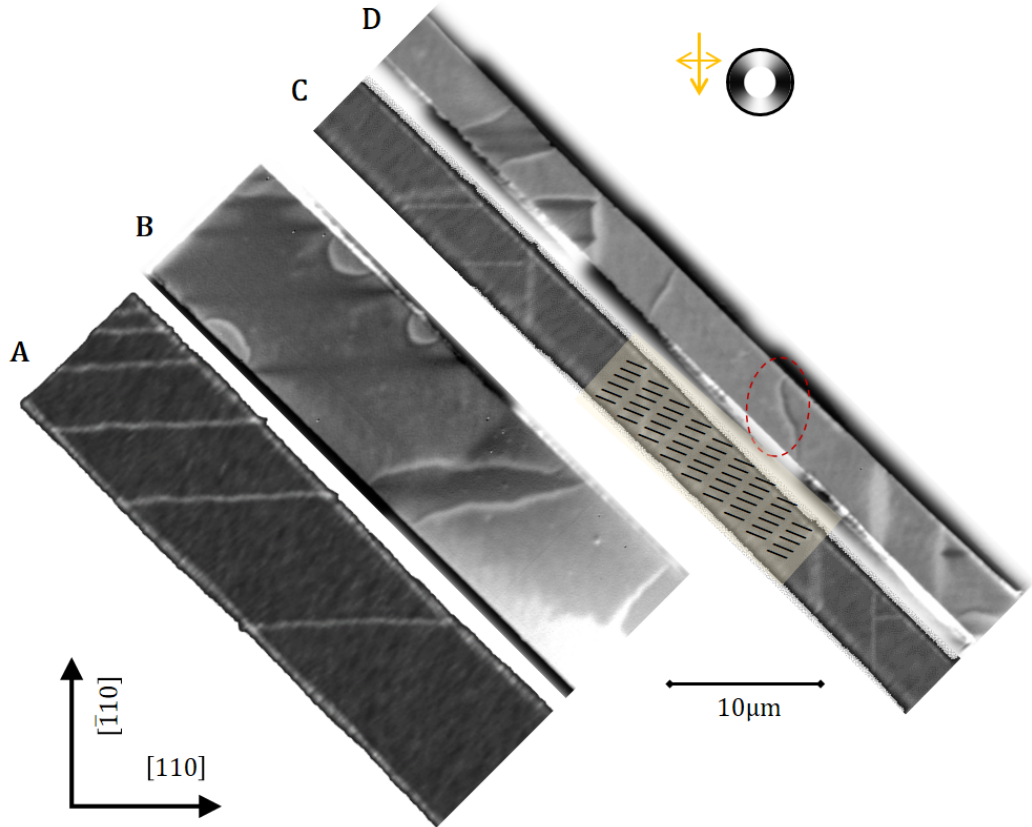


Figure 6.6: Patterning along the magnetic hard axis. Comparison of the microtwin pattern and the AF domain structure in bars aligned with the magnetic hard axis fabricated from the layer with the lowest microtwin density. **A:** SXDM intensity map of the microtwin pattern in a $50\ \mu\text{m} \times 10\ \mu\text{m}$ sized bar. The bottom short edge is open, the top short edge is closed. **B:** AF domain structure of the same bar measured in XMLD-PEEM with $\vec{E} \parallel [110]$ yielding contrast as indicated by the greyscale wheel. **C, D:** Same as **A, B** but for a section of a $80\ \mu\text{m} \times 5\ \mu\text{m}$ sized bar. The closed short edge is not shown. Due to serious issues during the SXDM-data acquisition, the SXDM contrast in the area overlayed with the broken line pattern is not considered reliable. The red dashed circle in panel **D** marks a 180° domain wall.

In devices with higher microtwin density, the relative importance of the effect of microtwins and the effect of the edges on the AF domain structure shifts, as

shown in Fig. 6.7. The figure shows AF domain structure images of four 30 μm long bars aligned with the CuMnAs [010] direction fabricated from a layer with intermediate microtwin density. Panels **A-D** show XMLD-PEEM images with x-ray polarisation along the CuMnAs [110] direction yielding sensitivity on domains aligned with microtwins which are the magnetic easy axes in non-patterned areas. The domain morphology differs considerably from the one observed in bars fabricated along the magnetic easy axes. In the narrower bars (**A, B**), at least three different contrast levels and a generally more gradual contrast variation can be observed. The AF domain structure in the majority of the wider bars largely resembles the one in non-patterned areas consisting of two types of domains with spin axes along the [110] and $[\bar{1}10]$ and a lamellar domain morphology, following the direction of microtwins, here at 45° to the patterned edges. “Grey” areas corresponding to spin axis alignment along the magnetic hard axes are located mostly in the direct vicinity of the edge. This suggests that the edge-imposed anisotropy dominates only in the vicinity of the edge, whereas the effect of microtwins is dominant in the majority of the bar. Figure 6.7 **E-H** shows the same bars, but imaged with x-ray polarisation along the CuMnAs [010] directions. Consistent with the previous findings, the images show a gradual contrast variation in the narrower bars. Clearer 180° and 90° domain walls in the central regions of the wider bars alongside darker/lighter areas are also observed in the close vicinity of the edges, revealing areas where the spin axis does not follow the intrinsic magnetic easy axes. In particular, darker areas are located close to the long edge and lighter areas close to the short edge, indicating that the spin axis is rotated away from the edge, which would be opposite to what was observed for edges aligned with the magnetic easy axes. However, since additional “false” contrast can arise from the edge itself and in these devices the edge effect is difficult to disentangle from the effect of the surrounding microtwins, further evidence is needed.

To determine whether the spin axis is aligned parallel or perpendicular to patterned edges along the CuMnAs [100] and [010], the domain structure in

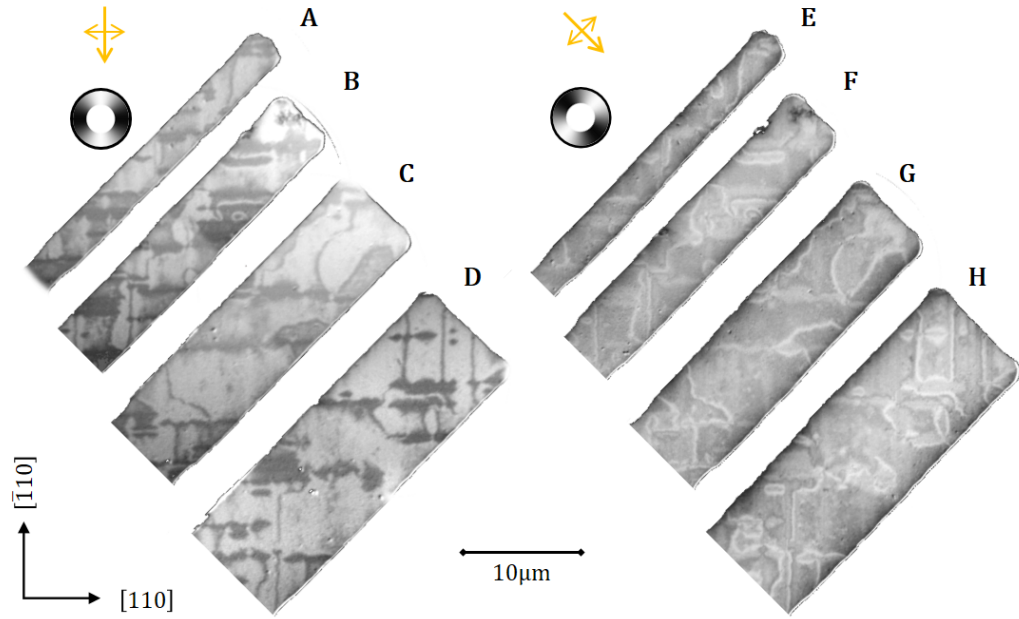


Figure 6.7: *Effect of patterned edges along the magnetic hard axis in a layer with intermediate microtwin density. XMLD-PEEM images of AF domain structures in 30 μm long bars oriented along the CuMnAs [010] direction fabricated from a layer with intermediate microtwin density. The width of the bars varies between 2.5 μm and 10 μm . **A-D:** XMLD-PEEM images with x-ray polarisation along the CuMnAs [110]. **E-H:** Same bars imaged with x-ray polarisation along the CuMnAs [010].*

devices, patterned from a mostly microtwin-free area of the film with lowest microtwin density is investigated. These devices consist of two bars aligned with the CuMnAs [100] and two bars aligned with the CuMnAs [010] directions which allows to directly compare the effect of patterning for the two axes. Figure 6.8 shows the AF domain structure in two devices imaged with x-ray polarisation along the CuMnAs [110] (top) and with x-ray polarisation along the CuMnAs [010] (bottom). Within the imaged area, there is only one microtwin located at the top corner of the device shown in Fig. 6.8 **A** and **B**, which, as before leads to a local spin axis alignment parallel to the microtwin. Two mutually orthogonal bars show the same XMLD signal in the images with x-ray polarisation along the CuMnAs [110], but opposite XMLD contrast in the images with $\vec{E} \parallel [010]$. The measurements with $\vec{E} \parallel [010]$ unambiguously show that the spin axis is aligned perpendicular to the edge in this case, as illustrated by the double-headed red arrows. This confirms that the effect

of patterned edges along the magnetic hard axis is opposite to the effect of patterned edges along a magnetic easy axes.

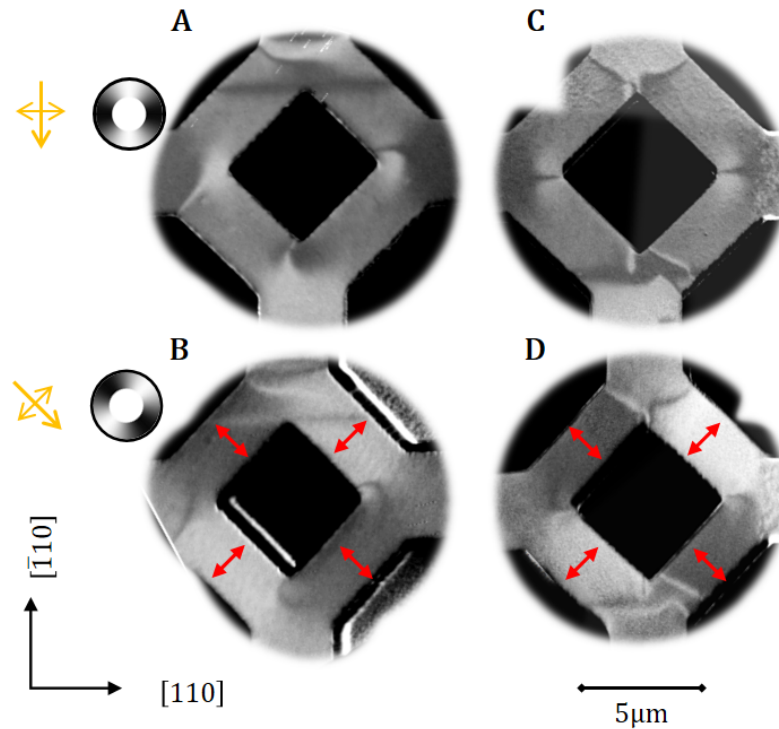


Figure 6.8: *AF domain structure in mostly microtwin-free devices with edges along the magnetic hard axis AF domain structure in two “Wheatstone-bridge”-shaped devices oriented along the $\text{CuMnAs}[010]$ and $[100]$ directions fabricated from the layer with lowest microtwin density in non-patterned areas. **A, C:** XMLD-PEEM images with x-ray polarisation along the CuMnAs $[110]$. **B, D:** Same devices imaged with x-ray polarisation along the CuMnAs $[010]$ yielding maximum XMLD-contrast between domains aligned parallel/perpendicular to the edges of the Wheatstone bridge. The red arrows indicated the local spin axis orientation in different areas of the devices. The bars of the two devices are $4\ \mu\text{m}$ (**A, B**) and $3\ \mu\text{m}$ (**C, D**) wide.*

6.3.3 AF domains in devices with complex geometries

Figure 6.9 XMLD-PEEM images shows of AF domains in a selection of devices with different shapes. All devices were fabricated from a $45\ \text{nm}$ $\text{CuMnAs}/\text{GaP}(001)$ layer with a moderate microtwin density with an average distance of just over $2\ \mu\text{m}$ between neighbouring defects. This leads to micron-sized domains in blanket films and lamellar domain structure (see Fig. 3.6 B). The selected images are characteristic for the AF domain patterns observed

in this geometry. In duplicates of the device geometry across this and other layers similar AF domain morphologies have been observed.

The strongest deviation of the domain morphology from the morphology observed in the blanket film can be observed in the zigzag shaped devices (Fig. 6.9 panels **A** and **B**), the spokes of the wheel (Fig. 6.9 **C**) and in the vicinity of the edges shown in Fig. 6.9 **E** and **F**. These geometries all have either patterned edges along the magnetic easy axes (CuMnAs $[110]$, $[\bar{1}10]$) or along the magnetic hard axes (CuMnAs $[100]$, $[010]$).

The domain morphologies in the spokes of the wheel (Fig. 6.9 **C**) aligned with the magnetic easy axes vary dramatically from the domain morphologies observed in spokes aligned with the magnetic hard axes. However, a similar morphology as in the spokes along the hard axes is observed in the zigzag shaped device with similar edge orientation in Fig. 6.9 **B** and similar domain morphology as in the spokes along the easy axes is found in the zigzag shaped device in Fig. 6.9 **A** as well as in the vicinity of the edges with corresponding orientation in Figs. 6.9 **E** and **F**. Domain morphologies reminiscent of those close to edges along the magnetic easy axes can also be observed in areas of the ring-shaped device in panel Fig. 6.9 **H** and **H** and in parts around the inner and outer circle in panel **D**, whenever the curved edge roughly follows those crystallographic directions.

In contrast, the AF domains in the central area of the wheel (Fig. 6.9 **C**) and in the spike-device (Fig. 6.9 **G**) where the edges are not aligned with the crystallographic directions largely resemble the AF domain structure in the blanket film, despite the strong geometric confinement.

The examples indicate that the the impact of patterning on the AF devices depends primarily on the direction of the patterned edge of the device.

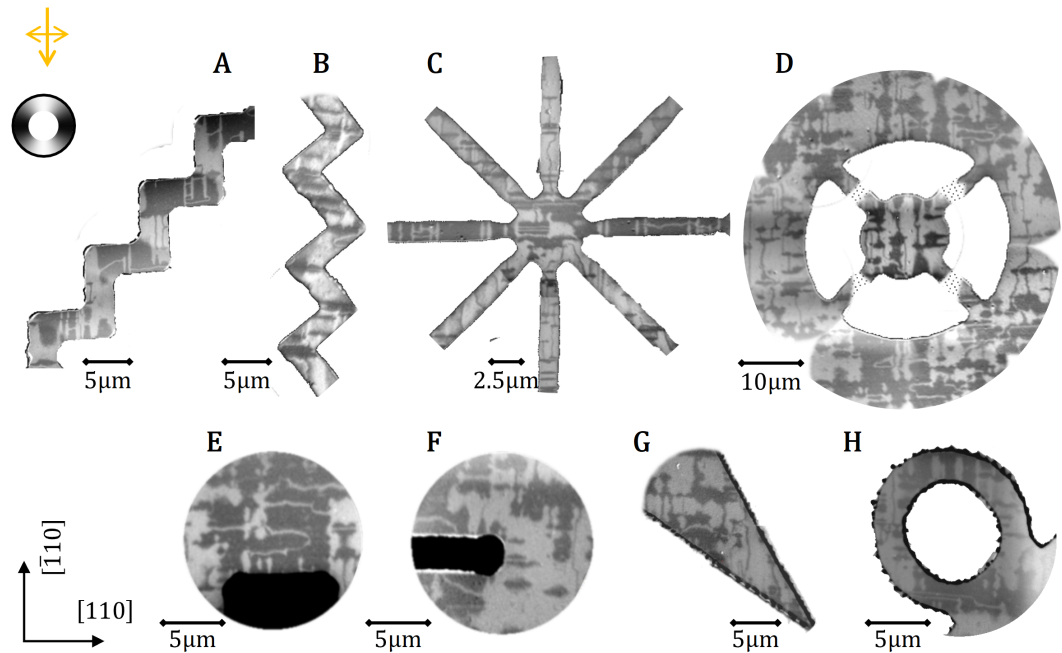


Figure 6.9: XMLD-PEEM images of AF domain structures in a variety of geometric devices fabricated from a CuMnAs/GaP film with micron-sized domains in non-patterned areas and moderate microtwin density (see reference Overview). The yellow arrow indicates the direction of the incident x-rays. The greyscale wheel indicates the local spin axis. The scaling varies between the panels as indicated by the corresponding scale bars. Rough, dark edges correspond to patterned edges. In **D** the dotted areas mark CuMnAs areas which have not been imaged. The black areas in **E** and **F** are the GaP substrate.

6.3.4 AF domain walls in the vicinity of edges

So far, the effect of patterned edges on the large-scale AF domain morphology and population has been considered. In the following the more subtle influence of the patterned edges on the orientation (alignment) and widths of antiferromagnetic domain walls is considered.

Domain wall alignment in the vicinity of edges In non-patterned areas (see chapter 5), 180° domain walls are found to either run along undulating paths without preferential direction or to form straight lines perpendicular to the spin axis orientation in the centre of the domain wall if confined between two neighbouring microtwins. A similar picture arises in patterned devices (see for example Figs. 6.3, 6.5 and 6.7). Yet, upon closer inspection it can be seen that in the direct vicinity of edges, 180° walls generally bend towards

the edge normal, as can be seen more clearly in Fig. 6.10 A. The figure shows close-up images of 180° domain walls terminating at a long-edge of bars aligned with the CuMnAs $[\bar{1}10]$. The alignment with the edge normal is typically lost within $1\ \mu\text{m}$. The examples shown here are domain walls where the alignment is kept relatively long as this allows to better see the angle with the patterned edge. Similar bending of 180° domain walls towards the surface normal has been observed in antiferromagnetic Cr_2O_3 single crystals and attributed to minimisation of the exchange interaction by normal incidence to surfaces [127], referenced to the derivation of this mechanism for ferromagnetic domain walls in [25]. The observations discussed here, in particular the fact that the bending of the domain walls towards the edge normal is limited to the close vicinity of the edge, confirm that the effect is a vicinity effect arising locally at the edge. Thus, the data are consistent with the interpretation suggested in [25, 127].

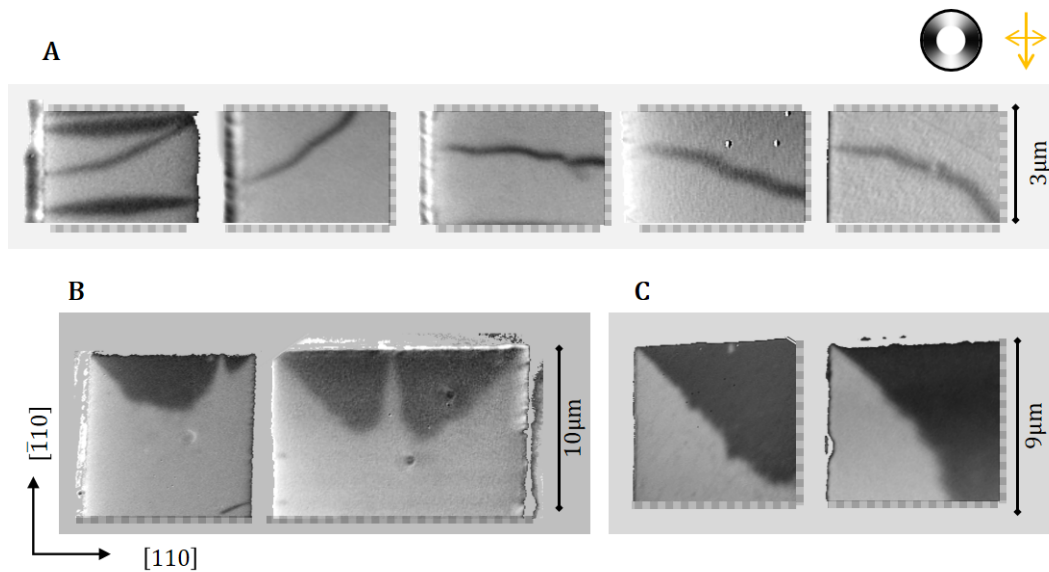


Figure 6.10: Domain wall orientation in the vicinity of edges **A:** XMLD-PEEM images of 180° domain walls terminating at a long edge of patterned bars (varying widths) oriented along the CuMnAs $[\bar{1}10]$. **B:** XMLD-PEEM images of 90° domain walls nucleating in the corners at the short-edges of patterned bars with similar orientation. The “gaps” in the dark end-domains result from vertical microtwin-defects. **C,** same as **B,** but in open corners. Grey-dotted lines mark edges of the X-PEEM images which are not patterned edges, but across which the film continues.

In contrast to 180° domain walls, 90° domain walls can only be observed at patterned edges if the edge forms a “T-junction” with a microtwin which re-

sults in the lens-shaped domains discussed in section 6.3.1, with one tip of the lens located at the junction. The lack of 90° domain walls at patterned edges without microtwins is a natural consequence of the observed preference for spin axis alignment parallel (perpendicular) to the edge for edges along the CuMnAs $[110]/[\bar{1}10]$ ($[100]/[010]$). For corners formed of two mutually orthogonal patterned edges, this, on the contrary, implies that the spin axis has to rotate by 90° in the area between the two edges. Indeed, for right-angled corners along the CuMnAs $[110]$ and $[\bar{1}10]$, a 90° domain wall is generally found to nucleate in the corner (see Fig. 6.10 **B, C**). For corners aligned with the CuMnAs $[100]$ and $[010]$ directions, the spin axis can vary more gradually (see e.g. Fig. 6.6) and the available data are not sufficient to draw a clear conclusion. Representative examples of right-angled corners along the CuMnAs $[110]$ and $[\bar{1}10]$ are shown in Fig. 6.10 **B, C**. The XMLD-PEEM images in Fig. 6.10 **B** show the closed, short edge of patterned bars, Fig. 6.10 **C** shows “open” corners formed by only two orthogonal edges. The corners in the bars and the open corners similarly show the nucleation of a 90° domain wall which locally forms an angle of 45° to the edges. The range of the alignment seems limited only by the presence of microtwin defects.

This, alongside the observation that the spin axis alignment in patterned bars along the CuMnAs $[110]$ and $[\bar{1}10]$ persists even in the widest bars studied, suggests that the effect of patterned edges along these directions is not limited to a vicinity (boundary) effect, but a long-range effect on the AF anisotropy.

6.3.5 AF domain walls as a measure of edge-imposed anisotropy

Directly addressing the question of whether patterned edges have a long-range effect on the AF anisotropy, requires a local probe of the magnetic anisotropy. As explained in section A and derived in many textbooks (see e.g. [25]), the widths of magnetic domain walls d_{DW} is a measure of the magnetic anisotropy

K . As such, spatial variations of the domain wall widths in a sample indicate spatial anisotropy changes. The inverse square root dependence between the domain wall widths and the magnetic anisotropy implies that even small changes of the domain wall widths indicate a strong change of the magnetic anisotropy. The functional dependence $d_{\text{DW}} \propto 1/\sqrt{K}$ is independent of the definition of the domain wall. Here, the domain wall width is measured by fitting the XMLD-intensity profile of linecuts across the domain wall, as explained in the following.

Phenomenological model The model assumes that the Néel vector rotates continuously across the wall, such that locally exchange and anisotropy energy are balanced. As shown in the appendix A, this assumption yields characteristic profiles for 180° domain walls in systems with uniaxial anisotropy and the profiles of 90° domain walls in systems with biaxial anisotropy.

Namely for 180° domain walls:

$$\theta - \theta_\infty = \text{acos}(-\tanh(\tilde{x}/d_{\text{DW}})) , \quad (6.1)$$

where θ is the angle of the Néel vector, θ_∞ the Néel vector orientation for $x \rightarrow -\infty$, $\tilde{x} := x - x_0$ is the distance from the centre of the domain wall and $d_{\text{DW}} := \sqrt{A/K}$ is the characteristic lengthscale of the rotation, the “domain wall widths”; and for a 90° using the same notation:

$$\theta - \theta_\infty = \text{acos}\left(\frac{1}{\sqrt{1 + \exp(2(\tilde{x}/d_{\text{DW}}))}}\right) . \quad (6.2)$$

XMLD-Intensity profiles In the XMLD-PEEM images, the contrast varies for x-ray polarisation along the CuMnAs [110] and [010] as

$$\begin{aligned} MLD_{[110]} &= a \cdot \cos^2 \theta + c \text{ and} \\ MLD_{[010]} &= \tilde{a} \cdot \cos \theta \sin \theta + \tilde{c}, \end{aligned} \quad (6.3)$$

with $a, c, \tilde{a}, \tilde{c}$ constants. This yields the following (expected) XMLD-intensity profiles:

180° domain wall :

$$MLD_{[110]} = A_1 \cdot (\tanh(\tilde{x}/d_{\text{DW}}))^2 + C_1, \quad (6.4)$$

$$MLD_{[010]} = \mathcal{A}_1 \cdot \frac{\tanh(\tilde{x}/d_{\text{DW}})}{\cosh(\tilde{x}/d_{\text{DW}})} + \mathcal{C}_1, \quad (6.5)$$

90° domain wall :

$$MLD_{[110]} = A_2 \cdot (1 - \tanh(2\tilde{x}/d_{\text{DW}})) + C_2, \quad (6.6)$$

$$MLD_{[010]} = \mathcal{A}_2 \cdot \frac{\exp(2\tilde{x}/d_{\text{DW}})}{\exp(4\tilde{x}/d_{\text{DW}}) + 1} + \mathcal{C}_2. \quad (6.7)$$

Note that the constants $A_i, C_i, \mathcal{A}_i, \mathcal{C}_i$ are different, and depend not only on the “real” XMLD-constants, but also on the image normalisation in experimental data.

The spin angle and XMLD-intensity profiles are visualised in Fig. 6.11. The figure also shows experimental intensity profiles retrieved from high-resolution XMLD-PEEM images and averaged over 10 linescans across a domain wall. Numerical fits of eqs: (6.4) to (6.7) are also shown. The good agreement of the data with the numerical fits validates the phenomenological model. The fitting routine uses $A_i, C_i, \mathcal{A}_i, \mathcal{C}_i, x_0$ and d_{DW} as fitting parameters and thus allows to estimate the domain wall widths.

Fitting protocol In this chapter, the domain wall widths as a function of distance to a reference (patterned edge or corner) is measured from XMLD-PEEM image. This is done stepwise for sections of a domain wall, following the protocol outlined below and illustrated in Fig. 6.12.

1. Choose a (flattened) XMLD-PEEM image with a domain wall

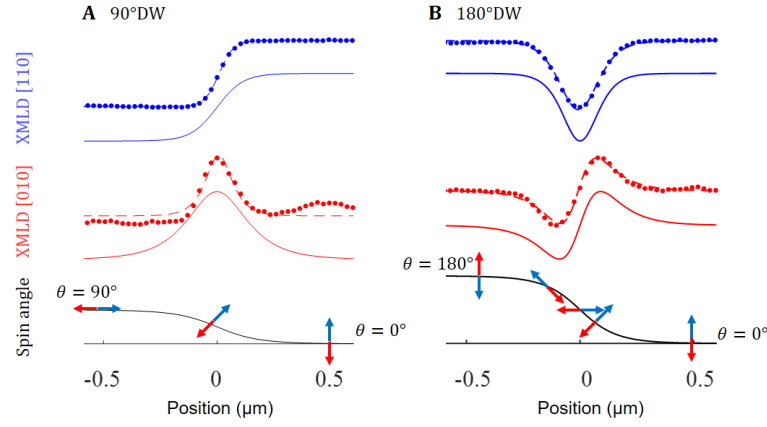


Figure 6.11: Simulated and measured domain wall profiles Visualisation of the domain wall profiles given and corresponding XMLD-intensity profiles. **A:** For a 90° domain wall. **B:** For a 180° domain wall. The solid black line depicts the rotation of the Néel vector (spin angle) across the wall, eqs. (6.1) and (6.2). The Néel vector at specific positions is also illustrated by the solid red and blue arrows at specific positions. The solid blue and red lines are the corresponding calculated XMLD intensity profiles, eqs. (6.4) to (6.7), for x-ray polarisation along the CuMnAs [110] (blue) and the CuMnAs [010] (red). The filled blue and red circles are experimental intensity profiles of domain walls measured in high-resolution XMLD-PEEM images of the 50 nm CuMnAs layer with the highest crystalline quality.

2. Trace a (section) of the domain wall on the image
 - (a) Manually define a line on one side of the domain wall, defining the start-points A_i
 - (b) For each point of the line, define a corresponding end-point on the opposite side of the wall B_i such that the connecting line $\overline{A_i B_i}$ is approximately aligned with the domain wall normal
 - (c) Retrieve line-profiles of the XMLD-image along $\overline{A_i B_i}$
 - (d) Fit the lineprofiles to the appropriate equation (from eqs. (6.4) to (6.7))
 - (e) From the values of x_0 calculate the corresponding pixel positions on the image, the array of the positions traces the domain wall (centre) on the image
 - (f) save the positions
3. Define reference position, *e.g.* patterned edge or corner

4. find domain wall widths d_{DW} , ensuring that the intensity profile is along the normal of the domain wall, (and distance to reference D). For each point on the domain wall:
 - (a) define series of lines centred at the domain wall position with various angles
 - (b) retrieve and fit the intensity profiles across all lines and choose cross-section with minimal value of d_{DW} , \rightarrow estimate for domain wall widths
 - (c) plot fit and with minimal d_{DW} and corresponding lineprofile, inspect visually to ensure that the fit is valid
 - (d) from corresponding x_0 , refine domain wall position
 - (e) calculate distance from reference

5. transform from image units (pixels) to real space (μm)

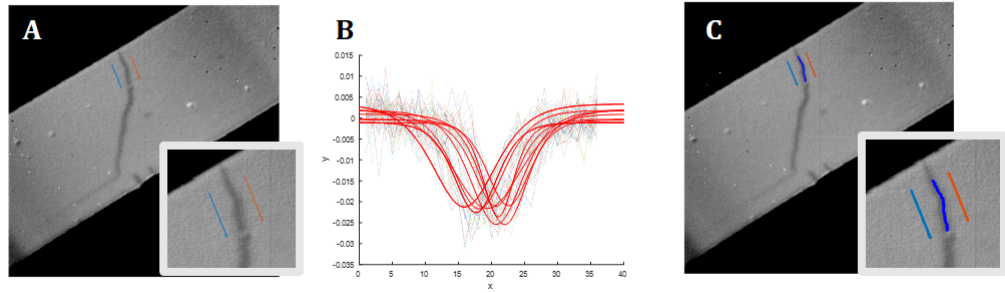
Steps 2-4 are realised with semi-automated matlab-procedures.

Results

Figure 6.13 illustrates measurements of the widths of three 180° domain walls in patterned bars which terminate at a long edge of the bar. 6.13 **A** shows the measured domain wall widths d_{DW} as a function of the distance D_{edge} to the nearest long edge of the bar, which is the edge at which the domain walls terminate. The XMLD-PEEM images corresponding to the datasets in Fig. 6.13 **A** are shown in panel **B**. The positions of the domain walls are marked by dotted lines with matching colour.

Close to the edges the width of the domain walls is around 100 nm. With increasing distance from the edge, the domain wall widths increase continuously and saturate between 150 nm and 250 nm in the centre of the bars. For three of the datasets the rise is almost monotonic. For the domain wall shown in the bottom panel of Fig. 6.13 **B** (blue dataset), an additional “kink” located

2. Trace Domain Wall



3., 4. Find D , d_{DW}

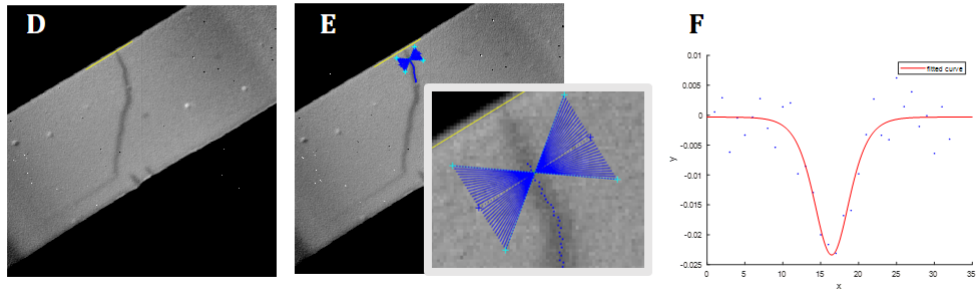


Figure 6.12: *Illustration of steps 2-4 of the protocol used to measure domain wall widths* **A:** Step 2.(a),(b); define startpoints and endpoints on either side of a domain wall section. **C:** Step 2.(e); pixel coordinates of centre on domain wall calculated from x_0 . **D:** Step 3. Define reference (here edge). **E:** Step 4.(a); Define lines centred at the domain wall point with various angles. Retrieve and fit intensity profiles for the cross sections (not shown). **F:** Step 4.(c); Plot the dataset and fit with minimal d_{DW} .

around $x/W_{\text{bar}} = 0.1$ can be observed. Comparison with the XMLD-PEEM image shows that the domain wall crosses a microtwin aligned parallel to the long edge at this position. Hence, the “kink” in the domain wall widths reveals the local anisotropy change due to the microtwin, which for microtwins parallel to the long edge will act in the same direction as the edge-imposed anisotropy, so that the microtwin locally enhances the uniaxial anisotropy. The size and width of the kink can give a qualitative estimate of the relative size and range of the two effects. The microtwin-induced anisotropy change seems to decay faster than the edge-imposed anisotropy. This is further evidence for the proposed coupling mechanism between microtwins and AF domains discussed in chapter 5, which attributes the coupling primarily to a local anisotropy change,

arising mostly from the magnetocrystalline anisotropy in the rotated lattice of the microtwin and not from magnetoelastic changes away from the microtwin.

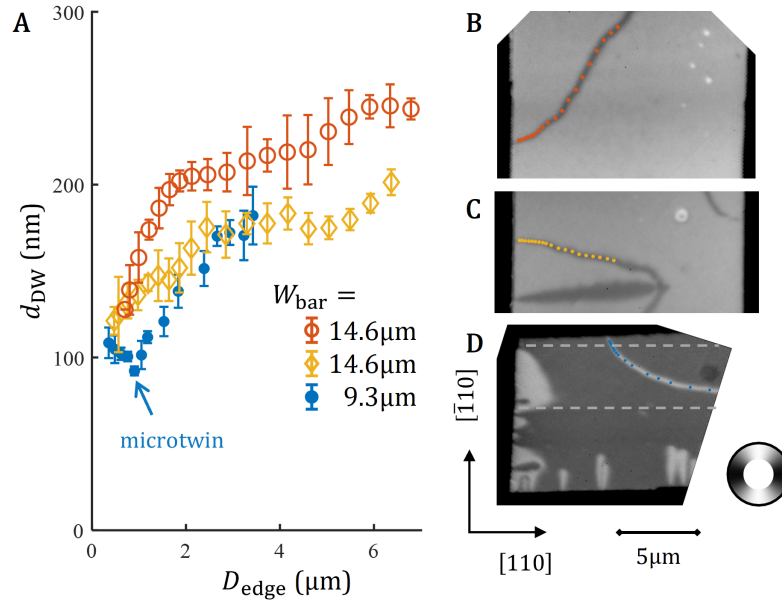


Figure 6.13: Spatial dependence of the edge-imposed anisotropy in patterned bars aligned with the magnetic easy axes. Dependence of the widths of 180° domain walls on the lateral position x in patterned bars. **A** Plot of the domain wall widths against distance from the edge D_{edge} . The different symbols correspond to different domain walls in bars of widths W_{bar} 9.3 μm and 14.6 μm . The yellow and orange symbols refer to two different domain walls in the same bar. Each datapoint is the average of all measurements within a given distance of the edge. The errorbar is given by the standard deviation of the measurements within the interval. **B** corresponding XMLD-PEEM images, obtained with $\vec{E} \parallel [110]$, with the positions of the domain wall measurements marked with corresponding colour. Dark edges are patterned edges, whereas the CuMnAs film continues across white edges. The dashed grey lines in the bottom image indicate the positions of two microtwins.

The increase of the domain wall width with distance from the edge occurs over several micrometers, much larger than the domain wall widths, which sets the lengthscale of effects which can be explained by direct AF exchange. This shows that the patterned edges alter the magnetic anisotropy not only in the direct vicinity of the edges, but over long distances.

In patterned bars, it seems evident that the effect of the long edges dominates and that the contributions of the two parallel edges enhance each other.

For two orthogonal patterned edges, as in corners, it is a priori not clear whether the effects cancel each other, resulting in no net change of the anisotropy,

or if, although the biaxial symmetry is not broken, the anisotropy is stronger than in non-patterned areas of the film. This is investigated in the following using 90° domain walls in patterned, right-angled corners.

The data shown in Fig. 6.14 **A** are obtained from three XMLD-PEEM images of open right-angled corners etched into the film with lowest microtwin density. Figures 6.14 **C** and **D** are XMLD-PEEM images of the same area, but imaged once with x-ray polarisation along the CuMnAs [110] and once with $\vec{E} \parallel [010]$. The domain wall widths are measured along the dotted lines in the XMLD-PEEM images and the results are plotted as a function of distance to the corner.

Despite considerable fluctuations, all datasets show a strong correlation: within the distance studied the domain wall widths roughly double from between 200 nm to 400 nm close to the corner to 500 nm to 900 nm.

The good agreement of the datasets for the same domain wall with different imaging configuration indicate that the fluctuations are most likely not purely noise from the measurement technique but show real variations of the domain wall widths likely to result from other types of defects which locally affect the magnetic anisotropy. Yet, the effect of the patterned edges can be clearly seen. The rising trend of the domain wall widths with distance to the corner is maintained even beyond the kinks and spikes which likely result from local crystallographic defects. This indicates that the patterning-induced anisotropy change is a long-range effect, propagating over distances of several μm and decaying with increasing distance from the corner.

The decreased widths of the 90° domain walls indicate that the patterning induced anisotropies add to and hence enhance the intrinsic anisotropy. Furthermore this dataset confirms that the long-range effects result from the patterned edges alone, and do not require geometric confinement, which fully justifies the term “edge-imposed” anisotropy instead of “shape-imposed” anisotropy.

Studies of lithographically-induced magnetic anisotropy in ferromagnetic thin film devices via magnetostriction [119, 120], the strain relaxation has been

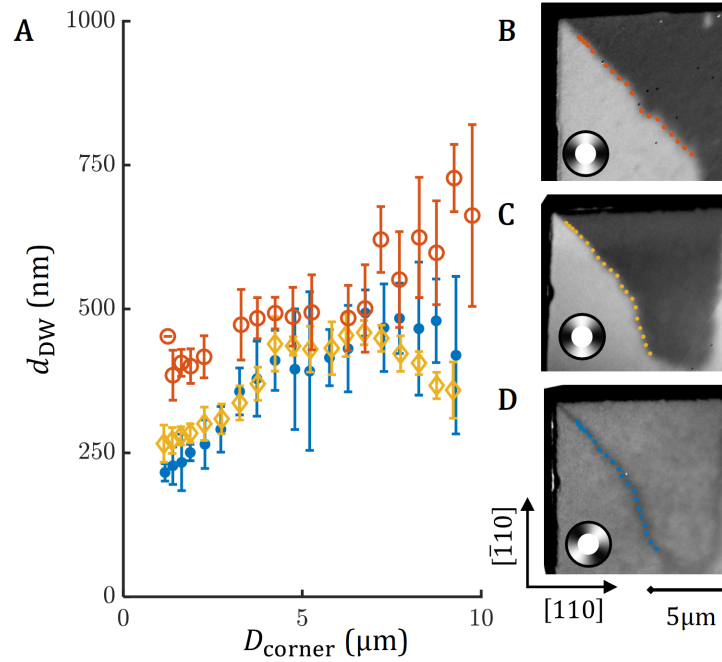


Figure 6.14: Spatial dependence of the edge-imposed anisotropy in right-angled corners aligned with the magnetic easy axes. Domain wall widths of 90° domain walls in patterned, right-angled corners as a function of distance from the corner. **A** Plot of the domain wall widths against the distance to the right-angled corner. Each datapoint is the average of all measurements within a given distance of the edge. The errorbar is given by the standard deviation of the measurements within the interval. The gap in the orange dataset is due to several dead pixel in the close vicinity of the domain wall in the X-PEEM image at that point. The yellow and blue datasets correspond to the same domain wall but imaged with $\vec{E} \parallel [110]$ (yellow) and $\vec{E} \parallel [010]$ respectively. **B** Corresponding XMLD-PEEM images with the positions of the domain wall corresponding to the datasets in **A** marked with dotted lines of matching colour. The top two panels are obtained with $\vec{E} \parallel [110]$, the bottom panel is obtained with $\vec{E} \parallel [010]$ yielding sensitivity to the spin axis as indicated by the greyscale wheel. The dark edges are patterned edges, whereas the CuMnAs film continues across the white edges.

considered independent of the magnetic order and the mechanism has been described as follows: The lithographic edges alter the strain relaxation, which changes the magnetic anisotropy. This explains effects within the range of significant strain relaxation, around 10 times the film thickness, consistent with what was observed experimentally.

In contrast, the data shown here show changes of the AF anisotropy over up to 200 times the film thickness. Conclusive data on the range of the lithographically-induced strain relaxation are not available for the CuMnAs/GaP, but it seems unlikely to exceed the range for similar materials ((Ga,Mn)As/GaAs,

$\text{Fe}_{81}\text{Ga}_{19}/\text{GaMnAs}$) by more than one order of magnitude [120]. This suggests that an explanation, which considers only the effect of changes of the elastic properties on the magnetic anisotropy, is not sufficient, but that the presence of magnetostriction also implies that the presence of (antiferro-)magnetic order affects the elastic properties, as discussed theoretically in reference [42, 122]. The authors consider the surfaces of the AF sample as a separated phase elastically conjugated with the bulk. Strains are considered to arise within the bulk due to magnetostrictive coupling and additional tension. The authors show that it is the incompatibility of the surface and bulk strains, which leads to long-range mechanical stresses. Hence, even if direct strain relaxation is limited to a narrow region at the edges, magnetoelastic coupling within the film can transfer the effect over long-ranges.

6.4 Summary and conclusion

This measurements shown in this chapter have revealed that the AF domain structure in CuMnAs thin film devices can differ considerably from the domain structure in blanket films. The effects have been found to originate at the patterned edges. The patterned edges affect the antiferromagnetic anisotropy over long-ranges, which can be described as an edge-imposed anisotropy which decays with distance from the edge. The edge-imposed anisotropy is found to be strongest for edges along the CuMnAs $[110]$ and $[\bar{1}10]$, matching the symmetry of the magnetic anisotropy in blanket films. For this configuration the spatial dependence of the edge-imposed anisotropy change has been investigated using domain wall widths as a probe of the local magnetic anisotropy. In this case, the edge-imposed anisotropy acts to favour spin alignment parallel to the edge, whereas patterned edges along the CuMnAs $[100]$ and $[010]$ favour spin alignment perpendicular to the edge. The opposite effects for edges patterned along different crystallographic directions are unequalled in ferromagnets, where shape (edge) imposed anisotropy is dominated by mag-

netic stray field minimisation. However, it has also been observed in micro- and nanostructures fabricated from antiferromagnetic LaFeO₃ thin films [123]. In patterned devices, the AF domain structure results from the competition of the edge-imposed anisotropy with the effect of microtwin defects. In the vicinity of edges along the CuMnAs [100] and [010], this results in a frustrated domain morphology with more gradual spin variation, whereas it leads to the formation of characteristic lens-shaped domains in the vicinity of edges along the CuMnAs [110] and $\bar{1}10$. The size and range of the edge-imposed anisotropy changes has largely been limited to a qualitative description. The effect of patterned edges along the CuMnAs [100] and [010] directions was found to be limited by the nearest microtwins, whereas the effect of edges along the CuMnAs [110] and $\bar{1}10$ has been shown to propagate beyond microtwin defects. Further analysis of the characteristic lens-domains at these edges, combined with micromagnetic simulations, might well allow to quantitatively determine the relative size and range of the effect of the patterned edges compared to the effect of microtwins, but is beyond this work.

Nevertheless, the domain wall widths measurements clearly show that the effect of patterned edges along the CuMnAs [110] and $\bar{1}10$ is not a local, vicinity effect, but long-range effect on the AF anisotropy. Local changes of the magnetic anisotropy at the boundary can have multiple origins, like small uncompensated AF moments at the surface or chemical changes, but these cannot explain the observed range of the effect exceeding several micrometers. In contrast, long-range forces have been shown theoretically to result from incompatibility of surface and bulk strains in magnetostrictive materials [42, 122]. Hence, the data can be seen as evidence for the theoretical model, but only a combined theoretical/experimental study including micromagnetic simulations can give strong evidence and demonstrate the predictive power of the theory.

Additionally, relevant for applications, this chapter shows, how different, domain morphologies can be realised by choosing suitable device geometries and microtwin-configurations. Particular for electrical devices based and SOT-

switching, the observed reversal of the sign of the edge-imposed anisotropy depending on the orientation of the patterning with respect to the crystallographic axes allows to realise either spin axis alignment parallel to the current or spin axis alignment perpendicular to the current. This allows to achieve maximal torque either on domains or on domain walls. Similar sign-reversal has been observed in another AF material [123], but is unprecedented in ferromagnets where shape-imposed anisotropy is dominated by stray-field minimisation. This highlights the versatility of AF materials compared to their FM counterpart.

Changing the device geometry is straight-forward, choosing the microtwin-configuration might seem more challenging. Encouragingly, the films show a significant variation of microtwin-densities, the microtwin-configurations can be measured in the blanket films and specific areas of the sample can be chosen for device fabrication. Hence it seems possible to find parts of a layer with suitable twin configuration prior to fabrication. Yet, as will be shown in the next section, not only the AF domain structure, but also the microtwin structure can be influenced by patterned edges as will be shown in the following section.

Chapter 7

Magnetostructural kinetics in CuMnAs films

7.1 Introduction

The previous two chapters have revealed that the AF domain structure in CuMnAs thin films is highly sensitive to structural properties and crystallographic microstructure of the sample. The AF domain structure has been shown to be largely dominated by characteristic microtwin defects in a non-patterned, as-grown films, and to be strongly susceptible to patterning. In particular, edges along the CuMnAs $[110]$ and $[\bar{1}10]$ have a significant, long-range effect on the AF anisotropy. The effect was attributed to the edge-induced strain field, which affects the AF anisotropy via magnetoelastic coupling.

Although not explicitly stated, the AF domain structure has been considered to be in equilibrium, or at least in a steady state, corresponding to a local energy minimum. The kinetics of the domain formation during growth and patterning have not been investigated and seems experimentally unfeasible with the XMLD-PEEM imaging techniques, since neither growth nor patterning can be performed in-situ. Furthermore, precessional AF dynamics occur over timescales of picoseconds (THz-range), way faster than the standard acquisition time during XMLD-PEEM imaging. For AF domain wall motion,

theoretical studies predict high speeds of up to several tens of km/s [44], beyond the resolution limit of the XMLD-PEEM imaging technique.

However, as will be shown in this chapter, not only the AF properties of CuMnAs samples are susceptible to patterning, but also the defect structure. It will be shown that the CuMnAs samples respond to patterned edges along the CuMnAs [110] and $[\bar{1}10]$ by nucleating microtwins at the edges which grow perpendicular to the edge over the timescales of days to months at room-temperature. AF lens-domains nucleate and grow with the microtwins. Over months, the microtwin nucleation and propagation can change the AF domain structure dramatically and even reverse the domain population.

Similar magnetostructural changes are observed in temperature-cycles of blanket CuMnAs films. At slightly elevated temperatures, around 45 °C to 75 °C, the microtwins are found to grow over minutes, inducing fluid-like AF dynamics over similar timescales. At higher temperatures, around ~ 360 °C, the microtwin-density is found to reduce considerably. During cooling, the microtwins (re-)nucleate and grow, often in similar places. The magnetostructural dynamics occur in a similar temperature region during the cooling and heating part of the cycles. The data highlight that in antiferromagnets, the AF and structural properties cannot be decoupled.

7.2 Methods

Material and devices All data are obtained from 50 nm CuMnAs/GaP(001) films. They are a subset of the films which were studied in the previous two chapters 5 and 6. The measurements in the first part, section 7.3.1, are performed on devices fabricated by e-beam lithography and ion-beam milling from one chip of the Al-capped film with the highest crystalline quality. The measurements in the second part, section 7.3.2, are performed on two non-patterned samples (A and B), from different films capped with 30 nm As, then de-capped in ultra-high vacuum just prior to the measurements.

Surface preparation The As-capped samples are prepared to approximately 360 °C (pyrometer measurement of the surface with $\epsilon = 0.1$) for 20 min to 30 min which removes the As cap. The temperature is achieved by resistive heating of a tungsten filament located underneath the sample on the X-PEEM cartridge. The sample preparation is done in ultra-high vacuum ($\leq 5 \times 10^{-9}$ mbar). The prepared samples are then transferred in ultra-high-vacuum into the X-PEEM chamber, see section 2.9 for details.

X-PEEM measurements The AF domain structure is imaged using XMLD-PEEM imaging, see section 2.8.2 for the experimental protocol and sections 2.5.2 and 2.7 for further information.

The measurements of the Al-capped samples, section 7.3.1, are at room-temperature or when the sample environment is cooled to approximately 200 K. This cooling enhances the XMLD-signal, but no effect the AF domain structure has been observed.

Scanning X-ray diffraction microscopy (SXDM) The measurements of the microtwin configuration of Al-capped samples was measured with SXDM measurements using the CuMnAs 003 reflection. The shown SXDM intensity maps 63 days after sample fabrication are measured with the x-ray beam impinging along the CuMnAs [100] following exactly the procedure used in the previous two chapters, (see section 2.11.2). The measurements performed 3 months later (not shown explicitly) follow a similar procedure, but with the X-ray beam impinging along the CuMnAs [110].

Low energy electron microscopy (LEEM) LEEM-imaging in-situ in the X-PEEM chamber allows to obtain structural images and AF domain images of the same area. LEEM and X-PEEM imaging use the same electron microscope and only the illumination of the sample is changed. The LEEM images shown here are bright-field LEEM images with positive start voltage (~ 15 V) to reduce surface contrast and enhance “bulk” sensitivity to the microtwin defects.

For details see section 2.9. LEEM imaging requires exposed surfaces, hence is not possible on the Al-capped samples. Furthermore, problems prevented LEEM measurements on sample A.

Temperature cycles In the measurements presented in the second part of this chapter, section 7.3.2, the sample temperature is raised using the same tungsten filament heater on the cartridge as during surface preparation. Different temperatures can be achieved by varying the filament current and allowing for sufficient time to stabilise. This mostly heats the sample stage and only slightly the rest of the experimental set-up (including the microscope). Cooling is limited to heat dissipation after the filament current is reduced or switched off. No active cooling is available. For sample B, the temperature was measured with a thermocouple attached to the sample plate. However, this is located further away from the filament than the sample and has been found to significantly underestimate the sample temperature when the filament current is increased quickly or above 1.1 A \sim 100 °C. In the absence of a different temperature measure, the thermocouple reading is referred to as a guide. Read-out of the thermocouple was disabled during the measurements on sample A. Here, the temperature is estimated by repeating the heating protocol, and monitoring the thermocouple temperature afterwards. For sample B also the exact time of each LEEM or PEEM image is recorded, whereas for sample A only the time of the beginning and order of image series are known. The measurements consist of several heat-cycles in which the sample is heated over 40 min to 60 min from room-temperature to the point where the As cap evaporated during the surface preparation of the sample, estimated to be 360 °C but definitely beyond 260 °C which is 50 °C above the Néel temperature. The filament current is increased step-wise, with enough time for the temperature to stabilise at 0.5 A, 0.75 A and 1 A, then the filament is raised quickly to 1.6 A. The corresponding temperature ranges are referred to as “intermediate-low”, “intermediate”, “intermediate-high” and “high” in the following. The samples

are left at high temperatures for a minimum of 10 min, before the filament current is switched off and the sample left to cool down.

7.3 Results and interpretation

7.3.1 Patterning-induced magnetostructural kinetics

In the previous chapter, it has been shown that microtwins located at patterned edges result in lens-shaped AF domains oriented perpendicular to the edge. However, rather than being stationary, the lens domains associated with microtwin defects are observed to nucleate at the patterned edges and then propagate across the bar over a timescale of days at room temperature. A typical example is shown in Fig. 7.1 **A-D**, showing the growth of lens-domains in a $80 \times 10 \mu\text{m}$ bar fabricated from the layer with lowest microtwin density measured 5, 13 and 33 days after patterning. Between the measurements, the sample was stored in vacuum at room temperature. One large lens-domain crosses the whole width of the bar in all the images, while three domains nucleate and propagate from the left side of the bar. Microtwins, measured with SXDM (see section 2.11.2) 63 days after patterning, are consistent with the observed domain growths (Fig. 7.1 **E**). SXDM measurements performed another three months later, have confirmed that the microtwin growth continues until the twins extend across the whole width of the bar.

The example shown in Fig. 7.1 illustrates the rule and not the exception of post-fabrication changes in patterned devices with edges along the CuMnAs $[110]$ and $[1\bar{1}0]$. Similar changes have been observed in bars ranging between $2.5 \mu\text{m}$ and $20 \mu\text{m}$ width, fabricated by e-beam or photolithography from different layers. Initially the bars are nearly single domain with spin axis parallel to the long edge, with only a small number of lens-domains presumably resulting from microtwins which were present before patterning. The microtwins nucleate at the edges and grow towards the opposite edge, accompanied by AF

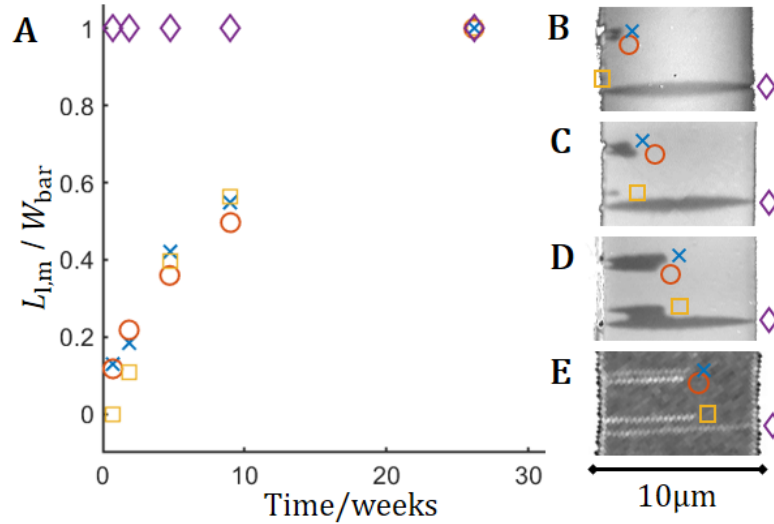


Figure 7.1: *Magnetostructural kinetics in CuMnAs in patterned bars.* **A:** Lens-domain and microtwin lengths, relative to the bar width, as a function of time after patterning in a $10\ \mu\text{m}$ wide bar. Each symbol represents a particular lens-domain. **B-D:** Corresponding XMLD-PEEM images 5 (**B**), 13 (**C**), 33 (**D**) days after patterning. **E** SXDM map of the microtwin configuration 63 days after device fabrication.

domains. The nucleation and growth of the microtwin-induced minority lens-domains can ultimately lead to a reversal of the average domain population. One example of such a significant change can be seen in Fig. 7.2 A. The panel shows XMLD-PEEM images of a $\sim 60\ \mu\text{m}$ long section of an $80\ \mu\text{m} \times 5\ \mu\text{m}$ sized bar taken 5 days (top) and 33 days (bottom) after device fabrication. Although recognisably the same bar and some parts have remained largely unchanged, other areas show a dramatic increase in the number of lens-domains, reversing the domain population from almost fully aligned with the long edge to primarily aligned perpendicular to the long edge.

The nucleation of lens-domains is not limited to the long edge of the bar, but also occurs at the short edge, as can be seen in Fig. 7.2 B-D, which breaks up the end-domains located at the short edge. Figure 7.2 B-D also show further examples of lens-domain nucleation and growth at the long edge. Typical for our measurements, the number of additional lenses is highest in the thinnest bar, but does not vary monotonically with increasing bar-widths.

It is known from material science that microtwins can form in response to

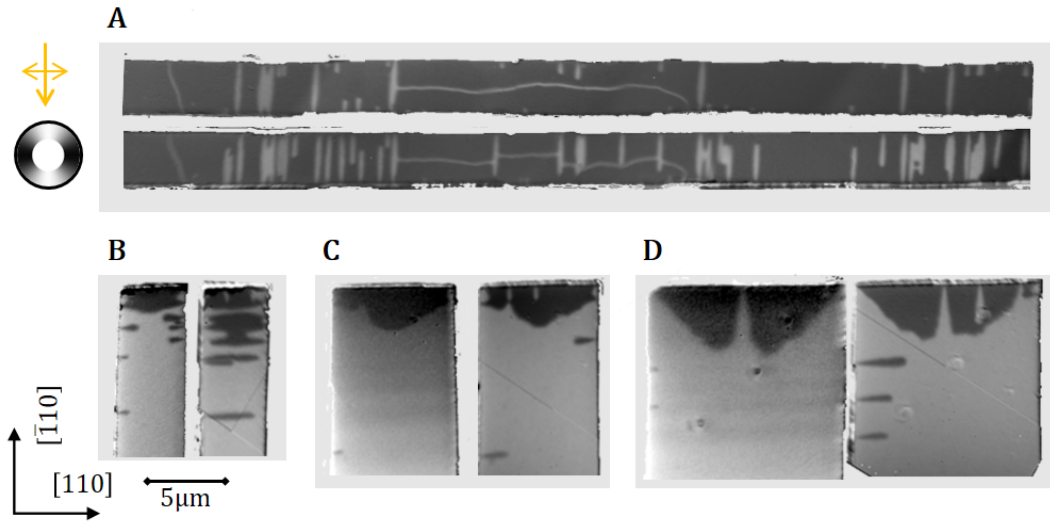


Figure 7.2: *Examples of the progression of AF domain structures in patterned bars* AF domain structure in four representative areas, measured in XMLD-PEEM 5 and 33 days after device fabrication respectively. All devices were fabricated from the layer with lowest microtwin density. **A:** $\sim 60 \mu\text{m}$ long section of an $80 \mu\text{m} \times 5 \mu\text{m}$ long bar. The image taken closer to fabrication is at the top. **B-D:** Closed ends of $5 \mu\text{m}$, $10 \mu\text{m}$ and $15 \mu\text{m}$ wide bars with orthogonal orientation, with the image taken closer to fabrication at the left.

strain, either during thermal annealing or externally applied [112, 128], and for blanket CuMnAs films, it has been suggested that the twins relax the strain resulting from the mismatch between the film and substrate lattices [46]. Thus, it seems natural that the microtwin nucleation and growth in patterned bars is the samples' intrinsic response to the patterning induced strain and the edge roughness only matters since it can provide points with reduced energy for twin nucleation.

In patterned bars along the CuMnAs $[110]/[\bar{1}10]$, the uniaxial strain can be expected to match the direction along which microtwins can relax strain. This is not the case for bars oriented along the CuMnAs $[100]$ and $[010]$ directions. Consistently, no additional microtwin nucleation after device fabrication has been observed in $\langle 110 \rangle$ oriented bars, and also the AF domain structure has been found to be largely stable over months. One example of the AF domain structure in a $50 \mu\text{m} \times 30 \mu\text{m}$ sized bar oriented along the CuMnAs $[100]$ is shown in Fig. 7.3. The XMLD-PEEM image taken 5 days after device fabrication (panel A) and 3.5 months after device fabrication show only minor

changes, although the sample has not been stored in vacuum and even been imaged in SXDM in between¹. The most notable changes are the reduced sizes of the white area close to the open-edge of the bar and the reduced size and disappearance of the curved 180° domain walls in the top half of the bar. The 180° domain walls are considered to be purely magnetic objects and have generally been found to be, unless highly confined between two microtwins, very mobile features which can show spontaneous fluctuations during X-PEEM imaging. The different behaviour depending on the crystallographic orientation of the device edges is clear evidence that the magnetostructural kinetics indeed result from the patterning-induced strain.

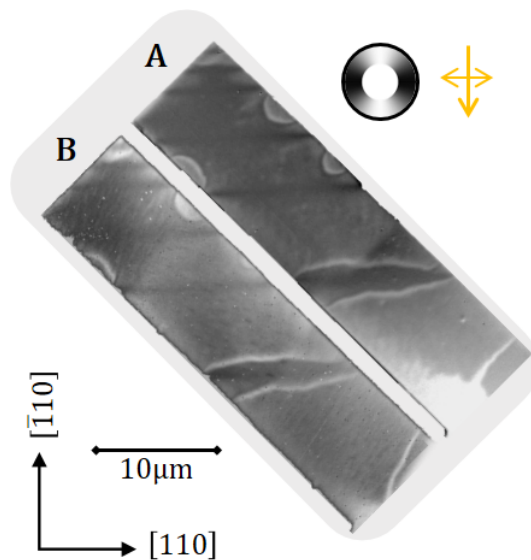


Figure 7.3: Comparison of the AF domain structure in a bar oriented along the CuMnAs [100] 5 days and 3.5 months after device fabrication **A:** XMLD-PEEM image taken 5 days after device fabrication. **B:** Same bar imaged 3.5 months later.

Patterning is only one way to change the strain state in a sample. Further mechanisms include externally applied strain or temperature changes, since film and substrate can be expected to have different thermal expansion coefficients. The first might be important, when strain-mediated switching, e.g. for magnetic memory, is attempted, but is not discussed here. The latter, however, is relevant not only during material growth and the initial formation of the AF domain structure, but also in electrical measurements in which Joule-

¹*i.e.* the sample was dismantled from the PEEM cartridge in England, travelled to Sweden, measured in SXDM, travelled back, remounted on a PEEM cartridge and imaged again in X-PEEM.

heating can lead to significant temperature changes and gradients in a device. Thus, the next part focuses on the effect of heating on the AF domains and microtwin defects of the CuMnAs films.

7.3.2 Heating-induced magnetostructural kinetics

XMLD-PEEM measurements of temperature cycles in which the film is heated beyond $\sim 80^\circ\text{C}$ are limited to CuMnAs films without an Al cap, since the surface of the Al capped films becomes too rough for XMLD-PEEM imaging, most likely due to a thermally activated interface reaction. The data presented in the following are obtained from exposed surfaces of 45 nm CuMnAs/GaP(001) films, which were prepared as explained in section 2.9.1. The exposed surface is rough with many step edges, which can overlay the magnetic contrast in the X-PEEM images.

This section reports on observations from two similar samples prepared in the same way. Sample A was only imaged in X-PEEM during the temperature cycles. This sample reveals dynamic changes at intermediate temperature and shows semi-reversible AF domain structures in temperature cycles through the Néel temperature. In the second sample, sample B, both the magnetic AF domain configuration and the microtwin pattern was studied during the heat cycles and direct evidence of the interpretation as magnetostructural changes is found.

Observation of AF domain changes during heat cycles, Sample A

Figure 7.4 illustrates AF domain reconfigurations observed in a, randomly chosen, but typical area of a prepared surface upon heating from room-temperature to approximately 100°C over ~ 25 min. The changes can best be seen in the time-lapsed movie of the XMLD-PEEM images recorded during the heating, supplementary video S3 available here short.at/awAU9. Figure 7.4 shows selected frames of the movie with corresponding timestamp of the measurement.

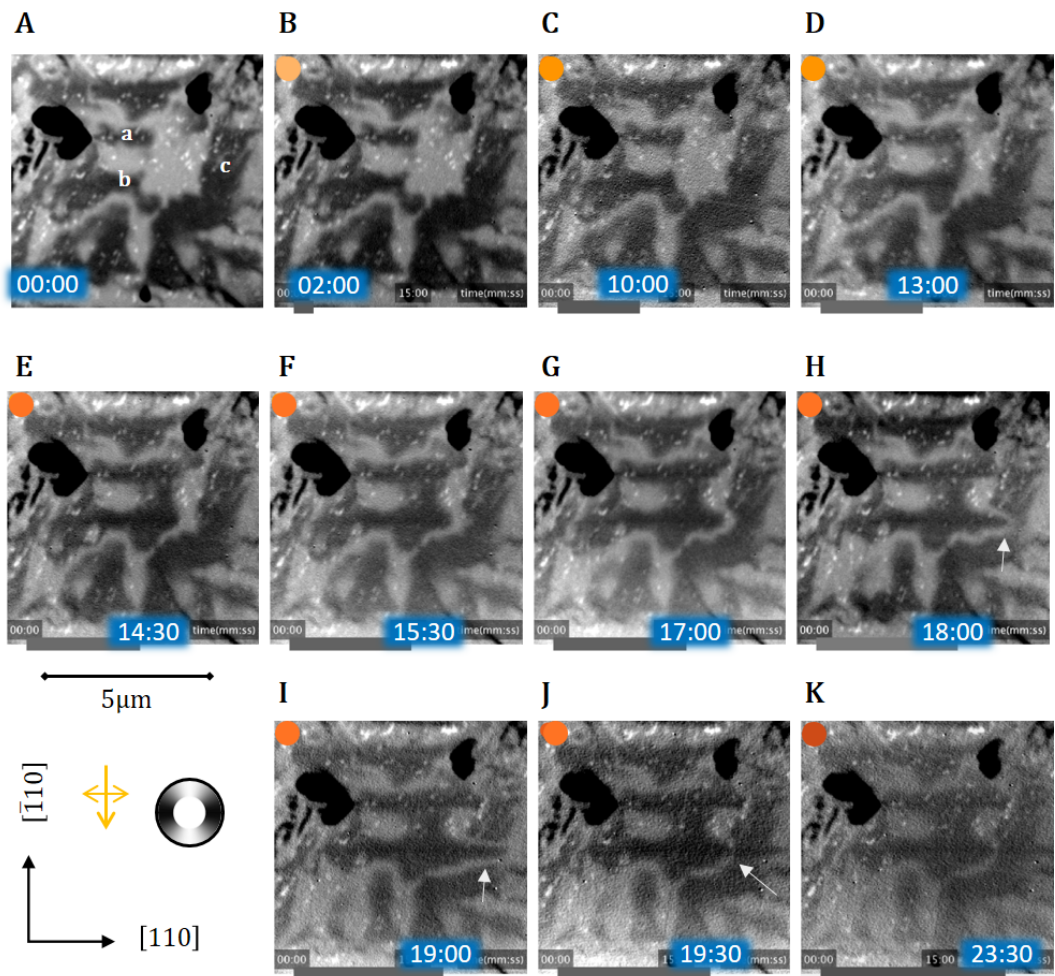


Figure 7.4: *Time-series of XMLD-PEEM images of the AF domain structure during heating, Sample A cycle I. A Initial domain configuration at room temperature. The small letters are used to label three domains. B-K XMLD-PEEM images during heating. The approximate time (in minutes:seconds) between the measurement and the switching on of the heating filament current is indicated in the blue boxes. Between D and E the filament current was increased from 0.5 A to 0.75 A. The coloured circle serve as a guide to indicate the temperature rise, from light-yellow room-temperature to dark red at the highest temperature. Between J and K the filament current was increased to 1 A. The white arrows intend to guide the eye towards the separation of domain b and c. A time-lapsed movie of all XMLD-PEEM images recorded during the heating can be found in supplementary video S3 available here short.at/awAU9.*

The initial AF domain configuration at room-temperature is shown in Fig. 7.4 A. The area shows a typical domain structure for 45 nm CuMnAs/GaP(001) films, with micron-sized domains aligned with the CuMnAs [110] (dark) and $[\bar{1}10]$ (light) directions. The black patches are areas where significant AsO_x is left on the surface. The CuMnAs film underneath is expected to be intact, but hidden due to the surface sensitivity of the PEEM measurements. The very

bright roughly circular dots are a different defect on the surface of unknown origin. Initially, the central area shows a large light domain and two horizontally aligned dark domains, labelled **a** and **b**. At the right, the light domain adjoins a vertically aligned dark domain labelled **c**. Upon heating to $\sim 30^\circ\text{C}$ to 45°C ($I_{\text{fila}} = 0.5\text{ A}$), the two domains **a** and **b** grow horizontally towards domain **c**. In panel **D** of Fig. 7.4 the **a** and **b** merge vertically in one area.

Upon further temperature increase to $\sim 50^\circ\text{C}$ to 65°C ($I_{\text{fila}} = 0.75\text{ A}$), Fig. 7.4 **E-K**, domain **b** grows faster, but remains clearly separated from domain **c** by a white channel, interpreted as a 180° domain wall and marked with the white arrow. Domain **b** continues growing at the expense of domain **c**, which retracts. In Fig. 7.4 **I** it splits into two domains separated by domain **b** with 180° domain walls on either side (indicated by the white arrow in Fig. 7.4 **I**). Additionally, between two frames, Fig. 7.4 **I** and Fig. 7.4 **J**, the two 180° domain walls are found to merge (white arrow in Fig. 7.4 **J**) and the two halves of **c** merge again. In contrast to the slow domain growth this occurs beyond the timescale of the XMLD-PEEM images and looks instantaneous in the time-lapsed movie.

When the temperature increases to $\sim 100^\circ\text{C}$ ($I_{\text{fila}} = 1\text{ A}$), Fig. 7.4 **K**, the XMLD contrast starts fading.

To reset the AF domain configuration, the sample was heated to $\sim 300^\circ\text{C}$ to 360°C which is more than 75°C above the Néel temperature of tetragonal CuMnAs. Upon cooling back through the Néel temperature, the AF domain structure reforms, as shown in Fig. 7.5. The first image of the time-series, Fig. 7.5 **A**, is measured while the sample is still heated. As expected, the image shows only structural and no magnetic contrast. Figure 7.5 **B-E** show XMLD-PEEM images recorded after the heating current was switched off and the sample cools slowly. Figure 7.5 **B**, recorded nearly 10 min later still shows no magnetic contrast. The first XMLD-PEEM image with measurable magnetic contrast, Fig. 7.5 **C**, already shows an AF domain structure largely reminiscent of the equilibrium configuration at room-temperature, with similar sized, or slightly larger AF domains. Domain nucleation as small domains and

subsequent coarsening dynamics were not observed and are likely to occur on timescales below the temporal resolution of the measurements.

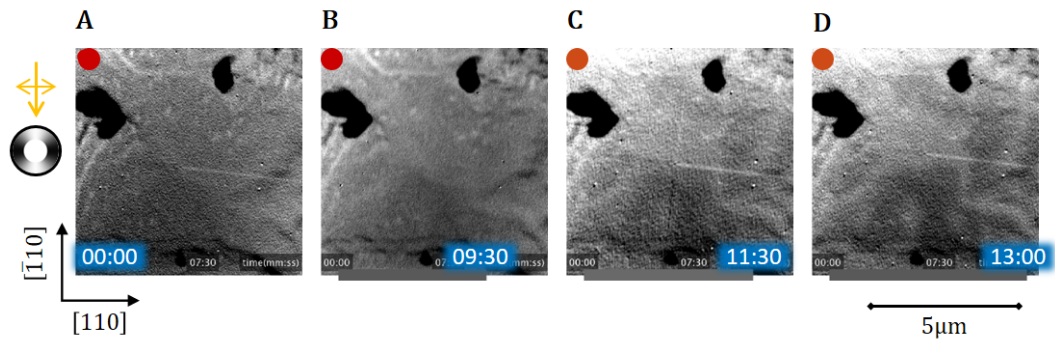


Figure 7.5: *Time-series of XMLD-PEEM images of the AF domain structure when cooling through the Néel temperature, Sample A cycle I. A XMLD-PEEM image of an area above the Néel temperature. No magnetic contrast can be observed. B-E XMLD PEEM images of the same area during cooling. The relative time (in minutes:seconds) between the measurement and the switching off of the heating filament current is indicated in the blue boxes. The sample was not cooled actively. The supplementary video S4 available here short.at/awAU9 is a time-lapsed movie of the entire dataset.*

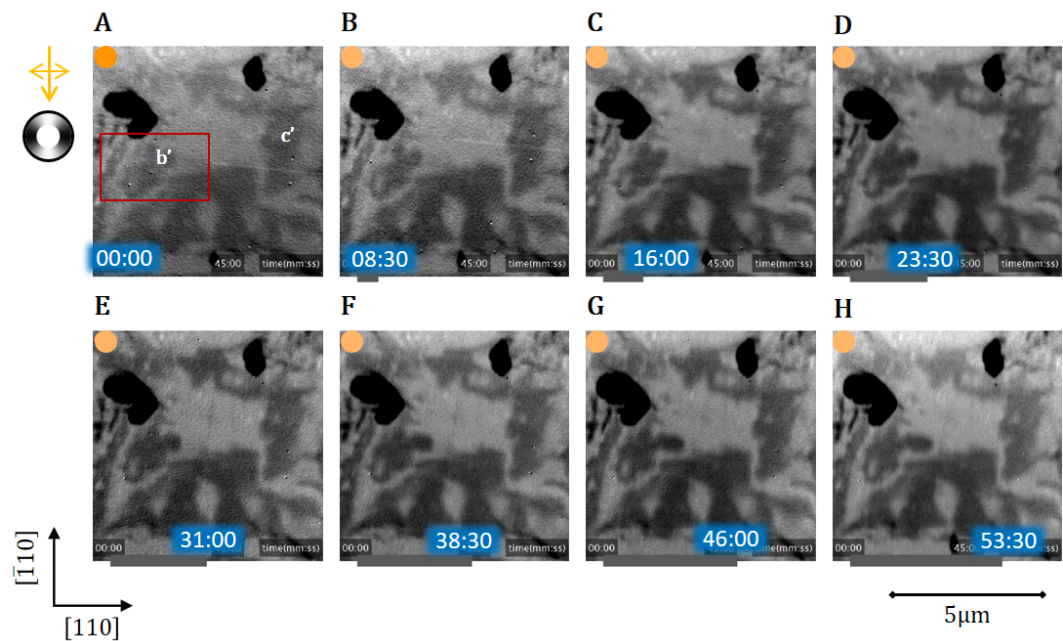


Figure 7.6: *Time-series of XMLD-PEEM images of the AF domain structure during cooling, Sample A cycle I. Continuation of the time-series shown in Fig. 7.5. Here, the relative time (in minutes:seconds), indicated in the blue boxes, is not measured relative to the switching off of the heating current, but with respect to the first image of the sequence. See also supplementary video S5 available here short.at/awAU9*

The AF domain structure in the area cooling down to $\sim 35^\circ\text{C}$ is shown in

Fig. 7.6. Most striking is the strong resemblance to the AF domain pattern measured before the sample before heating, Fig. 7.4 **A**, with nearly a one-to-one correspondence of AF domains of similar shapes in similar positions. The most notable changes are that, one of the two domains which grew in the first heating cycle (domain **a**) is missing and the other one (formerly **b**, now **b'**) is significantly smaller. The AF domain structure is found to be largely stable over approximately 1 hour. However, close inspection shows that in the area marked by the red rectangle, the dark domain **b'** grows horizontally.

Close-ups of this area are shown in Fig. 7.7. From top to bottom, the dark domain grows horizontally, covering about $0.5\ \mu\text{m}$ within the measurement time. The growth continues and accelerates when the sample is heated again, shown in Fig. 7.8. The area shown here and the one shown in in Fig. 7.4 overlap in most parts, but are slightly shifted with respect to each other. The dark kidney-shaped AsO_x patch can be used as a reference. The observed AF domain reconfigurations strongly resemble the ones in the first heat cycle. The dark domain **b'** grows follows mostly the same path as domain **b**. However, in this case domains **b'** and **c'** merge instead of remaining separated as in the first cycle.

Additionally a white domain, labelled **d'** in Fig. 7.8 **A** grows downwards, slowly at intermediate-low temperatures and faster at intermediate temperatures. The XMLD-PEEM contrast fades at intermediate-high temperatures, Fig. 7.8 **L** and disappears above the Néel temperature, Fig. 7.9 **A**.

Again, the AF domain structure that forms after cooling back across the Néel temperature, strongly resembles the one observed before heating with almost one-to-one correspondence of individual domains.

During cooling the domain labelled **b''** in Fig. 7.9 **B** grows almost along the same path as domain **b** and **b'** previously. This time, domains **b''** and **c''** do not merge but remain clearly separated. Domain **b''** grows at the expense of domain **c''**, which splits into two domains between Fig. 7.9 **J** and Fig. 7.9 **K**. This is strikingly similar to the dynamics observed of the domains **b** and **c** in

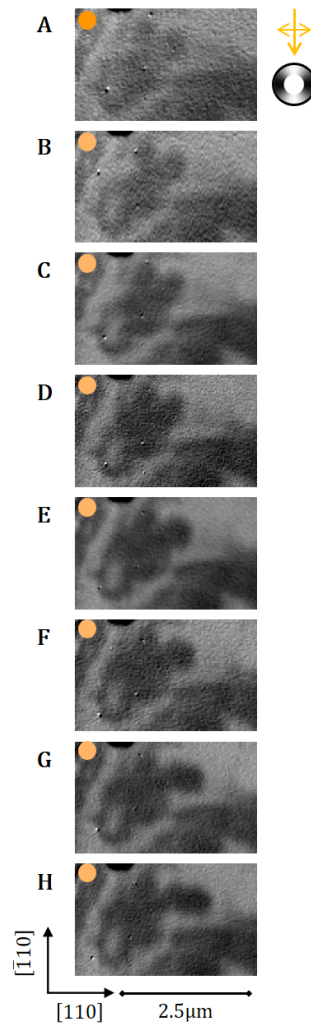


Figure 7.7: *AF domain growth during cooling, Sample A cycle I. A-H Same XMLD-PEEM images as in Fig. 7.6, but cropped to the area marked by the red rectangle Fig. 7.6 A.*

the first heat cycle, but different to what was found for domains **b'** and **c'**. A time-lapsed movie of the entire dataset can be found in the supplementary video S4 available here short.at/awAU9. The movie also shows several smaller changes, which will not be discussed in detail here, but are left for the reader to discover.

The data shown here are limited to a relatively short period of the cooling and the last frame in Fig. 7.9 does not show the steady state. Domain **b''** continued growing for over 8 hours after the filament current was switched off, but the growth slowed down considerably over the time.

In summary, the observations on sample **A** reveals the following features, discussed briefly below, during temperature cycling:

i) AF domains growing in a direction parallel to the spin axis of the domain over the timescale of minutes at intermediate temperatures 30 °C to 65 °C, faster at

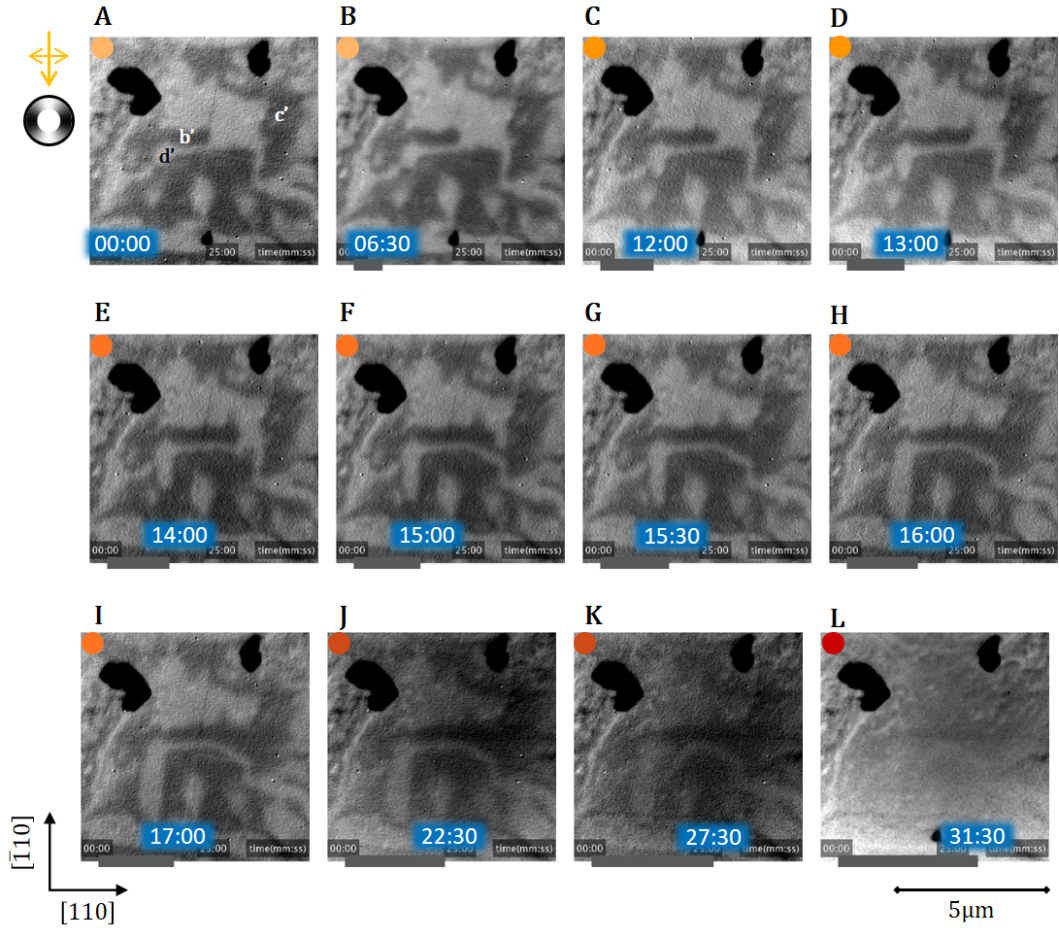


Figure 7.8: *AF domain changes during heating from 30 °C to > 100 °C, Sample A cycle II. Time-series of XMLD-PEEM images during heating, similar to Fig. 7.4. A-D intermediate-low temperatures ~ 30 °C to 45 °C ($I_{\text{fila}} = 0.5$ A). E-I intermediate temperatures ~ 50 °C to 65 °C ($I_{\text{fila}} = 0.75$ A), J, K: intermediate-high temperatures ~ 75 °C to 100 °C ($I_{\text{fila}} = 1$ A). L: Below the Néel temperature, but close to where XMLD contrast disappears ($I_{\text{fila}} = 1.2$ A). Shown is nearly the same area as in Fig. 7.4, use the dark kidney-shaped AsO_x patch as reference. A time-lapsed movie can be found in the supplementary video S6 available here short.at/awAU9.*

higher and slower at lower temperature; ii) Interaction of AF domains with parallel spin axis, showing either domain merging or domain growth of one at the expense of the other domain; iii) 180° domain wall reconfigurations occurring between different frames; iv) Strong correlation of the AF domain structure before and after heating above the Néel temperature and domain growth along similar paths.

The timescale of the domain growth (i) is inconsistent with precessional AF dynamics, considered to happen approximately 10^{14} times faster (picoseconds

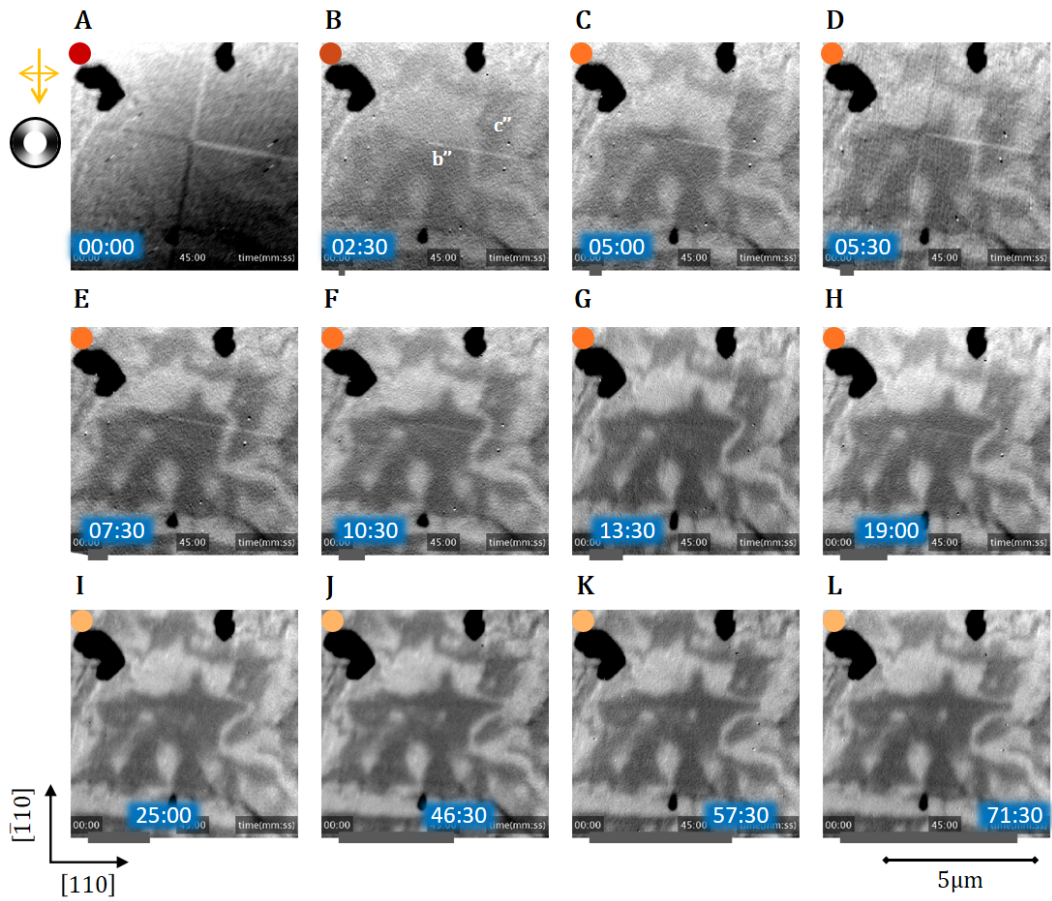


Figure 7.9: *AF domain reconfiguration during cooling, sample A, cycle II.* Continuation of the time-series of XMLD-PEEM images in Fig. 7.8, showing approximately the same area upon cooling. **A:** above the ordering temperature, no measurable AF contrast. **B:** around $\sim 100^\circ\text{C}$, faint AF contrast. **C-L:** Cooling from intermediate-high to intermediate-low temperatures. The coloured circle in each panel serve to indicate the temperature changes. The time is measured with respect to the first image in the sequence. The images are a subset of the frames of the time-lapsed movie supplementary video S7 available here short.at/awAU9. The straight lines are artefacts from the detector.

compared to minutes), or stimulated AF domain wall motion for which theory has predicted domain wall velocities in the order of km/s [44]. Experimental observation of AF domain wall motion with speeds of 0.3 m/s, 4 orders of magnitude slower than the theoretical prediction, but still 6 orders of magnitude faster than the observations shown here, were classified as domain wall creep, slowed down due to magnetoelectric coupling [129]. This indicates that the dynamics observed here are coupled to structural changes, which can happen over this timescale. Consistent with this interpretation is that the dynamics accelerate with higher temperatures. It is suggested that the domain growth

results from the growth of a microtwin in this direction, similar to the kinetics observed in the vicinity of edges. The observed directionality, parallel to the spin axis, matches the coupling between the twin orientation and the spin axis (see chapter 5).

The different interaction of domain \mathbf{b}' and \mathbf{c}' compared to \mathbf{b} , \mathbf{c} and \mathbf{b}'' , \mathbf{c}'' (ii) can be interpreted as follows. Domains \mathbf{b}' and \mathbf{c}' do not only share the same spin axis, but also have the same sign of the Néel vector. Thus they can merge, similar to lens-domains with matching orientation. In contrast, the domains \mathbf{b} and \mathbf{c} and domains \mathbf{b}'' and \mathbf{c}'' have opposite sign (antiparallel Néel vector) and remain separated by a 180° domain wall.

The reconfiguration of 180° domain walls (iii) occurs on faster timescales than the temporal resolution of the X-PEEM imaging, as can be expected for purely magnetic rather than magnetostructural dynamics. Similar 180° domain wall motion has also been observed spontaneously during imaging in several samples. Here the domain wall is shorter after the movement, which reduces the exchange energy. Both positions are consistent with the same microtwin configuration.

The strong correlation of the AF domain structure before and after heating beyond the Néel temperature (iv) could suggest that the sample was heated insufficiently and the AF order had not been wiped out completely. However, this seems unlikely since the sample was heated beyond the evaporation temperature of AsO_x which is more than 50°C above the Néel temperature of CuMnAs . Additional evidence is that the relative orientation of domains \mathbf{b} and \mathbf{c} reverses, from parallel to antiparallel (and vice versa in the second cycle). A more likely explanation is that the AF domains are strongly dictated by structural features, presumably the microtwins, present before and after heating. Yet, observation (iii) shows only the axis is pinned and not the orientation. This is further evidence for the proposed coupling mechanism between microtwins and AF domains given in chapter 5. However, the observation that also domain growth occurs along similar ways, and that domain \mathbf{a} “disappears”

and that domain \mathbf{b}' is (initially) shorter than domain \mathbf{b} can only be explained if it is assumed that the microtwins can annihilate at high temperatures.

Summarizing we suggest that observations (i) and (iv) are directly coupled to microtwins and microtwin dynamics in the sample, whereas observations (ii) and (iii) arise only from the sign of the Néel vector, a degree of freedom of the AF domains which is not related to the structural defects.

The following section shows direct evidence of the suggested magnetostructural interpretation of the dynamics.

AF dynamics and microtwin dynamics during temperature cycling

The following describes experiments which aim to prove two hypotheses of the magnetostructural model suggested above, namely i) Direct correlation of AF domain reconfigurations to the growth of microtwins at intermediate temperatures; ii) Annealing of microtwins at high temperatures.

This is done by combining AF domain imaging during temperature cycles with LEEM imaging of the microtwin pattern in a following experiment. The measurements are performed on a chip of a similar 45 nm CuMnAs/GaP(001) film prepared in the same way (see section 2.9.1). The sample shows slightly smaller AF domains, which is attributed to a higher microtwin density in this sample. The indicated timestamps below are reliable. The indicated temperature refer to the temperature measured by a thermocouple in the vicinity of the sample, which has been found to underestimate the temperature considerably, up to 100 °C at high temperatures.

The following addresses the hypotheses in reverse order.

Annealing of microtwins at high temperatures To investigate the effect of high temperatures on the microtwin configuration, heating of a (previously) prepared 50 nm CuMnAs/GaP film was imaged in LEEM.

Measurements of the effect of high temperatures on the microtwin configuration, as observed by LEEM imaging, are shown in Fig. 7.10. In the LEEM

images, the surface terminations of the microtwins show up as horizontal and vertical lines. Dark lines with different orientation are step edges. Larger dark patches are residual, amorphous AsO_x .

Figures 7.10 **A** and **B** compare LEEM images of the stationary configuration, measured at intermediate-high temperatures (**A**) and at high temperatures (**B**) in a typical area. The sample was left to stabilise at each temperature for at least 20 min and the configuration was found to be stable for at least 10 min.

The indicated temperature refers to the thermocouple measurement, which is known to underestimate the sample temperature significantly in this temperature regime. The measurement temperature of Fig. 7.10 **A**, intermediate-high temperatures, is slightly higher than the temperature where magnetic contrast is lost in the XMLD-PEEM image, although the thermocouple measurement of 137°C is below the Néel temperature of CuMnAs . Figure 7.10 **B** was obtained at the temperature where the As-cap evaporates, presumably beyond 250°C , although the thermocouple measures only 178°C . Figures 7.10 **A** and **B** are the average of 15 individual frames taken with 5 s exposure each.

The LEEM image of the stationary configuration at intermediate high temperatures (Fig. 7.10 **A**) shows a very dense microtwin pattern. Each microtwin is found to terminate at another twin, at a step edge or disappears under an AsO_x patch. The following LEEM image at high temperatures is considerably more blurred although attempts were made to achieve the best focus, but LEEM imaging at high temperatures is challenging (see section 2.6.1). It seems as if the number of microtwin lines has decreased significantly. However, due to the blurriness of the image at high temperatures, the two images are difficult to compare. Evidence for the hypothesis that indeed the number of microtwins reduces at high temperatures from LEEM measurements, requires measurements of changes of the microtwin configuration for fixed imaging conditions and resolution. Due to the intrinsic sensitivity of LEEM imaging to the temperature this cannot be obtained from measurements of the station-

ary state at two different temperatures, but only by imaging the dynamical behaviour at a fixed temperature, before the microtwin pattern has had time to stabilise. Attempts to image the dynamics, occurring between the measurements of Fig. 7.10 **A** and Fig. 7.10 **B** are shown in Fig. 7.10 **C**. The panel shows a time-series of LEEM images cropped to a selected area of the sample measured at almost stationary temperatures. The corresponding area in Fig. 7.10 **A** and **B** is marked with a red rectangle. Each image shown in **C** is an average of 4 LEEM images with 5 s exposure time. Two neighbouring images were measured with a gap of 10 s. The yellow ovals in panel **C** encircle microtwins which are observed in the first image of the sequence, but which are significantly shorter or fully absent in the last image of the sequence. Contrast disappears selectively on parts of the microtwin, whereas the contrast on other twins in the imaged area or the surface topography in the close vicinity of the twin remains unaffected. This can even better be seen when comparing the individual (5 s exposure) frames of the full dataset in the supplementary videos S8a and S8b available here short.at/awAU9. The data strongly support the hypothesis that microtwins anneal at this temperature regime and suggest that they retract (“grow backwards”). A different explanation would be that only their surface termination disappears and they are still present within the bulk of the film. This hypothesis could only be ruled out with a bulk-sensitive probe, such as SXDM, but since microtwins in CuMnAs become narrower towards the bottom interface with the substrates and wider towards the free surface this assumption seems unlikely (see chapter 5, Fig. 5.1 and reference [46]).

Magnetostructural dynamics at intermediate temperatures Direct evidence for the second hypothesis, suggesting that the AF dynamics at intermediate temperatures are directly correlated to the growth of microtwins is obtained from the same area of the sample upon subsequent cooling.

A time-lapsed movie of the reformation of the microtwin pattern at intermediate-

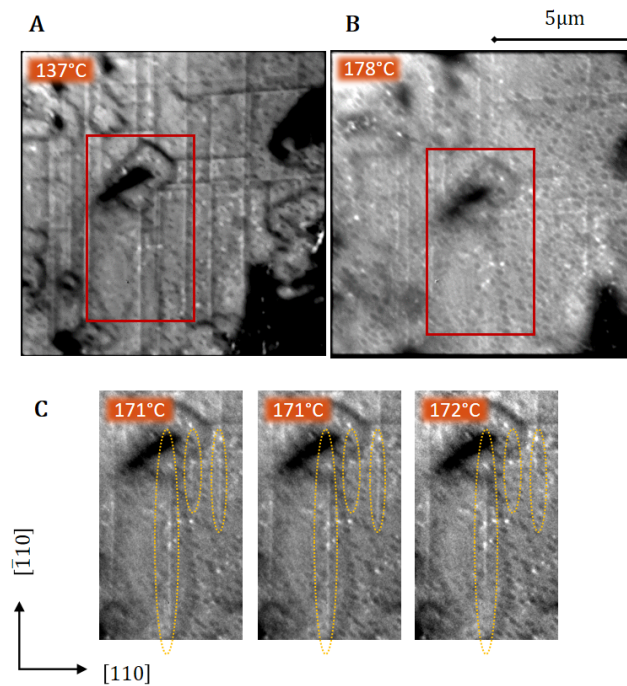


Figure 7.10: Comparison of the microtwin pattern at intermediate-high and high temperatures LEEM images of a typical area of a 50 nm CuMnAs/GaP film after surface preparation. The horizontal and vertical lines in the LEEM images are the microtwins. Other dark lines are step edges. The dark patches are residual, amorphous AsO_x . The temperature is a thermocouple measurement and only is a lower bound. **A, B:** Stationary microtwin configuration, when left to stabilise for over 20 min at intermediate-high temperatures (**A**) and high temperatures **B**. **C:** Time-series of LEEM images of the area marked by the red rectangle showing the stabilisation dynamics of the microtwin configuration. The images are averaged over 20s with a 10s gap between each other. The yellow dotted lines mark where changes in the microtwin configuration are observed. See also supplementary videos S8a and S8b available here short.at/awAU9.

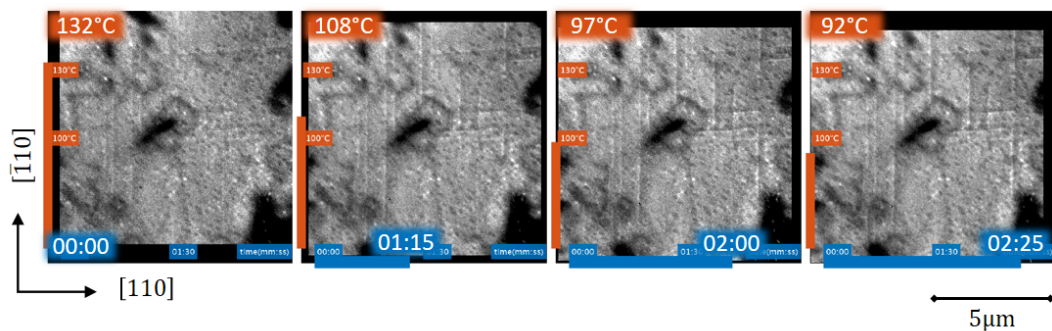


Figure 7.11: Reformation of the microtwin structure during cooling. Subset of the frames of the time-lapsed movie available in the supplementary information consisting of LEEM images of the CuMnAs surface. The microtwins are the vertical and horizontal lines. Shown is the same area as in Fig. 7.10. The black “frames” is where the area of interested drifted out of the imaged area. The orange bar indicates the temperature, the blue bar the elapsed time with respect to the first frame. See also the supplementary video S9 available here short.at/awAU9

high temperatures can be found in the supplementary video S9 available here short.at/awAU9. Figure 7.11 shows a subset of the frames. The LEEM images confirm that in this temperature regime, which is above the threshold where magnetic contrast is lost, the microtwin pattern reforms. Over less than 2 min several microtwins are observed to nucleate and grow up to a few micrometres. However the microtwin pattern is considerably less dense than the one before heating to high temperatures (Fig. 7.10 **A**). Since not only the microtwin pattern is partially recovered, but also the image quality this has to be a physical change and cannot be attributed to loss of sensitivity of the LEEM imaging. Figure 7.12 and 7.13 shows that at slightly lower (intermediate-high) temperatures, when magnetic contrast is recovered, the microtwin growth continues, alongside inducing similar AF dynamics as observed in the previous sample. Figure 7.12 **A** and **B** show LEEM images of the microtwin configuration recorded approximately 30 min apart at intermediate temperatures. Comparing the images shows that several microtwins have grown and additional microtwins formed. Those are marked in Fig. 7.12 **C** with yellow broken lines. Between the LEEM images the AF domain structure of the same area was monitored in XMLD-PEEM while the sample was left to cool down from intermediate to intermediate-low temperatures. Figure 7.12 **D** and **E** show the first and last image of the sequence, taken ~ 27 min apart from each other. Figure 7.12 **F** shows the last frame overlaid with the broken yellow lines (from panel **D**) indicating where microtwins grew or newly formed. Comparing panels **D** and **E** shows that in all cases also an AF domain with spin axis parallel to the twin nucleated or expanded along the microtwin line. In some cases, the AF domain is shorter than the corresponding microtwin which is consistent with the interpretation that the twin continued growing between the XMLD-PEEM image and the LEEM image.

The AF dynamics occurring between the images shown in Fig. 7.12 **D** and **E**, best seen in the supplementary video S10 available here short.at/awAU9, show the same features as the dynamics observed in sample A, studied previ-

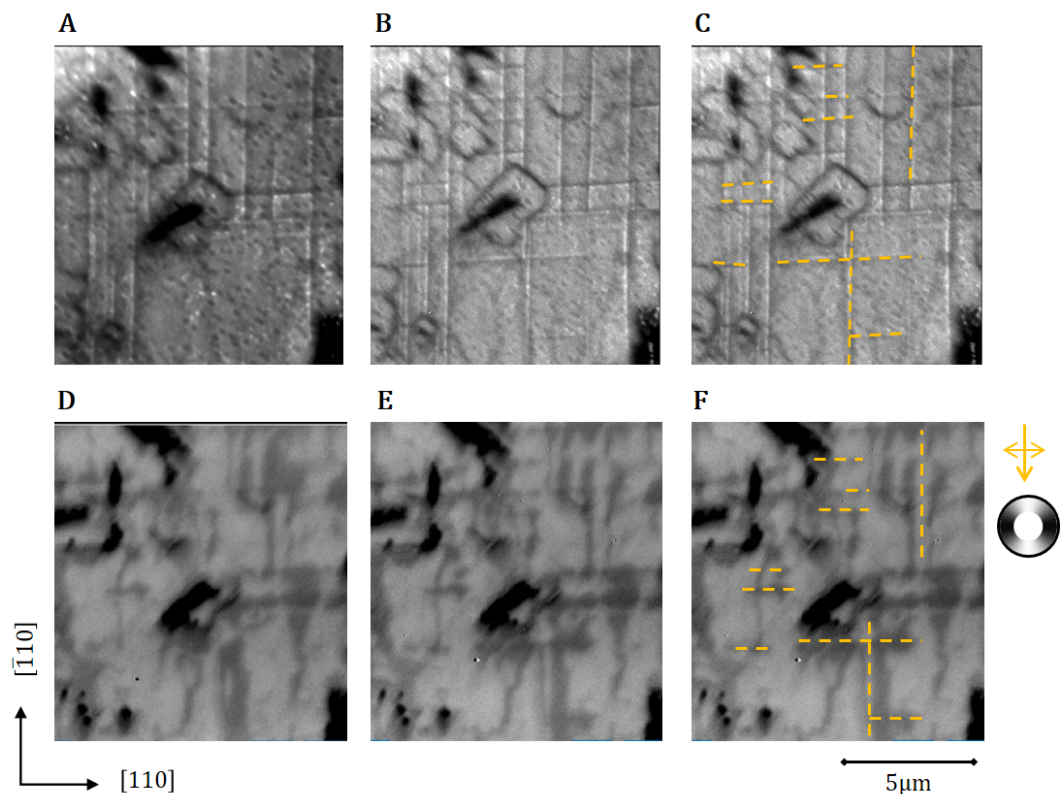


Figure 7.12: *Direct Comparison of AF domain changes and microtwin growth at intermediate temperatures during cooling. A: LEEM image at high temperature taken before a series of XMLD-PEEM images. B: LEEM image of the same area taken after the series of XMLD-PEEM image. C: Same as B, but microtwins which are not present in A or are significantly longer in B than in A marked by broken yellow lines. D: First image of a series of XMLD-PEEM images of the same area measured shortly after A. E: Last image of the series measured just before B. F: Same as E but overlaid with the broken yellow lines indicating the microtwins which are present after, but not before the X-PEEM imaging series.*

ously. Selected frames of the movie, illustrating the dynamics, can be found in Fig. 7.13. Compared to sample A, this sample shows smaller AF domains, due to a higher microtwin density. Consistently, the imaged area shows more AF domains growing, but each covering shorter distances which thus are more difficult to see in the stationary images.

For better visualisation of the dynamics, Fig. 7.14 A and B show a time-series of close-ups of two areas with significant dynamics. Figure 7.14 C illustrates where the areas are located. The panel is the area marked by the red rectangle in Fig. 7.13. Here, also the changes in the microtwin structure are indicated. Within the area marked in green one vertical and two horizontal microtwins formed. In the area marked in red, a vertical microtwin was found to grow.

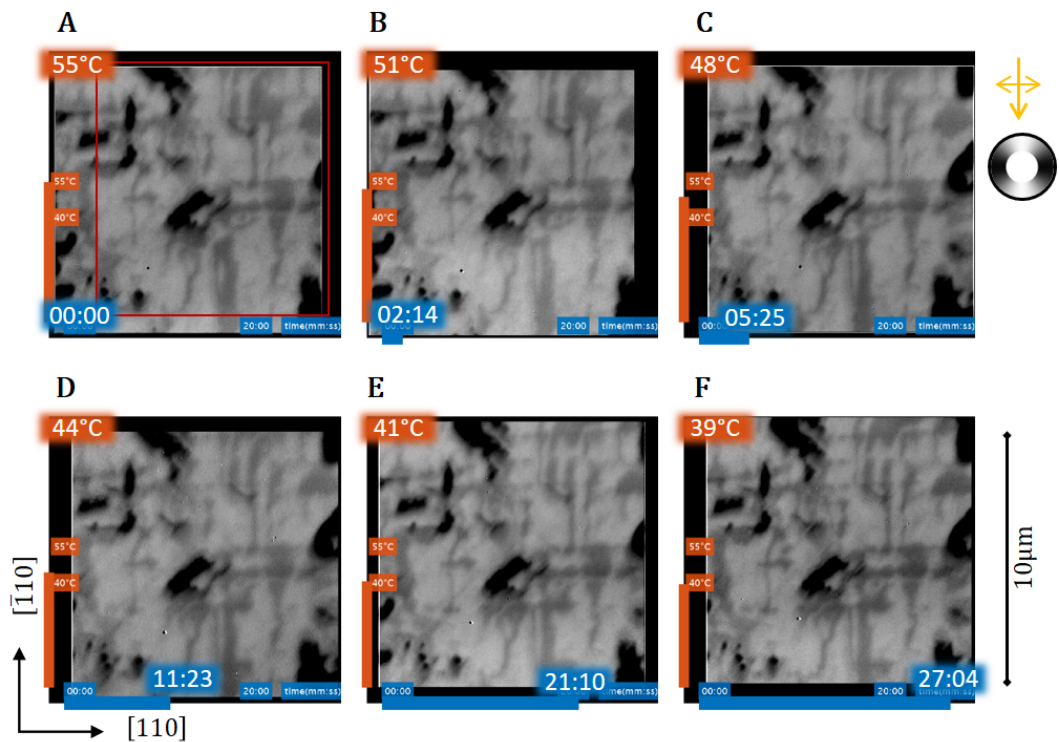


Figure 7.13: *AF domain changes during cooling, sample B. Time-series of XMLD-PEEM images taken between the images shown in Fig. 7.12D and E at intermediate-low temperatures. The images are a subset of the frames of the time-lapsed movie available in the supplementary video S10 available here short.at/awAU9. The temperature refers to the reading of the thermocouple. The time is measured with respect to the first image of the sequence. The red square in panel A is not shown in the time-lapsed movie and marks the area shown in Fig. 7.14 C.*

The length of the twin before the sequence of XMLD-PEEM images is shown by the orange broken line, the broken yellow line shows the additional length observed after the XMLD-PEEM imaging. The time-series of the close-ups in Fig. 7.14 A and B confirm that indeed with the vertical microtwins light domains grow and with the two horizontal microtwins two dark domains grow along the microtwin direction. The growth of the dark domains occurs after the growth of the white domain shown in Fig. 7.14 B. This suggests that also the vertical microtwin grows first and serves as a nucleation point for the horizontal microtwins.

Thus, the measurements on this sample confirm the observation on sample A and provide clear evidence for the suggested interpretation as magnetostructural dynamics.

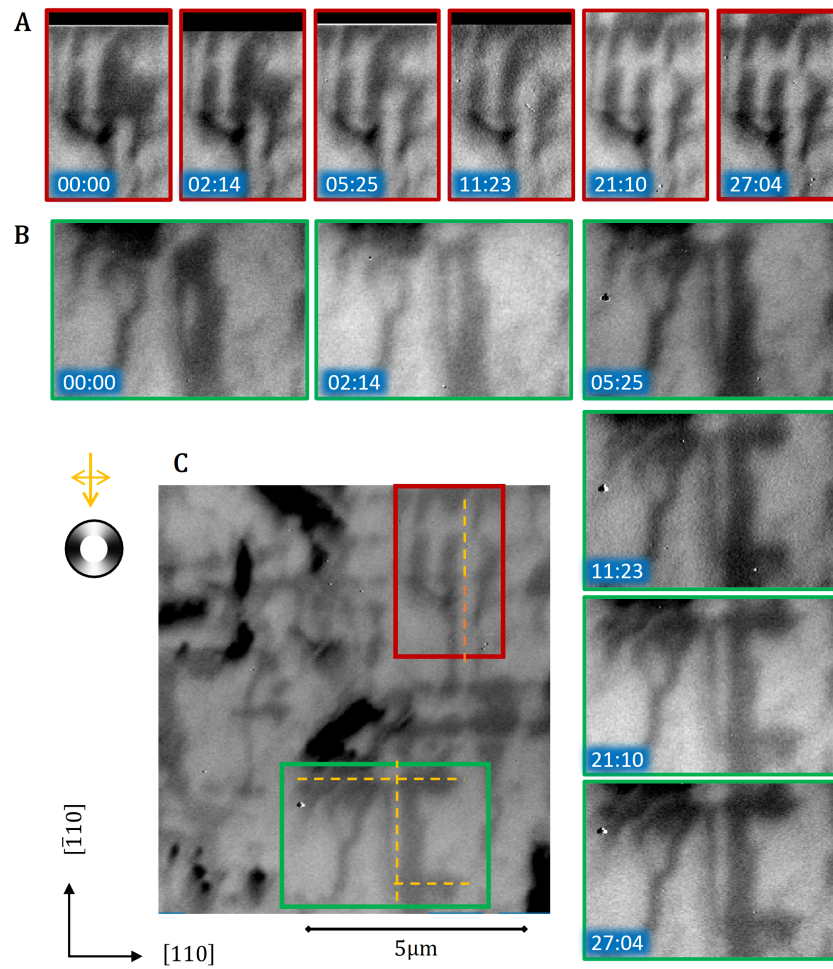


Figure 7.14: *Examples of AF domain directly correlated to microtwin growth at intermediate temperatures. A, B:* Time-series of XMLD-PEEM images during cooling of close-ups of two selected areas, marked by the red and green rectangle in panel C, which shows the last image image of the sequence shown in Fig. 7.13. Each frame in A and B directly corresponds to a frame in Fig. 7.13. The broken orange line in the red rectangle in panel C indicates a microtwin observed in LEEM before the series of XMLD-PEEM series. The yellow dashed line indicates the additional extend of the microtwin, measured after the XMLD-PEEM series which directly corresponds to the growth of the light AF domain in panel A. The broken yellow lines in the green rectangle indicate microtwins which were measured in LEEM after the XMLD-PEEM image series, but not before. Again these are directly correlated to AF domain growth shown in panel B.

7.4 Summary and conclusion

This chapter has reported on magnetostructural dynamics in AF thin films which occur several orders of magnitude more slowly than what is expected for purely AF dynamics.

The changes in the AF domain structure are directly correlated to the growth of microtwins. The growths can be triggered by patterned edges which provide

nucleation points for microtwins. At room temperature, the microtwin growths and the AF domain changes happen over days to months. Similar kinetics can be induced in non-patterned films by heat-cycling. At slightly elevated temperatures, the microtwin growth and consequently the AF domain changes accelerate occurring over minutes. In both cases, it seems likely that the microtwins are a response to a change of strain, either induced by temperature changes or patterning which is expected to relax strain uniaxially. This is consistent with the observation reported in reference [46] that the microtwin density is directly correlated to the amount of strain in a sample.

Due to the dramatic difference of the intrinsic timescales of AF dynamics (picoseconds) to structural dynamics (seconds/minutes/hours/months), the timescale of the dynamics can be inferred to be governed by the structural microtwin growths. For the magnetic order the structure can be seen as stationary, and the AF order can always reach an (local) equilibrium state. For the crystallographic dynamics, the AF order can be considered to react “instantaneously” to the changes.

Although initiated by and directly correlated to the microtwin growth, the AF domain pattern yields richer dynamics than the microtwin pattern comprising not only slow AF domain growth, but also merging(repelling) of domains with parallel (antiparallel) Néel vector and movement of 180° domain walls which occurs faster than the resolution of the XMLD-PEEM imaging. Both features arise from the sign of the Néel vector, an additional degree of freedom of the AF domains which has no counterpart in the crystallographic structure and is not coupled to the microtwin pattern.

The data shown here are also relevant when interpreting the (numerous) electrical switching experiments with this material, in particular as 45 nm CuMnAs/GaP(001) films are widely studied for orthogonal electrical AF domain switching.

For example, the dramatic current-induced change, the “shattering” of the AF domain structure, shown in Fig. 4.11 in section 4.4, followed by AF domain

coarsening dynamics over hours (also Fig. 4.11) can be interpreted as follows: The initial domain structure was pinned by a (dense) microtwin pattern, which stabilises the AF domain pattern and leads to the biaxial domain structure. The current pulse locally heated the AF device beyond the annihilation point of microtwins. In the absence of microtwins, the AF domain structure becomes more sensitive to the influence of the edges (with various orientations) and other local defects since the intrinsic in-plane anisotropy of CuMnAs films is small. This leads to the smaller more granular domain structure; the “shattering” of the AF domains is actually a “shattering” of the microtwin pattern. The following domain coarsening dynamics are governed by the slow reformation of the microtwin configuration, since intrinsic AF dynamics and “purely” AF domain wall motion can be expected to occur several orders of magnitude faster [44, 129].

The microtwins preferentially nucleate at the edges oriented along the CuMnAs [110] and $[\bar{1}10]$ as can be inferred from the small lens-domains at the edges) and at other microtwins. Consistently the AF domain coarsening starts and propagates from the area which was less affected by the current-pulse.

Additionally, it was found that the AF domain was more susceptible to (lower) electrical current pulses after the shattering of the AF domain structure than before (see Fig. 4.10 and Fig. 4.12), consistent with the interpretation that the strong AF domain pinning to the microtwin defects stabilises the AF domain structure. Hence, lower current pulses are needed to manipulate AF domains in the absence of microtwins.

The data clearly show that the microtwins are part of the equilibrium configuration and the way the samples approach the equilibrium state.

To a material scientist, it might seem obvious that a material reacts to changes in strain by growing microtwin defects (see [112, 130, 131]), and to a theoretician it might seem trivial that the AF domain structure is sensitive to structural defects. Yet, to the best of the author’s knowledge, the direct imaging of AF domain (creeping) motion with direct correlation to structural changes

is unprecedented. Even direct imaging of only twin-defect dynamics upon external strain has only just been reported (see [112]), becoming feasible by the continuous improvement of electron imaging over the last decades. It also shows at which detailed microscopic level AF materials need to be understood in order to predict their response to external stimuli and ultimately to build efficient spintronic devices, crystallographic defects might even become a tool, as they are in TWIP-steels (see [112]). For 45 nm CuMnAs/GaP (001), the microtwins are found to be crucial, for films with different thickness or different materials, other crystallographic defects or interface effects are likely to be equally relevant.

Chapter 8

Surface and interface effects in CuMnAs films

8.1 Introduction

In the last two decades, there have been considerable advances in AF spintronics research, and new device concepts with functionality based on antiferromagnetic order were suggested. The properties of those devices were predicted to be highly advantageous compared to current technology.

Nevertheless, current technological application of crystal antiferromagnets (as opposed to synthetic AFs) is still largely restricted to devices where the functionality arises from a ferro- or ferrimagnetic material and the role of the antiferromagnet is to alter the magnetic anisotropy of the other component, via exchange bias and stabilise its magnetisation.

Exchange bias Exchange bias arises in AF/FM bilayers or multilayers from an interface effect which couples the magnetisation of the FM layer to the orientation to the spin moment of the AF at the interface. In structures with well-defined interface termination of the AF system, this coupling can lead to a unidirectional anisotropy of the FM layer (a shift of the hysteresis loop along the magnetic field axis) and hence can stabilise the FM magnetisation against

field perturbations. This is used, for example to pin the magnetisation in read heads of hard disk drives [132]. Due to its use for technological applications, exchange bias has been investigated in detail [133] following its first observation more than 65 years ago [134]. Collinear (parallel and antiparallel) coupling of the magnetisation and the Néel vector or at an angle has been observed [135]. In a multi-domain state or in the absence of a well-defined interface termination of the AF layer, the local interface coupling mechanism can still persist, but might affect the properties of the multilayer system in a more subtle way, *e.g.* by imposing only an axial and not directional anisotropy [136] or by affecting the microscopic domain structures of the layers [135]. Often the microscopic origin of the coupling mechanism is not well understood.

Direct correlation of the AF and FM domain structures in AF/FM bilayers has been observed in several systems [124, 135, 137, 138]. As discussed in reference [137], the first report of the direct imaging of such “domain imprinting”, the morphology of the interface plays an important role. Local variations of the interface can not only result in a reduced strength of the coupling, but also lead to locally alternating coupling between the FM magnetisation and AF Néel vector. The coexistence of parallel and antiparallel coupling between the AF Néel vector and the FM magnetisation was observed in ferromagnetic Co - antiferromagnetic LaFeO₃ bilayers [137] and ferromagnetic LSMO - antiferromagnetic LSFO superlattices [124]. In contrast for ferromagnetic Permalloy - antiferromagnetic Mn₂Au bilayers a one-to-one correspondance between the magnetisation direction and the sign of the Néel vector was observed [138].

Coupling implies that the two layers affect each other and the resulting properties are not always dominated by one or the other layer only. The behaviour of the multilayer systems depends sensitively on the (relative) size of the (intrinsic) magnetic anisotropies of each layer, the strength of the coupling mechanism, external fields and potentially its magnetic history.

For example, in reference [138] investigating Mn₂Au-Permalloy bilayers, the antiferromagnetic Mn₂Au layer was found to dominate the behaviour and the

authors suggests to use the interface coupling as a (local) probe the AF spin order. In contrast, in reference [53] it is demonstrated that the AF spin axis of 5 nm CuMnAs/GaP(001) films can be rotated by rotating the magnetisation of a Fe surface layer on the CuMnAs film with a small magnetic field. A collinear coupling between the Néel vector of the CuMnAs film and the magnetisation of the Fe surface layer was reported.

Here we investigate similar CuMnAs - Fe bilayers, but with a thicker 50 nm antiferromagnetic CuMnAs/GaP(001) film. The thickness of the ferromagnetic Fe surface layer is unchanged. It will be shown that in these thicker samples the AF layer dominates in the absence of external fields. Direct comparison of XMCD-PEEM images of the FM domains of the Fe layer and XMLD-PEEM images of the antiferromagnetic CuMnAs domain structure of the CuMnAs film reveals that the AF domains are directly imprinted onto the FM domain structure. Consistent with reference [53], a collinear coupling between the magnetisation and Néel vector is found. The data show FM domain boundaries without corresponding XMLD-PEEM resolvable AF domain boundary. This could reflect that the FM domains can be used to reveal the surface terminations of atomically sharp AF domain boundaries, suggested in reference [88]. In order to strengthen that hypothesis, measurements of the surface structure of exposed CuMnAs films will be presented. The analysis of those data is not yet concluded, so that this chapter must be seen primarily as an outlook for future work.

8.2 Methods

Material The measurements in the first part are performed on 2 nmAl / 1.4 nm Fe / 50 nmCuMnAs / GaP(001) layers. The 50 nm CuMnAs films are grown epitaxially on the GaP(001) substrates, similar to all other CuMnAs layers. The 1.4 nm Fe surface layer is grown at approximately 0 °C ferromagnetic. The Al cap serves to prevent oxidation of the Fe and CuMnAs layers.

The measurements in the second part use epitaxially grown 50 nm CuMnAs/GaP(001) films capped initially with 30 nm amorphous As. The As cap is removed prior to the measurement by heating the sample to $\sim 350^\circ\text{C}$ for approximately 20 min in a dedicated decapping chamber. The prepared surfaces are transferred in ultra-high-vacuum into the measurement chamber. For details see 2.9.1.

8.2.1 X-PEEM and LEEM

All microscopic measurements are performed at ambient temperature on the X-PEEM endstation on beamline I06, DLS.

XMLD-PEEM Imaging of the antiferromagnetic CuMnAs domains of the Fe-CuMnAs bilayers and the exposed CuMnAs surfaces is achieved using XMLD-PEEM, at the Mn $L_{2,3}$ absorption edge, using the experimental protocol described in section 2.8.2. For further information see also sections 2.5.2 and 2.7. This yields maximum contrast between domains with spin axis parallel and perpendicular to the x-ray polarisation, corresponding to perpendicular and parallel to the in-plane projection of the incident x-ray beam in this experimental geometry.

XMCD-PEEM The ferromagnetic domains of the Fe surface layer of the Fe-CuMnAs samples are imaged using XMCD-PEEM at the Fe $L_{2,3}$ edge, which yields maximum contrast between magnetic domains parallel and antiparallel to the direction of the incident x-ray beam. Domains with mutually antiparallel spin axis perpendicular to the x-ray beam cannot be distinguished. For details see section 2.8.4. The element-specific, spectroscopic imaging technique allows to clearly separate the contributions of the Fe and CuMnAs layers.

The measurements on the Fe-CuMnAs bilayers are performed on a sample as-grown and on a patterned chip fabricated via photolithography and chemical wet etching. After patterning, the sample was exposed to a 0.1 T magnetic

field aligned with one of the CuMnAs $\langle 110 \rangle$ directions approximately 24 hours before the measurement.

Structural measurements using LEEM The surface structure of the exposed CuMnAs surfaces is investigated using the same microscope, but as a LEEM. For the experimental protocol see section 2.9. For further information on LEEM see 2.6.1 The kinetic energy of the energy of the electrons when interacting with the sample is defined by the start-voltage (STV).

MEM Mirror-electron microscopy of the sample surface uses the specular reflection for imaging and a start-voltage of 1.5 eV. Hence the electrons primarily interact with the sample surface and contrast mainly arises on step edges and other topographic features.

BF-LEEM BF-LEEM imaging uses the specular reflection for imaging and is in the measurements presented here performed with a start-voltage of 38 eV.

DF-LEEM The CuMnAs LEED pattern shows additional half-order spots ($\pm(0.5, 0)$ and $\pm(0, 0.5)$), corresponding to a doubling of the lattice constant in the corresponding direction. These reflections are used in the DF-LEEM measurements presented here. The start-voltage of the measurements is set to 38 eV, as in the BF-LEEM images. Selectively always one of the four equivalent half-order spots is used for imaging and $N = 5$ images are taken, drift corrected and averaged. This yields four intensity images $I_{(0.5,0.0)}$, $I_{(\overline{0.5},0.0)}$, $I_{(0.0,0.5)}$ and $I_{(0.0,\overline{0.5})}$. To enhance contrast the images of the collinear reflections are averaged and the asymmetry of the averaged two images calculated:

$$I_{\text{asym}} = \frac{I_{(0.5,0.0)} + I_{(\overline{0.5},0.0)} - (I_{(0.0,0.5)} + I_{(0.0,\overline{0.5})})}{I_{(0.5,0.0)} + I_{(\overline{0.5},0.0)} + I_{(0.0,0.5)} + I_{(0.0,\overline{0.5})}}.$$

LEED LEED measurements are performed in the LEEM instrument (see section 2.7). This allows to restrict the illuminated sample area to selected re-

gions with the illumination aperture. Additionally, the positions of the diffraction spots on the camera do not move when the energy of electrons interacting with the sample (given by the start-voltage) is changed. The diffraction pattern is imaged. For LEED-IV data are obtained by scanning the start-voltage step-wise and taking one exposure at each energy. The intensity of each spot is integrated for each intensity over a circular region of interest (ROI), closely matched to the spot position and size. A local background, defined as the intensity integrated over a ring around the spot with the same area size as the ROI, is subtracted to account for diffuse scattering. The ROI is constant for all energies of the scan. The measurements were performed with the MCP-camera so that full LEED-IV datasets can be measured with constant scaling and the measured intensity is directly proportional to the number of incident electrons.

The LEED-IV data presented here are not taken on the same sample as the imaging data, but on a similar sample grown and prepared in the same way. It was confirmed that the LEED patterns of the two samples have the same symmetry and that the AF domain patterns show the same characteristics.

Magnetic hysteresis loops Magnetic hysteresis loops of as-grown samples of the Fe-CuMnAs-layers were measured using SQUID (=superconducting quantum interference device) magnetometry, which can detect the magnetic moment of samples with $10 \times 10^{-11} \text{ Am}^2$. The high sensitivity is required to measure the small moment of thin film samples. Being sensitive to the magnetic field only, SQUID magnetometry is not element-specific. The measurements were performed in a commercial Quantum Design MPMS SQUID magnetometer which combines temperature control of the sample (range 2 K to 300 K), the application of magnetic fields up to 7 T, with SQUID magnetometry in one experimental set-up [139]. The direction of the field is fixed. The measurements shown here are performed at 300 K, 200 K, 150 K and 100 K. Magnetic fields were applied in the range -1400 Oe to 1400 Oe , which is well below the

spin-flop field of tetragonal CuMnAs ($\sim 2T$). Measurements are performed with fields applied along a CuMnAs $\langle 100 \rangle$ and a CuMnAs $\langle 110 \rangle$ direction. This is realised in separate measurements by mounting samples with different orientations on sample holders. The surface size of the samples is restricted by the sample holder. In order to fit the holder, the sample with orientation such that the field direction matches the CuMnAs $\langle 100 \rangle$ is larger than the sample mounted with $\langle 110 \rangle$ orientation. Additionally, as SQUID magnetometry is not element-specific the contributions of the substrate and sample holder (diamagnetic) needs to be considered in measurements with applied fields.

8.3 Results

8.3.1 Domain imprinting in Fe–CuMnAs - bilayers

In reference [53], it was shown that the spin axis in a 5 nm thin CuMnAs film can be rotated by rotating the magnetic moment of a Fe surface layer using a small external magnetic field. Here, it is shown that vice-versa the AF domain structure of a thicker, 50 nm CuMnAs film is imprinted on the ferromagnetic domains of a Fe surface layer.

Figure 8.1 directly compares the domain structures of the CuMnAs and Fe layers of a representative $9\ \mu\text{m} \times 9\ \mu\text{m}$ wide area. The AF domains of the CuMnAs layer are imaged using XMLD-PEEM at the Mn L_3 adsorption edge (panels **B** and **F**), the FM domains are imaged with XMCD-PEEM at the Fe L_3 adsorption edge, hence the signals can be clearly related to one or the other layer. The X-ray absorption image of the area is also shown with several features that can be used to align the XMLD and XMCD with respect to each other. The first and middle column correspond to images taken with the x-ray beam impinging along two orthogonal crystallographic directions. The XMLD-PEEM images reveal an AF domain pattern typical for 50 nm CuMnAs/GaP(001) layers with two types of domains with mutually orthogonal

spin axes (see chapters 3 and 5). The two domain types appear as light and dark areas in this imaging configuration. The similarity of the AF domains with other 50 nm CuMnAs films suggests that the Fe layer does not significantly affect the AF properties.

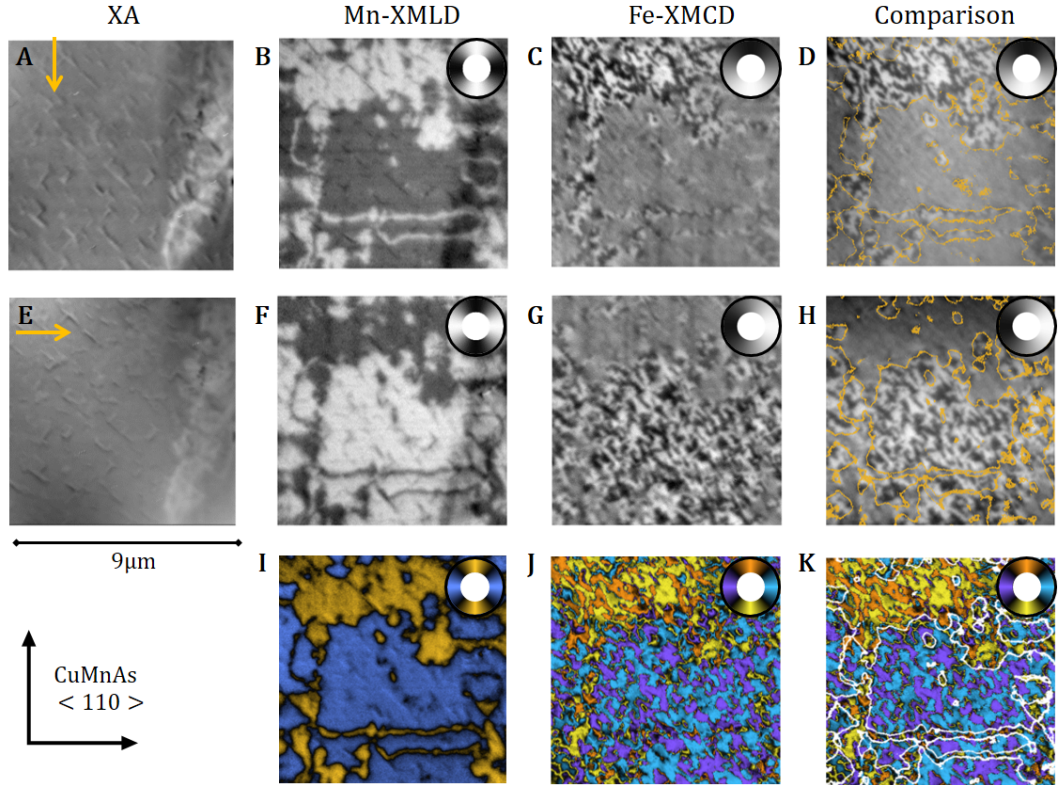


Figure 8.1: Comparison of the AF and FM domain structure in CuMnAs/Fe bilayers. **A** X-ray absorption image with photon energy at the Fe L_3 absorption edge. The white feature is a crystallographic defect used for alignment of images. The remaining contrast results from the surface morphology. **B** XMLD-PEEM image at the Mn L_3 absorption edge of the same area revealing the AF domain structure of the CuMnAs film. **C**, XMCD-PEEM image at the Fe absorption edge of the same area showing the vertical component of the Fe magnetisation vector. All images in panels **A** - **D** are taken with x-rays impinging along the CuMnAs $[110]$ (top) crystalline axes, as indicated by the yellow arrow. **E**, Comparison of the AF and FM domain images from **B** and **C**, showing the Fe-XMCD-PEEM image overlaid with the domain boundaries (yellow) of the Mn-XMLD-PEEM image. **E** - **H**, same as **A** - **E**, but with the x-rays impinging along the CuMnAs $[110]$ showing reversed contrast in the Mn-XMLD images and revealing the horizontal component of the Fe magnetisation respectively. **I**, AF spin axis map calculated from the Mn-XMLD-PEEM images. **J**, FM vector map calculated from the Fe-XMCD-PEEM images. **K**, Overlay of the FM vector map with the AF domain boundaries (white). The colour wheels in panels **B**, **F**, **I** refer to the AF spin axis, the colour wheels in the remaining panels to the orientation of the FM magnetisation. The scalebar refers to all panels.

The two XMLD-PEEM images with orthogonal direction of the x-ray beam show the expected reversed contrast. A clear correlation between the AF

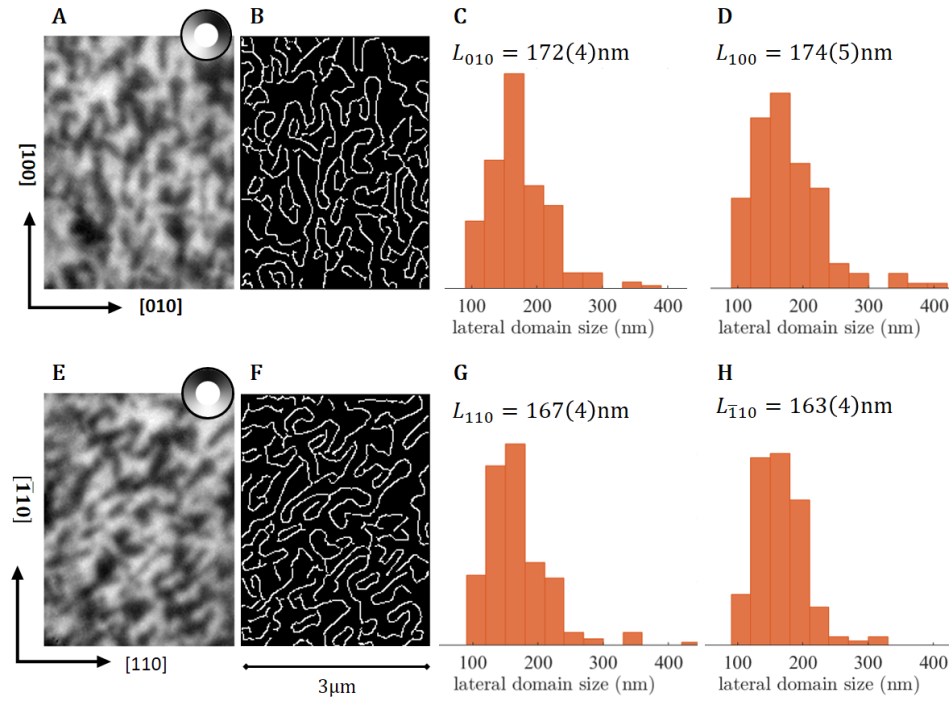


Figure 8.2: Length-scale of FM domains in CuMnAs/Fe bilayers **A:** Part of an Fe-XMCD-PEEM image with the edges aligned with the CuMnAs $\langle 100 \rangle$ directions showing FM domains parallel/antiparallel to the CuMnAs $[110]$ direction. **B:** Corresponding domain boundaries obtained by applying a sobel edge-filter to the image. **C and D:** Histogram of the distribution of distances between two neighbouring boundaries measured horizontally (**C**) and vertically (**D**) in the edge-filtered image. The average value is also stated. **E-H:** Same as **A-D**, but with the XMCD image rotated along the CuMnAs $\langle 110 \rangle$ directions. Panels **A** and **E** overlap partially. The crystallographic directions refer to the CuMnAs layer. The scalebar refers to panels **A, B, E** and **F**.

domains of the CuMnAs film and the FM domains of the Fe layer can be observed: For both x-ray directions, the areas which appear dark in the XMLD-PEEM images appear grey in the XMCD-PEEM images of the FM domains, whereas the areas which appear light in the XMLD-PEEM images are broken up into small FM domains with minimum and maximum intensity. This means that the spin axes of the AF and the FM layer are collinear, but each CuMnAs domain corresponds to two types of Fe domains with mutually antiparallel magnetisation. This can be seen in the AF spin axis maps and the FM vector maps calculated from the XMLD-PEEM and XMCD-PEEM images and shown in panels **I - K**. The collinear coupling is consistent with what was reported in reference [53].

On close inspection, it can be seen that the boundaries between the antiparallel

FM domains tend to follow the CuMnAs $\langle 100 \rangle$ directions. The lateral size of the FM domains is in the order of 100 nm to 200 nm, measured as the distance between two neighbouring boundaries along a fixed crystallographic direction, as illustrated in Fig. 8.2.

Splitting of the AF domains into two mutually antiparallel FM domains could then result from two scenarios: (i) The interface coupling has only axial properties and the two types of FM domains form to minimise FM stray fields. (ii) The direction of the FM magnetisation is dictated by the termination of the staggered AF spin order at the interface, which does not yield contrast in XMLD-PEEM.

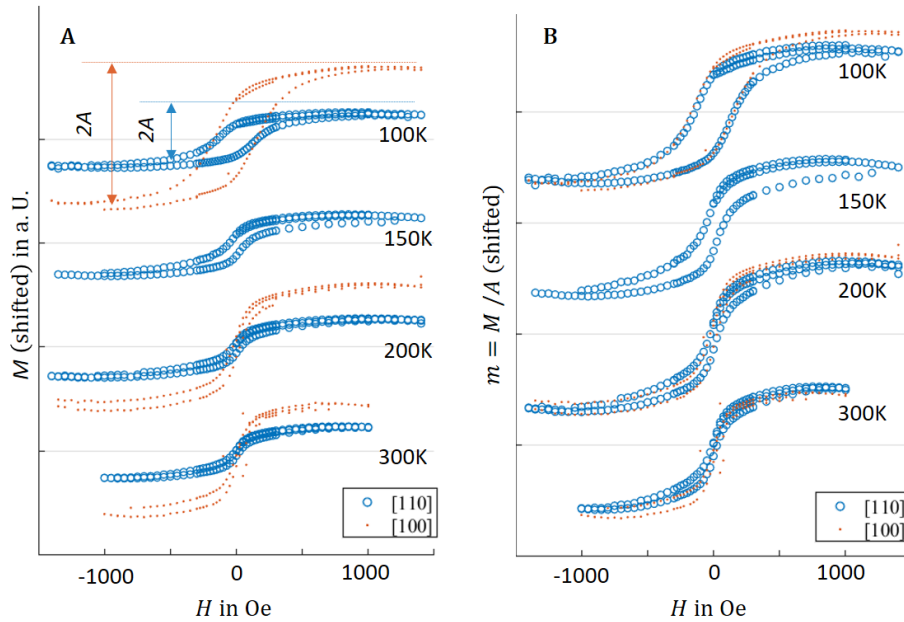


Figure 8.3: Magnetic hysteresis loops at various temperatures of Fe/CuMnAs bilayers for magnetic fields along the CuMnAs $[110]$ (blue) and $[010]$ (red) directions. Left: Raw data, shifted. Right: Data scaled by the saturation magnetisation.

To garner further insight into the coupling, the effects of small magnetic fields on the magnetisation of the sample are investigated using SQUID magnetometry. The SQUID measurements are expected to be only sensitive to the magnetisation of the Fe layer, since even a small uncompensated magnetic moment of the CuMnAs layer at the interface is expected to be way below the sensitivity of the instrument.

Figure 8.3 compares SQUID-measurements of hysteresis loops at various temperatures for magnetic fields applied along the CuMnAs [110] and the CuMnAs [100] directions. A linear background was subtracted from the data in order to correct for the effect of substrate and sample holder. The size of the signal depends on the surface area contributing to the measurements, which varies for the different field directions. This is accounted for by scaling the datasets by the amplitude A of the hysteresis loops, defined as illustrated in Fig. 8.3 A. At room temperature, the coercivity fields are below 50 Oe. From these measurements, no significant dependence on the field direction can be observed, indicative of a weak anisotropy. The coercivity fields increase with decreasing temperature, but the latter remain below 200 Oe at 100 K. The remanent magnetisation cannot be determined from the measurements as it shows a time-dependent decay, as described below.

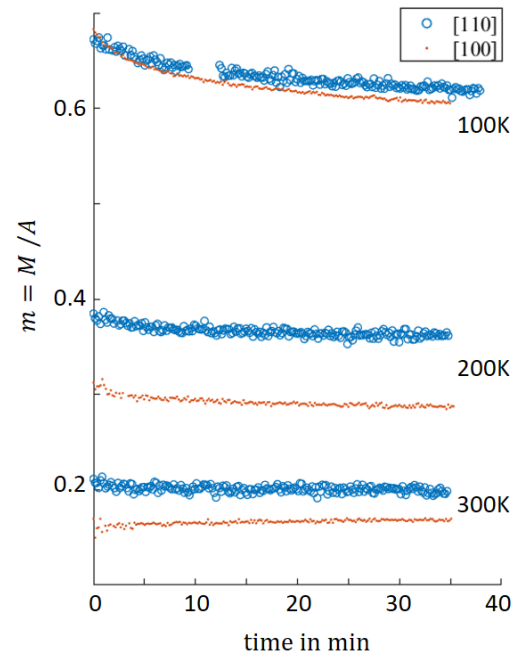


Figure 8.4: *Decay of the magnetisation of Fe/CuMnAs bilayers at various temperatures after application of 1.4 k Oe fields along the CuMnAs [110] and [100] directions. The time is measured relative to the time, when the field was switched off.*

The decay of the magnetisation monitored over 35 min at zero field is shown in Fig. 8.4. The data are scaled by the amplitude of the corresponding hysteresis loops. As expected, the highest magnetisation is observed at the lowest temperature (here 100 K). At 300 K the curves are almost flat, suggesting that the majority of the signal has already decayed before the first measurement

and the remaining signal either reflects the remanent effect or an offset of the experimental set-up. The remanent magnetisation is larger along the CuMnAs [110] directions for all temperatures.

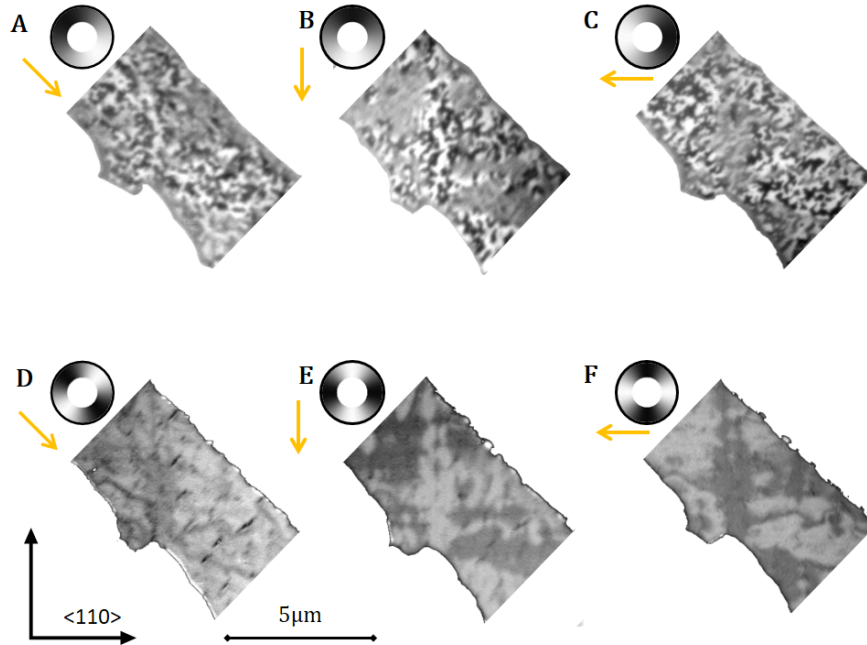


Figure 8.5: *AF and FM structure in a CuMnAs/Fe bilayer after exposure to a small magnetic field along the CuMnAs [110] direction. All panels show the same section of a bar oriented along the CuMnAs [010] direction. Panels A-C are XMCD-PEEM images with different incident direction of the x-ray beam as indicated by the yellow axis. Maximum contrast is achieved between domains with parallel and antiparallel orientation of the FM magnetisation with respect to the x-ray beam, as indicated in the colour wheels. No contrast is achieved on domains with magnetisation perpendicular to the x-ray beam. Panels D-F are XMLD-PEEM images of the AF domain structure for the same x-ray orientation. Here, maximum contrast occurs between domains with spin axis parallel and perpendicular to the x-rays.*

Figure 8.5 shows XMLD-PEEM images of the AF domain structure and XMCD-PEEM images of the FM domain structure ~ 24 hours after application of a small magnetic field in the order of 0.1 T along the CuMnAs [110] direction at room temperature. The sample was exposed to the field for ~ 30 min.

From the SQUID measurements it is evident that fields of this size are sufficient to saturate the FM magnetisation. Nonetheless, the domains show no evidence of a remanent effect of the magnetic field. In particular, FM domains with magnetisation parallel and antiparallel to the field direction are present and

approximately equally populated and the overall domain morphology of the AF and FM domains resembles the one in the as-grown virgin sample. The FM domains are of similar size as in the as-grown sample and also the preferred alignment of the FM domain boundaries with the CuMnAs $\langle 100 \rangle$ directions is observed. This hints that the FM magnetisation is indeed defined by the AF order.

The images are obtained from a patterned bar aligned with the CuMnAs [100] direction, but similar observations were made also in non-patterned regions of the sample. Further evidence can be retrieved from the FM and AF spin orientations in the vicinity of the patterned edge. For the AF domains in CuMnAs films, it has been shown in chapter 6 that the effect of patterned edges aligned a $\langle 100 \rangle$ direction is limited by the nearest microtwin density and sets a preference for AF spin axes perpendicular to the edge. This layer has a high microtwin density and barely any effect of the edge on the AF domains is visible in the XMLD-PEEM images. The XMCD-PEEM image, shows a small boundary region at the edges which appears grey, when imaged with x-rays impinging parallel to the bar, indicating FM magnetisation perpendicular to the edge. This is opposite to shape anisotropy resulting from minimisation of stray fields, but consistent with the collinear coupling and the previously found effect of patterning on the AF domains in CuMnAs films.

Hence it is suggested that the direction of a FM domain is determined by the termination of the staggered AF magnetisation at the interface. The splitting of (apparently) one AF domain into two FM domains can then result as follows. (i) The antiferromagnetic CuMnAs layer can terminate at the interface with one or the other magnetic sublattice. The boundaries between two FM domains with antiparallel orientation result from step edges of the CuMnAs layer which are not full unit-cells. Hence, the AF Néel vector has the same orientation and sign and only the surface termination of the AF crystal changes. This behaviour has been reported for ferromagnetic 1.2 nm Co on antiferromagnetic LaFeO₃/SrTiO₃(001) [137].

(ii) The AF layer always terminates with the same crystallographic layer at the interface and the FM boundaries reflect sharp 180° reversals of the Néel vector which cannot be resolved in XMLD-PEEM. A uniquely defined sublattice termination at an AF/FM interface and a one-to-one imprinting of the AF domains onto the FM domains, including the sign of the Néel vector, has been reported for ferromagnetic permalloy on antiferromagnetic $\text{Mn}_2\text{Au}/\text{Al}_2\text{O}_3$ [138]. Here, each boundary between two FM domains with antiparallel orientation was found to coincide with an XMLD-PEEM resolvable 180° domain wall of the AF layer. No splitting of the domains in the XMLD-PEEM into several FM domains in XMCD images was observed for this layer. However, for CuMnAs films, the presence of atomically sharp AF domain boundaries (sub-lattice swap) has been evidenced in reference [88] using differential phase contrast imaging within aberration corrected scanning transmission electron microscopy. The majority of the atomically sharp AF domain boundaries have been related to the crystallographic antiphase boundaries (APBs), the crystallographic slips along the c direction and most abundant crystallographic defect type in the CuMnAs films (see section 2.1). A smaller number of atomically sharp AF domain boundaries without obvious relation to a crystallographic defect, were also reported. In particular, the authors state that the APBs induce a swap of the magnetic sublattices. Hence, the crystallographic APBs coincide with, what is effectively an atomically sharp 180° AF domain boundary. The APBs are the most abundant defects in epitaxial CuMnAs whose density has been estimated to the order of one every 20 nm ([46] and private conversations with the author). The APBs start at the interface with the substrate, but do not always penetrate across the whole layer (see [46, 88]), yet if they do, then they terminate at the surface as lines along a CuMnAs $\langle 100 \rangle$ direction. Thus, their direction matches the boundaries between FM domains in the XMCD-PEEM images without counterpart in the XMLD-PEEM images of the CuMnAs-Fe bilayers.

Therefore, if, as in Mn_2Au -Permalloy bilayers, the CuMnAs layer would have

a uniquely defined interface termination, then imaging of the FM domain (boundaries) would effectively be imaging of the atomically sharp AF domain boundaries. This would allow to investigate the “interaction” of the atomically sharp AF domain boundaries with standard micromagnetic spin textures as well as their response to electrical current pulses. In particular, the hypothesis that the high-resistive switching signal reported in reference [111] results from the creation of atomically sharp AF domain boundaries, unrelated to crystallographic APBs, could be tested.

Yet, before this identification can be made, the interface between the CuMnAs and the Fe, in particular the interface termination of the CuMnAs layer, needs to be understood. Ideally, this would be investigated directly, for example using high-resolution transmission electron microscopy, which unfortunately has not been possible as part of this work. Indirectly, evidence for the interface termination of the CuMnAs film might also be garnered from measurements of exposed CuMnAs surfaces, as discussed in the following.

Surface structure of exposed CuMnAs surfaces

The following part describes investigations of the structural and antiferromagnetic properties of exposed surfaces of 50 nm CuMnAs/GaP(001) films using LEEM and LEED to achieve sensitivity to the crystallographic properties and XMLD-PEEM for measurements of the AF properties. The measurements cannot be performed in-situ in the growth chamber, but the films are initially protected by a 30 nm amorphous As cap, which is removed by heating just prior to the measurements (see section 2.9.1).

LEED LEED images of exposed CuMnAs surfaces were recorded with circular apertures with 6 μm and 400 nm diameter from various positions on a series of samples with sample bias (start voltages) within the range of 30 eV to 400 eV. The LEED data measured from different areas were found to vary in the quality of the LEED pattern, *i.e.* the brightness of the LEED

spots and the amount of diffuse scattering, but no variation of the symmetry of the patterns and the positions of the diffraction spots above the noise level were observed, even for the smallest aperture used.

Figure 8.6 **A** shows a LEED image, measured with a 6 μm wide circular aperture and a start voltage of 106 eV, without image normalisation. In addition to the integer spots, the pattern shows diffraction spots at the $q = \pm(0.5, 0)$ and $q = \pm(0, 0.5)$ (marked by red circles). The half-order spots indicate two types of structural domains with doubled periodicity in real space along one or the other direction, *i.e.* with unit cells sized $2a \times a$ and $a \times 2a$. The half-order spots have been observed on all decapped CuMnAs films with clear LEED patterns. In LEED measurements with illumination apertures with a diameter of 6 μm or larger all four half-order spots were observed simultaneously. Measurements with the smallest 400 nm illumination aperture have been hampered by a significant sample drift. As such *i.e.* the real-space variation of the LEED-pattern could not be resolved by scanning the sample in LEED measurements.

The LEED image shown in Fig. 8.6 **A** is part of a scan of LEED images with start-voltages varying within 32 eV to 300 eV with a step-size of 1 eV, with otherwise fixed measurement conditions. The full dataset can be seen in supplementary video S11 available here short.at/awAU9. Figure 8.6 shows LEED-IV curves obtained from the datasets. The curves have been extracted, with local background subtraction, from individual spots of the LEED-scan. Curves from equivalent spots have been averaged, because the positions of the extrema match for curves from different, but equivalent spots.

Additionally, the curves are normalised to the maximal peak intensity and shown with a relative offset between each other.

Most interesting for this work, is, if the structural domains are related to the magnetic order. Therefore, XMLD-PEEM imaging of the AF structure is combined with dark-field LEEM imaging using the fractional-order spots. A high-resolution AF domain image of a representative area is shown in Fig. 8.7 **A**. The image shows two types of AF domains aligned with mutually orthogonal spin

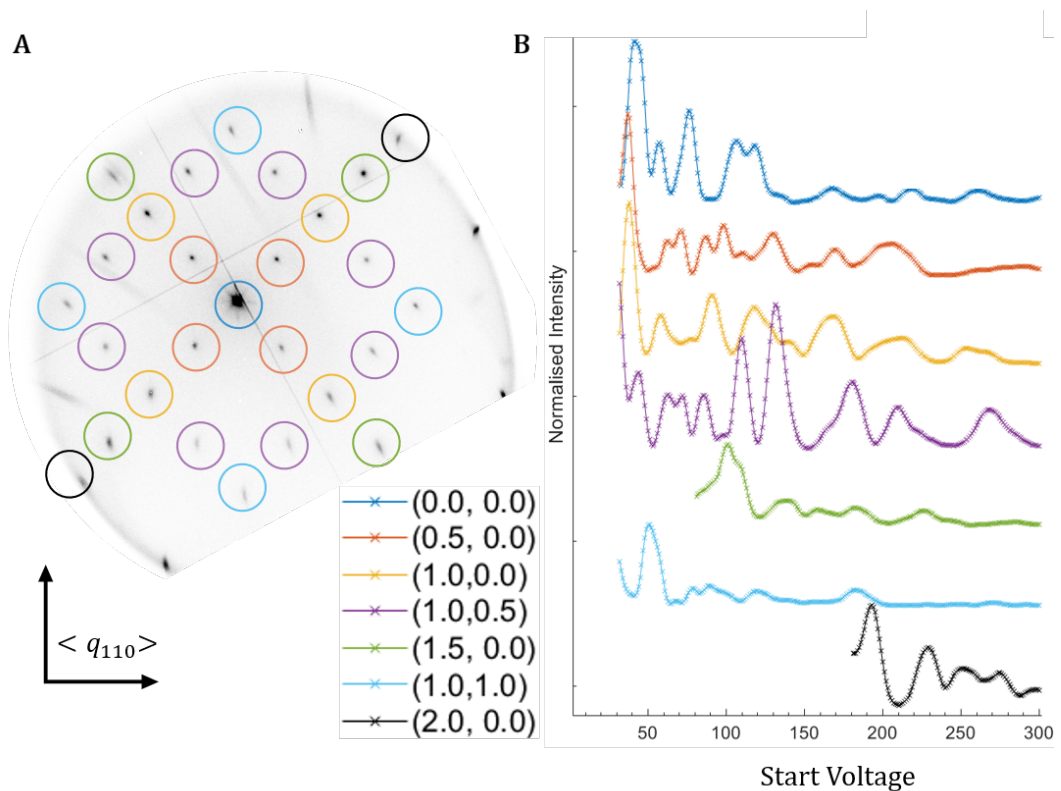


Figure 8.6: LEED-IV of a prepared CuMnAs surface. **A:** LEED image of a prepared CuMnAs surface at a sample bias of 106 eV. The colour scale is inverted, i.e. black is maximal intensity. The coloured circles indicate the labelling of the spots. The sharp edge on the right bottom corner is the edge of the detector. The curved smooth edge is the edge of the electron cone, limited by the imaging optics to below the Ewald sphere. **B:** LEED-IV curves extracted from a LEED-IV scan for the spots indicated in **A**, averaged over equivalent spots. The LEED-IV scan (ranging within 32 eV to 300 eV) can be found in supplementary video S11 available here short.at/awAU9.

axes aligned with the $\langle 110 \rangle$ crystallographic directions. This domain structure is characteristic for CuMnAs films of this thickness grown on GaP (see chapter 3) and has been related to microtwin defects in the samples, which appear as line-defects along the $\langle 110 \rangle$ directions on the surface and locally set a strong uniaxial anisotropy parallel to the microtwin surface termination. The relationship of the AF domains to the microtwin defects in this sample is further confirmed by a bright-field LEEM image of the area shown in Fig. 8.7 C. In this imaging configuration, the microtwins appear as dark or dual coloured horizontal and vertical lines.

In contrast to the clear correlation of the AF domain image and the bright-field LEEM image of the microtwin pattern of the same area, no correlation between

the AF domain image and dark-field LEEM imaging using the half-order spots (Fig. 8.7 **B**) is observed. The image is the asymmetry of dark-field LEEM images with the $\pm(0.5, 0.0)$ and the $\pm(0.0, 0.5)$ spots (see section 8.2.1). Hence maximum intensity (white) indicates areas which contribute to the $\pm(0.5, 0.0)$ diffraction spots, and minimum intensity (black) corresponds to areas which contribute to the $\pm(0.0, 0.5)$ diffraction spots. Grey areas either do not produce fractional order diffraction spots or are composed of structural domains with sizes below the spatial resolution of the LEEM instrument. The imaged area is fragmented into well-defined white, black and regions. This confirms that there are two types of structural domains with periodicity doubling of the unit cells along the $[100]$ (type A) and $[010]$ (type B) crystallographic direction, *i.e.* rectangular unit cells shaped $2a \times a$ and $a \times 2a$.

The average size of the structural domains is at least one order of magnitude smaller than the AF domains. The size of the domains with minimum/maximum intensity approaches the resolution of the instrument. The structural domains generally take the form of narrow stripes oriented with the $[100]$ or $[010]$ axes. Both types of structural domains form stripes along either of those. Thus, the elongated stripe domains can be aligned both parallel and perpendicular to the elongation of the crystallographic unit cell. crystallographic unit cell.

Comparison with the surface topography, imaged with mirror electron microscopy (*i.e.* using the specular reflection and start-voltage close to 0, here 0.5 eV), Fig. 8.7 **D** shows a strong correlation between step edges and the structural domains. Most structural domains directly correlate to a step edge. The structural domains are wider than the contrast of the step edge in the MEM image. The most pronounced step edges seem to correspond to adjacent black-white stripes.

The lack of correlation between the AF domains and the structural domains suggests that the latter are not related to the AF spin axis. In measurements of the LEED pattern upon heating the sample, the half-order spots were found

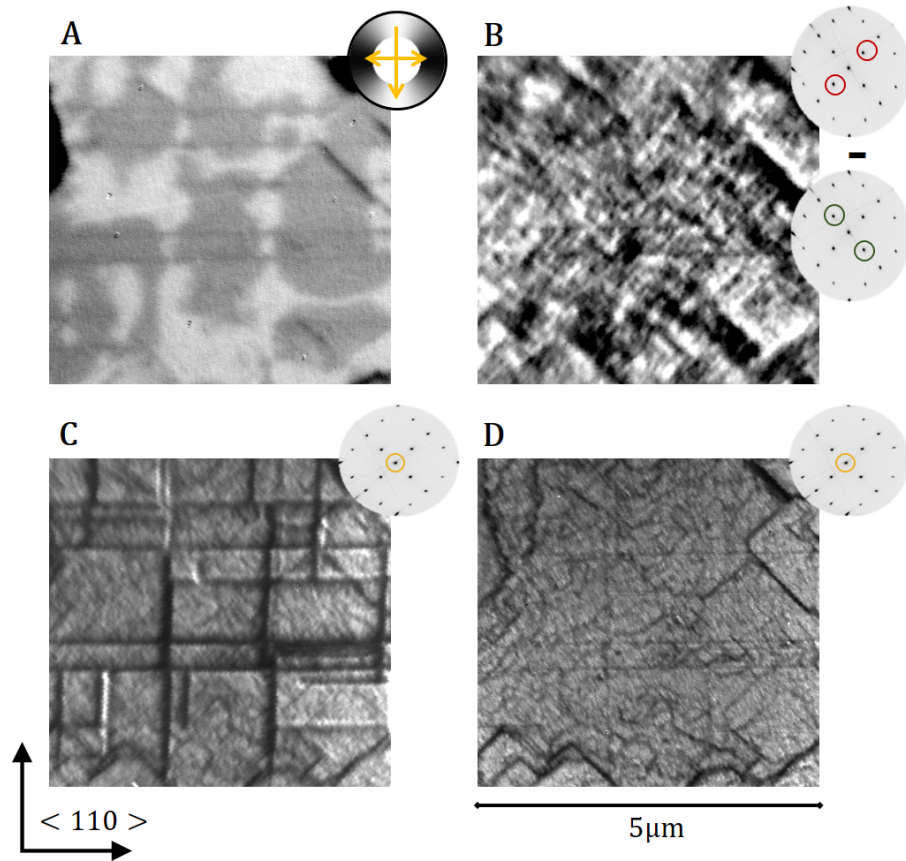


Figure 8.7: Comparison of LEEM imaging of the surface structure and XMLD-PEEM imaging of the AF domains on an exposed CuMnAs surface. **A:** AF domain structure of a typical $5\ \mu\text{m} \times 5\ \mu\text{m}$ large region imaged with XMLD-PEEM and maximum contrast on domains with spin axis along the CuMnAs $\langle 110 \rangle$ directions. **B:** Structural domains of the same area, imaged using the asymmetry of dark-field LEEM images with the half-order spots. **C:** Microtwin structure of the same area measured with bright-field LEEM. **D:** Surface topography of the area measured with mirror electron microscopy. The insets indicate the imaging method.

to persist beyond the Néel temperature, which confirms that the structural domains are not affected by the AF order. Yet, they might well be relevant for the interface coupling in the CuMnAs - Fe bilayers. The fact that the directionality of the structural domain boundaries and the boundaries between mutually antiparallel FM domains match and that the variations occur on similar lengthscales can be seen as indication that both are related to the same crystallographic features.

The next steps would be to resolve the atomic structure of the surface, *e.g.* by fitting theoretical models to the LEED-IV datasets. First attempts of modelling and fitting have been made in collaboration with Prof. G. Held

using the CLEED program package¹, but so far no satisfactory agreement between the theoretical and experimental curves was achieved. Tetragonal CuMnAs crystals have five non-equivalent atomic layers perpendicular to the (001) direction: The copper basal planes and two non-equivalent manganese and arsenic layers each. Modelling of the LEED-IV data was attempted with surface terminations at either of those atomic layers, as illustrated in Fig. 8.8. Thus far, the best agreement was obtained with a model assuming that the surface terminates with the As layer above the Cu basal plane (Fig. 8.8 D), but the fits did not converge.

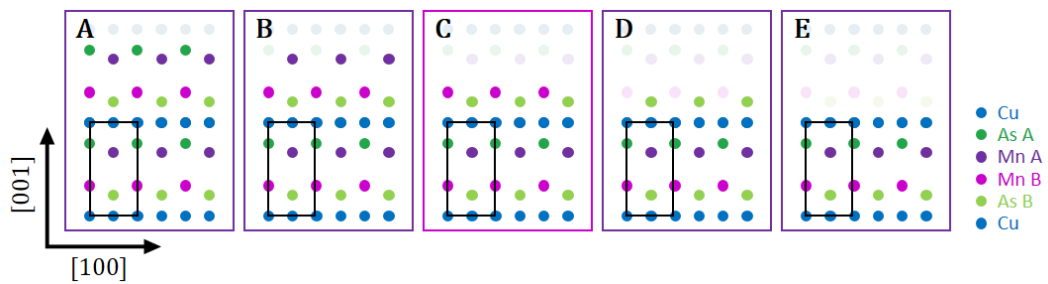


Figure 8.8: Potential terminations of exposed CuMnAs surfaces tested in LEED-IV fitting. Schematic representation of the atomic layer structure (cross section perpendicular to the CuMnAs [100] direction). The small black boxes mark the CuMnAs unit cell of the bulk crystal. The semi-transparent circles show how the crystal would continue in the bulk. Models **A** and **D** were suggested in reference [1]. The large boxes serve to separate the different panels and their colour indicates the uppermost magnetic sublattice. Only in model **C** this is the Mn A lattice. In all other cases, the Mn B is at the top.

Neither a combination of different surface terminations, nor the effect of antiphase boundaries or residual As from the capping layer at the surface was incorporated in the models. Due to the wide input-parameter space for the modelling, further analysis was postponed until information on the surface termination obtained with a different measurement technique are available.

Hypotheses and plan for further analysis

To guide the modelling of the LEED-IV data, scanning tunneling microscopy measurements (STM) of exposed CuMnAs surfaces at Nottingham Univer-

¹available on request

sity were planned, but the measurements were not concluded. Other reports of STM measurements of exposed surfaces of 50 nm CuMnAs/GaP(001) films, prepared and grown in the same way, have been published [140]. The measurements reveal step edges along the CuMnAs $\langle 100 \rangle$ directions and flat plateaus between the step edges. This is consistent with the MEM measurements of the surface topography in this work. Step heights of integer multiples of the out-of-plane lattice constant, $n \cdot c$, consistent with full unit cells as well as smaller step heights (non-integer steps in the following) are reported. Two distinct heights of the non-integer steps matching the distance between adjacent As-layers respectively were reported. On an atomic scale, the non-integer steps revealed a zigzag-like pattern which results in a 2×1 periodicity locally. No such reduced symmetry was reported for the plateau regions. Evidence that all plateaus have the same chemical surface termination has also been obtained by comparing LEED-IV characteristics of different plateaus. The authors in reference [140] suggest that the CuMnAs layer can terminate on either of the two As layers, which would explain the observed step heights. The zigzag-pattern of the non-integer steps was interpreted as As-vacancies at the edge.

However, the authors did not consider the effect of crystallographic defects. In particular, the measured step heights are consistent with the lattice shift across an APB and the direction of the step edge ($\langle 100 \rangle$) matches the direction of the APBs. Hence the data can equally well be explained with a uniquely defined surface termination and step edges coinciding with APBs. Additionally, although the two surface terminations proposed in reference [140] terminate with the same atom, the surfaces can be expected to be chemically very different which renders it unlikely that they show the same LEED-IV characteristics, hence is evidence for the hypothesis that the non-integer steps coincide with APBs and that the surface always terminates with the same crystallographic layer. This model also allows for other explanations of the zigzag-pattern and the reduced symmetry at the interface, which have not been considered before. As such, the author suggests that the STM data and LEED-IV data are re-

analysed taking into account the crystallographic defects.

Successful reanalysis of the LEED-IV also relies on the correct interpretation of the half-order spots. The STM data presented in reference [140] suggests that the reduced symmetry is only located at non-integer steps. This is consistent with the dark-field LEEM images, which show mostly narrow stripes with minimum/maximum intensity oriented on the corresponding crystallographic directions alongside grey areas. The fact that the half-order spots are pronounced in the spatially averaged LEED data must then be attributed to a very high density of step edges. Indeed, in the sample studied in LEEM and LEED, extended plateaus, without visible step edges in the MEM images of the topography are scarce and the distance between neighbouring steps is below 100 nm in many places. Implementing this model in the fitting of the LEED-IV data is not trivial, but would be necessary. If done successfully, evidence of the surface termination of CuMnAs layers might well be obtained. Once the surface structure is resolved the interpretation of the interface-coupled CuMnAs–Fe bilayers needs to be considered. The growth of the As-capped CuMnAs layer used in the STM and LEED/LEEM measurements and the Fe–CuMnAs bilayers follow the same protocol for the CuMnAs growth. Afterwards, the As cap or the Fe surface layers are grown. Hence the surface onto which the Fe layer is grown is the same as the one prior to adding the As cap. Subsequent removal of the As cap could be incomplete, so, if the STM/LEEM measurements reveal an As top layer, this might not be present on the surface onto which the Fe layer is grown. Yet, the atomic layers underneath are most likely to be the same atomic layers onto which the Fe film is grown (with or without As layer). Additionally, interface reactions between the Fe and CuMnAs could mix the uppermost layers and locally shift the atom positions. For this work, it is most relevant to determine if the 180° domain boundaries in the ferromagnetic Fe layer without counterpart in the Mn XMLD-PEEM images of the antiferromagnetic order result from sharp, AF 180° domain boundaries or if they result purely from two adjacent regions with different surface

terminations of the CuMnAs layer (non-trivial step edges) and opposite coupling of the Néel vector to the Fe magnetisation. In reference [53], it has been shown that the Fe magnetisation couples antiparallel to the uppermost magnetic sublattice of the CuMnAs layer. Hence, if the uppermost magnetic layer is always the same, then there is a one-to-one correlation between the direction of the FM magnetisation and the sign of the Néel vector and the narrow 180° domain boundaries in the ferromagnetic Fe would directly reflect the presence of ultra-sharp 180° domain boundaries in the AF CuMnAs film. Otherwise, non-trivial step edges of the CuMnAs film terminating with one magnetic sublattice on one side and the other on the opposite side would result in a ferromagnetic domain boundary, although the AF order is the same on either side.

Below, different scenarios are discussed. First, we consider a defect-free area. Trivial step edges consisting of integer multiples of the CuMnAs unit cell do not need to be considered, since then it is obvious that the coupling between the Néel vector and the Fe magnetisation is the same on either side. The possible non-trivial step edges taken discussed below are selected following the evidence in reference [140]. The work has revealed non-trivial step edges which have the heights corresponding to the distance between the two As sublattices and suggested that the surface always terminates with the same chemical atom. From Fig. 8.8 it can be seen that the only possible configuration in which the Mn B layer is closer to the surface (respective interface) than the Mn A atom is the one terminating exactly on this atomic layer. Hence the only non-trivial step edge with the same chemical element on either side but different top AF sublattice would be obtained when the CuMnAs film terminates with the Mn A layer on one and with the Mn B layer on the other side of the edge. This is illustrated in Fig. 8.9 **A**. Yet, the step heights do not match with the ones reported in reference [140]. The non-trivial step edges brought forward in reference [140] are shown in Fig. 8.9 **B** and **D**. However, here, the magnetic sublattice closest to the surface is the same on either side. Thus,

they can not explain ferromagnetic 180° domain walls without counterpart in the XMLD-PEEM images of the AF order.

We next consider the effect on crystallographic antiphase boundaries propagating to the interface. If the CuMnAs layer terminates with the same atomic layer on either side of the APB, then the step heights match exactly the step heights between two As layers and hence is consistent with reference [140]. According to reference [88], the Néel vector switches sign across these APB. This then results into a sharp 180° FM domain boundary as depicted in Fig. 8.9 C and E. For simplicity this is only shown for one possible interface termination (on the As A layer), but the arguments holds also for all other possible interface terminations, as long as they are the same on either side of the APB. In summary, atomic step edges of the CuMnAs film at the interface coinciding with crystallographic APBs and the same surface termination on either side can explain both the data in reference [140] and the observed ferromagnetic 180° domain walls without counterpart in the XMLD-PEEM images of the exchange-coupled bilayer structures. Consistent with this hypothesis, the directionality of the ferromagnetic 180° domain walls and the crystallographic APBs at the surface (along the CuMnAs $\langle 100 \rangle$) match and the density of crystallographic APBs (estimated to be below 100 nm) is in the same order of magnitude as the FM domain walls.

8.4 Conclusion and outlook

The data presented could form the basis for most interesting research as described in the following. If it can be confirmed that the magnetisation of the Fe layer directly reflect the sign of the Néel vector of the antiferromagnetic CuMnAs films, then imaging the FM domains would be a tool to (almost directly) image the atomically sharp 180° AF domain boundaries. Electrical pulsing experiments in-situ in the XMCD-PEEM chamber (or using a different imaging method of the Fe order), could then be used to provide evidence for

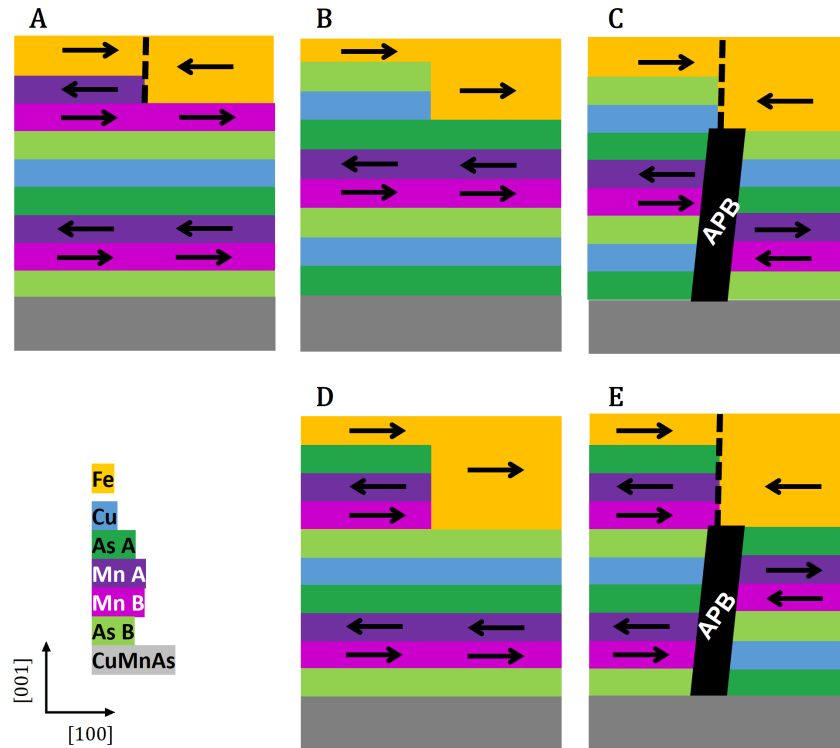


Figure 8.9: *Schematic representation of possible, non-trivial CuMnAs step edges at the interfaces and effect on the Fe magnetisation in CuMnAs-Fe bilayers.* The CuMnAs crystal at the interface is represented in atomic layers. The grey box represents the rest of the CuMnAs film closer to the substrate. The yellow part represents the Fe film. The arrows indicate the direction of the magnetic moment. The layers are not to scale. Dashed black lines indicate a ferromagnetic 180° domain wall. Thick black tilted boxes represent crystallographic APBs. **A:** Step edge between areas terminating on either Mn sublattice resulting in a ferromagnetic domain wall. **B, D:** Step edges suggested in reference [140]. No ferromagnetic domain wall. **E, F:** Step edges coinciding with an APB and the same surface termination on either side and Néel vector reversal across the boundary. They have the same step heights as **B** and **D**, but a ferromagnetic 180° domain wall forms.

or against the presented model in reference [111].

If the reanalysis of the data shows that there are two different ways the CuMnAs layer can couple to the Fe layer, then the sign of the Fe magnetisation is locally defined by the combination of the Néel vector and the surface termination. Hence atomically sharp domain boundaries and purely structural boundaries between different surface terminations could not be distinguished in the stationary state. However, it seems likely that the interface terminations are mostly stable and unaffected by electrical current pulses. Hence an area where the FM magnetisation is coupled antiparallel to the Néel vector will stay

coupled antiparallel and vice versa. Therefore, in electrical pulsing experiments changes in the pattern of sharp domain boundaries between two antiparallel FM domains, without counterpart in XMLD-PEEM measurements of the AF layer, could still be attributed to the creation or annihilation of atomically sharp AF domains boundaries. Thus electrical current pulses combined with imaging of the Fe-domain structure and electrical resistance measurements could provide clear evidence for the model that the high-resistive switching occurs via the formation of atomically sharp AF domain boundary, presented in reference [111]. Therefore, the author of this work highly suggests attempting these experiments since a positive result would be highly beneficial to the understanding of the observations in electrical measurements. The disadvantage of the proposed experiments is that a negative result would not rule out the proposed mechanisms, since the imaging technique is only sensitive to the top interface/surface layer(s) and the formation of domain walls could well be restricted to areas in the bulk, *e.g.* between APBs which do not penetrate up to the interface/surface, which are also commonly observed. Yet direct imaging of those would be considerably more challenging and require sophisticated three-dimensional imaging of the AF structure with sensitivity to the sign. It is not impossible that, considering the recent advances in the development of coherent X-ray imaging techniques such as ptychography alongside the upgrades of several large-scale x-ray light-sources, might in the future provide such a tool, but it currently seems beyond or at least close to the limit of current experimental feasibility.

Chapter 9

Concluding remarks

Tetragonal CuMnAs films have often been mentioned as a key material for AF spintronic research and future AF spintronic device applications. Yet, the microscopic AF domain structure and in-plane anisotropy of samples fabricated from thin films of this material has remained mostly unknown - unless directly imaged, although these are crucial parameter for realising efficient AF spintronic devices and interpreting indirect measurements of AF order, such as electrical measurements.

This thesis is largely concerned with elucidating the AF domain structure in this material. The “material-intrinsic” in-plane anisotropy was found to be almost negligibly small compared to effects from the substrate-film interface, crystallographic defects and patterned edges. The relevance for the AF domain properties which can be described within common continuous micromagnetic theory has been investigated here and a tool to study the recently-proposed ultra-sharp AF domain boundaries, beyond micromagnetic theory, has been proposed in the last chapter. Also for those, crystallographic defects are likely to play an important role.

Crystallographic defects, interfaces, surfaces and edges are what distinguishes a real sample from an ideal, perfect crystal. Hence, the magnetic properties of this material are defined by its imperfections.

The measurements show that “one can get almost any AF domain structure”

from a CuMnAs film, revealing an extreme sensitivity to the crystallographic microstructure. Therefore to date, the first XMLD-PEEM measurement of a new CuMnAs growth has often been a surprise, but this work has shed light on the underlying mechanisms and thus paves and has paved the way for targeted device and domain engineering. For example, patterning along a certain crystallographic direction was already exploited repeatedly to create frustrated AF domain patterns, more susceptible to electric current pulses.

One final gedankenexperiment is missing to conclude this work: What would happen if CuMnAs was ferromagnetic, with otherwise unchanged properties. Then, in magnetostatic energy and long-range magnetic dipole interactions cannot be neglected. These terms are likely to be dominant (along with exchange energy) in finite samples and thus hide the effects of the crystallographic micro- and nanostructure.

Hence, it is the weak intrinsic in-plane anisotropy (material-specific) combined with the lack of magnetic stray fields (characteristic for all AFs) in antiferromagnetic CuMnAs which yields the important role of the crystallographic microstructure on the AF domain pattern.

Thus, this thesis shows the potential of AF materials for targeted domain engineering, but also highlights that the crystallographic microstructure can not be neglected in the theoretical description of antiferromagnetic structures and AF devices.

Bibliography

- [1] E. Du Trémolet de Lacheisserie, U. J. Fourier, D. Gignoux, and M. Schlenker, *Magnetism*, ser. Collection Grenoble Sciences. Springer, 2005, no. v. 1. [Online]. Available: <https://books.google.co.uk/books?id=MgCExarQD08C>
- [2] L. Shu-hua, “Origine de la boussole ii. aimant et boussole,” *Isis*, vol. 45, no. 2, pp. 175–196, 1954. [Online]. Available: <https://doi.org/10.1086/348315>
- [3] R. K. Goyal, *Nanomaterials and Nanocomposites: Synthesis, Properties, Characterization Techniques, and Applications*. CRC Press, 2017. [Online]. Available: <https://doi.org/10.1201/9781315153285>
- [4] G. Florio, “Applications of magnetic materials,” in *Reference Module in Materials Science and Materials Engineering*. Elsevier, 2021. [Online]. Available: <https://www.sciencedirect.com/science/article/pii/B978012815732900067X>
- [5] S. A. Wolf, D. D. Awschalom, R. A. Buhrman, J. M. Daughton, S. von Molnár, M. L. Roukes, A. Y. Chtchelkanova, and D. M. Treger, “Spintronics: A Spin-Based Electronics Vision for the Future,” *Science*, vol. 294, no. 5546, pp. 1488–1495, 2001. [Online]. Available: <http://science.sciencemag.org/content/294/5546/1488>
- [6] A. Hirohata, K. Yamada, Y. Nakatani, I.-L. Prejbeanu, B. Diény, P. Pirro, and B. Hillebrands, “Review on spintronics: Principles and device applications,” *Journal of Magnetism and Magnetic Materials*, vol. 509, p. 166711, 2020. [Online]. Available: <https://www.sciencedirect.com/science/article/pii/S0304885320302353>
- [7] *Antiferromagnetism*. John Wiley & Sons, Ltd, 2008, ch. 5, pp. 151–173. [Online]. Available: <https://onlinelibrary.wiley.com/doi/abs/10.1002/9780470386323.ch5>
- [8] T. Jungwirth, X. Marti, P. Wadley, and J. Wunderlich, “Antiferromagnetic spintronics,” *Nature Nanotechnology*, vol. 11, no. 3, pp. 231–241, 2016. [Online]. Available: <https://doi.org/10.1038/nnano.2016.18>
- [9] S. Loth, S. Baumann, C. P. Lutz, D. Eigler, and A. J. Heinrich, “Bistability in atomic-scale antiferromagnets,” *Science*, vol. 335, no. 6065, pp. 196–199, 2012.

- [10] V. Baltz, A. Manchon, M. Tsoi, T. Moriyama, T. Ono, and Y. Tserkovnyak, “Antiferromagnetic spintronics,” *Rev. Mod. Phys.*, vol. 90, p. 015005, Feb 2018. [Online]. Available: <https://link.aps.org/doi/10.1103/RevModPhys.90.015005>
- [11] P. Wadley, B. Howells, J. Železný, C. Andrews, V. Hills, R. P. Campion, V. Novák, K. Olejník, F. Maccherozzi, S. S. Dhesi, S. Y. Martin, T. Wagner, J. Wunderlich, F. Freimuth, Y. Mokrousov, J. Kuneš, J. S. Chauhan, M. J. Grzybowski, A. W. Rushforth, K. W. Edmonds, B. L. Gallagher, and T. Jungwirth, “Electrical switching of an antiferromagnet,” *Science*, vol. 351, no. 6273, pp. 587–590, 2016. [Online]. Available: <http://science.sciencemag.org/content/351/6273/587>
- [12] E. V. Gomonay and V. M. Loktev, “Spintronics of antiferromagnetic systems (review article),” *Low Temperature Physics*, vol. 40, no. 1, pp. 17–35, 2014. [Online]. Available: <https://doi.org/10.1063/1.4862467>
- [13] N. L. Schryer and L. R. Walker, “The motion of 180° domain walls in uniform dc magnetic fields,” *Journal of Applied Physics*, vol. 45, no. 12, pp. 5406–5421, 1974. [Online]. Available: <https://doi.org/10.1063/1.1663252>
- [14] O. J. Amin, K. W. Edmonds, and P. Wadley, “Electrical control of antiferromagnets for the next generation of computing technology,” *Applied Physics Letters*, vol. 117, no. 1, p. 010501, 2020. [Online]. Available: <https://doi.org/10.1063/5.0013917>
- [15] J. Sklenar, W. Zhang, M. B. Jungfleisch, W. Jiang, H. Saglam, J. E. Pearson, J. B. Ketterson, and A. Hoffmann, “Spin hall effects in metallic antiferromagnets—perspectives for future spin-orbitronics,” *AIP Advances*, vol. 6, no. 5, p. 055603, 2016.
- [16] A. MacDonald and M. Tsoi, “Antiferromagnetic metal spintronics,” *Philosophical Transactions of the Royal Society of London A: Mathematical, Physical and Engineering Sciences*, vol. 369, no. 1948, pp. 3098–3114, 2011.
- [17] D. J. Griffiths, *Introduction to electrodynamics; 4th ed.* Boston, MA: Pearson, 2013, re-published by Cambridge University Press in 2017. [Online]. Available: <https://cds.cern.ch/record/1492149>
- [18] N. W. Ashcroft and N. D. Mermin, *Solid State Physics*. Holt-Saunders, 1976.
- [19] S. Blundell, *Magnetism in condensed matter*, ser. Oxford master series in condensed matter physics. Oxford: Oxford University Press, 2001.
- [20] C. Kittel, *Introduction to solid state physics*. Wiley, 1971.
- [21] L. Néel, “Propriétés magnétiques de l’état métallique et énergie d’interaction entre atomes magnétiques,” *Annales De Physique*, vol. 11,

- no. 5, pp. 232–279, 1936, annales de Physique, Review articles or monographs on all aspects of physics. [Online]. Available: <https://hal.archives-ouvertes.fr/hal-02888365>
- [22] Néel, L., “Influence des fluctuations du champ moléculaire sur les propriétés magnétiques des corps,” *Ann. Phys.*, vol. 10, no. 18, pp. 5–105, 1932. [Online]. Available: <https://doi.org/10.1051/anphys/193210180005>
- [23] Néel, M. Louis, “Propriétés magnétiques des ferrites ; ferrimagnétisme et antiferromagnétisme,” *Ann. Phys.*, vol. 12, no. 3, pp. 137–198, 1948. [Online]. Available: <https://doi.org/10.1051/anphys/194812030137>
- [24] E. Coronado, B. S. Tsukerblat, and R. Georges, *Exchange Interactions I: Mechanisms*. Dordrecht: Springer Netherlands, 1996, pp. 65–84. [Online]. Available: https://doi.org/10.1007/978-94-017-2319-0_3
- [25] A. Hubert and R. Schäfer, *Magnetic Domains: The Analysis of Magnetic Microstructures*. Springer, 1998. [Online]. Available: <https://books.google.co.uk/books?id=pBE42ILYs-MC>
- [26] T. Moriya, “Anisotropic superexchange interaction and weak ferromagnetism,” *Phys. Rev.*, vol. 120, pp. 91–98, Oct 1960. [Online]. Available: <https://link.aps.org/doi/10.1103/PhysRev.120.91>
- [27] I. Dzyaloshinsky, “A thermodynamic theory of “weak” ferromagnetism of antiferromagnetics,” *Journal of Physics and Chemistry of Solids*, vol. 4, no. 4, pp. 241–255, Jan. 1958.
- [28] L. M. Sandratskii, “Insight into the dzyaloshinskii-moriya interaction through first-principles study of chiral magnetic structures,” *Phys. Rev. B*, vol. 96, p. 024450, Jul 2017. [Online]. Available: <https://link.aps.org/doi/10.1103/PhysRevB.96.024450>
- [29] J. Nogués and I. K. Schuller, “Exchange bias,” *Journal of Magnetism and Magnetic Materials*, vol. 192, no. 2, pp. 203–232, 1999. [Online]. Available: <https://www.sciencedirect.com/science/article/pii/S0304885398002662>
- [30] R. L. Stamps, “Mechanisms for exchange bias,” *Journal of Physics D: Applied Physics*, vol. 33, no. 23, pp. R247–R268, nov 2000. [Online]. Available: <https://doi.org/10.1088/0022-3727/33/23/201>
- [31] M. Stiles, *Interlayer Exchange Coupling*. Ultrathin Magnetic Structures III, Springer-Verlag, New York, NY, 2004-12-13 2004, no. 200. [Online]. Available: https://tsapps.nist.gov/publication/get_pdf.cfm?pub_id=620544
- [32] T. Blachowicz and A. Ehrmann, “Exchange bias in thin films—an update,” *Coatings*, vol. 11, no. 2, 2021. [Online]. Available: <https://www.mdpi.com/2079-6412/11/2/122>

- [33] Y. Kato, R. Myers, A. Gossard, and D. Awschalom, “Current-induced spin polarization in strained semiconductors,” *Physical review letters*, vol. 93, no. 17, p. 176601, 2004.
- [34] A. Y. Silov, P. Blajnov, J. Wolter, R. Hey, K. Ploog, and N. Averkiev, “Current-induced spin polarization at a single heterojunction,” *Applied physics letters*, vol. 85, no. 24, pp. 5929–5931, 2004.
- [35] J. Wunderlich, B. Kaestner, J. Sinova, and T. Jungwirth, “Experimental discovery of the spin-hall effect in rashba spin-orbit coupled semiconductor systems,” *Preprint on arXiv*, 2004. [Online]. Available: <http://arxiv.org/abs/cond-mat/0410295v1>
- [36] Q. Liu, X. Zhang, J.-W. Luo, A. Freeman, and A. Zunger, “Hidden spin polarization in inversion-symmetric bulk crystals,” in *APS March Meeting Abstracts*, 2014.
- [37] J. Železný, H. Gao, K. Výborný, J. Zemen, J. Mašek, A. Manchon, J. Wunderlich, J. Sinova, and T. Jungwirth, “Relativistic néel-order fields induced by electrical current in antiferromagnets,” *Phys. Rev. Lett.*, vol. 113, p. 157201, Oct 2014. [Online]. Available: <https://link.aps.org/doi/10.1103/PhysRevLett.113.157201>
- [38] C. Kittel, “Physical theory of ferromagnetic domains,” *Rev. Mod. Phys.*, vol. 21, pp. 541–583, Oct 1949. [Online]. Available: <https://link.aps.org/doi/10.1103/RevModPhys.21.541>
- [39] O. Gomonay, V. Baltz, A. Brataas, and Y. Tserkovnyak, “Antiferromagnetic spin textures and dynamics,” *Nature Physics*, vol. 14, no. 3, pp. 213–216, 2018. [Online]. Available: <https://doi.org/10.1038/s41567-018-0049-4>
- [40] K. Everschor, “Current-induced dynamics of chiral magnetic structures: Skyrmions, emergent electrodynamics and spin-transfer torques,” Ph.D. dissertation, Universität zu Köln, 2012. [Online]. Available: <https://kups.ub.uni-koeln.de/4811/>
- [41] E. Gomonay and V. Loktev, “Magnetostriction and domain structure in antiferromagnets,” *J. Magn. Magn. Mat.*, vol. 242-245, pp. 1418–1420, apr 2002. [Online]. Available: <http://linkinghub.elsevier.com/retrieve/pii/S030488530100960X>
- [42] O. Gomonay, S. Kondovych, and V. Loktev, “Shape-induced anisotropy in antiferromagnetic nanoparticles,” *J. Magn. Magn. Mat.*, vol. 354, pp. 125–135, 2014. [Online]. Available: <https://doi.org/10.1016/j.jmmm.2013.11.003>
- [43] E. Folven, Y. Takamura, and J. K. Grepstad, “X-peem study of antiferromagnetic domain patterns in lafeo3 thin films and embedded nanostructures,” *Journal of Electron Spectroscopy and Related Phenomena*, vol. 185, no. 10, pp. 381 – 388, 2012, photoelectron microscopy, Time resolved pump-probe PES. [Online]. Available: <http://www.sciencedirect.com/science/article/pii/S0368204812000734>

- [44] O. Gomonay, T. Jungwirth, and J. Sinova, “High antiferromagnetic domain wall velocity induced by néel spin-orbit torques,” *Phys. Rev. Lett.*, vol. 117, p. 017202, Jun 2016. [Online]. Available: <https://link.aps.org/doi/10.1103/PhysRevLett.117.017202>
- [45] P. Wadley, V. Novak, R. P. Campion, C. Rinaldi, X. Martí, H. Reichlova, J. Zelezny, J. Gazquez, M. A. Roldan, M. Varela, D. Khalyavin, S. Langridge, D. Kriegner, F. Maca, J. Masek, R. Bertacco, V. Holy, A. W. Rushforth, K. W. Edmonds, B. L. Gallagher, C. T. Foxon, J. Wunderlich, and T. Jungwirth, “Tetragonal phase of epitaxial room-temperature antiferromagnet CuMnAs,” *Nat. Commun.*, vol. 4, p. 2322, 2013.
- [46] F. Krizek, Z. c. v. Kašpar, A. Vetushka, D. Kriegner, E. M. Fiordaliso, J. Michalicka, O. c. v. Man, J. Zubáč, M. Brajer, V. A. Hills, K. W. Edmonds, P. Wadley, R. P. Campion, K. Olejník, T. c. v. Jungwirth, and V. Novák, “Molecular beam epitaxy of cumnas,” *Phys. Rev. Materials*, vol. 4, p. 014409, Jan 2020. [Online]. Available: <https://link.aps.org/doi/10.1103/PhysRevMaterials.4.014409>
- [47] F. Máca, J. Mašek, O. Stelmakhovych, X. Martí, H. Reichlová, K. Uhlířová, P. Beran, P. Wadley, V. Novák, and T. Jungwirth, “Room-temperature antiferromagnetism in CuMnAs,” *Journal of Magnetism and Magnetic Materials*, vol. 324, no. 8, pp. 1606–1612, 2012.
- [48] F. Maca, J. Kudrnovský, V. Drchal, K. Carva, P. Baláž, and I. Turek, “Physical properties of the tetragonal cumnas: A first-principles study,” *Physical Review B*, vol. 96, 08 2017.
- [49] P. Wadley, V. Hills, M. R. Shahedkhah, K. W. Edmonds, R. P. Campion, V. Novák, B. Ouladdiaf, D. Khalyavin, S. Langridge, V. Saidl, P. Nemeč, A. W. Rushforth, B. L. Gallagher, S. S. Dhesi, F. Maccherozzi, J. Železný, and T. Jungwirth, “Antiferromagnetic structure in tetragonal cumnas thin films,” *Scientific Reports*, vol. 5, no. 1, p. 17079, 2015. [Online]. Available: <https://doi.org/10.1038/srep17079>
- [50] T. Matalla-Wagner, M.-F. Rath, D. Graulich, J.-M. Schmalhorst, G. Reiss, and M. Meinert, “Electrical néel-order switching in magnetron-sputtered cumnas thin films,” *Physical Review Applied*, vol. 12, no. 6, Dec 2019. [Online]. Available: <http://dx.doi.org/10.1103/PhysRevApplied.12.064003>
- [51] V. A. Hills, “MBE growth, characterisation and physics of antiferromagnetic copper manganese arsenide,” Ph.D. dissertation, University of Nottingham, 2016.
- [52] B. Park, J. Wunderlich, X. Martí, V. Holý, Y. Kurosaki, M. Yamada, H. Yamamoto, A. Nishide, J. Hayakawa, H. Takahashi *et al.*, “A spin-valve-like magnetoresistance of an antiferromagnet-based tunnel junction,” *Nature materials*, vol. 10, no. 5, p. 347, 2011.
- [53] P. Wadley, V. Hills, M. R. Shahedkhah, K. W. Edmonds, R. P. Campion, V. Novak, B. Ouladdiaf, D. Khalyavin, S. Langridge, V. Saidl, P. Nemeč,

- A. W. Rushforth, B. L. Gallagher, S. S. Dhesi, F. Maccherozzi, J. Zelezny, and T. Jungwirth, “Control of antiferromagnetic spin axis orientation in bilayer Fe/CuMnAs films,” *Sci. Rep.*, vol. 5, p. 17079, 2015.
- [54] A. Y. Cho and J. Arthur, “Molecular beam epitaxy,” *Progress in solid state chemistry*, vol. 10, pp. 157–191, 1975.
- [55] W. P. McCray, “Mbe deserves a place in the history books,” *Nature nanotechnology*, vol. 2, no. 5, pp. 259–261, 2007.
- [56] V. L. Ginzburg and S. I. Syrovatskii, “Cosmic magnetobremstrahlung (synchrotron radiation),” *Annual Review of Astronomy and Astrophysics*, vol. 3, no. 1, pp. 297–350, 1965. [Online]. Available: <https://doi.org/10.1146/annurev.aa.03.090165.001501>
- [57] G. A. Schott, *Electromagnetic radiation and the mechanical reactions arising from it: being an Adams Prize Essay in the University of Cambridge*. University Press, 1912.
- [58] H. Bulou, L. Joly, J.-M. Mariot, and F. Scheurer, *Magnetism and Accelerator-Based Light Sources Proceedings of the 7th International School “Synchrotron Radiation and Magnetism”, Mittelwihr (France), 2018: Proceedings of the 7th International School “Synchrotron Radiation and Magnetism”, Mittelwihr (France), 2018*, 01 2021.
- [59] F. R. Elder, A. M. Gurewitsch, R. V. Langmuir, and H. C. Pollock, “Radiation from electrons in a synchrotron,” *Phys. Rev.*, vol. 71, pp. 829–830, Jun 1947. [Online]. Available: <https://link.aps.org/doi/10.1103/PhysRev.71.829.5>
- [60] H. C. Pollock, “Combination of betatron and synchrotron for electron acceleration,” *Phys. Rev.*, vol. 69, pp. 125–125, Feb 1946. [Online]. Available: <https://link.aps.org/doi/10.1103/PhysRev.69.125>
- [61] *Synchrotron Physics*. John Wiley & Sons, Ltd, 2019. [Online]. Available: <https://onlinelibrary.wiley.com/doi/abs/10.1002/9781119280453.ch3>
- [62] D. L. Source, “Science& Machine,” <https://www.diamond.ac.uk/Science/Machine.html>, 09 2021.
- [63] M. Hand, H. Wang, F. Maccherozzi, M. Apollonio, J. Zhu, S. S. Dhesi, and K. Sawhney, “Quantitative investigation of linear arbitrary polarization in an APPLE-II undulator,” *Journal of Synchrotron Radiation*, vol. 25, no. 2, pp. 378–384, Mar 2018. [Online]. Available: <https://doi.org/10.1107/S1600577518001960>
- [64] Tavares, Pedro F. and Al-Dmour, Eshraq and Andersson, Åke and Cullinan, Francis and Jensen, Brian N. and Olsson, David and Olsson, David K. and Sjöström, Magnus and Tarawneh, Hamed and Thorin, Sara and Vorozhtsov, Alexey, “Commissioning and first-year operational results of the MAX IV 3 GeV ring,” *Journal of synchrotron radiation*, vol. 25, no. Pt 5, pp. 1291–1316, 2018.

- [Online]. Available: <https://pubmed.ncbi.nlm.nih.gov/30179168https://www.ncbi.nlm.nih.gov/pmc/articles/PMC6140400/>
- [65] M. IV, “Accelerators & beamlines – beamlines – nanomax – beamline optics,” <https://www.maxiv.lu.se/accelerators-beamlines/beamlines/nanomax/optics/>, 09 2021.
- [66] A. Björling, S. Kalbfleisch, M. Kahnt, S. Sala, K. Parfeniukas, U. Vogt, D. Carbone, and U. Johansson, “Ptychographic characterization of a coherent nanofocused x-ray beam,” *Opt. Express*, vol. 28, no. 4, pp. 5069–5076, Feb 2020. [Online]. Available: <http://www.osapublishing.org/oe/abstract.cfm?URI=oe-28-4-5069>
- [67] D. Carbone and et al., Design and Performance of NanoMAX diffraction endstation, manuscript in preparation for *Journal of Synchrotron Radiation*.
- [68] M. IV, “Accelerators & beamlines – beamlines – nanomax – diffraction station,” <https://www.maxiv.lu.se/accelerators-beamlines/beamlines/nanomax/diffraction-station/>, 09 2021.
- [69] P. Fischer, T. Eimüller, G. Schütz, and G. Denbeaux, “Imaging magnetic domain structures with soft x-ray microscopy,” *Structural Chemistry*, vol. 14, no. 1, pp. 39–47, 2003. [Online]. Available: <https://doi.org/10.1023/A:1021612908943>
- [70] A. Yaresko, A. Perlov, V. Antonov, and B. Harmon, “Band-structure theory of dichroism,” *Lecture Notes in Physics*, vol. 697, pp. 121–141, 2006.
- [71] G. van der Laan, N. D. Telling, A. Potenza, S. S. Dhesi, and E. Arenholz, “Anisotropic x-ray magnetic linear dichroism and spectromicroscopy of interfacial co/nio(001),” *Phys. Rev. B*, vol. 83, p. 064409, Feb 2011. [Online]. Available: <https://link.aps.org/doi/10.1103/PhysRevB.83.064409>
- [72] S. Amelinckx, D. van Dyck, J. van Landuyt, and G. van Tendeloo, *Electron Microscopy: Principles and Fundamentals*. Wiley, 2008. [Online]. Available: <https://books.google.co.uk/books?id=VgkBEidIU8C>
- [73] Elmitec, “Elmitec - leem imaging modes,” <https://elmitec.de/Leem.php?Bereich=Imaging>, 09 2021.
- [74] E. Bauer, “Surface microscopy with low energy electrons: Leem,” *Journal of Electron Spectroscopy and Related Phenomena*, vol. 241, p. 146806, 2020, sources, Interaction with Matter, Detection and Analysis of Low Energy Electrons (SIMDALEE2). [Online]. Available: <https://www.sciencedirect.com/science/article/pii/S0368204818301737>
- [75] G. Held, “Low-energy electron diffraction crystallography of surfaces and interfaces,” *Bunsen-Magazin 12*, no. 12, pp. 124–131, April 2010. [Online]. Available: <http://centaur.reading.ac.uk/15540/>

- [76] D. L. Source, “Photo of peem, preparation chamber and load-lock.” <https://www.diamond.ac.uk/Instruments/Magnetic-Materials/I06/sample.html>, 09 2021.
- [77] T. Schmidt, S. Heun, J. Slezak, J. Diaz, K. C. Prince, G. Lilienkamp, and E. Bauer, “Speleem: Combining leem and spectroscopic imaging,” *Surface Review and Letters*, vol. 05, no. 06, pp. 1287–1296, 1998. [Online]. Available: <https://doi.org/10.1142/S0218625X98001626>
- [78] P. AG, “pco.2000 product sheet 08/2008,” https://www.pco.de/fileadmin/user_upload/db/products/datasheet/pco2000_20080805.pdf, 09 2021.
- [79] M. Collaboration, “Medipix. a family of pixel detector read-out chips for particle imaging and detection developed by the medipix collaborations,” <https://medipix.web.cern.ch/>, 09 2021.
- [80] I. Sikharulidze, R. van Gastel, S. Schramm, J. Abrahams, B. Poelsema, R. Tromp, and S. van der Molen, “Low energy electron microscopy imaging using medipix2 detector,” *Nuclear Instruments and Methods in Physics Research Section A: Accelerators, Spectrometers, Detectors and Associated Equipment*, vol. 633, pp. S239–S242, 2011, 11th International Workshop on Radiation Imaging Detectors (IWORID). [Online]. Available: <https://www.sciencedirect.com/science/article/pii/S0168900210013677>
- [81] Elmitec, “LEEM2000 Control Software for Elmitec Electron Microscopes – LEEM2000 software developed by Uwe Knipping,” Manual, 2013.
- [82] S. Poole, “Leem-analysis routines,” <https://github.com/stupoole/LEEM-analysis>, 09 2021.
- [83] T. A. de Jong, “Leem-analysis routines,” <https://github.com/TAdJong/LEEM-analysis/releases/tag/v0.2.1>, 09 2021.
- [84] T. de Jong, D. Kok, A. van der Torren, H. Schopmans, R. Tromp, S. van der Molen, and J. Jobst, “Quantitative analysis of spectroscopic low energy electron microscopy data: High-dynamic range imaging, drift correction and cluster analysis,” *Ultramicroscopy*, vol. 213, p. 112913, Jun 2020. [Online]. Available: <http://dx.doi.org/10.1016/j.ultramic.2019.112913>
- [85] Bryn Howells, “Studies of spin-orbit coupling phenomena in magnetic semiconductors,” Ph.D. dissertation, School of Physics and Astronomy, The University of Nottingham, Nottingham, 2015. [Online]. Available: <http://eprints.nottingham.ac.uk/29005/1/Bryn%20Howells%20Thesis%20corrected%201st%20May.pdf>
- [86] D. Kriegner, E. Wintersberger, and J. Stangl, “*xrayutilities*: a versatile tool for reciprocal space conversion of scattering data recorded with linear and area detectors,” *Journal of Applied Crystallography*, vol. 46, no. 4, pp. 1162–1170, Aug 2013. [Online]. Available: <https://doi.org/10.1107/S0021889813017214>

- [87] C. Teodosiu, *Elastic Models of Crystal Defects*. Berlin, Heidelberg: Springer Berlin Heidelberg, 1982. [Online]. Available: <http://link.springer.com/10.1007/978-3-662-11634-0>
- [88] F. Krizek, S. Reimers, Z. Kašpar, A. Marmodoro, J. Michalička, O. Man, A. Edstrom, O. J. Amin, K. W. Edmonds, R. P. Champion, F. Maccherozzi, S. S. Dnes, J. Zubáč, J. Železný, K. Výborný, K. Olejník, V. Novák, J. Rusz, J. C. Idrobo, P. Wadley, and T. Jungwirth, “Atomically sharp domain walls in an antiferromagnet,” 2020. [Online]. Available: <https://arxiv.org/abs/2012.00894>
- [89] M. Wang, C. Andrews, S. Reimers, O. J. Amin, P. Wadley, R. P. Champion, S. F. Poole, J. Felton, K. W. Edmonds, B. L. Gallagher, A. W. Rushforth, O. Makarovskiy, K. Gas, M. Sawicki, D. Kriegner, J. Zubáč, K. Olejník, V. Novák, T. Jungwirth, M. Shahrokhvand, U. Zeitler, S. S. Dhesi, and F. Maccherozzi, “Spin flop and crystalline anisotropic magnetoresistance in cumnas,” *Phys. Rev. B*, vol. 101, p. 094429, Mar 2020. [Online]. Available: <https://link.aps.org/doi/10.1103/PhysRevB.101.094429>
- [90] G. Wastlbauer and J. A. C. B. *, “Structural and magnetic properties of ultrathin epitaxial fe films on gaas(001) and related semiconductor substrates,” *Advances in Physics*, vol. 54, no. 2, pp. 137–219, 2005. [Online]. Available: <https://doi.org/10.1080/00018730500112000>
- [91] A. T. HINDMARCH, “Interface magnetism in ferromagnetic metal–compound semiconductor hybrid structures,” *SPIN*, vol. 01, no. 01, pp. 45–69, 2011. [Online]. Available: <https://doi.org/10.1142/S2010324711000069>
- [92] O. J. Amin, “Ph.D. dissertation in preparation,” 2021, The University of Nottingham.
- [93] L. Barton, “Ph.D. dissertation in preparation,” 2021, The University of Nottingham.
- [94] M. J. Grzybowski, P. Wadley, K. W. Edmonds, R. Beardsley, V. Hills, R. P. Champion, B. L. Gallagher, J. S. Chauhan, V. Novak, T. Jungwirth, F. Maccherozzi, and D. S. S., “Imaging Current-Induced Switching of Antiferromagnetic Domains in CuMnAs,” *Phys. Rev. Lett.*, vol. 118, no. 5, p. 057701, jan 2017. [Online]. Available: <https://journals.aps.org/prl/abstract/10.1103/PhysRevLett.118.057701>
- [95] Michał Jakub Grzybowski, “Electrical manipulation of the domain structure of antiferromagnetic cumnas,” Ph.D. dissertation, Polish Academy of Sciences, Institute of Physics, International Centre for Interfacing Magnetism and Superconductivity with Topological Matter – MagTop, Warszawa, 2019.
- [96] Sonka Reimers, “Electrical manipulation of cumnas thin film devices,” Master Thesis, 1. Physikalisches Institut, Georg-August Universität Göttingen in collaboration with School of Physics and Astronomy, The University of Nottingham, Göttingen, 2018.

- [97] K. Olejník, T. Seifert, Z. Kašpar, V. Novák, P. Wadley, R. P. Champion, M. Baumgartner, P. Gambardella, P. Němec, J. Wunderlich, J. Sinova, P. Kužel, M. Müller, T. Kampfrath, and T. Jungwirth, “Terahertz electrical writing speed in an antiferromagnetic memory,” *Science Advances*, vol. 4, no. 3, 2018. [Online]. Available: <https://advances.sciencemag.org/content/4/3/eaar3566>
- [98] M. Meinert, D. Graulich, and T. Matalla-Wagner, “Electrical switching of antiferromagnetic mn_2Au and the role of thermal activation,” *Phys. Rev. Applied*, vol. 9, p. 064040, Jun 2018. [Online]. Available: <https://link.aps.org/doi/10.1103/PhysRevApplied.9.064040>
- [99] L. Baldrati, O. Gomonay, A. Ross, M. Filianina, R. Lebrun, R. Ramos, C. Leveille, F. Fuhrmann, T. R. Forrest, F. Maccherozzi, S. Valencia, F. Kronast, E. Saitoh, J. Sinova, and M. Kläui, “Mechanism of Néel Order Switching in Antiferromagnetic Thin Films Revealed by Magnetotransport and Direct Imaging,” *Phys. Rev. Lett.*, vol. 123, no. 17, p. 177201, oct 2019. [Online]. Available: <https://journals.aps.org/prl/abstract/10.1103/PhysRevLett.123.177201>
- [100] Z. Kašpar, M. Surynek, J. Zubac, F. Krizek, V. Novak, R. P. Champion, M. S. Wornle, P. Gambardella, X. Marti, P. Nemeč, K. W. Edmonds, S. Reimers, O. J. Amin, F. Maccherozzi, S. S. Dhesi, P. Wadley, J. Wunderlich, K. Olejník, and T. Jungwirth, “Quenching of an antiferromagnet into high resistivity states using electrical or ultrashort optical pulses,” *Nature Electron.*, vol. 4, p. 30, 2021.
- [101] H. Meer, F. Schreiber, C. Schmitt, R. Ramos, E. Saitoh, O. Gomonay, J. Sinova, L. Baldrati, and M. Kläui, “Direct Imaging of Current-Induced Antiferromagnetic Switching Revealing a Pure Thermomagnetoelastic Switching Mechanism in NiO,” *Nano Lett.*, vol. 21, p. 114, 2021.
- [102] P. Wadley, S. Reimers, M. J. Grzybowski, C. Andrews, M. Wang, J. S. Chauhan, B. L. Gallagher, R. P. Champion, K. W. Edmonds, S. S. Dhesi, F. Maccherozzi, V. Novak, J. Wunderlich, and T. Jungwirth, “Current polarity-dependent manipulation of antiferromagnetic domains,” *Nat. Nanotechnol.*, vol. 13, no. 1, pp. 362–365, mar 2018. [Online]. Available: <https://www.nature.com/articles/s41565-018-0079-1>
- [103] S. Y. Bodnar, M. Filianina, S. P. Bommanaboyena, T. Forrest, F. Maccherozzi, A. A. Sapozhnik, Y. Skourski, M. Kläui, and M. Jourdan, “Imaging of current induced Néel vector switching in antiferromagnetic Mn_2Au ,” *Phys. Rev. B*, vol. 99, no. 14, p. 140409, mar 2019. [Online]. Available: <https://journals.aps.org/prb/abstract/10.1103/PhysRevB.99.140409>
- [104] T. Janda, J. Godinho, T. Ostatnický, E. Pfitzner, G. Ulrich, A. Hoehl, S. Reimers, Z. Šobáň, T. Metzger, H. Reichlová, V. Novák, R. P. Champion, J. Heberle, P. Wadley, K. W. Edmonds, O. J. Amin, J. S. Chauhan, S. S. Dhesi, F. Maccherozzi, R. M. Otxoa, P. E. Roy,

- K. Olejník, P. Němec, T. Jungwirth, B. Kaestner, and W. J., “Magneto-Seebeck microscopy of domain switching in collinear antiferromagnet CuMnAs,” *Phys. Rev. Mater.*, vol. 4, no. 9, p. 094413, sep 2020. [Online]. Available: <https://journals.aps.org/prmaterials/abstract/10.1103/PhysRevMaterials.4.094413>
- [105] J. McCord, “Progress in magnetic domain observation by advanced magneto-optical microscopy,” *Journal of Physics D: Applied Physics*, vol. 48, no. 33, p. 333001, jul 2015. [Online]. Available: <https://doi.org/10.1088/0022-3727/48/33/333001>
- [106] K. S. R. Menon, S. Mandal, J. Das, T. O. Menteş, M. A. Niño, A. Locatelli, and R. Belkhou, “Surface antiferromagnetic domain imaging using low-energy unpolarized electrons,” *Phys. Rev. B*, vol. 84, p. 132402, Oct 2011. [Online]. Available: <https://link.aps.org/doi/10.1103/PhysRevB.84.132402>
- [107] A. Scholl, J. Stohr, J. Lüning, J. W. Seo, J. Fompeyrine, H. Siegwart, J.-P. Locquet, F. Nolting, S. Anders, E. E. Fullerton, M. R. Scheinfein, and H. A. Padmore, “Observation of Antiferromagnetic Domains in Epitaxial Thin Films,” *Science*, vol. 287, pp. 1014–1016, 2000.
- [108] E. Folven, T. Tybell, A. Scholl, A. T. Young, S. T. Retterer, Y. Takamura, and J. K. Grepstad, “Antiferromagnetic Domain Reconfiguration in Embedded LaFeO₃ Thin Film Nanostructures,” *Nano Lett.*, vol. 10, no. 11, pp. 4578–4583, sep 2010. [Online]. Available: <https://pubs.acs.org/doi/abs/10.1021/nl1025908>
- [109] O. Bezencenet, D. Bonamy, R. Belkhou, P. Ohresser, and A. Barbier, “Origin and Tailoring of the Antiferromagnetic Domain Structure in α -Fe₂O₃ Thin Films Unraveled by Statistical Analysis of Dichroic Spectromicroscopy Images,” *Phys. Rev. Lett.*, vol. 106, p. 107201, 2011.
- [110] E. Folven, J. Linder, O. V. Gomonay, A. Scholl, A. Doran, A. T. Young, S. T. Retterer, V. K. Malik, T. Tybell, Y. Takamura, and J. K. Grepstad, “Controlling the switching field in nanomagnets by means of domain-engineered antiferromagnets,” *Phys. Rev. B*, vol. 92, no. 9, p. 094421, sep 2015. [Online]. Available: <http://link.aps.org/doi/10.1103/PhysRevB.92.094421>
- [111] Z. Kaspar, M. Surýnek, J. Zubáč, F. Krizek, V. Novak, R. Campion, M. Wörnle, P. Gambardella, X. Marti, P. Němec, K. Edmonds, S. Reimers, O. Amin, F. Maccherozzi, S. Dhesi, P. Wadley, J. Wunderlich, K. Olejník, and T. Jungwirth, “Quenching of an antiferromagnet into high resistivity states using electrical or ultrashort optical pulses,” *Nature Electronics*, vol. 4, pp. 1–8, 01 2021.
- [112] B. C. De Cooman, Y. Estrin, and S. K. Kim, “Twinning-induced plasticity (twip) steels,” *Acta Materialia*, vol. 142, pp. 283–362, 2018. [Online]. Available: <https://www.sciencedirect.com/science/article/pii/S1359645417305219>

- [113] U. Pietsch, V. Holy, and T. Baumbach, *High-Resolution X-Ray Scattering: From Thin Films to Lateral Nanostructures*, ser. Advanced Texts in Physics. Springer New York, 2004. [Online]. Available: <https://books.google.co.uk/books?id=p8r9PdpYrAC>
- [114] F. Bloch, “Zur Theorie des Ferromagnetismus,” *Zeitschrift fur Physik*, vol. 61, no. 3-4, pp. 206–219, Mar. 1930.
- [115] L. Landau and E. Lifshitz, “On the theory of the dispersion of magnetic permeability in ferromagnetic bodies,” 1935.
- [116] H. J. Williams, “Direction of domain magnetization in powder patterns,” *Phys. Rev.*, vol. 71, pp. 646–647, May 1947. [Online]. Available: <https://link.aps.org/doi/10.1103/PhysRev.71.646.2>
- [117] H. J. Williams, R. M. Bozorth, and W. Shockley, “Magnetic domain patterns on single crystals of silicon iron,” *Phys. Rev.*, vol. 75, pp. 155–178, Jan 1949. [Online]. Available: <https://link.aps.org/doi/10.1103/PhysRev.75.155>
- [118] H. J. Williams and W. Shockley, “A simple domain structure in an iron crystal showing a direct correlation with the magnetization,” *Phys. Rev.*, vol. 75, pp. 178–183, Jan 1949. [Online]. Available: <https://link.aps.org/doi/10.1103/PhysRev.75.178>
- [119] J. Wenisch, C. Gould, L. Ebel, J. Storz, K. Pappert, M. J. Schmidt, C. Kumpf, G. Schmidt, K. Brunner, and L. W. Molenkamp, “Control of magnetic anisotropy in (Ga,Mn)As by lithography-induced strain relaxation,” *Phys. Rev. Lett.*, vol. 99, p. 077201, Aug 2007. [Online]. Available: <https://link.aps.org/doi/10.1103/PhysRevLett.99.077201>
- [120] R. P. Beardsley, D. E. Parkes, J. Zemen, S. Bowe, K. W. Edmonds, C. Reardon, F. Maccherozzi, I. Isakov, P. A. Warburton, R. P. Campion, B. L. Gallagher, S. A. Cavill, and A. W. Rushforth, “Effect of lithographically-induced strain relaxation on the magnetic domain configuration in microfabricated epitaxially grown fe₈₁ga₁₉,” *Scientific Reports*, vol. 7, no. 1, p. 42107, 2017. [Online]. Available: <https://doi.org/10.1038/srep42107>
- [121] T. Kaneyoshi, “Surface magnetism; magnetization and anisotropy at a surface,” *Journal of Physics: Condensed Matter*, vol. 3, no. 25, pp. 4497–4522, jun 1991. [Online]. Available: <https://doi.org/10.1088/0953-8984/3/25/001>
- [122] H. V. Gomonay and V. M. Loktev, “Shape-induced phenomena in finite-size antiferromagnets,” *Phys. Rev. B*, vol. 75, p. 174439, May 2007. [Online]. Available: <https://link.aps.org/doi/10.1103/PhysRevB.75.174439>
- [123] A. D. Bang, I. Hallsteinsen, R. V. Chopdekar, F. K. Olsen, S. D. Sløetjes, K. Kjærnes, E. Arenholz, E. Folven, and J. K. Grepstad, “Shape-imposed anisotropy in antiferromagnetic complex oxide nanostructures,” *Applied Physics Letters*, vol. 115, no. 11, p. 9 2019.

- [124] M. S. Lee, P. Lyu, R. V. Chopdekar, A. Scholl, S. T. Retterer, and Y. Takamura, “Controlling antiferromagnetic domains in patterned $\text{La}_{0.7}\text{Sr}_{0.3}\text{FeO}_3$ thin films,” *Journal of Applied Physics*, vol. 127, no. 20, p. 203901, 2020. [Online]. Available: <https://doi.org/10.1063/5.0006228>
- [125] S. Czekaj, F. Nolting, L. J. Heyderman, P. R. Willmott, and G. van der Laan, “Sign dependence of the x-ray magnetic linear dichroism on the antiferromagnetic spin axis in LaFeO_3 thin films,” *Phys. Rev. B*, vol. 73, p. 020401, Jan 2006. [Online]. Available: <https://link.aps.org/doi/10.1103/PhysRevB.73.020401>
- [126] J. Lüning, F. Nolting, A. Scholl, H. Ohldag, J. W. Seo, J. Fompeyrine, J.-P. Locquet, and J. Stöhr, “Determination of the antiferromagnetic spin axis in epitaxial LaFeO_3 films by x-ray magnetic linear dichroism spectroscopy,” *Phys. Rev. B*, vol. 67, p. 214433, Jun 2003. [Online]. Available: <https://link.aps.org/doi/10.1103/PhysRevB.67.214433>
- [127] N. Hedrich, K. Wagner, O. V. Pylypovskiy, B. J. Shields, T. Kosub, D. D. Sheka, D. Makarov, and P. Maletinsky, “Nanoscale mechanics of antiferromagnetic domain walls,” *Nature Physics*, vol. 17, no. 5, pp. 574–577, 2021. [Online]. Available: <https://doi.org/10.1038/s41567-020-01157-0>
- [128] M. A. Meyers and K. K. Chawla, *Mechanical metallurgy: principles and applications*. Englewood Cliffs, N.J: Prentice-Hall, 1984.
- [129] Y. Shiratsuchi, H. Yoshida, Y. Kotani, K. Toyoki, T. V. A. Nguyen, T. Nakamura, and R. Nakatani, “Antiferromagnetic domain wall creep driven by magnetoelectric effect,” *APL Materials*, vol. 6, no. 12, p. 121104, 2018. [Online]. Available: <https://doi.org/10.1063/1.5053928>
- [130] K. Hattar, “8 - deformation structures including twins in nanograined pure metals,” in *Nanostructured Metals and Alloys*, ser. Woodhead Publishing Series in Metals and Surface Engineering, S. H. Whang, Ed. Woodhead Publishing, 2011, pp. 213–242. [Online]. Available: <https://www.sciencedirect.com/science/article/pii/B9781845696702500083>
- [131] O. Grässel, L. Krüger, G. Frommeyer, and L. Meyer, “High strength fe-mn-(al, si) trip/twip steels development - properties - application,” *International Journal of Plasticity*, vol. 16, no. 10-11, pp. 1391–1409, 2000.
- [132] S. Maat and A. C. Marley, *Physics and Design of Hard Disk Drive Magnetic Recording Read Heads*. Dordrecht: Springer Netherlands, 2013, pp. 1–45. [Online]. Available: https://doi.org/10.1007/978-94-007-7604-3_35-1
- [133] J. Nogués and I. K. Schuller, “Exchange bias,” *Journal of Magnetism and Magnetic Materials*, vol. 192, no. 2, pp. 203–232, 1999. [Online]. Available: <https://www.sciencedirect.com/science/article/pii/S0304885398002662>

- [134] W. H. Meiklejohn and C. P. Bean, “New magnetic anisotropy,” *Phys. Rev.*, vol. 105, pp. 904–913, Feb 1957. [Online]. Available: <https://link.aps.org/doi/10.1103/PhysRev.105.904>
- [135] J. Wu, D. Carlton, J. S. Park, Y. Meng, E. Arenholz, A. Doran, A. T. Young, A. Scholl, C. Hwang, H. W. Zhao, J. Bokor, and Z. Q. Qiu, “Direct observation of imprinted antiferromagnetic vortex states in coo/fe/ag(001) discs,” *Nature Physics*, vol. 7, no. 4, pp. 303–306, 2011. [Online]. Available: <https://doi.org/10.1038/nphys1891>
- [136] Y. Xie, Q. Zhan, Y. Hu, X. Hu, X. Chi, C. Zhang, H. Yang, W. Xie, X. Zhu, J. Gao, W. Cheng, D. Jiang, and R.-W. Li, “Magnetocrystalline anisotropy imprinting of an antiferromagnet on an amorphous ferromagnet in ferh/cofeb heterostructures,” *NPG Asia Materials*, vol. 12, no. 1, p. 67, 2020. [Online]. Available: <https://doi.org/10.1038/s41427-020-00248-x>
- [137] F. Nolting, A. Scholl, J. Stohr, J. W. Seo, J. Fompeyrine, H. Siegwart, J. P. Locquet, S. Anders, J. Luning, E. E. Fullerton, M. F. Toney, M. R. Scheinfein, and H. A. Padmore, “Direct observation of the alignment of ferromagnetic spins by antiferromagnetic spins,” *Nature*, vol. 405, pp. 767+, 2000. [Online]. Available: <https://link.gale.com/apps/doc/A188111179/HRCA?u=anon~2c52fb5c&sid=googleScholar&xid=126d9b0a>
- [138] S. P. Bommanaboyena, D. Backes, L. S. I. Veiga, S. Dhési, Y.-R. Niu, B. Sarpi, T. Denneulin, A. Kovacs, T. Mashoff, O. Gomonay, J. Sinova, K. Everschor-Sitte, D. Schonke, R. M. Reeve, M. Klaui, H. J. Elmers, and M. Jourdan, “Readout of a antiferromagnetic spintronics systems by strong exchange coupling of mn2au and permalloy,” 2021.
- [139] Q. Design, “Mpms3 squid magnetometer,” <https://qd-europe.com/de/en/product/mpms3-squid-magnetometer/>, 09 2021.
- [140] G. D. Nguyen, K. C. Pitike, P. Wadley, V. R. Cooper, M. Yoon, T. Berlijn, and A.-P. Li, “Emerging edge states on the surface of the epitaxial semimetal cumnas thin film,” *Applied Physics Letters*, vol. 116, no. 6, p. 061603, 2020. [Online]. Available: <https://doi.org/10.1063/1.5130624>
- [141] QCAD.org. Open Source CAD, “QCAD: 2D CAD,” <https://www.qcad.org/en/>, 10 2021.
- [142] AUTODESK, “AutoCAD[®],” <https://www.autodesk.co.uk/products/autocad/overview?term=1-YEAR&tab=subscription#what-is-autocad>, 10 2021.

Appendix A

Modelling antiferromagnetic domain walls

In antiferromagnets, magnetic stray fields are generally small, so magnetostatic energy can usually be neglected. Here, we consider a static configuration without external or current-induced fields.

Remaining relevant contributions to the energy AF exchange and anisotropy. Anisotropy can contain the material-characteristic magnetocrystalline anisotropy. Other effects, for example magnetostrictive effects in the presence of strain (induced by clamping to the substrate in thin films or externally applied) can also be incorporated in the anisotropy.

Phenomenological Model

Here, we consider a two-dimensional AF system with strong in-plane anisotropy, so that the Néel vector is confined within the sample plane, $\vec{n} = (n_x, n_y, 0)$ and can fully be describe \vec{n} by its in-plane angle θ . It is furthermore assumed that the Néel vector orientation is constant across the whole thickness of the film: $\vec{n} = \vec{n}(x, y)$.

WLOG x can be defined along the domain wall normal. In a stationary configuration, the magnetic exchange energy must (locally) balance the magnetic anisotropy:

$$\begin{aligned} \text{Exchange} &= \text{Anisotropy} \\ A \left(\frac{d\theta}{dx} \right)^2 &= W_{\text{an}}(\theta), \end{aligned} \tag{A.1}$$

where A is the phenomenological exchange constant.

Thus, a theoretical description of domain walls relies on a (phenomenological) model of the anisotropy. Since relevant for this thesis, 180° domain walls in systems with uniaxial anisotropy, and 90° domain walls in systems with biaxial anisotropy are considered in the following.

Systems with uniaxial anisotropy

Uniaxial anisotropy can be modelled as

$$W_{\text{an}}(\theta) = K \sin^2 \theta,$$

with the angle θ measured with respect to the easy axis and a phenomenological anisotropy constant K .

Hence, using equation eq. (A.1):

$$\begin{aligned} A \left(\frac{d\theta}{dx} \right)^2 &= K \sin^2 \theta \\ \Rightarrow \frac{d\theta}{dx} &= \pm \sqrt{\frac{K}{A}} \sin \theta \\ \Rightarrow \int \frac{1}{\sin \theta} d\theta &= \pm \sqrt{\frac{K}{A}} \int dx \\ \Leftrightarrow \ln(\tan(\theta/2)) &= \pm \sqrt{\frac{K}{A}} x + c, \quad c \in \mathbb{R} \\ \Leftrightarrow \theta &= 2 \operatorname{atan} \left(c \cdot \exp \left(\pm \sqrt{K/A} x \right) \right) + 2k\pi, \quad k \in \mathbb{Z} \end{aligned} \quad (\text{A.2})$$

Defining $d_{\text{DW}} = \sqrt{A/K}$, equation eq. (A.2) can be rewritten as

$$\begin{aligned} \theta &= 2 \operatorname{atan} \left(e^{\pm(x-x_0)/d_{\text{DW}}} \right) + 2k\pi \\ &= \operatorname{acos} \left(\tanh(\pm(x-x_0)/d_{\text{DW}}) \right) + 2k\pi \end{aligned} \quad (\text{A.3})$$

for $x_0 \in \mathbb{R}$ and $k \in \mathbb{Z}$ obtained from the boundary condition. In particular, it follows $\lim_{x \rightarrow \pm\infty} \theta(x) = k\pi$ and $|\lim_{x \rightarrow +\infty} \theta(x) - \lim_{x \rightarrow -\infty} \theta(x)| = \pi$.

Hence, equation indeed describes a 180° domain wall between domains aligned parallel/antiparallel to the easy axis. The two different signs in the exponential in equation eq. (A.3) correspond to the two possible senses of rotation (chiralities). The domain wall is centred at x_0 and the widths over which the spin axis rotates scales with $d_{\text{DW}} = \sqrt{A/K}$.

Thus $d_{\text{DW}} = \sqrt{A/K}$ is a meaningful definition for the domain wall widths.

Systems with biaxial anisotropy

Anisotropy in systems with two mutually orthogonal, equivalent easy axes can be modelled as

$$W_{\text{an}}(\theta) = K \sin^2 2\theta,$$

with the angle θ measured with respect to one of the easy axes.

Analogous to the above argumentation it follows using the same definitions

$$d_{\text{DW}} := \sqrt{A/K}:$$

$$\begin{aligned}
 A \left(\frac{d\theta}{dx} \right)^2 &= K \sin^2 2\theta \\
 \Rightarrow \frac{d\theta}{dx} &= \pm \sqrt{\frac{K}{A}} \sin 2\theta \\
 \Rightarrow \int \frac{1}{\sin 2\theta} d\theta &= \pm \frac{1}{d_{\text{DW}}} \int dx \\
 \Leftrightarrow \frac{1}{2} \ln(\tan \theta) &= \pm \frac{1}{d_{\text{DW}}} x + c, \quad c \in \mathbb{R} \\
 \Leftrightarrow \theta &= \text{atan} \left(e^{\pm 2(x-x_0)/d_{\text{DW}}} \right) + k\pi, \quad k \in \mathbb{Z}. \quad (\text{A.4})
 \end{aligned}$$

Since $\lim_{x \rightarrow \pm\infty} \theta(x) = k\frac{\pi}{2}$ and $|\lim_{x \rightarrow +\infty} \theta(x) - \lim_{x \rightarrow -\infty} \theta(x)| = \frac{\pi}{2}$, equation eq. (A.4) indeed describes a 90° domain wall between domains aligned with the two orthogonal easy axes.

Appendix B

Device Fabrication

Below is a step-by-step description of the device fabrication protocols.

B.1 Photolithography and chemical wet etching

Photolithography the device design must be printed onto a chrome plated soda lime mask with suitable size. The devices are designed (internally) using QAD [141], but the fabrication of the photomask is done externally. The following fabrication steps are carried out in the cleanroom facilities at Nottingham.

1. Scribe chip from the wafer along the cleave edges of the substrate with a Dynapert scriber.
2. Solvent clean samples in the following solvents:
 - Ethyl lactate (> 2 min)
 - Methanol (> 2 min)
 - Acetone (> 2 min)
 - IPA (> 2 min)
3. Spin coat a layer of AZ ECI 3007 positive photoresist onto the chip, using Laurell spin-coater at 4000 rpm for 30 s.
4. Remove edge beading with fine-tip cotton bud.
5. Bake chip on a hotplate at 85 °C to 90 °C for 1 min.
6. Load chip into a Suss MJB-3 photolithography aligner with the photomask containing the device design.
7. Align the chip edges with the mask as desired.
8. Expose (to UV-light) for 6 s with a dose of 9.5 mW cm⁻²
9. Develop the pattern in a developer solution of AZ400K:H₂O (ratio 1 : 6) for 15 s. This removes the exposed photoresist and the Al cap underneath.

10. Dip chip in deionised water to avoid overdevelopment.
11. Etch the chip in $\text{H}_2\text{O}:\text{H}_2\text{O}_2:\text{H}_3\text{PO}_4$, ratio 400:10:1, for a sufficiently long time, depending on the CuMnAs layer thickness. The CuMnAs layer is etched at a rate of 1 nm s^{-1} .
12. Rinse in deionised water.
13. Remove remaining photoresist with acetone and rinse directly in IPA.

For metallic (here gold) contact pads (not always used):

15. Repeat steps 6-10, but with a different mask, leaving free the areas for the contact pads.
16. Evaporate a 150 nm thin gold layer onto the chip, using an evaporator in a low vacuum chamber ($\sim 1 \times 10^{-3}$ mbar).
17. Repeat step 13 to remove the remaining photoresist (with the gold layer on top of it). The gold layer in photoresist-free regions remains.

B.2 Electron beam lithography and ion beam milling

For electron beam lithography (EBL) a software-file of the device design is sufficient, here created using AutoCAD software [142]. No physical mask is required. The fabrication runs as follows.

1. Scribe chip and solvent clean sample (Steps 1,2 for photolithography).
2. spin coat a 200 nm thick layer of AR-P 6200.09 (allresist GmbH, Strausberg) onto the chip, using Laurell spin-coater at 4000 rpm for 60 s.
3. Bake on a hot plate for 6 min at 85°C
4. load into the EBL-machine: nanobeam nB5 (nanobeam limited, Cambridge) and load the pattern. The nB5 software fractures the pattern into $500 \mu\text{m}$ write fields which are stitched together.
5. Set EBL acceleration voltage to 80 kV, current of 2 nA
6. Focus beam using a scratch on a corner.
7. Use automatic astigmatism and alignment control.
8. Ensure that the edges of the (separate) write fields do not cross critical areas of the sample.
9. Expose the pattern using a dose of $465 \mu\text{C cm}^{-2}$.
10. Develop the sample in AR 600-546 for 60 s.
11. Rinse in IPA for 30 s to halt development.
12. Give the sample to Andrew Rushforth for Ar+ ion beam milling.

Appendix C

Supplementary Videos

All supplementary videos as well as the individual frames can be accessed online here

shorturl.at/awAU9. The individual frames of each video are stored in the folder with the corresponding name.

Supplementary Video S1, corresponding to Fig. 3.7. 6.4 μm XMLD-PEEM images of one area with increasing x-ray polarisation angles from $\phi = -73^\circ$ to $\phi = 105^\circ$ measured clock-wise with respect to the CuMnAs [110] direction, horizontal in the image, namely:

$\phi = -73, -60, -50, -45, -30, -15, 0, 15, 30, 45, 65, 80, 95, 105^\circ$.

Supplementary Video S2, corresponding to Fig. 3.13. 5.9 μm XMLD-PEEM images of one area with increasing x-ray polarisation angles from $\phi = -68^\circ$ to $\phi = 110^\circ$ measured clock-wise with respect to the CuMnAs [110] direction, horizontal in the image: $\phi = -73, -60, -45, -30, -15, 0, 15, 30, 45, 60, 75, 90, 105^\circ$.

Supplementary Video S3, corresponding to Fig. 7.4. Time-series of XMLD-PEEM images of the AF domain structure when cooling through the Néel temperature, Sample A cycle I.

Supplementary Video S4, corresponding to Fig. 7.5. Time-series of XMLD-PEEM images of the AF domain structure when cooling through the Néel temperature, Sample A cycle I.

Supplementary Video S5, corresponding to Fig. 7.6. Time-series of XMLD-PEEM images of the AF domain structure during cooling, Sample A cycle I - full field-of view.

Supplementary Video S6, corresponding to Fig. 7.8. Time-series of XMLD-PEEM images of the AF domain structure during heating, Sample A cycle II.

Supplementary Video S7, corresponding to Fig. 7.9. Time-series of XMLD-PEEM images of the AF domain structure during cooling, Sample A

cycle II.

Supplementary Video S8a, corresponding to Fig. 7.10. Time-series of LEEM images of the microtwin pattern when heating from intermediate to high temperatures, Sample B. Full field of view.

Supplementary Video S8b, corresponding to Fig. 7.10. Time-series of LEEM images of the microtwin pattern when heating from intermediate to high temperatures, Sample B. Cropped to the area shown in panel C.

Supplementary Video S9, corresponding to Fig. 7.11. Time-series of LEEM images of the microtwin pattern when heating from intermediate to high temperatures, Sample B.

Supplementary Video S10, corresponding to Fig. 7.13. Time-series of XMLD-PEEM images of the AF domain structure during cooling, Sample B.

Supplementary Video S11, corresponding to Fig. 8.6. LEED pattern of an exposed 50 nm CuMnAs/GaP(001) film measured in the LEEM instrument while increasing the sample bias from 32 eV to 300 eV. The straight horizontal and vertical lines are artefacts from the detector. The rotation of the LEED pattern with respect to the image axes is due to the imaging optics.

Appendix D

List of Abbreviations

APB	antiphase boundary (crystallographic defect)
AF	antiferromagnet/antiferromagnetic
AMR	anisotropic magnetoresistance
DLS	Diamond Light Source
DW	domain wall, here every magnetic texture which separates two areas with uniform magnetisation
EBL	Electron beam lithography
FM	ferromagnet /ferromagnetic
HAADF	high-angle annular dark-field
LEEM	low energy electron microscopy
PEEM	photoelectron emission microscopy
STEM	scanning transmission electron microscopy
(S)XRD	(scanning) x-ray diffraction
SXDM	Scanning x-ray diffraction microscopy
XLD	x-ray linear dichroism, considered as structural (natural dichroism in contrast to magnetic linear dichroism)
XMCD	x-ray magnetic circular dichroism
XMLD	x-ray magnetic linear dichroism